Cortical circuits underlying social and spatial exploration in rats

DISSERTATION

zur Erlangung des akademischen Grades

D o c t o r r e r u m n a t u r a l i u m

(Dr. rer. nat.)

im Fach Biologie

eingereicht an der

Lebenswissenschaftlichen Fakultät

der Humboldt-Universität zu Berlin

von

M.Sc.

Christian Laut Ebbesen

Präsidentin der Humboldt-Universität zu Berlin

Prof. Dr.-Ing. Dr. Sabine Kunst

Dekan der Lebenswissenschaftlichen Fakultät

Prof. Dr. Bernhard Grimm

Gutachter

1. Prof. Matthew Larkum, Ph.D.
2. Dr. James Poulet
3. Prof. Dr. Michael Brecht

Tag der mündlichen Prüfung: 6. Juli 2017

Cortical circuits underlying social and spatial exploration in rats

Doctoral candidate:
Christian Laut Ebbesen

Supervisors:
Prof. Dr. Michael Brecht
Prof. Dr. Gabriel Curio

April 2017

Berlin School of Mind and Brain
Bernstein Center for Computational Neuroscience
Animal Physiology / Systems Neurobiology and Neural Computation
Humboldt Universität zu Berlin, Berlin, Germany

Table of Contents

1. Abstract **1**

2. Zusammenfassung **3**

3. General Introduction & Thesis Outline **4**

3.1 General Introduction 4

3.1.1 Why do we study the brain?. 4

3.1.2 Three heuristics for investigating neural circuits 4

3.1.3 Neuroethology & functional localization 5

3.1.4 How should we look a cortical data? 7

3.2 Thesis Outline 8

3.2.1 Two investigations into cortical function 8

3.2.2 Part 1: Parahippocampal cortex and neural circuits underlying spatial exploration 9

3.2.3 Part 2: Motor cortex and neural circuits underlying social exploration 12

3.3 References 15

4. Pyramidal and Stellate Cell Specificity of Grid and Border Representations in Layer 2 of Medial Entorhinal Cortex **22**

4.1 Introduction. 23

4.2 Results. 23

4.3 Discussion. 28

4.4 Experimental Procedures 28

4.5 References 29

4.6 Supplemental Information. 30

5. Functional Architecture of the Rat Parasubiculum **52**

5.1 Introduction. 53

5.2 Materials and Methods 54

5.3 Results. 56

5.4 Discussion. 59

5.5 References 64

6. Cell Type-Specific Differences in Spike Timing and Spike Shape in the Rat Parasubiculum and Superficial Medial Entorhinal Cortex **66**

6.1 Introduction. 68

6.2 Results. 69

6.3 Discussion. 74

6.4 Experimental Procedures 76

6.5 References 77

6.6 Supplemental Information. 79
7. Vibrissa motor cortex activity suppresses contralateral whisking behavior 90
7.1 Introduction. 93
7.2 Results. 94
7.3 Discussion. 99
7.4 References 102
7.5 Figures. 107
7.6 Methods. 120
7.7 Methods References 128
8. Motor cortex – To act or not to act? 130
8.1 Introduction. 133
8.2 From motor cortex to muscle output 135
8.3 Inactivation studies: Acting without motor cortex. 142
8.4 Motor cortex – not to act?. 144
8.5 Conclusions 147
8.6 References 150
8.7 Figures. 161
9. General Discussion 168
9.1 Parahippocampal cortex and neural circuits underlying spatial exploration 168
9.1.1 Structure-function relationships in parahippocampal cortex 168
9.1.2 How are grid cells made? 168
9.1.3 What does the grid cell system teach us about cortical computation? 170
9.2 Motor cortex and neural circuits underlying social exploration 172
9.2.1 What is the function of rat vibrissa motor cortex?. 172
9.2.2 Social computations in sensorimotor cortex. 173
9.3 References 174
10. Curriculum vitae 182
11. List of publications 184
12. Declaration of contribution 185
13. Acknowledgements 190

PLACER

List of Figures

Figure 1 The cerebral cortex is the outermost cell layers of the mammalian telencephalon. . . . 5

Figure 2 An example of viewing cortical data in the 'right' way? 7

Figure 3 Schematic showing the location of motor cortex and parahippocampal cortex in the rat brain. 9

Figure 4 Hippocampal place cells. 9

Figure 5 Spatial discharge patterns of neurons in parahippocampal cortex. 10

Figure 6 Social facial touch 13

Figure 7 Movement suppression is under-represented in depictions of motor cortex 14

Figure 8 Graphical abstract outlining the main message of this chapter. 22

Figure 9 A Wistar rat it reins. 90

Figure 10 Modular cytoachitectonics of parahippocampal cortex. 148

Figure 11 Grid-cell-like responses of entorhinal neurons to saccades across a visual scene. . . . 149

Figure 12 What are cortical neurons doing? 151

Declaration

I declare that the doctoral thesis entitled *Cortical circuits underlying social and spatial exploration in rats* represents an original work of the author apart from the references and declared contributions under the provisions § 6 (3) of the doctoral degree regulations, dated 5 March 2015, of the faculty of Life Sciences of Humboldt-Universität zu Berlin. The work involved no collaborations with commercial doctoral degree supervisors. I affirm that I have neither applied for nor hold a corresponding doctoral degree and this work has not been submitted in full or part to another academic institution. Further, I acknowledge the doctoral degree regulations which underlie this procedure, and state that I abided by the principles of good academic practice of Humboldt-Universität zu Berlin.

Unterschrift von PDF entfernt

Christian Laut Ebbesen, April 2017

1. Abstract

In order to understand how the mammalian brain works, we must investigate how neural activity contributes to cognition and generates complex behavioral output. In this thesis I present work, which focuses on two regions of the cerebral cortex of rats: parahippocampal cortex and motor cortex. In the first part of the thesis we investigate neural circuits in the parasubiculum and the superficial medial enthorhinal cortex, two structures that play a key role in spatial cognition. Briefly, we find that the in these regions, anatomical identity and microcircuit embedding is a major determinant of both spatial discharge patterns (such as the discharge patterns of grid cells, border cells and head-direction cells) and temporal coding features (such as spike bursts, theta-modulation and phase precession). In the second part of the thesis we investigate the activity of neurons in vibrissa motor cortex during complex motor behaviors, which play a vital role in rat ecology: self-initiated bouts of exploratory whisking in air, whisking to touch conspecifics during social interactions and whisking to palpate objects. Briefly, we find that neural activity decreases during whisking behaviors, that microstimulation leads to whisker retraction and that pharmacological blockade increases whisker movement. Thus, our observations collectively suggest that a primary role of vibrissa motor cortex activity is to suppress whisking behaviors. The second part of the thesis concludes with a literature review of motor suppressive effects of motor cortical activity across rodents, primates and humans to put this unexpected finding in a broader context.

2. Zusammenfassung

Um zu verstehen, wie das Gehirn von Säugetieren funktioniert, untersuchen wir wie neuronale Aktivität einerseits zu Kognition beträgt und andererseits komplexe Verhaltensweisen ermöglicht. Im Fokus dieser Doktorarbeit stehen dabei zwei Regionen der Großhirnrinde der Ratte: der parahippocampale Cortex und der motorische Cortex. Im ersten Teil haben wir neuronale Schaltkreise im parahippocampalen Cortex und in den oberen Schichten des enthorhinalen Cortex untersucht, während Ratten ihre Umgebung räumlich erkunden. Diese beiden Regionen tragen wesentlich zum Orientierungssinn bei. Dabei haben wir herausgefunden, dass anatomische Identität und Einbindung in den Microschaltkreis einerseits räumliche neuronale Signale, wie zum Beispiel der Aktivität von grid cells, border cells und head-direction cells, bestimmen. Andererseits tragen diese beiden Eigenschaften auch zur temporalen Präzision neuronaler Signale bei, wie zum Beispiel in Form von spike bursts, theta Modulation und phase precession. Im zweiten Teil dieser Doktorarbeit untersuchen wir die Aktivität von Neuronen im Vibrissen Motorcortex während komplexer Bewegungsabläufe der Schnurrhaare, die dem natürlichen Repertoire der Ratte entstammen: eigeninitiierte Bewegungen in freier Luft, Berührung von Artgenossen zur sozialen Interaktion und das Abtasten von Objekten. Dabei haben wir herausgefunden, dass neuronale Aktivität im Motorcortex während der Bewegung der Schnurrhaare unterdrückt ist, dass elektrische Microstimulation zum Rückzug der Schnurrhaare führt und, dass pharmakologische Blockade Bewegung der Schnurrhaare fördert. Um diese überraschende Beobachtung in einen breiteren Kontext zu integrieren, endet dieser Teil mit einer Bewertung der Literatur zu der bewegungsunterdrückenden Wirkung von Motorcortex Aktivität bei Nagetieren, Primaten und Menschen.

3. General Introduction & Thesis Outline

3.1 General Introduction

3.1.1 Why do we study the brain?

Three major factors make the mammalian forebrain one of the most interesting structures in the universe: a perspective of basic health care, a perspective of introspection and a political perspective. First, a better understanding of the mammalian neurobiology would be immensely helpful in designing novel therapeutic strategies for mental conditions. These conditions have high incidence and major impact on life quality, but presently totally dissatisfactory treatment options (Connell et al., 2014; Diener et al., 1999; Lehman, 1996; WHO, 1995). Thus, advances in this regard would have massive positive effects on public welfare. Secondly, understanding the neural circuits, which give rise to our own conscious first-person perspective, is intrinsically interesting. It provides a unique avenue to explore our own subjectivity as humans and as part of the mammalian family. Thirdly, while some aspects of political ideology are strictly normative, they also often encompass (in a more or less explicit manner) assumptions about neurobiology. Suppositions about how e.g. reward, competition and motivation modulate behavior are ultimately statements about brain function, which presently remain largely unverified. Clearly, any extrapolation from scientific findings to societal policy must be extremely cautious (cf. historical 'scientific' racism, classism and heteronormativity (Bashford and Levine, 2010; Belkhir, 1994)). Nevertheless, aligning 'folk psychology' assumptions underlying how e.g. society and economics is currently structured more closely with empirical studies of the neural control of behavior is bound to positively influence how we collectively organize (Churchland, 1981; Fitzgerald et al., 2014; Žižek, 1989).

3.1.2 Three heuristics for investigating neural circuits

To effectively investigate how brain structure contributes to the generation of cognition and complex behavioral output, we must design our studies such that three practical conditions are satisfied: First, we must be able to record and manipulate neural activity with high fidelity and high temporal and anatomical resolution. Secondly, we must investigate neural activity when the animal is doing behaviors, which actually drive the neural circuits in a way, which allows them to reveal their function experimentally. Finally, when we have good data from interesting behaviors, we must analyze and look at these data in an appropriate way.

In the last decade, our capability in the first domain has made immense advances. There has been

a massive progress in the technical tools, which we can use to monitor and manipulate neural activity of awake, behaving animals with (sub)-cellular resolution, e.g. abundantly available transgenic animals and viral tools (Harris et al., 2014; Heldt and Ressler, 2009; Witten et al., 2011), optogenetics (Deisseroth, 2015; Kim et al., 2017), DREADDs (Whissell et al., 2016), in-vivo multi-photon imaging of various sensors (Broussard et al., 2014; Yang and Yuste, 2017), high-density electrophysiology (Buzsáki et al., 2015), advanced statistical/data-mining methods (Aljadeff et al., 2016; Harris et al., 2016), etc. However, our main challenge is not only to record neural activity from an ever-increasing number of cells with ever-increasing fidelity. Rather, we also need advances in our ability to satisfy the second and third condition, i.e. to identify correct behaviors to drive cortical activity and to analyze and view the data in the proper way. This is beautifully illustrated by two classic studies on the mammalian cerebral cortex: The discovery of motor cortex by Fritch and Hitzig (Fritsch and Hitzig, 1870) and the discovery of orientation tuning in visual cortex by Hubel and Wiesel (Hubel and Wiesel, 1959).

3.1.3 Neuroethology & functional localization

The cerebral cortex (Figure 1) is the most recently evolved brain structure across phylogeny and a massive amount of evidence coherently points to a major role of cortex in 'high-level' cognitive capacities (DeFelipe, 2011; Molnár et al., 2014). The neural 'workload' is not uniformly distributed across cortical neurons, but rather, certain domains of neural computation are – at least to some degree – localized to distinct cortical regions (Brett et

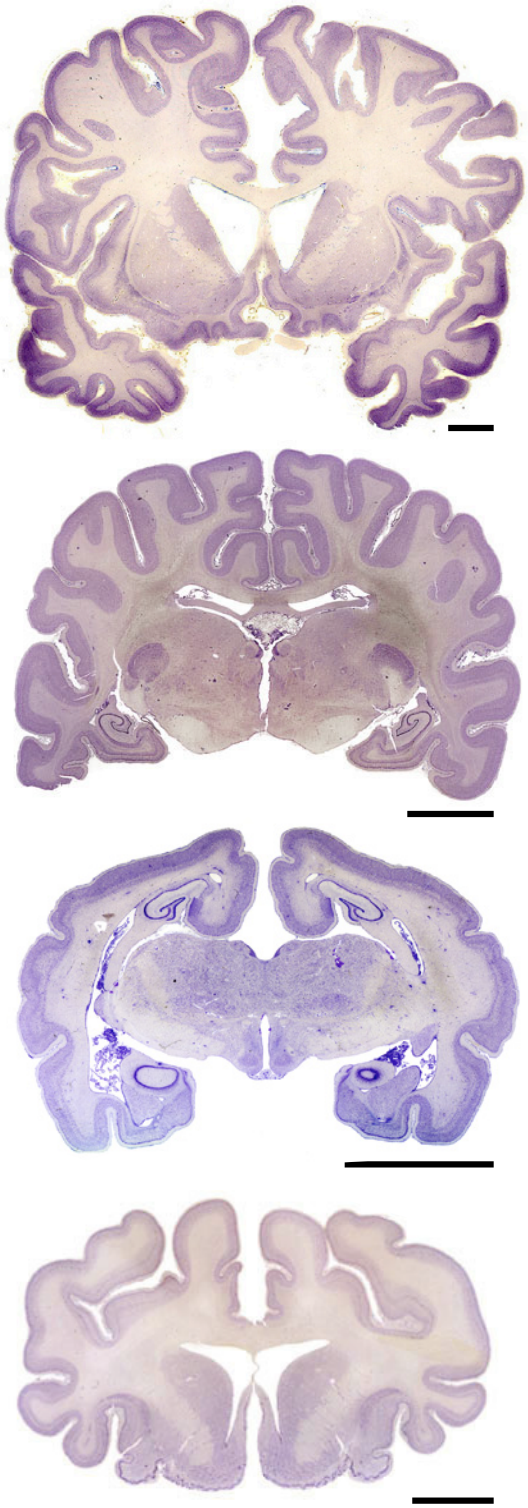

Figure 1: The cerebral cortex is the outermost cell layers of the mammalian telencephalon. Top to bottom: Brain of human, lion, grey kangaroo and polar bear (coronal sections, thionin stain, cell bodies appear dark purple in color). Scale bar = 1 cm. Adapted with permission from http://www.brains.rad.msu.edu, supported by the US National Science Foundation.

al., 2002; Campbell, 1905; Zola-Morgan, 1995). This cortical localization can be revealed by interventions, which manipulate neural activity in a pinpointed way, for example by the focal inactivation (classically e.g. by lesioning) or activation (classically e.g. by intra-cortical electrical stimulation) of neural activity. Such localized perturbations of cortical activity lead to highly domain-specific changes (i.e. deficits) in cognitive or behavioral function.

The first and most 'classic' cortical localization experiment was done in Berlin in the 1870s. Two young doctors discovered, that when they applied weak stimulation currents to the cortical surface of anaesthetized rabbits and dogs, they would sometimes elicit muscle twitches. These twitches were only elicited in certain, specific parts of the frontal cortex, a brain region we now refer to as primary motor cortex (Fritsch and Hitzig, 1870). This discovery was a major breakthrough in cortical physiology, since it gave a hint that neurons in this part of the cortex must be somehow involved the control of muscle output, i.e. motor control. Thus, to investigate these function of these neurons, subsequent investigations in awake animals and humans have focused on recording the activity patterns of motor cortical neurons during various behaviors, which require movement, muscle action and fine motor control (Graziano, 2011; Lemon, 2008; Shenoy et al., 2013).

Such studies on motor cortical activity during motor behavior have yielded major insights (Lemon, 2008; Shenoy et al., 2013), and exemplify the power of recording the activity pattern of neurons during behaviors, which actually drive their activity in a natural, biological way. We can draw a general conclusion: in order to satisfy the second heuristic mentioned above, neurobiology must rely heavily on ethological approaches. In order to investigate neural coding, we must incorporate findings from the study of animal behavior in natural conditions and design our experiments such that we investigate neural signals in animals performing behaviors, which resemble the naturally occurring environmental challenges that these neural circuits have evolved to overcome (e.g. the activity of motor cortical neurons during motor behaviors) (Krakauer et al., 2017). If we design our experiments such that the experimental animal must e.g. repeatedly perform an experimental task (e.g. respond to a repeated sensory stimulus (Connor et al., 2010; O'Connor et al., 2009)), we are almost certain to find neurons which spuriously correlate with task-related parameters, simply due to the repeated structure of the task design. The neural activity pattern may not in any meaningful way reflect what these neurons are 'really doing' (Krakauer et al., 2017).

3.1.4 How should we look a cortical data?

Neural signals are recorded in the temporal domain, so relating the function of cortical spikes to behavior requires appropriate mathematical transformations. This means, that even if we can record neural activity with high fidelity during relevant, ecological behavior, where these neurons are highly involved in the task, it is not guaranteed that we will gain any new insights about neural function. In fact, major breakthroughs in our understanding of neural coding have not been driven by technical advances, but by conceptual advances: By looking at neural data in the 'right' way.

The Nobel-Prize winning discovery of visual orientation tuning by Hubel and Wiesel is an example of this principle. At the time of their discovery, anatomical observations and observations on behavioral changes following cortical lesions suggested that striate cortex (now 'primary visual cortex') was involved in visual processing (Hubel and Wiesel, 1998; Wurtz, 2009). However, it was unclear how neurons physically implemented the representation of visual stimuli. It was known that the neuronal response to a circular light stimulus, a classically used visual stimulus at the time, depended on the retinal location. Some retinal locations elicited an increase in spike rate, and some retinal locations lead to suppression of spike rates, but there were no obvious correlations between the stimulus and the spike discharges (Wurtz, 2009). Hubel & Wiesel discovered that if they recorded the activity of single neurons when the cat was being presented with a light bar

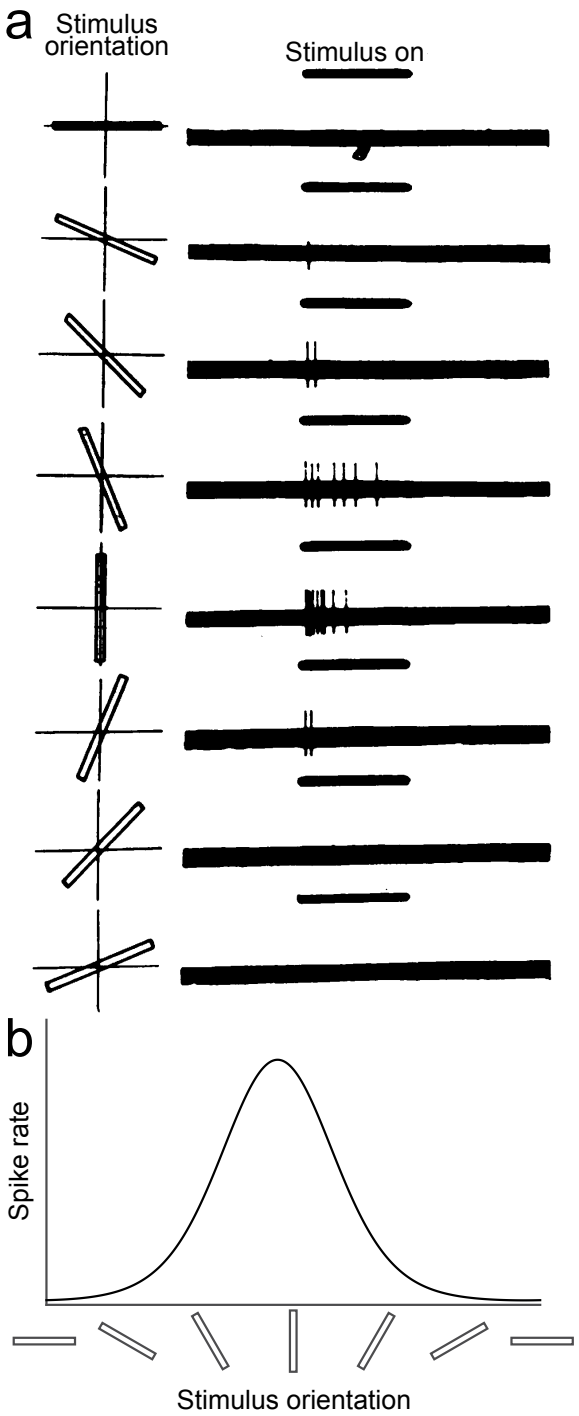

Figure 2: An example of viewing cortical data in the 'right' way? (a) Example responses (right) of a single neuron in cat visual cortex to various orientations of light bar stimulus (left). Single spikes are visible as vertical lines, stimulus presened for 1s. (b) Plotting the spike rate during stimulus presentation as a function of the stimulus orientation reveals a clear and elegant pattern: the neuron is symmetrically tuned for a specific orientaion (schematic depicts a von Mises pdf). (Adapted from Hubel & Wiesel, 1959, with permission, Wiley and Sons)

stimulus at various orientations (Figure 2a) and the neuronal discharge rate was plotted as a function of the stimulus orientation, a simple and elegant pattern emerged: single neurons showed sharp, symmetric tuning to the orientation of the bar (Figure 2b) (Hubel and Wiesel, 1959).

Discovering such a beautiful pattern makes it appear likely, that we are now looking at the neural data in the 'correct' way. However, it is important to keep in mind, that from a standpoint of information theory, there is in principle no reason why neurons should implement neural algorithms in a way such that the activity of single cells display beautiful patterns. In a wide range of computational problems, it is fully possible for a network to reach equal (and better) performance using distributed network representations, which have no obvious patterns or 'aesthetic' qualities when considering intermediate levels or subsets of nodes (Borst and Theunissen, 1999; Dayan et al., 2011; Fairhall et al., 2012; Harris, 2005; Kaufman and Churchland, 2016; Shenoy et al., 2013). A similar argument can be made about physical laws in general. There is – in principle – no reason why it should be possible to express fundamental laws of e.g. field theory or quantum mechanics in simple, elegant equations. Nonetheless, it *is* possible and seems to be a deep organizational principle of known physics (Elliott and Dawber, 1979; Feynman et al., 1963).

The concept of searching for elegant patterns in nature has historically been an incredible successful guiding heuristic in physics. In physics, there are statistical arguments which may provide some explanations as to why the patterns we observe in nature are so 'neat' (Hardy, 2001; Aaronson, 2004), but these arguments are not easy to make about biological systems which have arisen through evolution. Nonetheless, in cortical physiology, we may use the discovery of easily interpretable spiking patterns (e.g. clear orientation tuning), as a heuristic principle to guide investigations into neural coding in the cortex: If we discover neurons with obvious, elegant patters, this can serve as a good starting point for our investigations.

3.2 Thesis Outline

3.2.1 Two investigations into cortical function

In this thesis, I will present work, which focuses on two parts of the cerebral cortex of rats: the parahippocampal cortex and motor cortex (Figure 3). We have investigated the neural activity in these two cortical regions during two kinds of complex, ecological behaviors: spatial exploration and social exploration. Our knowledge about the two cortical regions, which we have studied, aligns differentially

with the three heuristics discussed above. Consequently, the questions we could ask and the scientific contributions we could make to the study of these two cortical areas have different characteristics. In this thesis, I will only present work from studies during PhD, where I had a major contribution (i.e. first or co-first authorships). For a full list of publications during my PhD studies, please refer to Chapter 11.

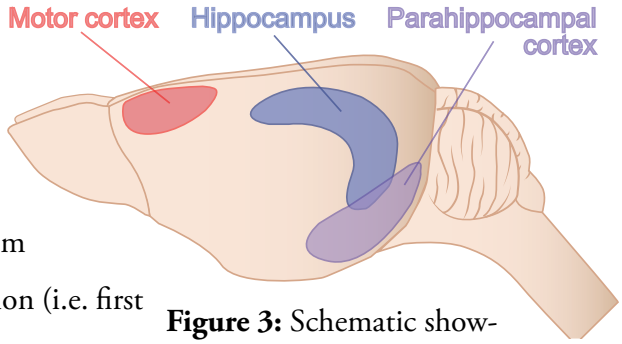

Figure 3: Schematic showing the location of motor cortex (red) and parahippocampal cortex (purple) in the rat brain. (Adapted from Poucet & Sargolini, 2013, w. permission, Nature NPG)

3.2.2 Part 1: Parahippocampal cortex and neural circuits underlying spatial exploration

In the first part of the thesis, we investigate the activity in parahippocampal cortex during spatial exploration. Specifically, we look at activity in the superficial layers of the medial entorhinal cortex and at the parasubiculum, when rats are foraging for chocolate rewards in an open arena, in darkness.

Even though such a chocolate foraging task appears very simple, it forces the animal to perform sophisticated neural computations. The fact that the task is done in darkness means that the animal is excluded from using distant visual cues to guide its movement. Rather, to navigate the open arena, the animal must integrate haptic, olfactory and proprioceptive information to generate an internal cognitive representation of the external space. Famously, in the dorsal hippocampus, there is a population of neurons which discharge spikes only when the animal is moving in specific parts of space ('place cells', O'Keefe and Dostrovsky, 1971; Muller et al., 1987; Figure 4). Numerous lesion studies point to a major role of these neurons in the generation of an internal cognitive 'map' (Bird and Burgess, 2008; Eichenbaum, 2017; McNaughton et al., 2006; Moser et al., 2008).

The medial entorhinal cortex is an elongated structure at the most posterior end of the rodent cerebral cortex, which provides a massive,

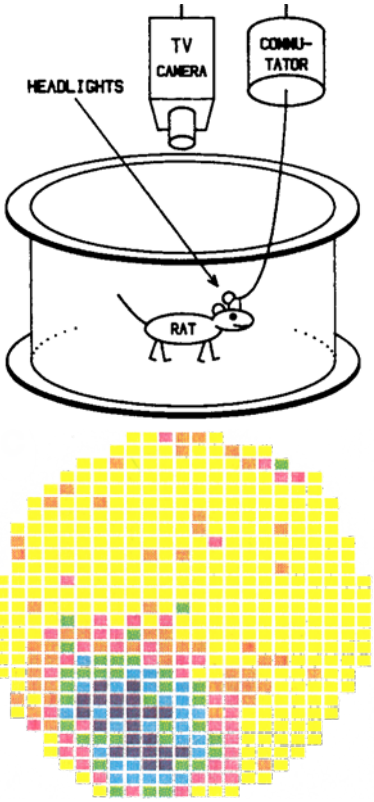

Figure 4: Hippocampal place cells. Top: setup for recording behavior ('headlights' and camera) and neural activity (to commutator, etc.) of a freely moving rat. Below: Firing probabilty of a hippocampal neuron as a function of the rat's location in the arena (yellow = low, dark blue = high probability). (Adapted from Muller et al., 1987, with permission, Soc. for Neurosci)

excitatory input to the hippocampus (Ray et al., 2014; Varga et al., 2010). Since the medial entorhinal cortex is 'upstream' of the hippocampal place cells, several studies have investigated the activity patterns in medial entorhinal cortex during spatial behavior to elucidate which kind of 'spatial' input patterns hippocampal neurons might inherit from the medial entorhinal cortex (Bush et al., 2014; Rowland et al., 2016). These studies have described an array of striking spatial firing patterns, most prominently grid cells (neurons, which discharge in a regular, hexagonal 'grid' pattern, Figure 5, left, Hafting et al., 2005), border cells (neurons, which discharge when the animal is near borders in the environment, Figure 5, middle, Solstad et al., 2008) , band cells (neurons which discharge in periodic 'bands' across the arena, Krupic et al., 2012) and head-direction cells (neurons, which discharge when the animal is facing a specific direction, Figure 5, right, Taube et al., 1990; Boccara et al., 2010).

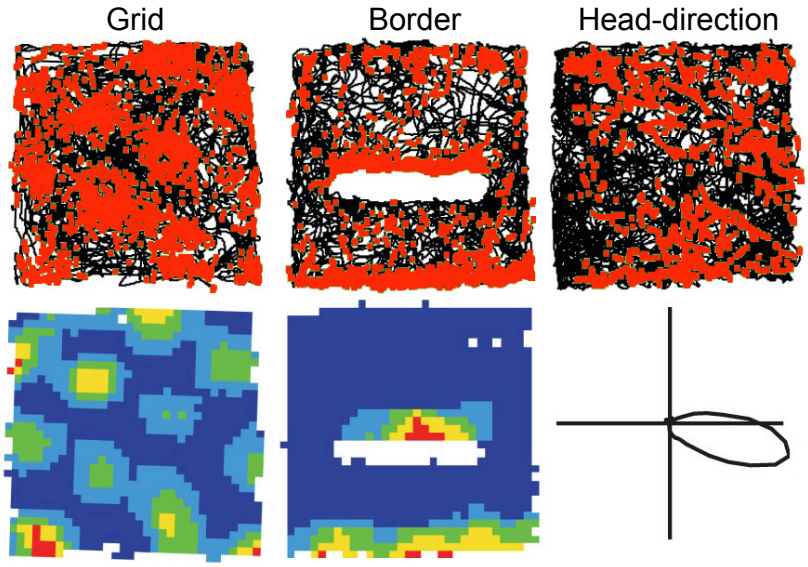

Figure 5: Spatial discharge patterns of neurons in parahippocampal cortex: A grid cell, a border cell and a head-direction cell. Top row shows running trajectory (black line) and spatial locations of spikes of a single neuron (red dots) from a rat exploring a square arena, or a sqare arena with a high 'wall-like' obstacle in the center. Bottom row shows the spiking probability as a function of the rat's location in the arena (blue = low, red = high prob.) or as a function of the rat's heading direction (indicated by compass cross). (Adapted from Hartley et al. 2014, with permission, The Royal Soc.).

When I started my PhD work, there was already a wealth of theoretical and computational models, which proposed various cellular-level and network-level mechanisms, which could generate hippocampal place cells from spatial inputs from the entorhinal cortex (Burgess and O'Keefe, 2011; Giocomo et al., 2011; Zilli, 2012). Layer 2 of the medial entorhinal cortex contains two excitatory cell types: stellate neurons and pyramidal neurons (Alonso and Klink, 1993) (arguably with additional subdivisions, Fuchs et al., 2016). These two cell types are arranged in a remarkable modular fashion, which mirrors the hexagonal pattern of the grid cells (Kitamura et al., 2014; Ray et al., 2014). Crucially, these two cell types have very different projection patterns: stellate neurons project primarily to the dentate gyrus (Ray et al., 2014; Varga et al., 2010), while pyramidal send a comparatively much smaller projection to CA1 (Kitamura et al., 2014). Thus, the interpretation of what e.g. the entorhinal grid cells contribute

to spatial coding in the hippocampus depends on which hippocampal subfields receive these inputs. In **Chapter 4** of this thesis, I present a study, where we used statistical machine learning methods combined with juxtacellular recordings from identified neurons and tetrode recordings from unidentified neurons to investigate how spatial response patterns (grid, border, head-direction) map onto stellate and pyramidal neurons:

(*)Tang, Q., (*)Burgalossi, A., **(*)Ebbesen, C.L.**, Ray, S., Naumann, R., Schmidt, H., Spicher, D. & Brecht, M. (2014) Pyramidal and Stellate Cell Specificity of Grid and Border Representations in Layer 2 of Medial Entorhinal Cortex. **Neuron**, 84(6):1191-1197.

The parasubiculum is a thin structure, which wraps around the medio-dorsal edge of the medial entorhinal cortex (Andersen et al., 1971), receives various cortical and subcortical input and sends a major projection to the superficial layers of medial entorhinal cortex (Caballero-Bleda and Witter, 1993, 1994; van Groen and Wyss, 1990). In **Chapter 5** of this thesis I present a study, where we investigate which kind of spatial and temporal response patterns are already present in the parasubiculum (Boccara et al., 2010), 'upstream' of the medial entorhinal cortex, and how the modular cytoarchitechture of the medial entorhinal cortex determines how entorhinal microcircuits may inherit such information from the parasubiculum:

(*)Tang, Q., (*)Burgalossi, A., **(*)Ebbesen, C.L.**, (*)Sanguinetti-Scheck, J.I., Schmidt, H., Tukker, J.J., Naumann, R., Ray, S., Preston-Ferrer, P., Schmitz, D., Brecht, M. (2016) Functional Architecture of the Rat Parasubiculum. **Journal of Neuroscience** 36(7):2289-2301.

The role of hippocampal spike timing in (spatial) memory is the most studied example of temporal coding in all of neuroscience (Colgin, 2016; Hasselmo, 2005; Howard and Eichenbaum, 2015). Despite the enormous scientific interest, we still know surprisingly little about how temporal coding features like spike bursts, theta-modulation (rhythmicity, locking, skipping) and phase precession map onto hippocampal and parahippocampal microcircuits. The paucity of data on the relationship between phase precession and microcircuits reflects the fact that the majority of studies have recorded tetrode data. This has given rise to a pleathora of theory and modeling of how the temporal coding patterns are generated and what their function might be (Colgin, 2016; Giocomo et al., 2011; Hasselmo, 2005; Zilli, 2012). The only way to prune this forest of models is to establish how temporal coding maps onto anatomically distinct cell types and microcircuits. In **Chapter 6** of this thesis, I present a

study where we analyze a large sample of cells recorded juxtacellularly in freely moving rats and ask how temporal coding maps onto the modular organization of parahippocampal cortex:

Ebbesen, C.L., Reifenstein, E.T., Tang, Q., Burgalossi, A., Ray, S., Schreiber, S., Kempter, R. & Brecht, M. (2016) Cell type-specific differences in spike timing and spike shape in rat parasubiculum and superficial medial entorhinal cortex. **Cell Reports** 16(4):1005-1015.

3.2.3 Part 2: Motor cortex and neural circuits underlying social exploration

When we studied spatial coding in the medial entorhinal cortex, we could align our intuitions with the third heuristic mentioned above: the remarkable spatial response patterns of e.g. grid cells and border cells strongly suggests that neurons in this cortical area are somehow involved in the mental representation of allocentic space. However, perturbation of the activity in medial entorhinal cortex only has very subtle effects on behavior, and the 'function' of the grid cell systems still remains unresolved (Van Cauter et al., 2013; Hales et al., 2014; Sasaki et al., 2014). In contrast, our studies of the vibrissa motor cortex align much more closely with the second heuristic mentioned above: From anatomical studies and microstimulation experiments, there is strong evidence that neurons in vibrissa motor cortex are highly involved in the muscular control of whisking output (Brecht et al., 2004; Gioanni and Lamarche, 1985; Hall and Lindholm, 1974; Neafsey et al., 1986). However, while we have good indications of the 'function' of these neurons, we know of no way of plotting the activity of motor cortical neurons in a way, which generates as elegant and striking patterns as the 'spatial' responses found in entorhinal cortex. Previous investigations had identified a subpopulation of neurons in vibrissa motor cortex, which show significant correlations with whisking kinematics, such as whisking amplitude or phase of the whisking cycle, but these neurons are rare and the correlations are generally weak (Carvell et al., 1996; Friedman et al., 2012; Gerdjikov et al., 2013; Hill et al., 2011, Kleinfeld et al., 1999).

It remains an open question whether the striking patterns of e.g. spatial responses in entorhinal cortex is a general feature of cortical spike trains. We do not know whether a mathematical transformation exists, such that also e.g. motor cortical neurons would display spike patters during some motor behaviors, which are as easily interpretable as grid cells. Perhaps no such transformation exists (as is predicted by theories interpreting motor cortical activity patterns as trajectories in a high-dimensional dynamical system, Shenoy et al., 2013), or perhaps the highly controlled and 'reduced' motor behaviors of most previous investigations into activity patterns in vibrissa motor cortex (generally head-fixed ani-

mals whisking in air) does not drive the cortical network in a way where obvious patterns reveal themselves (Krakauer et al., 2017). In **Chapter 7** of this thesis, I present a study where we contributed to resolve this question by investigating the activity of neurons in vibrissa motor cortex in freely moving animals during naturalistic behaviors, which are part of their ecological repertoire of whisker behaviors (Deschênes et al., 2012; Grant et al., 2012; Sachdev et al., 2002; Welker, 1964; Wolfe et al., 2011): self-initiated bouts of exploratory whisking in air, whisking to touch conspecifics during social interactions (Figure 6) and whisking to palpate objects.

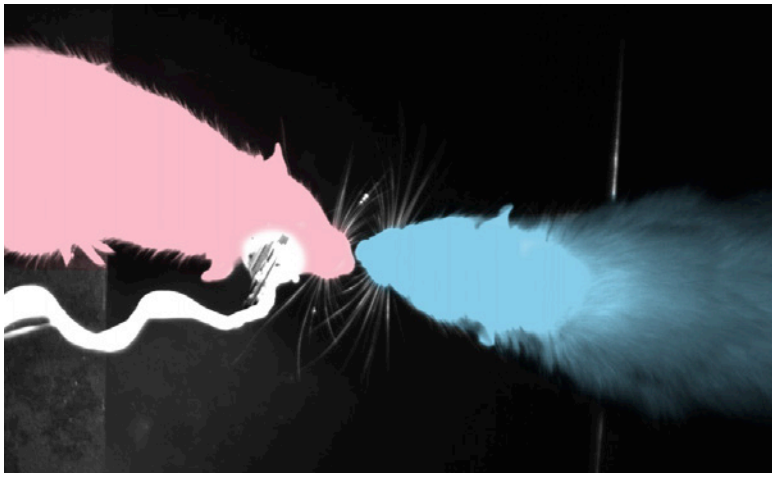

Figure 6: Social facial touch is a delicate, multisensory behavior, where rats put their noses together and palpate each other's faces with their whiskers, while they emit ultrasound vocalizations and sniff each others breath and pheromones. The whisking patterns during such social interactions are complex and require fine motor control.The picture is recorded with a highspeed camera under infrared light (i.e. in visual darkness for the rats), overlayed colors indicate sex of the rats.

Ebbesen, C.L., Doron, G., Lenschow, C., Brecht, M. (2017). Vibrissa motor cortex activity suppresses contralateral whisking behavior. **Nature Neuroscience** 20(1):82-89

In the above study, we found that allowing the animals to freely perform more complex movement patterns allowed us to identify overall patterns in the modulation of motor cortical activity during whisker behaviors. However, surprisingly, we most often observed that motor cortical activity decreased during whisking behavior. Ever since the discovery of motor cortex about a 150 years ago (Fritsch and Hitzig, 1870), the prime function attributed to this cortical region has been generation of movement, hence the name „motor' cortex (Lemon, 2008). However, our observations on vibrissa motor cortex (across recording, microstimulation and inactivation) collectively point to the conclusion that the primary role of vibrissa motor cortex activity is to suppresses whisker movements (i.e. this cortical area serves a "brake" rather than "motor" function).

When we presented our work at conferences, the response of our colleagues was also often surprise, since it was generally assumed that rodent motor cortex should respond to movement with an increase of activity, as is classically the case in e.g. monkey distal limb motor cortex. However, our observations

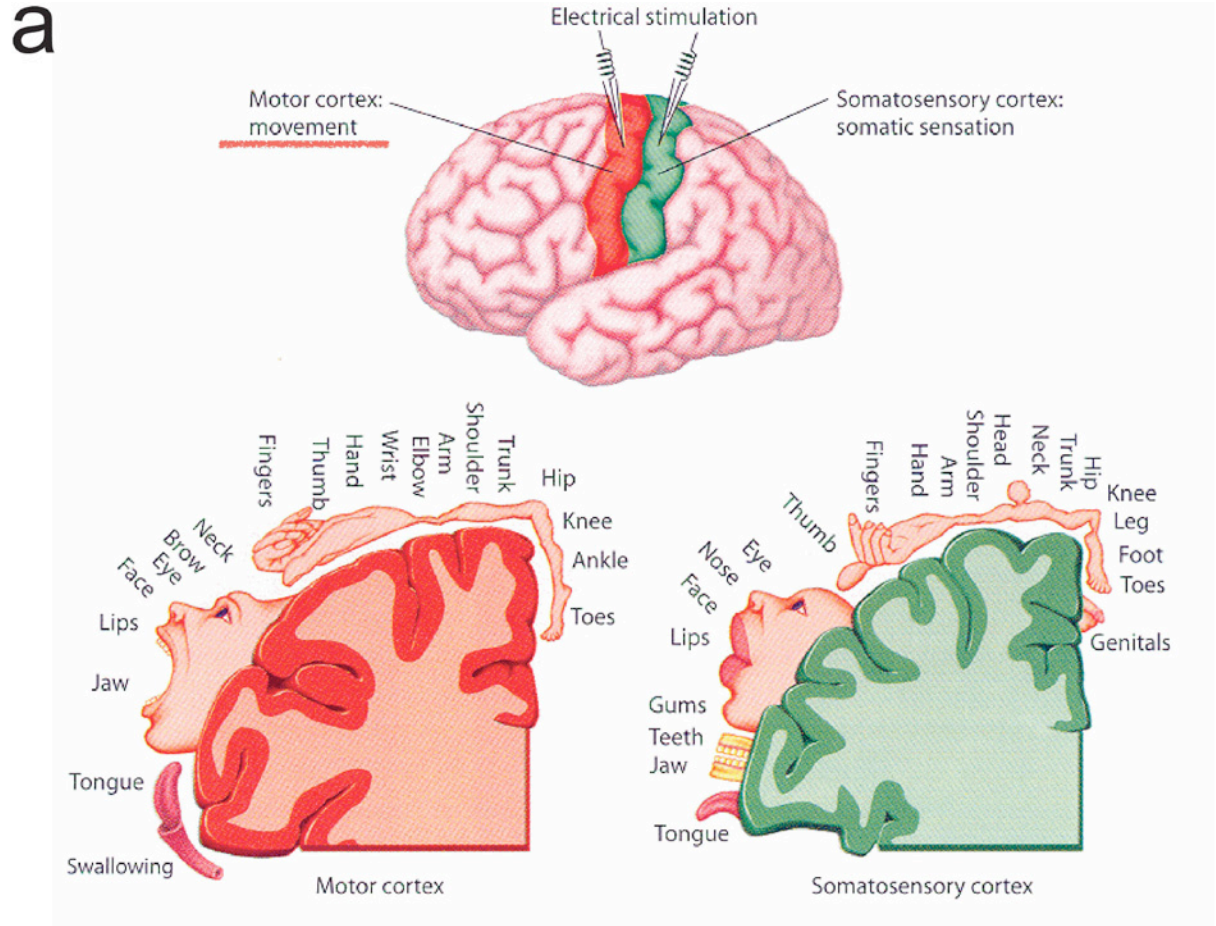

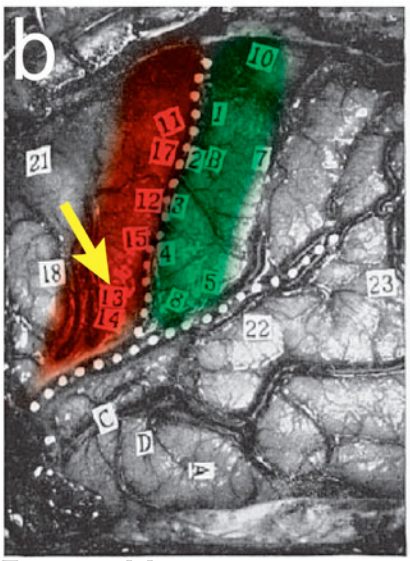

13 (1½v)—Repeated, while patient was squeezing Dr. Stephen's hand. After it was over he said, "I could not do it." The hand had relaxed instantly when stimulation was carried out. When stimulation was withdrawn, he squeezed the hand again.

14 (1½v)—Patient said, "Yes, it felt like a paralysis going down my right leg." When asked again he said that it felt like a numbness.

14 (1½v)—Restimulated while patient was carrying out voluntary movement of the foot. Movement relaxed during stimulation and came again when stimulation was withdrawn. [...]

13 (1½v)—Restimulated. "Oh, my right hand. I couldn't move it." When asked what attracted his attention to his hand, he said, "I had a sensation I wanted to move it."

14 (1½v)—Restimulated. Strange numbness in the right hand. No movement in the hand. No sensation in the arm, but it moved a little.

14 (1½v)—Restimulated 2 mm. lower, in edge of fissure of Sylvius. Sensation in foot, from the ankle down. A feeling of numbness as though he wanted to move it toward him, but he could not move it.

Figure 7: Movement suppression is under-represented in depictions of motor cortex

(a) A textbook illustration of the human 'motor' (red) and somatosensory (green) cortex after the intraoperative stimulation experiments by Penfield & Rasmussen. The textbooks interpret human motor cortex as a 'motor homunculus', that is a muclelotopic motor map: "Motor cortex: movement" (red underscore, added) (Adapted from Heeger, 2006, with permission).

(b) Intraoperative photograph of an actual human motor (red, color added) and somatosensory cortex (green, color added) mapping experiment, as reported in the famous book by Penfield & Rasmussen (1952). Right, we see what the patient reports, when site 13 and 14 (yellow arrow, middle of motor cortex) are stimulated: a clear suppression of movement. (Adapdted from Penfield and Rasmussen, 1952, with permission)

are actually not unique, and several recent investigations of the function of motor cortices (especially in rodents) have found a puzzling predominance of neurons, which decrease their firing with movement and large amounts of movement-related motor cortical inhibition. However, while many authors have made observations, which indicate that motor cortex sometimes exerts a 'negative control' of motor output, there observations generally receive little attention. For example, Figure 7a shows a schematic included in almost every neuroscience textbook: a depiction of human motor cortex with a 'motor homunculus', which symbolizes a muclelotopic motor map. What is very little known and greatly underrated however, is that almost all stimulation effects observed by Penfield and Rasmussen were motor suppressive, to quote from the original paper: *'Oh, my right hand. I couldn't move it.'* (Penfield and Rasmussen, 1952). In **Chapter 8** of this thesis, I conclude by presenting a review highlighting both 'classic' and recent observations on the primary motor cortex, which point to major movement-suppressive functions. As illustrated with the example of the textbook-figure above, there is a tendency that motor cortex findings are presented in a way, which is mostly centered around movement generation, and there is a tradition of attaching less significance to motor suppressive effects. We therefore think that a coherent presentation of motor suppressive effects could have a positive impact on the field and contribute to a more balanced view of motor cortex function by emphasizing movement-suppression as a neglected theme in motor control:

Ebbesen, C.L., Brecht, M. (2017) Motor cortex – to act or not to act? (in review at Nature Reviews Neuroscience)

3.3 References

Aljadeff, J., Lansdell, B.J., Fairhall, A.L., Kleinfeld, D., Adelman, T.L., Bialek, W., Olberg, R.M., Arcas, B.A. y, Fairhall, A.L., Akaike, H., et al. (2016). Analysis of Neuronal Spike Trains, Deconstructed. Neuron 91, 221–259.

Alonso, A., and Klink, R. (1993). Differential electroresponsiveness of stellate and pyramidal-like cells of medial entorhinal cortex layer II. J. Neurophysiol. 70, 128–143.

Andersen, P., Bliss, T.V.P., and Skrede, K.K. (1971). Lamellar organization of hippocampal excitatory pathways. Exp. Brain Res. 13, 222–238.

Bashford, A., and Levine, P. (2010). The Oxford Handbook of the History of Eugenics (Oxford: Oxford University Press).

Belkhir, J. (1994). Race, Sex, Class & "Intelligence" Scientific Racism, Sexism & Classism. Race, Sex

Cl. 1, 53–83.

Bird, C.M., and Burgess, N. (2008). The hippocampus and memory: insights from spatial processing. Nat. Rev. Neurosci. 9, 182–194.

Boccara, C.N., Sargolini, F., Thoresen, V.H., Solstad, T., Witter, M.P., Moser, E.I., and Moser, M.-B. (2010). Grid cells in pre- and parasubiculum. Nat. Neurosci. 13, 987–994.

Borst, A., and Theunissen, F.E. (1999). Information theory and neural coding. Nat. Neurosci. 2, 947–957.

Brecht, M., Krauss, A., Muhammad, S., Sinai-Esfahani, L., Bellanca, S., and Margrie, T.W. (2004). Organization of rat vibrissa motor cortex and adjacent areas according to cytoarchitectonics, microstimulation, and intracellular stimulation of identified cells. J. Comp. Neurol. 479, 360–373.

Brett, M., Johnsrude, I.S., and Owen, A.M. (2002). The problem of functional localization in the human brain. Nat. Rev. Neurosci. 3, 243–249.

Broussard, G.J., Liang, R., and Tian, L. (2014). Monitoring activity in neural circuits with genetically encoded indicators. Front. Mol. Neurosci. 7, 97.

Burgess, N., and O'Keefe, J. (2011). Models of place and grid cell firing and theta rhythmicity. Curr. Opin. Neurobiol. 21, 734–744.

Bush, D., Barry, C., and Burgess, N. (2014). What do grid cells contribute to place cell firing? Trends Neurosci. 37, 136–145.

Buzsáki, G., Stark, E., Berényi, A., Khodagholy, D., Kipke, D.R., Yoon, E., and Wise, K.D. (2015). Tools for Probing Local Circuits: High-Density Silicon Probes Combined with Optogenetics. Neuron 86, 92–105.

Caballero-Bleda, M., and Witter, M.P. (1993). Regional and laminar organization of projections from the presubiculum and parasubiculum to the entorhinal cortex: An anterograde tracing study in the rat. J. Comp. Neurol. 328, 115–129.

Caballero-Bleda, M., and Witter, M.P. (1994). Projections from the presubiculum and the parasubiculum to morphologically characterized entorhinal-hippocampal projection neurons in the rat. Exp. Brain Res. 101, 93–108.

Campbell, A.W. (1905). Histological studies on the localization of cerebral function. (Cambridge: The Macmillan Company).

Carvell, G.E., Miller, S.A., and Simons, D.J. (1996). The relationship of vibrissal motor cortex unit activity to whisking in the awake rat. Somatosens. Mot. Res. 13, 115–127.

Van Cauter, T., Camon, J., Alvernhe, A., Elduayen, C., Sargolini, F., and Save, E. (2013). Distinct Roles of Medial and Lateral Entorhinal Cortex in Spatial Cognition. Cereb. Cortex 23, 451–

459.

Churchland, P. (1981). Eliminative materialism and the propositional attitudes. J. Philos. 78, 67–90.

Colgin, L.L. (2016). Rhythms of the hippocampal network. Nat. Rev. Neurosci. 17, 239–249.

Connell, J., O'Cathain, A., and Brazier, J. (2014). Measuring quality of life in mental health: are we asking the right questions? Soc. Sci. Med. 120, 12–20.

Connor, D.H.O., Clack, N.G., Huber, D., Komiyama, T., Myers, E.W., and Svoboda, K. (2010). Vibrissa-Based Object Localization in Head-Fixed Mice. 30, 1947–1967.

Dayan, P., Feller, M., and Feldman, D. (2011). Networks, circuits and computation. Curr. Opin. Neurobiol. 21, 661–663.

DeFelipe, J. (2011). The evolution of the brain , the human nature of cortical circuits , and intellectual creativity. 5, 1–17.

Deisseroth, K. (2015). Optogenetics: 10 years of microbial opsins in neuroscience. Nat. Neurosci. 18, 1213–1225.

Deschênes, M., Moore, J., and Kleinfeld, D. (2012). Sniffing and whisking in rodents. Curr. Opin. Neurobiol. 22, 243–250.

Diener, E., Suh, E.M., Lucas, R.E., and Smith, H.L. (1999). Subjective well-being: Three decades of progress. Psychol. Bull. 125, 276–302.

Eichenbaum, H. (2017). The role of the hippocampus in navigation is memory. J. Neurophysiol. 117, 1785–1796.

Elliott, J.P., and Dawber, P.G. (1979). Symmetry in physics (Oxford: Macmillan Press).

Fairhall, A., Shea-Brown, E., and Barreiro, A. (2012). Information theoretic approaches to understanding circuit function. Curr. Opin. Neurobiol. 22, 653–659.

Feynman, R.P. (Richard P., Leighton, R.B., and Sands, M.L. (Matthew L. (1963). The Feynman lectures on physics (Reading Mass.: Addison-Wesley Pub. Co).

Fitzgerald, D., Matusall, S., Skewes, J., and Roepstorff, A. (2014). What's so critical about Critical Neuroscience? Rethinking experiment, enacting critique. Front. Hum. Neurosci. 8, 365.

Friedman, W.A., Zeigler, H.P., and Keller, A. (2012). Vibrissae motor cortex unit activity during whisking. J. Neurophysiol. 107, 551–563.

Fritsch, G., and Hitzig, E. (1870). Ueber die elektrische Erregbarkeit des Grosshirns. Arch. Anat. Physiol. Wiss. Med. 37, 300–332.

Fuchs, E.C., Neitz, A., Pinna, R., Melzer, S., Caputi, A., and Monyer, H. (2016). Local and Distant Input Controlling Excitation in Layer II of the Medial Entorhinal Cortex. Neuron 89, 194–208.

Gerdjikov, T. V, Haiss, F., Rodriguez-Sierra, O.E., and Schwarz, C. (2013). Rhythmic whisking area

(RW) in rat primary motor cortex: an internal monitor of movement-related signals? J. Neurosci. 33, 14193–14204.

Gioanni, Y., and Lamarche, M. (1985). A reappraisal of rat motor cortex organization by intracortical microstimulation. Brain Res. 344, 49–61.

Giocomo, L.M., Moser, M.-B., and Moser, E.I. (2011). Computational models of grid cells. Neuron 71, 589–603.

Grant, R. a., Sperber, A.L., and Prescott, T.J. (2012). The role of orienting in vibrissal touch sensing. Front. Behav. Neurosci. 6, 1–12.

Graziano, M.S. a (2011). New insights into motor cortex. Neuron 71, 387–388.

van Groen, T., and Wyss, J.M. (1990). The connections of presubiculum and parasubiculum in the rat.

Hafting, T., Fyhn, M., Molden, S., Moser, M.-B., and Moser, E.I. (2005). Microstructure of a spatial map in the entorhinal cortex. Nature 436, 801–806.

Hales, J.B., Schlesiger, M.I., Leutgeb, J.K., Squire, L.R., Leutgeb, S., and Clark, R.E. (2014). Medial entorhinal cortex lesions only partially disrupt hippocampal place cells and hippocampus-dependent place memory. Cell Rep. 9, 893–901.

Hall, R.D., and Lindholm, E.P. (1974). Organization of motor and somatosensory neocortex in the albino rat. Brain Res. 66, 23–38.

Hardy, L. (2001). Quantum Theory From Five Reasonable Axioms. arXiv 34.

Harris, K.D. (2005). Opinion: Neural signatures of cell assembly organization. Nat. Rev. Neurosci. 6, 399–407.

Harris, J.A., Hirokawa, K.E., Sorensen, S.A., Gu, H., Mills, M., Ng, L.L., Bohn, P., Mortrud, M., Ouellette, B., Kidney, J., et al. (2014). Anatomical characterization of Cre driver mice for neural circuit mapping and manipulation. Front. Neural Circuits 8, 76.

Harris, K.D., Quiroga, R.Q., Freeman, J., and Smith, S.L. (2016). Improving data quality in neuronal population recordings. Nat. Neurosci. 19, 1165–1174.

Hartley, T., Lever, C., Burgess, N., and O'Keefe, J. (2014). Space in the brain: how the hippocampal formation supports spatial cognition. Philos. Trans. R. Soc. Lond. B. Biol. Sci. 369, 20120510.

Hasselmo, M.E. (2005). What is the function of hippocampal theta rhythm?—Linking behavioral data to phasic properties of field potential and unit recording data. Hippocampus 15, 936–949.

Heeger, D. (2006). Perception Lecture Notes: The Brain. [available: http://www.cns.nyu.edu/~david/courses/perception/lecturenotes/brain/brain.html]

Heldt, S.A., and Ressler, K.J. (2009). The Use of Lentiviral Vectors and Cre/loxP to Investigate the Function of Genes in Complex Behaviors. Front. Mol. Neurosci. 2, 22.

Hill, D.N., Curtis, J.C., Moore, J.D., and Kleinfeld, D. (2011). Primary motor cortex reports efferent control of vibrissa motion on multiple timescales. Neuron 72, 344–356.

Howard, M.W., and Eichenbaum, H. (2015). Time and space in the hippocampus. Brain Res. 1621, 345–354.

Hubel, D.H., and Wiesel, T.N. (1959). Receptive fields of single neurones in the cat's striate cortex. J. Physiol. 148, 574–591.

Hubel, D.H., and Wiesel, T.N. (1998). Early exploration of the visual cortex. Neuron 20, 401–412.

Kaufman, M.T., and Churchland, A.K. (2016). Many paths from state to state. Nat. Neurosci. 19, 1541–1542.

Kim, C.K., Adhikari, A., and Deisseroth, K. (2017). Integration of optogenetics with complementary methodologies in systems neuroscience. Nat. Rev. Neurosci. 18, 222–235.

Kitamura, T., Pignatelli, M., Suh, J., Kohara, K., Yoshiki, A., Abe, K., and Tonegawa, S. (2014). Island cells control temporal association memory. Science 343, 896–901.

Kleinfeld, D., Berg, R.W., and O'Connor, S.M. (1999). Anatomical loops and their electrical dynamics in relation to whisking by rat. Somatosens. Mot. Res. 16, 69–88.

Krakauer, J.W., Ghazanfar, A.A., Gomez-Marin, A., Maciver, M.A., and Poeppel, D. (2017). Neuron Perspective Neuroscience Needs Behavior: Correcting a Reductionist Bias. Neuron 93, 480–490.

Krupic, J., Burgess, N., and O'Keefe, J. (2012). Neural Representations of Location Composed of Spatially Periodic Bands. Science (80-.). 337, 853–857.

Lehman, A.F. (1996). Measures of quality of life among persons with severe and persistent mental disorders. Soc. Psychiatry Psychiatr. Epidemiol. 31, 78–88.

Lemon, R.N. (2008). An enduring map of the motor cortex. Exp. Physiol. 93, 798–802.

McNaughton, B.L., Battaglia, F.P., Jensen, O., Moser, E.I., and Moser, M.-B. (2006). Path integration and the neural basis of the "cognitive map." Nat. Rev. Neurosci. 7, 663–678.

Molnár, Z., Kaas, J.H., de Carlos, J.A., Hevner, R.F., Lein, E., and Němec, P. (2014). Evolution and development of the mammalian cerebral cortex. Brain. Behav. Evol. 83, 126–139.

Moser, E.I., Kropff, E., and Moser, M.-B. (2008). Place Cells, Grid Cells, and the Brain's Spatial Representation System. Annu. Rev. Neurosci. 31, 69–89.

Muller, U., Kubie, J.L., and Ranck, B. (1987). Spatial Firing Patterns Fixed Environment of Hippocampal Complex-Spike Cells in a. J. Neurosci. 7, 1935–1950.

Neafsey, E.J., Bold, E.L., Haas, G., Hurley-Gius, K.M., Quirk, G., Sievert, C.F., and Terreberry, R.R. (1986). The organization of the rat motor cortex: A microstimulation mapping study. Brain Res. Rev. 11, 77–96.

O'Connor, D.H., Huber, D., and Svoboda, K. (2009). Reverse engineering the mouse brain. Nature 461, 923–929.

O'Keefe, J., and Dostrovsky, J. (1971). The hippocampus as a spatial map. Preliminary evidence from unit activity in the freely-moving rat. Brain Res. 34, 171–175.

Penfield, W., and Rasmussen, T. (1952). The Cerebral Cortex of Man (New York: The Macmillan Company).

Poucet, B., and Sargolini, F. (2013). A Trace of Your Place. Science (80) 340, 35–36.

Ray, S., Naumann, R., Burgalossi, A., Tang, Q., Schmidt, H., and Brecht, M. (2014). Grid-layout and theta-modulation of layer 2 pyramidal neurons in medial entorhinal cortex. Science 343, 891–896.

Rowland, D.C., Roudi, Y., Moser, M.-B., and Moser, E.I. (2016). Ten Years of Grid Cells. Annu. Rev. Neurosci. 39, 19–40.

Sachdev, R.N.S., Sato, T., and Ebner, F.F. (2002). Divergent movement of adjacent whiskers. J. Neurophysiol. 87, 1440–1448.

Sasaki, T., Leutgeb, S., and Leutgeb, J.K. (2014). Spatial and memory circuits in the medial entorhinal cortex. Curr. Opin. Neurobiol. 32C, 16–23.

Shenoy, K. V, Sahani, M., and Churchland, M.M. (2013). Cortical Control of Arm Movements: A Dynamical Systems Perspective. Annu. Rev. Neurosci. 36, 337–359.

Solstad, T., Boccara, C.N., Kropff, E., Moser, M.-B., and Moser, E.I. (2008). Representation of Geometric Borders in the Entorhinal Cortex. Science (80-.). 322, 1865–1868.

Taube, J.S., Muller, R.U., and Ranck, J.B. (1990). Head-direction cells recorded from the postsubiculum in freely moving rats. I. Description and quantitative analysis. J. Neurosci. 10, 420–435.

Varga, C., Lee, S.Y., and Soltesz, I. (2010). Target-selective GABAergic control of entorhinal cortex output. Nat. Neurosci. 13, 822–824.

Welker, W.I. (1964). Analysis of Sniffing of the Albino Rat. Behaviour 22, 223–244.

Whissell, P.D., Tohyama, S., and Martin, L.J. (2016). The Use of DREADDs to Deconstruct Behavior. Front. Genet. 7, 70.

WHO (1995). The World Health Organization quality of life assessment (WHOQOL): Position paper from the World Health Organization. Soc. Sci. Med. 41, 1403–1409.

Witten, I.B., Steinberg, E.E., Lee, S.Y., Davidson, T.J., Zalocusky, K. a., Brodsky, M., Yizhar, O., Cho, S.L., Gong, S., Ramakrishnan, C., et al. (2011). Recombinase-driver rat lines: Tools, techniques, and optogenetic application to dopamine-mediated reinforcement. Neuron 72, 721–733.

Wolfe, J., Mende, C., and Brecht, M. (2011). Social facial touch in rats. Behav. Neurosci. 125, 900–

910.

Wurtz, R.H. (2009). Recounting the impact of Hubel and Wiesel. J. Physiol. 587, 2817–2823.

Yang, W., and Yuste, R. (2017). In vivo imaging of neural activity. Nat. Methods 14, 349–359.

Zilli, E. a. (2012). Models of Grid Cell Spatial Firing Published 2005–2011. Front. Neural Circuits 6, 1–17.

Žižek, S. (1989). The Sublime Object of Ideology (London: Verso).

Zola-Morgan, S. (1995). Localization of Brain Function: The Legacy of Franz Joseph Gall (1758-1828). Annu. Rev. Neurosci. 18, 359–383.

Aaronson, S. (2004). Is Quantum Mechanics an Island in Theory Space. arXiv:quant-ph/0401062 1–9.

4. Pyramidal and Stellate Cell Specificity of Grid and Border Representations in Layer 2 of Medial Entorhinal Cortex

This manuscript was published as:
(*)Tang, Q., (*)Burgalossi, A., **(*)Ebbesen, C.L.**, Ray, S., Naumann, R., Schmidt, H., Spicher, D. & Brecht, M. (2014) Pyramidal and Stellate Cell Specificity of Grid and Border Representations in Layer 2 of Medial Entorhinal Cortex. **Neuron**, 84(6):1191-1197.

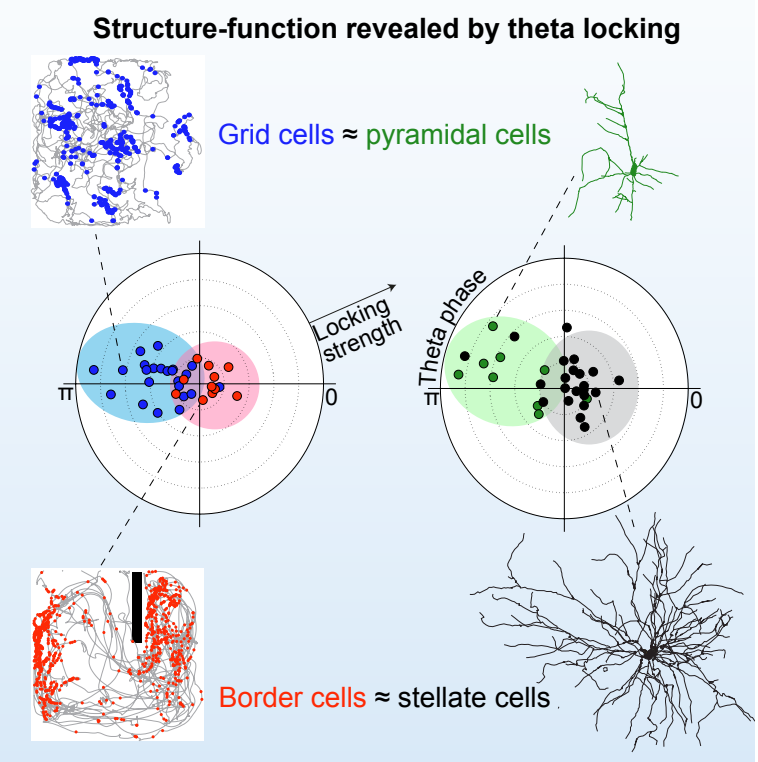

Figure 8: Graphical abstract outlining the main message of this chapter: The temporal firing pattern of grid cells in superficial medial entorhinal cortex (blue dots, left) corresponds to the temporal firing pattern of pyramidal neurons (green dots, right). Similarly, the temporal firing pattern of border cells in superficial medial entorhinal cortex (red dots, left) match the temporal firing pattern of stellate neurons (black dots, right).

Neuron
Report

Pyramidal and Stellate Cell Specificity of Grid and Border Representations in Layer 2 of Medial Entorhinal Cortex

Qiusong Tang,[1,3] Andrea Burgalossi,[1,3,4,5,*] Christian Laut Ebbesen,[1,2,3] Saikat Ray,[1] Robert Naumann,[1,6] Helene Schmidt,[1] Dominik Spicher,[1] and Michael Brecht[1,4,*]
[1]Bernstein Center for Computational Neuroscience, Humboldt University of Berlin, Philippstr. 13, Haus 6, 10115 Berlin, Germany
[2]Berlin School of Mind and Brain, Humboldt University of Berlin, Unter den Linden 6, 10099 Berlin, Germany
[3]Co-first author
[4]Co-senior author
[5]Present address: Werner Reichardt Centre for Integrative Neuroscience, Otfried-Müller-str. 25, 72076 Tübingen, Germany
[6]Present address: Max Planck Institute for Brain Research, Max-von-Laue-Str. 4, 60438 Frankfurt am Main, Germany
*Correspondence: andrea.burgalossi@cin.uni-tuebingen.de (A.B.), michael.brecht@bccn-berlin.de (M.B.)
http://dx.doi.org/10.1016/j.neuron.2014.11.009

SUMMARY

In medial entorhinal cortex, layer 2 principal cells divide into pyramidal neurons (mostly calbindin positive) and dentate gyrus-projecting stellate cells (mostly calbindin negative). We juxtacellularly labeled layer 2 neurons in freely moving animals, but small sample size prevented establishing unequivocal structure-function relationships. We show, however, that spike locking to theta oscillations allows assigning unidentified extracellular recordings to pyramidal and stellate cells with ~83% and ~89% specificity, respectively. In pooled anatomically identified and theta-locking-assigned recordings, nonspatial discharges dominated, and weakly hexagonal spatial discharges and head-direction selectivity were observed in both cell types. Clear grid discharges were rare and mostly classified as pyramids (19%, 19/99 putative pyramids versus 3%, 3/94 putative stellates). Most border cells were classified as stellate (11%, 10/94 putative stellates versus 1%, 1/99 putative pyramids). Our data suggest weakly theta-locked stellate border cells provide spatial input to dentate gyrus, whereas strongly theta-locked grid discharges occur mainly in hexagonally arranged pyramidal cell patches and do not feed into dentate gyrus.

INTRODUCTION

The medial entorhinal cortex is critically involved in spatial navigation and memory. Among other functionally specialized cell types (Sargolini et al., 2006; Solstad et al., 2008; Savelli et al., 2008), it contains grid cells (Hafting et al., 2005), spatially modulated neurons which show periodic, hexagonally arranged spatial firing fields. Given the striking regularity and invariance of the grid representation, these cells are thought to be part of the brain's coordinate system supporting spatial navigation (see Moser and Moser, 2013 for review).

Pure grid cells are primarily found in layer 2 (Boccara et al., 2010), which differs from other cortical laminae in its unique cell biology. Here the two types of principal cells, stellate and pyramidal neurons, have been described (Alonso and Klink, 1993; Germroth et al., 1989). Specifically, stellate and pyramidal neurons differ in conductances and projection patterns (Alonso and Llinás, 1989; Lingenhöhl and Finch, 1991; Klink and Alonso, 1997; Canto and Witter, 2012). Recent work indicates that stellate and pyramidal neurons can be reliably differentiated by calbindin immunoreactivity (Ray et al., 2014; Kitamura et al., 2014), and that these cells also differ in their inhibitory inputs (Varga et al., 2010). Calbindin-positive (calbindin$^+$) cells, which are clustered and arranged in a hexagonal grid (Ray et al., 2014), have been recently shown to project to the CA1 (Kitamura et al., 2014), while calbindin-negative (calbindin$^-$) neurons are homogeneously distributed and project primarily to the dentate gyrus (Varga et al., 2010; Ray et al., 2014). Few studies have so far explored structure-function relationships in entorhinal circuits (Schmidt-Hieber and Häusser, 2013; Domnisoru et al., 2013; Zhang et al., 2013; see Rowland and Moser, 2014 and Burgalossi and Brecht, 2014 for reviews). Thus, the functional implications of the remarkable cellular diversity of layer 2 have remained largely unresolved.

Resolving how differential spatial firing relates to principal cell types will clarify the cellular mechanisms of grid discharges and spatial input patterns to distinct subfields of the hippocampus. In the present work we aim at resolving layer 2 circuits by taking advantage of improved methodologies for identifying individual neurons recorded in freely moving animals. By cell identification and theta-locking-based classification of unidentified recordings, we provide evidence that grid and border responses are preferentially contributed by pyramidal and stellate cells, respectively.

RESULTS

To explore the cellular basis of grid cell activity in medial entorhinal cortex, we juxtacellularly recorded and labeled neurons in

Neuron
Layer 2 Grid and Border Cells

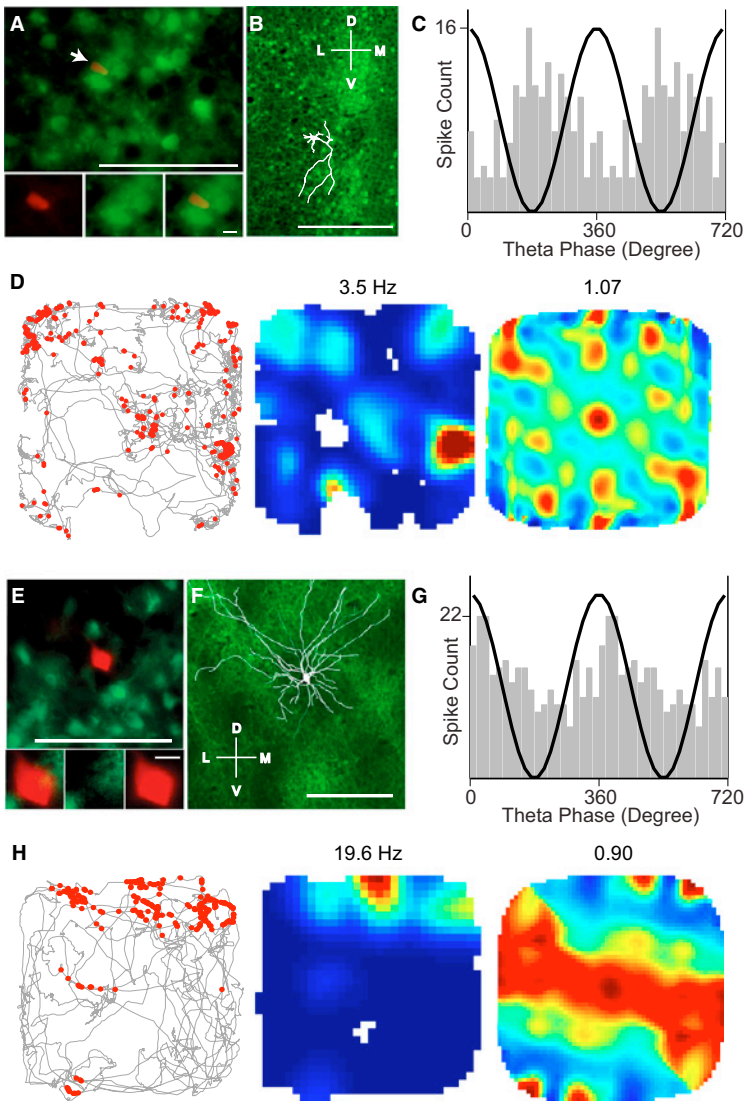

Figure 1. Grid-like Firing Properties in a Calbindin-Positive Pyramidal Neuron and Border Responses in a Calbindin-Negative Stellate Neuron

(A) Top, micrograph (tangential section) of a calbindin$^+$ neuron recorded in a rat exploring a 2D environment (1 × 1 m). Green, calbindin; red, neurobiotin. Bottom, soma in red, green channel, and overlay. Scale bars, 100 μm (top), 10 μm (bottom). (B) Micrograph of a tangential layer 2 section with calbindin immunoreactivity (green) and superimposed reconstruction of the pyramidal neuron (white). The cell was poorly stained, basal dendrites were minor, and a prominent apical dendrite extended toward the center of a calbindin patch ventral from the neuron. Scale bar, 250 μm. (C) Theta-phase histogram of spikes for the neuron shown in (A). For convenience, two repeated cycles are shown. The black sinusoid is a schematic local field potential theta wave for reference. (D) Spike-trajectory plot, rate map, and 2D spatial autocorrelation of the rate map revealing the hexagonal grid cell periodicity. Spike-trajectory plot: red dots indicate spike locations, gray lines indicate the rat trajectory. Rate map: red indicates maximal firing rate, value noted above. Spatial autocorrelation: color scale −1 (blue) through 0 (green) to 1 (red). For this cell, the grid score is 1.07. (E) Left, micrograph (tangential section) of a calbindin$^-$ neuron recorded in a rat exploring a 2D environment (70 × 70 cm). Green, calbindin; red, neurobiotin. Right, soma in red, green channel, and overlay. Scale bars, 100 μm (left), 10 μm (right). (F) Micrograph of the tangential layer 2 section with calbindin immunoreactivity (green) and superimposed reconstruction of the stellate neuron (white). The cell was well stained, and the huge dendritic field encompassed several calbindin patches. Scale bar, 250 μm. (G) Theta-phase histogram of spikes for the neuron shown in (A). For convenience, two repeated cycles are shown. The black sinusoid is a schematic local field potential theta wave for reference. (H) Spike-trajectory plot, rate map, and 2D spatial autocorrelation of the rate map revealing the elongated firing field. Spike-trajectory plot: red dots indicate spike locations, gray lines indicate the rat trajectory. Rate map: red indicates maximal firing rate, value noted above. Spatial autocorrelation: color scale −0.5 (blue) through 0 (green) to 0.5 (red). For this cell, the border score is 0.90. D, dorsal; L, lateral; M, medial; V, ventral.

layer 2 (which contains the largest percentage of pure grid cells; Boccara et al., 2010) in awake rats trained to explore 2D environments (Tang et al., 2014). Clear grid cell discharges were rare. The clearest grid-like firing pattern in our sample of 31 identified cells (17 of which met the criteria for spatial analysis; see Experimental Procedures) was observed in the calbindin$^+$ cell shown in Figure 1A. This neuron had pyramidal morphology, with simple dendritic arborization and a single large apical dendrite targeting a calbindin$^+$ patch (Figure 1B; see also Ray et al., 2014). During exploratory behavior, calbindin$^+$ neurons fired with strong theta rhythmicity and phase locked near the trough of the local field potential theta rhythm (Figure 1C; Ray et al., 2014). Spatial autocorrelation analysis of the firing pattern in the 2D environment revealed a hexagonal periodicity of firing fields (grid score = 1.07; Figure 1D), indicative of grid cell activity (Hafting et al., 2005). Because of its relatively low firing rate (~0.5 Hz) this cell was not included in the grid cell sample (see Experimental Procedures). Most other identified calbindin$^+$ neurons had no clear spatial firing patterns.

The clearest border discharge in our sample of identified cells was observed in the calbindin$^-$ cell shown in Figure 1E. This cell was a stellate neuron, which did not have a single apical dendrite, but instead extended multiple and widely diverging ascending dendrites; this dendritic tree spanned a vast field,

Neuron
Layer 2 Grid and Border Cells

which encompassed multiple calbindin$^+$ patches (Figure 1F; see also Ray et al., 2014). On average, spikes from calbindin$^-$ neurons were weakly modulated by the local theta rhythm (Figure 1G). In 3 out of 11 calbindin$^-$ cells from recordings with sufficient spatial coverage, we observed clear border firing patterns as in Figure 1H. While we did not observe grid cells, nonspatial firing patterns also dominated in calbindin$^-$ neurons.

While the small size of the data set of identified neurons prevented us from establishing firm structure-function relationships, four preliminary observations can be drawn: (i) grid cells are less abundant in layer 2 than previously assumed (Sargolini et al., 2006; Boccara et al., 2010; but see Mizuseki et al., 2009; Gupta et al., 2012; Bjerknes et al., 2014), and there is no one-to-one relationship between spatial discharge characteristics and cell type, (ii) calbindin$^+$ neurons probably include grid cells, (iii) the absence of grid cells in the 22 identified calbindin$^-$ stellate neurons suggests that grid cells are rare in this cell population, and (iv) calbindin$^-$ neurons include border cells.

Currently available evidence points to a correspondence between cytochemical (calbindin$^+$ versus calbindin$^-$) and morphological (pyramidal versus stellate) classification of principal neurons in layer 2 (Varga et al., 2010; Kitamura et al., 2014). To further explore these relationships, we determined the percentage of calbindin$^+$ cells in layer 2 and compared these data with related measurements in the literature (Figure S1A available online). In agreement with previous studies (Peterson et al., 1996; Kumar and Buckmaster, 2006; Varga et al., 2010), we found that layer 2 neurons consist of ~34% calbindin$^+$ and ~53% calbindin$^-$ (and reelin$^+$) principal cells, and ~13% interneurons (Figure S1B). We note that while Ray et al. (2014) found about 30% of calbindin$^+$ cells, most of which were shown to have pyramidal morphology (see also Varga et al., 2010; Kitamura et al., 2014), Gatome et al. (2010) found a slightly lower fraction of putative pyramidal cells. Calbindin$^+$ and calbindin$^-$ cells showed large quantitative differences in their morphology, but without a clear bimodality in individual morphological parameters (Figures S1C and S1D). Calbindin$^+$ cells had significantly (on average ~2.5-fold) smaller dendritic trees (Figure S1E). Dendritic trees also differed in shape between cell types. Calbindin$^+$ cells had a single long (always apical) dendrite, which accounted on average for 63% of the total dendritic length (Figure S1E) and which was polarized toward the center of pyramidal cell patches as shown previously (Ray et al., 2014). Calbindin expression matched well, but not perfectly, with pyramidal cell morphology (Figures S1C and S1D). Calbindin$^-$ cells featured similar-length dendrites with the longest dendrite contributing on average for 33% of the total dendritic length (Figure S1E). These results are in line with published data and indicate that calbindin$^+$ and calbindin$^-$ cells largely correspond to pyramidal and stellate neurons, respectively. However, the lack of clear morphological bimodality in layer 2 (see also Canto and Witter, 2012) implies that the correspondence between pyramidal/calbindin$^+$ and stellate/calbindin$^-$ might not be perfect. Interestingly, the spine density in calbindin$^+$ cells decreased as a function of distance from the soma, whereas the reverse was true for calbindin$^-$ cells (Figure S1F). These morphological differences, together with clustering of calbindin$^+$ cells in patches and the polarization of their apical dendrites toward the center of calbindin$^+$ patches (Ray et al., 2014), likely result in a local and overlapping sampling of inputs in neighboring calbindin$^+$ cells, whereas neighboring calbindin$^-$ stellate cells sample large and nonoverlapping input territories.

Calbindin$^-$ stellate and calbindin$^+$ pyramidal cells differ strongly in their temporal discharge properties (Figures 1C and 1G; Ray et al., 2014). We therefore wondered if temporal discharge properties could be used to classify layer 2 cells as putative pyramidal or stellate neurons. We used a support vector machine to classify neurons based on both the spike phase and strength of phase locking to local field potential theta oscillations, which indeed clearly segregated calbindin$^+$ and calbindin$^-$ cells with a large distance to the separating hyperplane (Figure 2A; see Supplemental Information). To further improve the purity of assigned cells, we added a guard zone around the hyperplane separating the Gaussian kernels classifying calbindin$^+$ (light green background) and calbindin$^-$ (gray background) cells (omitting the guard zone and classifying all cells did not qualitatively affect the results; data not shown). We tested our classifier by a bootstrapping approach (Figures S2A and S2B) and found that a large fraction of calbindin$^+$ and calbindin$^-$ cells could be correctly assigned (Figure S2C). More importantly, the specificity of classification procedure—reflected in the purity of the resulting cell samples—was excellent, i.e., ~89% for putative calbindin$^-$ cells and ~83% for putative calbindin$^+$ cells (Figure S2D), and even higher values for combination of identified and putatively assigned cells (Figure S2E). We further evaluated the robustness of the classifier by testing it on a larger data set of identified layer 2 neurons (Ray et al., 2014) recorded under urethane/ketamine anesthesia (Klausberger et al., 2003). We consider this a challenging test of the classifier, as theta phase and strength of locking might differ between the awake and anesthetized state. Similarly to the awake situation, however, the large majority of neurons recorded under anesthesia were also correctly classified (92% of calbindin$^+$ cells, 65% of calbindin$^-$ cells, $p < 0.001$, bootstrap; Figure 2B, bottom), suggesting that our classification criteria work robustly and can effectively generalize across very different recording conditions (Figure 2B). Encouraged by these results, we classified the larger data set of our hitherto unidentified layer 2 juxtacellular and tetrode recordings (classified + identified n = 193 cells).

To assess the relationship between cell identity and spatial firing properties, we pooled the nonidentified recordings, assigned to putative calbindin$^+$ and calbindin$^-$ cells, with the recordings from histologically identified neurons. The pooled data sets included n = 99 calbindin$^+$ and n = 94 calbindin$^-$ cells, respectively. In our first assessment of spatial discharge patterns, we attempted to classify grid and border cells solely using scores (grid score > 0.3, border score > 0.5; Solstad et al., 2008). According to visual inspection of individual rate maps, however, these criteria were not sufficiently stringent and returned a majority of weakly to nonmodulated neurons, i.e., possibly a majority of false-positive grid and border cells. To resolve this issue, we adopted the cell classification approach of Bjerknes et al. (2014), in which spatial discharge properties were only quantified in those cells that carried significant amounts of spatial information (as assessed by a spike-shuffling procedure, see Skaggs et al., 1993; Supplemental Experimental Procedures). This approach identified grid and border responses,

Neuron
Layer 2 Grid and Border Cells

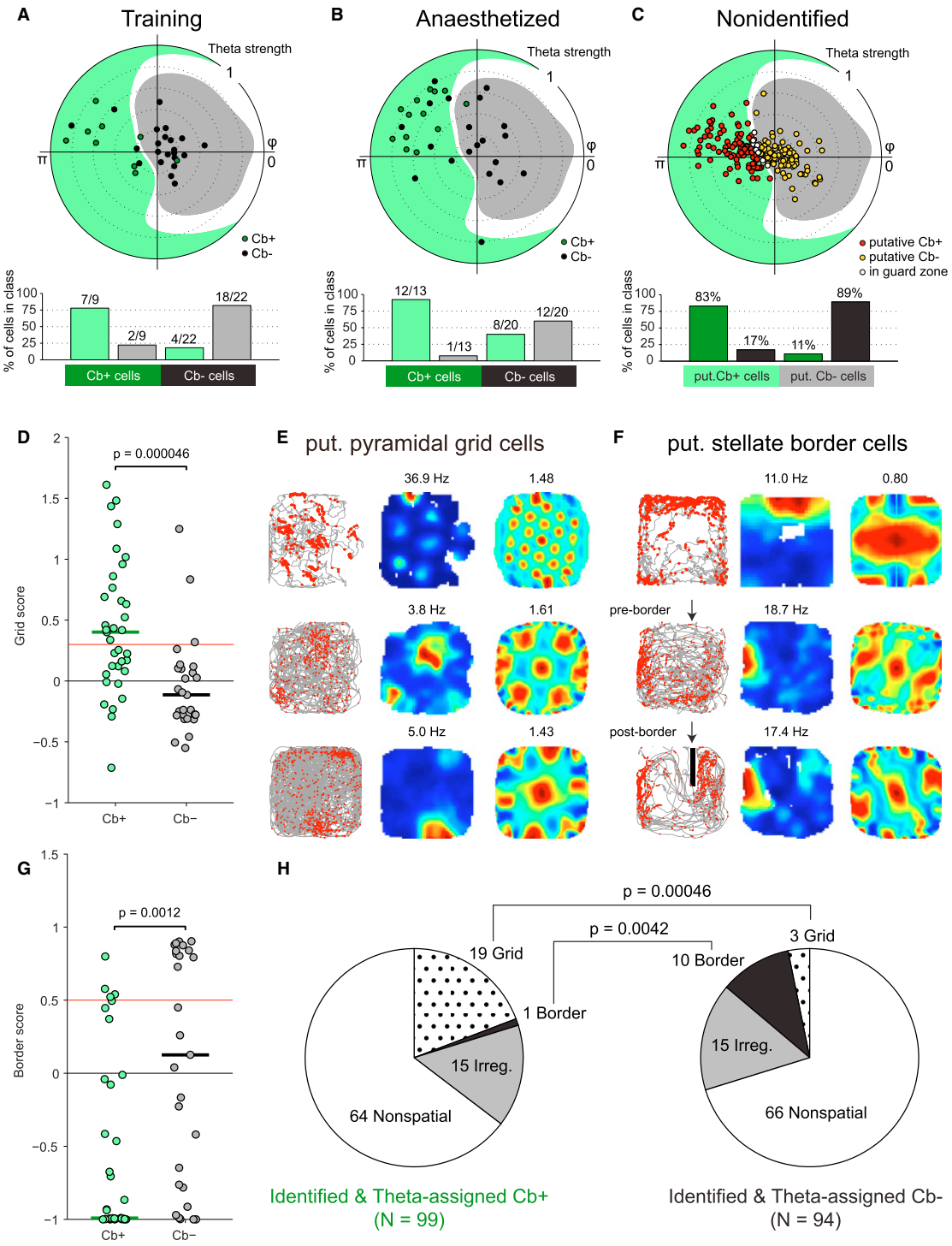

(legend on next page)

Neuron
Layer 2 Grid and Border Cells

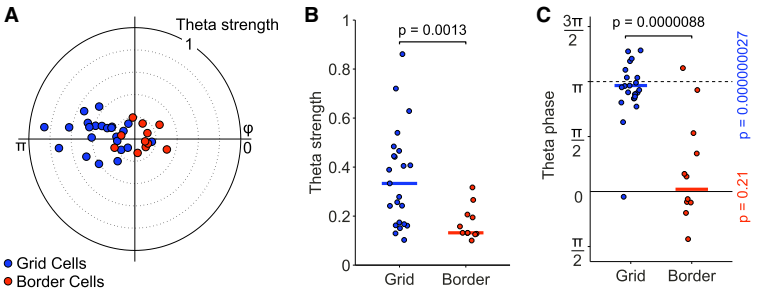

Figure 3. Temporal Spiking Properties of Grid Cells and Border Cells

(A) Polar plot of theta strength as a function of preferred theta phase angle (φ) for grid cells (blue dots) and border cells (red dots). (B) Theta strength of recorded grid cells (blue dots) and border cells (red dots) is significantly different. Blue and red lines indicate medians (p = 0.0013, Mann-Whitney U test). (C) Preferred theta phase for grid cells (blue dots) and border cells (red dots). Blue and red lines indicate circular means (p = 0.0000088, parametric Watson-Williams multisample test). Grid cells show a significant tendency to fire near the trough (p = 0.000000027, Rayleigh's test for nonuniformity). Border cells show a tendency to fire near the peak of theta rhythm, but the phase locking to theta peak did not reach significance in our data set (p = 0.21, Rayleigh's test for nonuniformity).

which in a majority of cases were convincing according to visual inspection. Consistent with previous studies (Hafting et al., 2005; Sargolini et al., 2006; Boccara et al., 2010; Burgalossi et al., 2011; Domnisoru et al., 2013), a fraction of layer 2 neurons (33%; n = 63 cells) were significantly spatially modulated. Weak hexagonal symmetry of spatial firing patterns was observed in both the calbindin$^+$ and calbindin$^-$ data set, in line with previous observations (Burgalossi et al., 2011; Domnisoru et al., 2013; Schmidt-Hieber and Häusser, 2013). However, grid scores in the calbindin$^+$ population were significantly higher than those in the calbindin$^-$ population (p = 0.000046, Mann-Whitney U test; Figures 2D and 2E), consistent with observations from the identified data set (Figure 1). On the other hand, in line with observations from the identified data set (Figure 1), calbindin$^-$ cells had significantly higher border scores than calbindin$^+$ cells (Figure 2G; p = 0.0012, Mann-Whitney U test). Border discharges in calbindin$^-$ cells are shown in Figure 2F, which also includes an example where border firing was confirmed by a border test (Solstad et al., 2008; Lever et al., 2009). Thus, according to the grid and border scores shown in Figures 2D and 2G, putative pyramidal and stellate cells have significantly different, but overlapping, spatial properties.

Figure 2H gives an overview of the spatial response properties of our pooled calbindin$^+$ and calbindin$^-$ data sets, respectively (see also Figure S3). The majority of both calbindin$^+$ and calbindin$^-$ neurons showed no significant spatial selectivity. Grid patterns were significantly more common in the calbindin$^+$ population, where 19% (19/99) of the cells passed our grid cell criteria, compared to only 3% (3/94) in the calbindin$^-$ population (p = 0.00046, Fisher's exact test). A higher fraction of calbindin$^-$ cells passed the border cell criterion (11% calbindin$^-$, 10/94 cells; versus 1% calbindin$^+$, 1/99 cells), and this difference was statistically significant (p = 0.0042, Fisher's exact test). These data confirm and extend the conclusion from our recordings of identified cells and indicate that grid cells are preferentially recruited from the calbindin$^+$ population, while border responses preferentially occur in calbindin$^-$ cells.

Unlike many studies based on tetrode recordings (Sargolini et al., 2006; Boccara et al., 2010; but see Zhang et al., 2013), a substantial fraction of cells showed head-direction selectivity both in identified and theta-assigned calbindin$^+$ and calbindin$^-$ cells (Figure S4). Head-direction selectivity was more common in calbindin$^+$ (19%, 19 out of 99 cells) than in calbindin$^-$ cells (12%, 11 out of 94 cells), but this difference was not significant (p = 0.17, Fisher's exact test), and both classes contained pure as well as conjunctive responses (Sargolini et al., 2006).

The grid and border cells recorded here showed systematic differences in spike locking to local field potential theta oscillations (Figure 3A). Spikes from most grid cells were strongly entrained by the theta rhythm, with strong phase locking (Figure 3B) and a phase preference near the theta trough (Figure 3C; p = 0.000000027, Rayleigh's test for nonuniformity). The modulation of spiking activity of border cells by the theta rhythm was significantly weaker than in grid cells (Figure 3B; p = 0.0013, Mann-Whitney U test) and showed on average only a weak, nonsignificant phase preference for the theta

Figure 2. Cell Classification and Grid and Border Responses in Pooled Identified and Theta-Assigned Cells

(A) Top, classification training set: polar plot of theta strength (value indicated by the upper-right number) and preferred theta phase angle (φ) for calbindin$^+$ cells (green dots) and calbindin$^-$ cells (black dots) identified in freely moving rats. Background color fill shows classification boundary based on φ and theta strength; cells in the pale green area and gray area will be classified as calbindin$^+$ and calbindin$^-$ cells, respectively. Bottom, fraction of cells in classification categories. (B) Top, polar plot of theta strength and of preferred theta phase angle (φ) for calbindin$^+$ cells (green dots) and calbindin$^-$ cells (black dots) identified in anaesthetized rats, overlaid on classification boundary. Bottom, fraction of cells in classification categories. (C) Top, polar plot of theta strength and preferred theta phase angle (φ) for nonidentified cells. Putative calbindin$^+$ cells (red dots) and putative calbindin$^-$ cells (yellow dots) are shown overlaid on the classification boundary, together with unclassified cells (white dots). Bottom, estimate of the purity of the theta-assigned cell categories. The sample of putative calbindin$^-$ cells are estimated to be 89% pure, and the sample of putative calbindin$^+$ cells are estimated to be 83% pure (see Figure S2). (D) Comparison of grid scores between (identified and putative) calbindin$^+$ and calbindin$^-$ neurons; the dotted line indicates the threshold for grid cell; vertical lines indicate medians (p = 0.000046, Mann-Whitney U test). (E) Representative grid firing pattern observed in calbindin$^+$ neurons (spike-trajectory plot, rate map, and spatial autocorrelation; maximum firing rate and grid score indicated above plots). (F) Border firing patterns in calbindin$^-$ neurons. Conventions as in (E). Arrows indicate insertion of additional border. (G) Comparison of border scores between (identified and putative) calbindin$^+$ and calbindin$^-$ neurons; the dotted line indicates the threshold for border cells; vertical lines indicate medians (p = 0.0012; Mann-Whitney U test). (H) Distribution of spatial discharge types in calbindin$^+$ (left) and calbindin$^-$ (right) neurons was found to be significantly different in numbers of grid cells and border cells (p = 0.00046 and 0.0042, respectively, Pearson's chi-square test). Cells that passed both grid and border score criteria were assigned to either grid or border cells, as specified in the Experimental Procedures.

CellPress

Neuron

Layer 2 Grid and Border Cells

peak (Figure 3C; p = 0.21, Rayleigh's test for nonuniformity), which differed significantly from the phase preference of grid cells (Figures 3B and 3C; p = 0.0000088, parametric Watson-Williams multisample test). Thus, in layer 2 grid and border signals mirrored the temporal differences between calbindin$^+$ pyramidal and calbindin$^-$ stellate cells reported earlier (Ray et al., 2014).

DISCUSSION

Relating functionally defined discharge patterns to principal cell diversity is an unresolved issue in cortical physiology. In layer 2 of medial entorhinal cortex, most studies suggested that spatially modulated responses are common, and that grid firing patterns are contributed by both stellate and pyramidal neurons (Burgalossi et al., 2011; Schmidt-Hieber and Häusser, 2013; Domnisoru et al., 2013; Zhang et al., 2013). In line with such evidence, we observed a consistent fraction of spatially modulated neurons in layer 2, and weakly hexagonal firing patterns in both stellate and pyramidal neurons. At the same time, however, most grid patterns that met our grid score and spatial information criteria (see Supplemental Experimental Procedures) were classified as putative calbindin$^+$ pyramidal cells (see Figure S3A). Border responses, on the other hand, were predominantly observed in the calbindin$^-$ stellate population (Figure S3B). Our data indicate a strong interdependence between cell type and spatial discharge pattern in layer 2, where a calbindin$^+$ cell is about six times more likely to be a grid cell and ten times less likely to be a border cell than a calbindin$^-$ neuron. Our confidence in classification is based on the striking differences between calbindin$^+$ and calbindin$^-$ cells in their temporal discharge properties (Ray et al., 2014), the assessment of classification quality by our bootstrapping approach, and the robustness of classification across widely differing recording conditions. It is important, however, to note that our conclusions rest on the validity and accuracy of our classification procedure.

A key finding from our work is that layer 2 principal cells can be classified with high accuracy by their distinct temporal discharge properties. Such classification can be extended to a large number of unidentified layer 2 recordings from other laboratories, provided that the required histology and local field potential data have been collected. To this end we provide our classification training data set (Table S1) and a custom-written MATLAB function (Supplemental Information, Note S1). Such post hoc assignment of principal cell types to recordings—i.e., supplying identity to formerly blind extracellular recordings—could be instrumental for understanding principal cell diversity and cortical microcircuitry.

Calbindin$^+$ pyramidal cells might be predetermined for grid cell function as they receive cholinergic inputs, are strongly theta modulated, and are arranged in a hexagonal grid (Ray et al., 2014). We suggested an "isomorphic mapping hypothesis," according to which an anatomical grid of pyramidal cells (Ray et al., 2014) generates grid cell activity (Brecht et al., 2014) and is an embodiment of the brain's representation of space in hexagonal grids. Representing grid discharge by a "cortical grid" might offer similar advantages as isomorphic representations of body parts, as barrel fields (Woolsey and Van der Loos, 1970), or nose stripes (Catania et al., 1993), in somatosensory cortices of tactile specialists. Notably, the local similarity of grid cell discharges is high, as neighboring grid cells share the same grid orientation and scaling and are phase coupled even across distinct environments (Hafting et al., 2005; Fyhn et al., 2007). We speculate that calbindin$^+$ pyramidal neuron clustering and apical dendrite bundling in patches (Ray et al., 2014) might impose this local similarity of grid discharges. A surprising implication of our data is that the spatial input to the dentate gyrus is provided mainly by stellate border cells, whereas pyramidal grid cells do not feed into this pathway (Kitamura et al., 2014; Ray et al., 2014). Border responses arise in stellate neurons, with long and widely diverging dendritic trees, i.e., such discharge patterns may result from a relatively global sampling of incoming inputs in medial entorhinal cortex and help generate place cell activity (Bjerknes et al., 2014; Bush et al., 2014). Recognizing the functional dichotomy of pyramidal and stellate cells in layer 2 will help elucidate how spatial discharge patterns arise in cortical microcircuits.

EXPERIMENTAL PROCEDURES

All experimental procedures were performed according to the German guidelines on animal welfare under the supervision of local ethics committees. Juxtacellular recordings and tetrode recordings in freely moving animals were obtained in male Wistar and Long-Evans rats (150–250 g), which were habituated to the behavioral arena and trained for 3–7 days. Experimental procedures were performed as previously described (Burgalossi et al., 2011; Herfst et al., 2012) with the exception that methodological developments allowed us to identify neurons in drug-free animals (Tang et al., 2014; see also Supplemental Experimental Procedures). Some of the data have been published in a previous report (Ray et al., 2014). Recordings in anesthetized animals were performed under urethane/ketamine/xylazine (Klausberger et al., 2003). Juxtacellularly labeled neurons were visualized with streptavidin conjugated to Alexa 546 (1:1,000). A Hilbert transform was used for assigning instantaneous theta phase of each spike based on theta in the local field potential in the spike-theta phase analysis. The spatial periodicity of recorded neurons was assessed by spatial autocorrelations. Grid scores were calculated as previously described (Barry et al., 2012) by taking a circular sample of the spatial autocorrelogram, centered on, but excluding the central peak. To determine the modulation of a cell firing along a border, we determined border scores as previously described or performed border tests (Solstad et al., 2008; Lever et al., 2009). Head-direction tuning was measured as the eccentricity of the circular distribution of firing rates. Classification based on strength of locking to theta phase (S) and preferred theta phase angle (φ) was done by building a support vector machine, trained on the vectors $(\cos(\varphi)\cdot S, \sin(\varphi)\cdot S)$ using a Gaussian radial basis function kernel. Classification of nonidentified cells into putative calbindin$^+$ and calbindin$^-$ cells was performed by applying a conservative classification threshold, where we did not classify cells close to the separating hyperplane. Detailed experimental and analytical procedures are provided in the Supplemental Information.

SUPPLEMENTAL INFORMATION

Supplemental Information includes four figures, one table, and Supplemental Experimental Procedures and can be found with this article online at http://dx.doi.org/10.1016/j.neuron.2014.11.009.

AUTHOR CONTRIBUTIONS

Q.T. and A.B. performed juxtacellular recordings. C.L.E. and Q.T. performed tetrode recordings. S.R., R.N., and H.S. performed and analyzed anatomical experiments. C.L.E. and D.S. developed the classifier and C.L.E. and Q.T. analyzed electrophysiology data. A.B. and M.B. conceived of the project and supervised experiments. All authors contributed to the writing of the manuscript.

Neuron
Layer 2 Grid and Border Cells

ACKNOWLEDGMENTS

This work was supported by Humboldt-Universität zu Berlin, BCCN Berlin (German Federal Ministry of Education and Research BMBF, Förderkennzeichen 01GQ1001A), NeuroCure, the Neuro-Behavior ERC grant, and the Gottfried Wilhelm Leibniz Prize of the DFG. We thank Moritz von Heimendahl for programming, and Andreea Neukirchner, Juliane Steger, John Tukker, and Undine Schneeweiß. We are thankful to Francesca Sargolini, May-Britt and Edvard Moser, and the other authors (Sargolini et al., 2006), who generously provided access to grid cell data, which were helpful in assembling an earlier version of this manuscript.

Accepted: November 6, 2014
Published: December 4, 2014

REFERENCES

Alonso, A., and Llinás, R.R. (1989). Subthreshold Na+-dependent theta-like rhythmicity in stellate cells of entorhinal cortex layer II. Nature *342*, 175–177.

Alonso, A., and Klink, R. (1993). Differential electroresponsiveness of stellate and pyramidal-like cells of medial entorhinal cortex layer II. J. Neurophysiol. *70*, 128–143.

Barry, C., Ginzberg, L.L., O'Keefe, J., and Burgess, N. (2012). Grid cell firing patterns signal environmental novelty by expansion. Proc. Natl. Acad. Sci. USA *109*, 17687–17692.

Bjerknes, T.L., Moser, E.I., and Moser, M.-B. (2014). Representation of geometric borders in the developing rat. Neuron *82*, 71–78.

Boccara, C.N., Sargolini, F., Thoresen, V.H., Solstad, T., Witter, M.P., Moser, E.I., and Moser, M.-B. (2010). Grid cells in pre- and parasubiculum. Nat. Neurosci. *13*, 987–994.

Brecht, M., Ray, S., Burgalossi, A., Tang, Q., Schmidt, H., and Naumann, R. (2014). An isomorphic mapping hypothesis of the grid representation. Philos. Trans. R. Soc. Lond. B Biol. Sci. *369*, 20120521.

Burgalossi, A., and Brecht, M. (2014). Cellular, columnar and modular organization of spatial representations in medial entorhinal cortex. Curr. Opin. Neurobiol. *24*, 47–54.

Burgalossi, A., Herfst, L., von Heimendahl, M., Förste, H., Haskic, K., Schmidt, M., and Brecht, M. (2011). Microcircuits of functionally identified neurons in the rat medial entorhinal cortex. Neuron *70*, 773–786.

Bush, D., Barry, C., and Burgess, N. (2014). What do grid cells contribute to place cell firing? Trends Neurosci. *37*, 136–145.

Canto, C.B., and Witter, M.P. (2012). Cellular properties of principal neurons in the rat entorhinal cortex. II. The medial entorhinal cortex. Hippocampus *22*, 1277–1299.

Catania, K.C., Northcutt, R.G., Kaas, J.H., and Beck, P.D. (1993). Nose stars and brain stripes. Nature *364*, 493.

Domnisoru, C., Kinkhabwala, A.A., and Tank, D.W. (2013). Membrane potential dynamics of grid cells. Nature *495*, 199–204.

Fyhn, M., Hafting, T., Treves, A., Moser, M.-B., and Moser, E.I. (2007). Hippocampal remapping and grid realignment in entorhinal cortex. Nature *446*, 190–194.

Gatome, C.W., Slomianka, L., Lipp, H.P., and Amrein, I. (2010). Number estimates of neuronal phenotypes in layer II of the medial entorhinal cortex of rat and mouse. Neuroscience *170*, 156–165.

Germroth, P., Schwerdtfeger, W.K., and Buhl, E.H. (1989). Morphology of identified entorhinal neurons projecting to the hippocampus. A light microscopical study combining retrograde tracing and intracellular injection. Neuroscience *30*, 683–691.

Gupta, K., Keller, L.A., and Hasselmo, M.E. (2012). Reduced spiking in entorhinal cortex during the delay period of a cued spatial response task. Learn. Mem. *19*, 219–230.

Hafting, T., Fyhn, M., Molden, S., Moser, M.-B., and Moser, E.I. (2005). Microstructure of a spatial map in the entorhinal cortex. Nature *436*, 801–806.

Herfst, L., Burgalossi, A., Haskic, K., Tukker, J.J., Schmidt, M., and Brecht, M. (2012). Friction-based stabilization of juxtacellular recordings in freely moving rats. J. Neurophysiol. *108*, 697–707.

Kitamura, T., Pignatelli, M., Suh, J., Kohara, K., Yoshiki, A., Abe, K., and Tonegawa, S. (2014). Island cells control temporal association memory. Science *343*, 896–901.

Klausberger, T., Magill, P.J., Márton, L.F., Roberts, J.D., Cobden, P.M., Buzsáki, G., and Somogyi, P. (2003). Brain-state- and cell-type-specific firing of hippocampal interneurons in vivo. Nature *421*, 844–848.

Klink, R., and Alonso, A. (1997). Muscarinic modulation of the oscillatory and repetitive firing properties of entorhinal cortex layer II neurons. J. Neurophysiol. *77*, 1813–1828.

Kumar, S.S., and Buckmaster, P.S. (2006). Hyperexcitability, interneurons, and loss of GABAergic synapses in entorhinal cortex in a model of temporal lobe epilepsy. J. Neurosci. *26*, 4613–4623.

Lever, C., Burton, S., Jeewajee, A., O'Keefe, J., and Burgess, N. (2009). Boundary vector cells in the subiculum of the hippocampal formation. J. Neurosci. *29*, 9771–9777.

Lingenhöhl, K., and Finch, D.M. (1991). Morphological characterization of rat entorhinal neurons in vivo: soma-dendritic structure and axonal domains. Exp. Brain Res. *84*, 57–74.

Mizuseki, K., Sirota, A., Pastalkova, E., and Buzsáki, G. (2009). Theta oscillations provide temporal windows for local circuit computation in the entorhinal-hippocampal loop. Neuron *64*, 267–280.

Moser, E.I., and Moser, M.-B. (2013). Grid cells and neural coding in high-end cortices. Neuron *80*, 765–774.

Peterson, D.A., Lucidi-Phillipi, C.A., Murphy, D.P., Ray, J., and Gage, F.H. (1996). Fibroblast growth factor-2 protects entorhinal layer II glutamatergic neurons from axotomy-induced death. J. Neurosci. *16*, 886–898.

Ray, S., Naumann, R., Burgalossi, A., Tang, Q., Schmidt, H., and Brecht, M. (2014). Grid-layout and theta-modulation of layer 2 pyramidal neurons in medial entorhinal cortex. Science *343*, 891–896.

Rowland, D.C., and Moser, M.-B. (2014). From cortical modules to memories. Curr. Opin. Neurobiol. *24*, 22–27.

Sargolini, F., Fyhn, M., Hafting, T., McNaughton, B.L., Witter, M.P., Moser, M.-B., and Moser, E.I. (2006). Conjunctive representation of position, direction, and velocity in entorhinal cortex. Science *312*, 758–762.

Savelli, F., Yoganarasimha, D., and Knierim, J.J. (2008). Influence of boundary removal on the spatial representations of the medial entorhinal cortex. Hippocampus *18*, 1270–1282.

Schmidt-Hieber, C., and Häusser, M. (2013). Cellular mechanisms of spatial navigation in the medial entorhinal cortex. Nat. Neurosci. *16*, 325–331.

Skaggs, W.E., McNaughton, B.L., Gothard, K.M., and Markus, E.J. (1993). An information-theoretic approach to deciphering the hippocampal code. In Advances in Neural Processing Systems, *Volume 5*, S.J. Hanson, J.D. Cowan, and C.L. Giles, eds. (San Mateo: Morgan Kaufmann).

Solstad, T., Boccara, C.N., Kropff, E., Moser, M.-B., and Moser, E.I. (2008). Representation of geometric borders in the entorhinal cortex. Science *322*, 1865–1868.

Tang, Q., Brecht, M., and Burgalossi, A. (2014). Juxtacellular recording and morphological identification of single neurons in freely moving rats. Nat. Protoc. *9*, 2369–2381.

Varga, C., Lee, S.Y., and Soltesz, I. (2010). Target-selective GABAergic control of entorhinal cortex output. Nat. Neurosci. *13*, 822–824.

Woolsey, T.A., and Van der Loos, H. (1970). The structural organization of layer IV in the somatosensory region (SI) of mouse cerebral cortex. The description of a cortical field composed of discrete cytoarchitectonic units. Brain Res. *17*, 205–242.

Zhang, S.-J., Ye, J., Miao, C., Tsao, A., Cerniauskas, I., Ledergerber, D., Moser, M.-B., and Moser, E.I. (2013). Optogenetic dissection of entorhinal-hippocampal functional connectivity. Science *340*, 1232627.

Neuron, Volume *84*

Supplemental Information

Pyramidal and Stellate Cell Specificity of Grid and Border Representations in Layer 2 of Medial Entorhinal Cortex

Qiusong Tang, Andrea Burgalossi, Christian Laut Ebbesen, Saikat Ray, Robert Naumann, Helene Schmidt, Dominik Spicher, and Michael Brecht

Inventory list of supplemental data

	Title	Related to
Figure S1	Anatomical characterization of calbindin-positive pyramidal and calbindin-negative stellate cells in layer 2 of medial entorhinal cortex	Figure 1
Figure S2	Testing of the classifier and error estimates	Figure 2
Figure S3	Firing properties of those identified and theta-assigned calbindin-positive and calbindin-negative neurons, which carry significant spatial information	Figure 2 & 3
Figure S4	Head-direction tuning of identified and theta-assigned calbindin-positive and calbindin-negative neurons	Figure 2
Table S1	Theta modulation (phase, strength) of juxtacellularly identified calbindin^{+} and calbindin^{-} cells from layer 2 of medial entorhinal cortex	Figure 2
Note S1	Custom-written Matlab script to classify non-identified cells into putative calbindin^{+} and calbindin^{-} by strength and preferred phase of theta locking	Figure 2

Tang et al. Layer 2 Grid & Border Cells Supplemental information

Figure S1, related to Figure 1

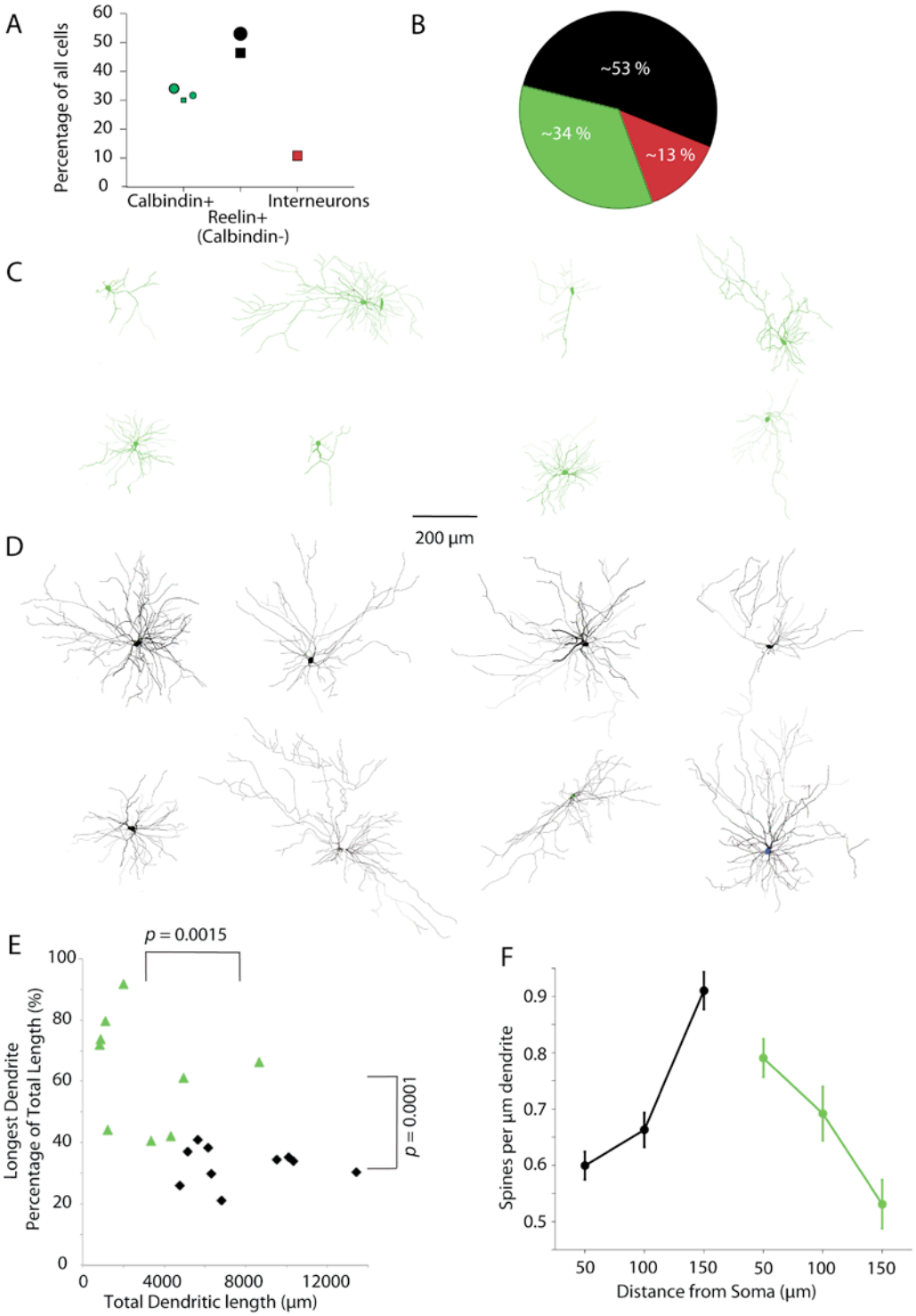

Tang et al. Layer 2 Grid & Border Cells Supplemental information

Figure S1. Anatomical characterization calbindin-positive pyramidal and calbindin-negative stellate cells in layer 2 of medial entorhinal cortex.
(A) Percentage of all neurons classified as calbindin$^+$, reelin$^+$ (calbindin$^-$) and interneurons in layer 2 of the medial entorhinal cortex of a rat. Absolute reelin$^+$ numbers have been extrapolated from calbindin$^+$ and reelin$^+$ counts. Circular markers indicate measurement made in this study. Square markers indicate measurements made by other studies (Peterson et al., 1996; Kumar and Buckmaster, 2006; Varga et al., 2010).
(B) Distribution of calbindin$^+$ neurons (green), reelin$^+$ neurons (black) and interneurons (red) in layer 2 of the medial entorhinal cortex of a rat. Numbers indicate averages of measurements indicated in panel A.
(C) Identified calbindin$^+$ cells have pyramidal morphologies. All cells come from tangential sections and are hence shown in 'views from the top'.
(D) Identified calbindin$^-$ cells have stellate morphologies. All cells come from tangential sections and are hence shown in 'views from the top'.
(E) Identified and reconstructed calbindin$^+$ cells and calbindin$^-$ cells show significant (*t*-test) size and shape differences.
(F) Spine distribution differs in calbindin$^+$ cells and calbindin$^-$ cells; data refer to ten cells each, for which we counted spine densities in multiple ~30 µm dendrite segments at the distances from the soma specified in the plot. Slopes of spine density differed significantly between calbindin$^+$ cells and calbindin$^-$ cells ($p = 0.0023$, *t*-test). Error bars indicate SEM.

Tang et al. Layer 2 Grid & Border Cells Supplemental information

Figure S2, related to Figure 2

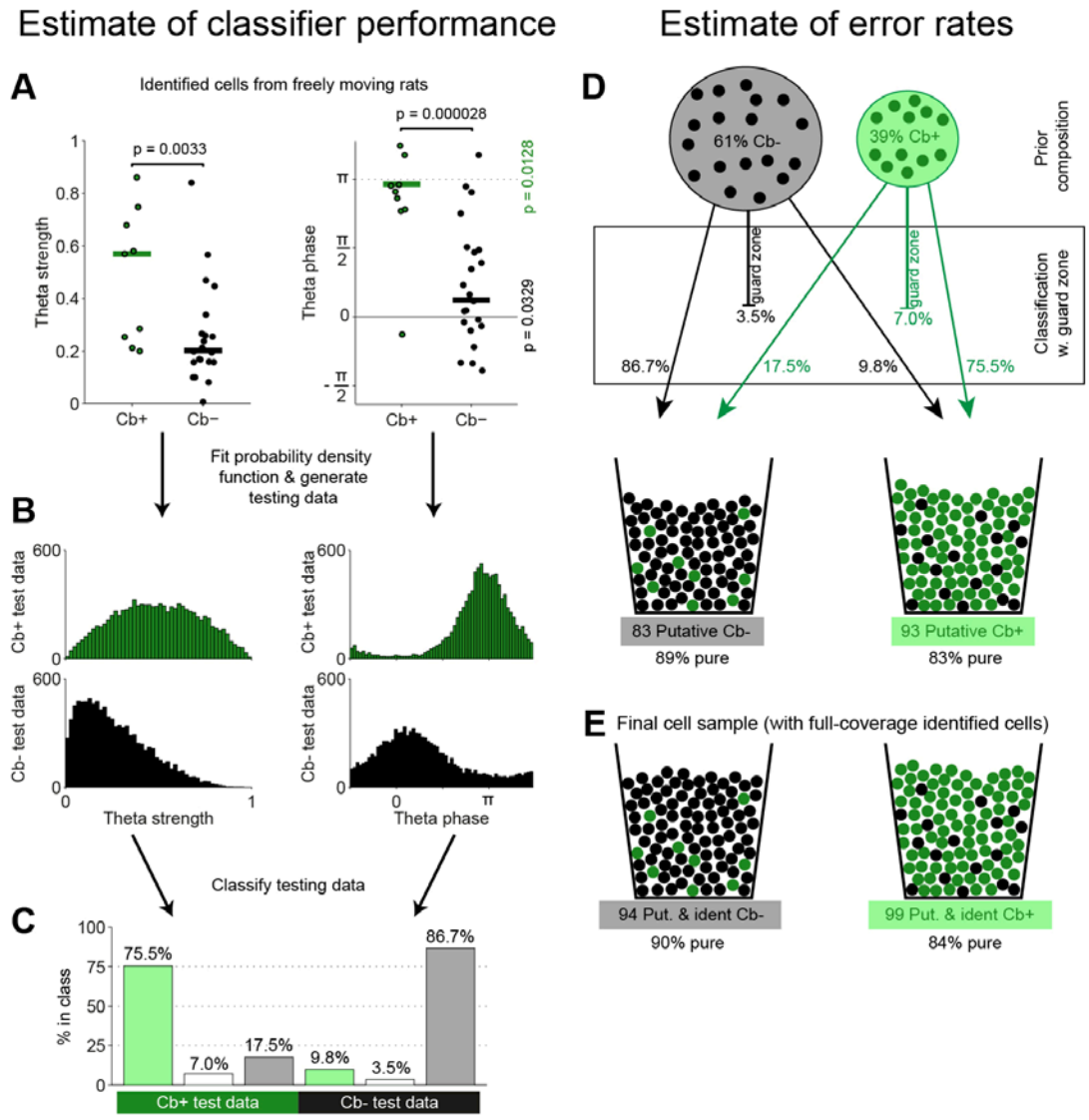

Tang et al. Layer 2 Grid & Border Cells Supplemental information

Figure S2. Testing of the classifier and error estimates.
(A) Theta strength and preferred theta phase of identified calbindin$^+$ cells (green dots) and calbindin$^-$ cells (black dots) is significantly different. Green and black lines indicate medians of theta strength (p = 0.0033, Mann-Whitney U-test). Green and black lines indicate circular means of preferred theta phase (p = 0.000028, Parametric Watson-Williams multi-sample test). Calbindin$^+$ cells show a significant tendency to fire near the trough (p = 0.013, Rayleigh's test for nonuniformity) and calbindin$^-$ cells show a tendency to fire near the peak of theta rhythm (p = 0.033, Rayleigh's test for nonuniformity).
(B) Distribution of testing data for estimation of classifier performance. Testing data is generated by fitting the appropriate probability density functions (beta distributions and circular Gaussian distributions, respectively) to the distributions of theta strength and preferred theta phase of identified calbindin$^+$ and calbindin$^-$ cells (N = 10.000 for both cell types).
(C) Result of classification of testing data shows that both calbindin$^+$ cells and calbindin$^-$ cells are classified with high accuracy and low false classification rates (75.5% correct and 17.5% incorrect for calbindin$^+$ cells, 86.7% correct and 9.8% incorrect for calbindin$^-$ cells). This shows that the classification boundary is robust and not just overfitting the small training set of identified cells.
(D) Estimation of the purity (positive predictive value) of the classifier based on the estimate of 34% calbindin$^+$, 53% reelin$^+$ (calbindin$^-$) and 13% interneurons in L2 of rat MEC (Figure S1A,B). The sample of 93 putative calbindin$^+$ cells is estimated to be 83% pure, and the sample of 83 putative calbindin$^-$ cells is estimated to be 89% pure.
(E) After addition of identified, full-coverage cells (11 calbindin$^-$ and 6 calbindin$^+$), we estimate the purity of our final cell sample to be 84% for calbindin$^+$ cell and 90% for calbindin$^-$ cells.

Tang et al. Layer 2 Grid & Border Cells Supplemental information

Figure S3, related to Figure 2 & 3

A

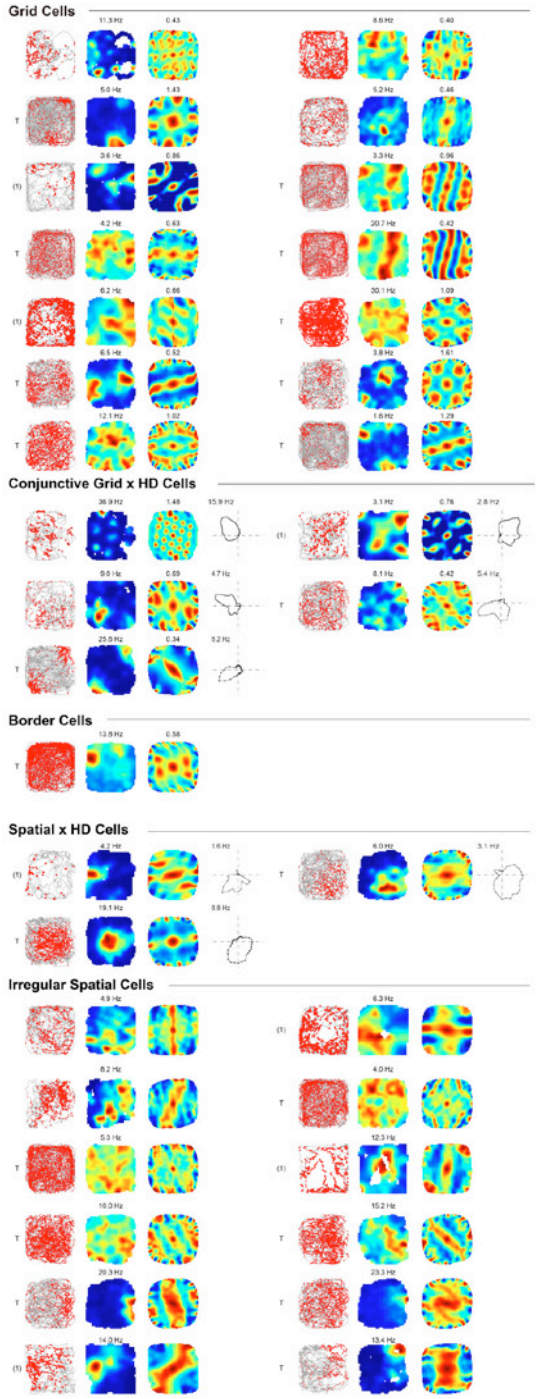

Tang et al. Layer 2 Grid & Border Cells Supplemental information

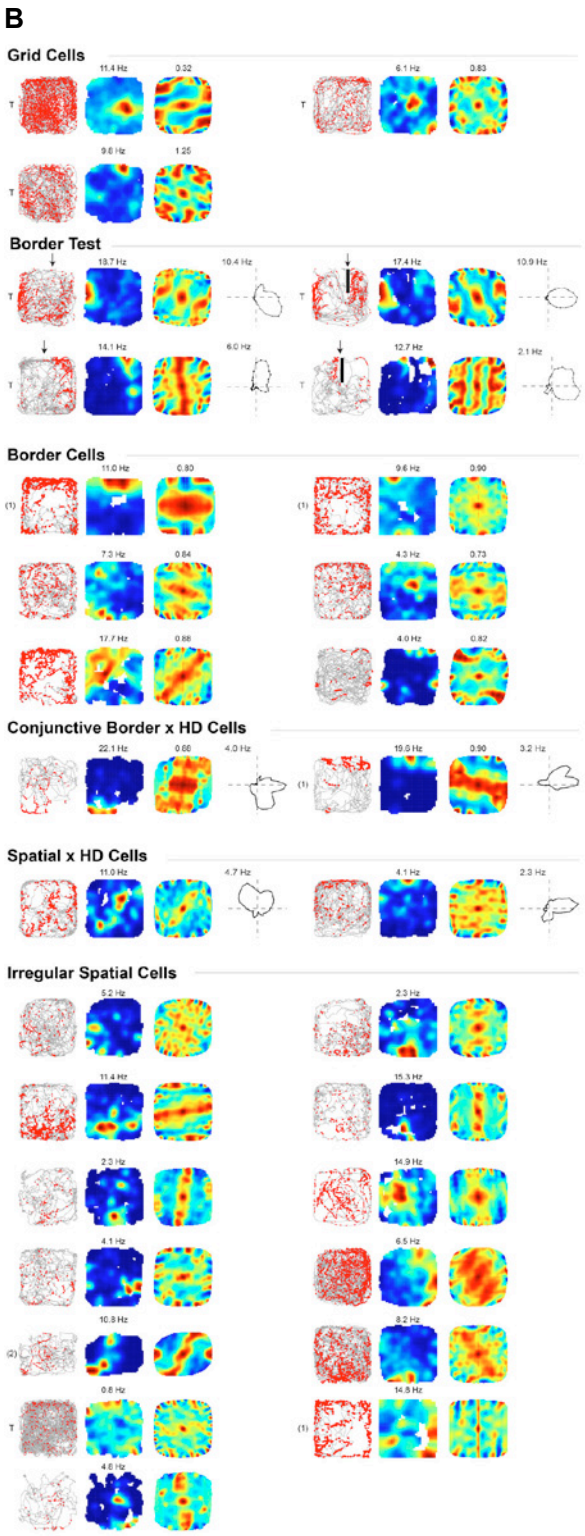

Tang et al. Layer 2 Grid & Border Cells Supplemental information

Figure S3. Firing properties of those identified and theta-assigned calbindin-positive and calbindin-negative neurons, which carry significant spatial information.
(A) Calbindin-positive neurons. Cells are ordered according to spatial firing properties. From left to right we show spike-trajectory plot, rate map, two-dimensional spatial autocorrelation and angular tuning (which is shown only for head-direction selective cells. Note that pure head-direction cells that do not carry positional information are not included in this Figure). Numbers above the rate map indicate maximum firing rate. Numbers above the spatial autocorrelation indicate grid or border scores with respect to their properties. (T) indicates cells recorded with tetrodes; all other cells are from juxtacellular recordings. (1) indicates cells recorded in 0.7 x 0.7 m arena, all other recordings are from 1 x 1 m arena.
(B) Calbindin-negative neurons. Cells are ordered according to spatial firing properties. From left to right we show spike-trajectory plot, rate map, two-dimensional spatial autocorrelation and angular tuning (which is shown only for head-direction selective cells. Note that pure head-direction cells that do not carry positional information are not included in this Figure). Numbers above the rate map indicate maximum firing rate. Numbers above the spatial autocorrelation indicate grid or border scores with respect to their properties. (T) indicates cells recorded with tetrodes; all other cells are from juxtacellular recordings. (1) indicates cells recorded in 0.7 x 0.7 m arena, (2) one cell recorded in a 0.6 x 0.8 m arena; all other recordings are from 1 x 1 m arena.

Tang et al. Layer 2 Grid & Border Cells Supplemental information

Figure S4, related to Figure 2

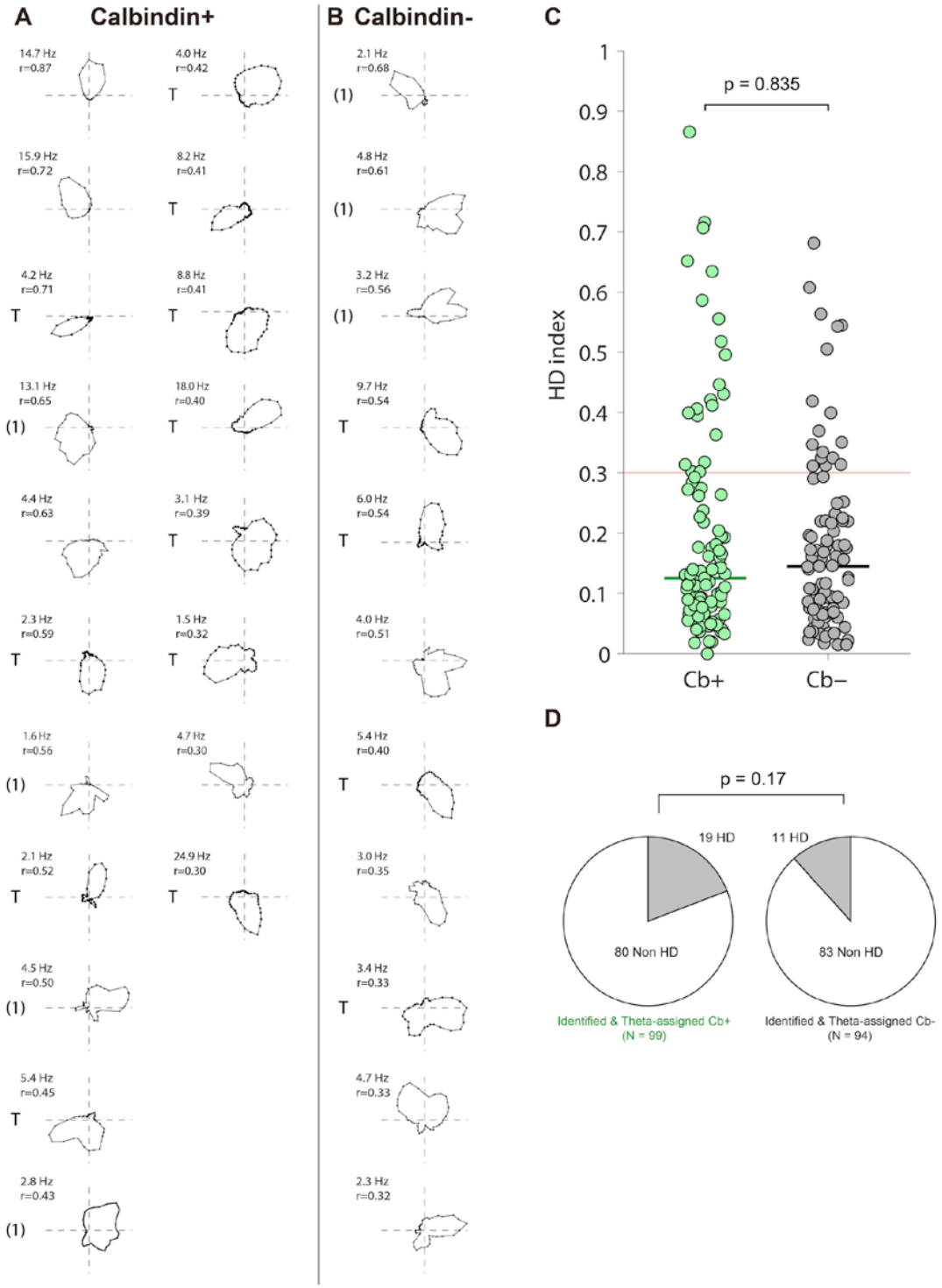

Tang et al. Layer 2 Grid & Border Cells Supplemental information

Figure S4. Head-direction tuning of those identified and theta-assigned calbindin-positive and calbindin-negative neurons.
(A) Polar plots of the head-direction tuning in identified and theta-assigned calbindin-positive neurons, which carry significant directional information. Cells are ranked according to Rayleigh vector lengths. (T) indicates cells recorded with tetrodes; all other cells are from juxtacellular recordings. (1) indicates cells recorded in 0.7 x 0.7 m arena, all other recordings are from 1 x 1 m arena.
(B) Polar plots of the head-direction tuning in identified and theta-assigned calbindin-negative neurons, which carry significant directional information. Cells are ranked according to Rayleigh vector lengths.
(C) Comparison of HD index (Rayleigh vector length) between (identified and putative) calbindin$^+$ and calbindin$^-$ neurons; the dotted line indicates the threshold for head-direction cell; vertical lines indicate medians (p = 0.835, Mann-Whitney U-test).
(D) Numbers of head-direction cells in (identified and putative) calbindin$^+$ (A) and calbindin$^-$ (B) neurons were not different (p = 0.17, Fisher's exact test).

Tang et al. Layer 2 Grid & Border Cells Supplemental information

Table S1, related to Figure 2

TYPE	PHASE	STRENGTH	
0	1,2318	0,238	Calbindin-
0	2,8419	0,84031	Calbindin-
0	1,5892	0,21271	Calbindin-
0	1,5243	0,46896	Calbindin-
0	0,14037	0,44728	Calbindin-
0	2,3605	0,56663	Calbindin-
0	-0,0628	0,1579	Calbindin-
0	0,3543	0,0073	Calbindin-
0	-1,0621	0,3383	Calbindin-
0	-0,2142	0,1004	Calbindin-
0	1,0873	0,15808	Calbindin-
0	-0,11996	0,25522	Calbindin-
0	1,4714	0,0817	Calbindin-
0	-0,31369	0,16922	Calbindin-
0	2,9724	0,1946	Calbindin-
0	-1,2278	0,1007	Calbindin-
0	-1,0479	0,25896	Calbindin-
0	0,50391	0,26567	Calbindin-
0	-0,69228	0,20623	Calbindin-
0	0,72691	0,16779	Calbindin-
0	0,12994	0,15958	Calbindin-
0	-2,5888	0,1987	Calbindin-
1	-2,3775	0,28433	Calbindin+
1	2,7056	0,56983	Calbindin+
1	-0,40718	0,19952	Calbindin+
1	-2,5879	0,2532	Calbindin+
1	3,0164	0,86095	Calbindin+
1	2,4491	0,7484	Calbindin+
1	2,9923	0,58077	Calbindin+
1	2,856	0,67846	Calbindin+
1	2,4112	0,21168	Calbindin+

Table S1. Classification training dataset of putative calbindin^{+} cells or calbindin^{-} cells. Cells were recorded and identified juxtacellularly in freely-moving animals. Phase value is the preferred firing phase in radians, in relation to theta rhythm. Strength is the average Rayleigh vector length of the phase locking to theta (0 to 1). Type = 1 means calbindin^{+}, Type = 0 means calbindin^{-}.

Tang et al. Layer 2 Grid & Border Cells Supplemental information

Note S1, related to Figure 2

```
function [CellClass,Distance] = CbClassify(Pha,Str)
% Function to classify unitentified cell as putative Cb+ and Cb-.
%
% Output of function is CellClass and Distance. CellClass = 1 means Cb+,
% CellClass = 0 means Cb-. Distance is the signed distance to the
% classification boundary.
%
% HOW TO USE - Example:
% Cell has Phase = 2.6, Strength = 0.45.
% To classify using Phase and Strength, call:
%   [CellClass,Distance] = CbClassify(2.6,0.45)
%
% Function can also run on many cells, if they are passed as column vectors
% of e.g. Phases and Strengths. Example:
%   [CellClass,Distance] = CbClassify([-3.0;2.7;0.3],[0.5;0.6;0.1])
%
% Training set of identified Cb+ and Cb- cells are also available as an
% MS Excel sheet.
%
% ----------------------------------------
%
% This is a supplementary file to:
% Qiusong Tang*, Andrea Burgalossi*, Christian Laut Ebbesen*, Saikat Ray,
% Robert Naumann, Helene Schmidt, Dominik Spicher & Michael Brecht: Pyramidal and Stellate
% Cell-specificity of Grid and Border Representations in Layer 2 of Medial
% Entorhinal Cortex (2014).
%
% Affiliation:
%   Bernstein Center for Computational Neuroscience
%   Humboldt University of Berlin
%   Philippstr. 13 Haus 6
%   10115 Berlin, Germany
%
% To whom correspondence should be addressed:
% andrea.burgalossi@bccn-berlin.de or michael.brecht@bccn-berlin.de
%
% You can redistribute it and/or modify it under the terms of the GNU
% General Public License as published by the Free Software Foundation.
%
% For the GNU General Public License, see <http://www.gnu.org/licenses/>.



%% Set the width of the guard zone for plotting
    GuardZone = 0.1;

%% Load the Training data from identified recordings

isCbPlus = [0;0;0;0;0;0;0;0;0;0;0;0;0;0;0;0;0;0;0;0;1;1;1;1;1;1;1;1;1]

trainPhases = [1.23180000000000;2.84190000000000;1.58920000000000;1.52430000000000;...
    0.140370000000000;2.36050000000000;-0.0628000000000000;0.354300000000000;...
    -1.06210000000000;-0.214200000000000;1.08730000000000;-0.119960000000000;...
    1.47140000000000;-0.313690000000000;2.97240000000000;-1.22780000000000;...
    -1.04790000000000;0.503910000000000;-0.692280000000000;0.726910000000000;...
```

```
    0.129940000000000;-2.58880000000000;-2.37750000000000;2.70560000000000;...
    -0.407180000000000;-2.58790000000000;3.01640000000000;2.44910000000000;...
    2.99230000000000;2.85600000000000;2.41120000000000]

trainStrength = [0.238000000000000;0.840310000000000;0.212710000000000;↙
0.468960000000000;...
    0.447280000000000;0.566630000000000;0.157900000000000;0.00730000000000000;...
    0.338300000000000;0.100400000000000;0.158080000000000;0.255220000000000;...
    0.081700000000000;0.169220000000000;0.194600000000000;0.100700000000000;...
    0.258960000000000;0.265670000000000;0.206230000000000;0.167790000000000;...
    0.159580000000000;0.198700000000000;0.284330000000000;0.569830000000000;...
    0.199520000000000;0.253200000000000;0.860950000000000;0.748400000000000;...
    0.580770000000000;0.678460000000000;0.211680000000000]


%% Classify cells using Pha & Str
% Calculate the training set for the classifier using phase and theta strength
TrainingSet = [cos(trainPhases).*trainStrength, sin(trainPhases).*trainStrength];
% Train the classifier
svmStruct = svmtrain(TrainingSet,isCbPlus,'kernel_function','rbf');

% Calculate the features of the cell to be classified
Cell = [cos(Pha).*Str sin(Pha).*Str];

% Classify the cell
CellClass = svmclassify(svmStruct, Cell);

% Calculate the distance to the classification boundary
    SampleScaleShift = bsxfun(@plus,Cell,svmStruct.ScaleData.shift);
    CellScaled = bsxfun(@times,SampleScaleShift,svmStruct.ScaleData.scaleFactor);
    sv = svmStruct.SupportVectors;
    alphaHat = svmStruct.Alpha;
    bias = svmStruct.Bias;
    kfun = svmStruct.KernelFunction;
    kfunargs = svmStruct.KernelFunctionArgs;
    Distance = kfun(sv,CellScaled,kfunargs{:})'*alphaHat(:) + bias;


% Colors for plotting
Black = [0 0 0];
DarkGrey = [0.6602 0.6602 0.6602];
PaleGreen = [0.5938 0.9833 0.5938];
Red = [1 0 0];
Gold = [1 0.8398 0];
White = [1 1 1];


% Start figure
figure();
    set(gcf,'PaperUnits','centimeters')
    xSize = 15; ySize = 15;
    xLeft = (21-xSize)/2; yTop = (30-ySize)/2;
    set(gcf,'PaperPosition',[xLeft yTop xSize ySize])
    X = 100;Y = 100;
    set(gcf,'Position',[X Y xSize*50 ySize*50]);
```

Tang et al. Layer 2 Grid & Border Cells Supplemental information

```
    set(gca,'TickDir','out')
hold on;

% make a big matrix to plot the area
rangesMax = [1.1 1.1];
rangesMin = [-1.1 -1.1];
xRange = linspace(rangesMin(1),rangesMax(1),1000);
yRange = linspace(rangesMin(2),rangesMax(2),1000);
[xx,yy] = meshgrid(xRange,yRange);
gridSamples = [xx(:),yy(:)];

% classify the big matrix
gridLabels = svmclassify(svmStruct, gridSamples);
xDisp = reshape(xx,1000,1000);
yDisp = reshape(yy,1000,1000);


% Calculate the distance to the classification boundary
    SampleScaleShift = bsxfun(@plus,gridSamples,svmStruct.ScaleData.shift);
    CellScaled = bsxfun(@times,SampleScaleShift,svmStruct.ScaleData.scaleFactor);
    sv = svmStruct.SupportVectors;
    alphaHat = svmStruct.Alpha;
    bias = svmStruct.Bias;
    kfun = svmStruct.KernelFunction;
    kfunargs = svmStruct.KernelFunctionArgs;
    MapDistance = kfun(sv,CellScaled,kfunargs{:})'*alphaHat(:) + bias;

% set the color map for guard zone plotting here
    guardLogic = abs(MapDistance) < GuardZone | sqrt(sum(gridSamples.^2,2)) > 1;
    gridLabels(guardLogic) = 0.5;
    labelDispGuard = reshape(gridLabels,1000,1000);



% plot the matrix using labelDisp as colormap
[ch,ch]=contourf(xDisp,yDisp,labelDispGuard);
     set(ch,'edgecolor','none');
set(gcf, 'ColorMap', [DarkGrey;White;PaleGreen])

plot([rangesMin(1) rangesMax(1)],[0 0],'-k')
plot([0 0],[rangesMin(1) rangesMax(1)],'-k')
axis square



% add sun
th = 0:0.005:2*pi;
for i=[0.2 0.4 0.6 0.8]
plot(i*cos(th),i*sin(th),':k')
end
plot(cos(th),sin(th),'k')


% Plot the non-ident cell and color them
for i=1:size(Cell,1)
```

Tang et al. Layer 2 Grid & Border Cells Supplemental information

```
    h=scatter(Cell(i,1),Cell(i,2),90);

    if Distance(i) > 0
        set(h,'MarkerEdgeColor',Black,...
            'MarkerFaceColor',Gold,...
            'LineWidth',1)

    elseif Distance(i) < 0
        set(h,'MarkerEdgeColor',Black,...
            'MarkerFaceColor',Red,...
            'LineWidth',1)
    end

    if abs(Distance(i)) < GuardZone
        set(h,'MarkerEdgeColor',Black,...
            'MarkerFaceColor',White,...
            'LineWidth',1)
    end
end


% Add axis labels
xlabel('$\cos(\phi) \times S$','Interpreter','LaTex','FontSize',20)
ylabel('$\sin(\phi) \times S$','Interpreter','LaTex','FontSize',20)

xlim([rangesMin(1) rangesMax(1)])
ylim([rangesMin(1) rangesMax(1)])

axis square



end
```

Note S1. MatLab code of the function to classify unidentified cells as putative calbindin^{+} cells or calbindin^{-} cells. Output of the function is CellClass and Distance. CellClass = 1 means calbindin^{+}, CellClass = 0 means calbindin^{-}. Distance is the signed distance to the classification boundary.

Tang et al. Layer 2 Grid & Border Cells Supplemental information

Supplemental Experimental Procedures

All experimental procedures were performed according to German guidelines on animal welfare.

Freely-moving juxtacellular recordings
Experimental procedures for obtaining juxtacellular recordings in freely moving animals were performed similar to earlier publications (Ray et al., 2014; Tang et al., 2014). Briefly, recordings were made from male Wistar and Long-Evans rats (150-350 g) maintained in a 12-h light / dark phase and were recorded in the dark phase. Glass pipettes with resistance 4-6 MΩ were filled with extracellular (Ringer) solution containing (in mM) NaCl 135, KCl 5.4, HEPES 5, $CaCl_2$ 1.8, and $MgCl_2$ 1 (pH = 7.2) and Neurobiotin (1-2%). Animal implantations were performed as previously described (Burgalossi et al., 2011; Herfst et al., 2012, Tang et al., 2014), with a basic head-implant including a metal post for head-fixation and placement of a miniaturized preamplifier, a plastic ring and a protection cap (Herfst et al., 2012). In order to target the dorsalmost region of medial entorhinal cortex, a plastic ring was glued on the skull surface 0.2-0.8 mm anterior to the transverse sinus and 4.5-5 mm lateral to the midline. After implantation, rats were allowed to recover from the surgery and were habituated to head-fixation for 3-5 days, as previously described (Houweling et al., 2008, Tang et al., 2014). Rats were trained in the experimental arena for 3-7 days (multiple sessions per day, 15-20 min duration each). Within the recording arena (70 x 70 cm or 1 x 1 m square black box, with a white cue card on the wall; 1 cell was recorded in a square arena, 60 cm x 80 cm), rats were trained to chase for chocolate or sugar pellets. Training was performed both before and after implantation (see below), or after implantation only. On the day of recording, under isoflurane anesthesia (1-3%), implants were completed, and an additional metal post was cemented, which served to anchor the miniaturized micromanipulator (Kleindiek Nanotechnik GmbH; Lee et al., 2006; Tang et al., 2014). 3-4 hours to 1 day later after recovery from anesthesia, rats were head-fixed, full implants were assembled, and the miniaturized micromanipulator and preamplifier were secured to the metal posts. The glass recording pipette was advanced into the brain; a thick agarose solution (4-5% in Ringer) was applied into the recording chamber for sealing the craniotomy and stabilization. Animals were then released and gently transferred into the behavioral arena. To minimize discomfort from the head implant, we sometimes supplied local anesthesia in the neck region. Juxtacellular recordings were established while animals were running in the arena. Juxtacellular labeling was attempted at the end of the recording session according to standard procedures (Pinault et al., 1996). A number of recordings (non-identified recordings; see data analysis) putatively in layer 2 (n = 61) were either lost before the labeling could be attempted, or the recorded neurons could not be unequivocally identified. After the experiment, the animals were euthanized with an overdose of ketamine or urethane and perfused transcardially with 0.1 M PB followed by 4% paraformaldehyde solution, shortly after the labeling protocol. Juxtacellular recordings in anesthetized animals (Ray et al., 2014) were performed under ketamine/urethane anesthesia according to established procedures (Klausberger et al., 2003, Quilichini et al., 2010). The juxtacellular signals were amplified by the ELC-03XS amplifier and sampled at 20 kHz by a data-acquisition interface under the control of PatchMaster 2.20 software. The animal's location and head-direction was automatically tracked at 25 Hz by the Neuralynx video tracking system and two head-mounted LEDs.

Tetrode recordings
Tetrode recordings (n = 126 layer 2 single units) were obtained as previously described in detail (von Heimendahl et al., 2012). Tetrodes were turned from 12.5 μm diameter nichrome wire

(California Fine Wire Company) and goldplated to ~250 kOhm impedance. Spiking activity and local field potential were recorded at 32 kHz (Neuralynx; Digital Lynx). Local field potential for theta phase assignment was recoded from the same tetrode as single units, relative to one tetrode left in superficial cortex. All recordings were done in a 1x1m box with behavioral training tasks same as juxtacellular procedures. The animal's location and head-direction was automatically tracked at 25 Hz by video tracking and head-mounted LEDs, as described above. After recordings, tetrode tracks were lesioned and the animal was trancardially perfused. The brain was sectioned tangentially and recording sites assigned by histology. Spikes were pre-clustered using KlustaKwik (K.D. Harris, Rutgers University) and manually using MClust (A.D. Redish, University of Minnesota). Cluster quality was assessed by spike shape, ISI-histogram, L-ratio and isolation distance, as previously described (von Heimendahl et al., 2012). Putative interneurons were identified based on firing rate, spike shape and ISI-histogram and were excluded from classification.

Neurobiotin labeling and calbindin immunohistochemistry
For histological analysis of juxtacellularly-labeled neurons, Neurobiotin was visualized with streptavidin conjugated to Alexa 546 (1:1000). Subsequently, immunohistochemistry for Calbindin was performed as previously described (Ray et al., 2014) and visualized with Alexa Fluor 488. After fluorescence images were acquired, the Neurobiotin staining was converted into a dark DAB reaction product. Neuronal morphologies were reconstructed by computer-assisted manual reconstructions (Neurolucida).

Spine density measurement
To assess the spine density of calbindin$^+$ and calbindin$^-$ dendrites, we labeled neurons in vivo juxtacellularly and identified the cells based on their calbindin immunoreactivity. We counted spines of fluorescent and DAB converted cells (10 calbindin$^+$ and 10 calbindin$^-$ neurons) at 50 µm, 100 µm and 150 µm from the soma. The spine counts were normalized by dendritic length to obtain the number of spines per µm.

Estimate of the fraction of unintentionally included non-layer 2 cells
Targeting recordings to layer 2 was achieved by mapping (1) the depth at which a pronounced increase in spiking activity and multi-unit synchrony during running was observed (Domnisoru et al., 2013) and (2) the L2/L1 border, which was always easy to identify as a reference point due to the drop in spiking activity and the more prominent local field potential gamma oscillations during theta epochs observed in L1 (Quilichini et al., 2010).
We estimated the fraction of non-layer 2 principal cells included in our sample and expect that this mistaken fraction is in the < 10% range and probably consists mainly of parasubicular cells. This estimate was computed as follows:
(1) We included 126 unidentified cells from tetrodes, and according to histology this sample does not contain off-target cells, as all recording sites could be reliably assigned to medial entorhinal cortex layer 2.
(2) The laminar mistakes in our assignment of juxtacellular recordings seem to be small, i.e. in 31 recording attempts where we aimed at layer 2, we never recovered layer 6, layer 5 and layer 4 cells, but indeed recovered cells in the expected target. In only 2 additional cases we recovered cells in layer 3, where we expected to find layer 2 cells. Hence we expect a 6% laminar error rate.
(3) Dorsoventral / mediolateral mistakes. We never recovered unintentionally postrhinal, retrospenial or lateral entorhinal cells in our medial entorhinal cortex recording attempts. However, in 9 experiments where we aimed at targeting layer 2, 9 parasubicular cells were

recovered instead. Thus, there are probably also parasubicular cells in the unidentified cells sample and this error might appear to be substantial (22% error rate). However, in 36 of the 61 included unidentified cells we could exclude such mistakes, because we identified the respective tracks in the correct target location. In 25 included unidentified juxtacellular recordings we could not rule out such mistakes, because tracks were not found, because of poor histology or proximity of tracks to the parasubiculum.
From these numbers we expect about 4 laminar mistakes (unintentionally recorded layer 3 cells) in the 61 included juxtacellular recordings. We expect about 6 dorsoventral / mediolateral mistakes (unintentionally recorded parasubicular cells) in the 25 included juxtacellular recordings, where we could not exclude such mistakes.
This leads to the following overall numbers: 16% unidentified recordings are expected to be non-layer 2 cells. This corresponds to a 5% rate of mistakes in our overall sample (identified and unidentified cells).

Analysis of theta locking
For all cells, we calculated the locking to theta phase based on spiking discharge in relation to theta rhythm in the local field potential. The local field potential was zero-phase band-pass filtered (4-12 Hz) and a Hilbert transform was used to determine the instantaneous phase of the theta wave. The strength of locking to theta phase, S, and the preferred phase angle, φ, was defined as the modulus and argument of the Rayleigh average vector of the theta phase at all spike times. Only spikes during running (speed cutoff = 1 cm/s for juxtacellular signals, 5 cm/s for tetrode recordings) were included in the analysis. Only cells with firing rate ≥ 0.5 Hz were included in the analysis (Barry et al., 2012b). Both the analysis procedures and the juxtacellular data set largely correspond to our recent publication (Ray et al., 2014), whereby a more stringent band-pass filtering was applied in a subset of cells.

Analysis of Spatial Modulation
The position of the rat was defined as the midpoint between two head-mounted LEDs. A running speed threshold (see above) was applied for isolating periods of rest from active movement. Color-coded firing maps were plotted. For these, space was discretized into pixels of 2.5 cm x 2.5 cm, for which the occupancy z of a given pixel x was calculated as

$$z(x) = \sum_t w(|x - x_t|)\Delta t$$

where x_t is the position of the rat at time t, Δt the inter-frame interval, and w a Gaussian smoothing kernel with σ = 5cm.
Then, the firing rate r was calculated as

$$r(x) = \frac{\sum_i w(|x - x_i|)}{z}$$

where x_i is the position of the rat when spike i was fired. The firing rate of pixels, whose occupancy z was less than 20 ms, was considered unreliable and not shown.
To determine the spatial periodicity of juxtacellularly recorded neurons, we determined spatial autocorrelations. The spatial autocorrelogram was based on Pearson's product moment correlation coefficient:

Tang et al. Layer 2 Grid & Border Cells Supplemental information

$$r(\tau_x, \tau_y) = \frac{\mathbf{n}\sum f(x,y)f(x-\tau_x, y-\tau_y) - \sum f(x,y)\sum f(x-\tau_x, y-\tau_y)}{\sqrt{n\sum f(x,y)^2 - (\sum f(x,y))^2}\sqrt{n\sum f(x-\tau_x, y-\tau_y)^2 - (\sum f(x-\tau_x, y-\tau_y))^2}}$$

where, $r(\tau_x, \tau_y)$the autocorrelation between pixels or bins with spatial offset τ_x and τ_y. f is the image without smoothing or the firing rate map after smoothing, n is the number of overlapping pixels or bins. Autocorrelations were not estimated for lags of τ_x and τ_y, where n < 20. For spatial and head-directional analysis, both a spatial (> 50% spatial coverage) and a firing rate inclusion criterion (> 0.5 Hz) were applied. Spatial coverage was defined as the fraction of visited pixels (bins) in the arena to the total pixels.

Analysis of Spatial Information

For all cells, we calculated the spatial information rate, *I*, from the spike train and rat trajectory:

$$I = \frac{1}{T}\int r(x)\log_2\frac{r(x)}{\bar{r}}o(x)dx$$

where $r(x)$ and $o(x)$ are the firing rate and occupancy as a function of a given pixel x in the rate map. $\bar{r}$ is the overall mean firing rate of the cell and T is the total duration of a recording session (Skaggs et al., 1993). A cell was determined to have a significant amount of spatial information, if the observed spatial information rate exceeded the 95th percentile of a distribution of values of *I* obtained by circular shuffling. Shuffling was performed by a circular time-shift of the recorded spike train relative to the rat trajectory by a random time $t' \in]0, T[$ for 1000 permutations (von Heimendahl et al., 2012; Bjerknes et al., 2014).

Analysis of Gridness

Grid scores were calculated as previously described (Barry et al., 2012a) by taking a circular sample of the autocorrelogram, centered on, but excluding the central peak. The Pearson correlation of this circle with its rotation for 60 degrees and 120 degrees was obtained (on peak rotations) and also for rotations of 30 degrees, 90 degrees and 150 degrees (off peak rotations). Gridness was defined as the minimum difference between the on-peak rotations and off-peak rotations. To determine the grid scores, gridness was evaluated for multiple circular samples surrounding the center of the autocorrelogram with circle radii increasing in unitary steps from a minimum of 10 pixels more than the width of the radius of the central peak to the shortest edge of the autocorrelogram. The radius of the central peak was defined as the distance from the central peak to its nearest local minima in the spatial autocorrelogram. The radius of the inner circle was increased in unitary steps from the radius of the central peak to 10 pixels less than the optimal outer radius. The grid score was defined as the best score from these successive samples. Grid scores reflect both the hexagonality in a spatial field and also the regularity of the hexagon. To disentangle the effect of regularity from this index, and consider only hexagonality, we transformed the elliptically distorted hexagon into a regular hexagon and computed the grid scores (Barry et al., 2012a). A linear affine transformation was applied to the elliptically distorted hexagon, to stretch it along its minor axis, until it lay on a circle, with the diameter equal to the major axis of the elliptical hexagon. The grid scores were computed on this transformed regular hexagon (Barry et al., 2012a).

Analysis of Border Cells

Tang et al. Layer 2 Grid & Border Cells Supplemental information

To determine the modulation of a cell firing along a border, we determined border scores (Solstad et al., 2008). Border fields were identified from a collection of neighboring pixels having a firing rate higher than 0.3 times the maximum firing rate and covering an area of at least 100 cm (Sargolini et al., 2006). The coverage (Cm) along a wall was defined as the maximum length of a putative border field parallel to a boundary, divided by the length of the boundary. The mean firing distance (Dm) of a field was defined as the sum of the square of its distance from the boundary, weighted by the firing rate (Solstad et al., 2008). The distance from a boundary was defined as the exponential of the square of the distance in pixels from the closest boundary, normalized by half the length of the boundary. Border scores were defined as the maximum difference between Cm and Dm, divided by their sum, and ranged from -1 to +1.

Analysis of Head Direction

Head-direction tuning was measured as the excentricity of the circular distribution of firing rates. For this, firing rate was binned as a function of head-direction (N = 36). A cell was said to have a significant head-direction tuning, if the length of the average vector exceeded the 95th percentile of a distribution of average vector lengths calculated from shuffled data and had a Rayleigh vector length > 0.3. Data was shuffled by applying a random circular time-shift to the recorded spike train for 1000 permutations.

Classification of non-identified cells into putative cell types

For classification based on strength of locking to theta phase, S, and preferred theta phase angle, φ, we built a support vector machine using the built-in functions of the MATLAB Statistics Toolbox (The MathWorks Inc., Natick, MA, USA) using pairs of φ and S obtained from juxtacellular recording of identified cells. Because the phase angle is a circular variable, we trained the classifier on a space of the vectors (cos(φ)·S,sin(φ)·S), scaled to zero mean and unit variance using a gaussian radial basis kernel function with a scaling factor, sigma, of 1. To avoid cross-contamination of the two clusters, we employed a guard zone and excluded cells with a distance to the classification hyperplane < 0.1 from classification (white dots in Figure 2C). Classifier robustness was evaluated using a bootstrapping approach. To test if the putative calbindin$^+$/calbindin$^-$ border suggested by the classifier based on our limited set of identified cells would also correctly classify a large number of non-identified cells, we fitted the appropriate probability density functions to the theta strength and phase angle of identified cells (beta distributions and circular Gaussian distributions, respectively) and generated 10.000 calbindin$^+$ and 10.000 calbindin$^-$ testing cells drawn from these distributions (Figure S2A and S2B). Testing cells were classified and found to be classified 75.5% correctly for calbindin$^+$ cells and 86.7 % correctly for calbindin$^-$ cells (Figure S2C), suggesting that our classifier generally performs well and is not just overfitting our small dataset of identified cells from freely-moving rats. Assuming the prior distribution of ~34% calbindin$^+$ neurons , ~53% reelin$^+$ (calbindin$^-$) neurons and ~13% interneurons in layer 2 of the medial entorhinal cortex of a rat (Figure S1A and S1B), we estimate the purity (positive predictive value) of putative calbindin$^+$ and putative calbindin$^-$ cells assigned by our classifier to be 83% and 89%, respectively (Figure S2D). This gives us the final cell sample purity of our putative and identified dataset of 84% and 90% for calbindin$^+$ and calbindin$^-$ cells, respectively.

Classification of cells into functional categories

Cells were classified as head-direction cells, grid cells, conjunctive cells, border cells and non-spatially modulated cells based on their grid score, border score, spatial information and significance of head-directionality according to the following criteria:

Tang et al. Layer 2 Grid & Border Cells Supplemental information

Head direction cells: Rayleigh vector length > 0.3 & significant head-direction tuning (Boccara et al., 2010)

Grid cells: Grid score > 0.3 & significant spatial information.

Border cells: Border score > 0.5 & significant spatial information (Solstad et al., 2008), or those who passed border test (Lever et al., 2009).

Spatially irregular cells: significant spatial information (Bjerknes et al., 2014).

Non-spatially modulated cell: no significant spatial information.

In agreement with previous work (Solstad et al., 2008), few cells (n = 6) passed both the border cell and the grid cell threshold. These six cells were assigned to be grid cells by visual inspection.

Supplemental References

Barry, C., Bush, D., O'Keefe, J., and Burgess, N. (2012). Models of grid cells and theta oscillations. Nature *488,* 103.

von Heimendahl, M., Rao, R.P., and Brecht, M. (2012). Weak and nondiscriminative responses to conspecifics in the rat hippocampus. J. Neurosci. *6*, 2129-41.

Houweling, A.R., Doron, G., Voigt, B.C., Herfst, L.J., and Brecht, M. (2010). Nanostimulation: manipulation of single neuron activity by juxtacellular current injection. J. Neurophysiol. *103,* 1696-704.

Lee, A.K., Manns, I.D., Sakmann, B., and Brecht, M. (2006). Whole-cell recordings in freely moving rats. Neuron *51,* 399-407.

Pinault, D. (1996). A novel single-cell staining procedure performed in vivo under electrophysiological control: morpho-functional features of juxtacellularly labeled thalamic cells and other central neurons with biocytin or Neurobiotin. J. Neurosci. Methods *65,* 113-136.

Quilichini, P., Sirota, A., and Buzsáki, G. (2010). Intrinsic circuit organization and theta-gamma oscillation dynamics in the entorhinal cortex of the rat. J. Neurosci. *18,* 11128-42.

5. Functional Architecture of the Rat Parasubiculum

This manuscript was published as:
(*)Tang, Q., (*)Burgalossi, A., **(*)Ebbesen, C.L.,** (*)Sanguinetti-Scheck, J.I., Schmidt, H., Tukker, J.J., Naumann, R., Ray, S., Preston-Ferrer, P., Schmitz, D., Brecht, M. (2016) Functional Architecture of the Rat Parasubiculum. **Journal of Neuroscience** 36(7):2289-2301.

The Journal of Neuroscience, February 17, 2016 • 36(7):2289–2301 • 2289

Systems/Circuits

Functional Architecture of the Rat Parasubiculum

Qiusong Tang,[1]* Andrea Burgalossi,[2]* Christian Laut Ebbesen,[1,3]* Juan Ignacio Sanguinetti-Scheck,[1]* Helene Schmidt,[1] John J. Tukker,[1,4] Robert Naumann,[1] Saikat Ray,[1] Patricia Preston-Ferrer,[2] Dietmar Schmitz,[4] and Michael Brecht[1]

[1]Bernstein Center for Computational Neuroscience, Humboldt Universität zu Berlin, 10115 Berlin, Germany, [2]Werner Reichardt Centre for Integrative Neuroscience, 72076 Tübingen, Germany, [3]Berlin School of Mind and Brain, Humboldt University of Berlin, 10115 Berlin, Germany, and [4]Charité Universitätsmedizin Berlin, 10117 Berlin, Germany

The parasubiculum is a major input structure of layer 2 of medial entorhinal cortex, where most grid cells are found. Here we investigated parasubicular circuits of the rat by anatomical analysis combined with juxtacellular recording/labeling and tetrode recordings during spatial exploration. In tangential sections, the parasubiculum appears as a linear structure flanking the medial entorhinal cortex mediodorsally. With a length of ~5.2 mm and a width of only ~0.3 mm (approximately one dendritic tree diameter), the parasubiculum is both one of the longest and narrowest cortical structures. Parasubicular neurons span the height of cortical layers 2 and 3, and we observed no obvious association of deep layers to this structure. The "superficial parasubiculum" (layers 2 and 1) divides into ~15 patches, whereas deeper parasubicular sections (layer 3) form a continuous band of neurons. Anterograde tracing experiments show that parasubicular neurons extend long "circumcurrent" axons establishing a "global" internal connectivity. The parasubiculum is a prime target of GABAergic and cholinergic medial septal inputs. Other input structures include the subiculum, presubiculum, and anterior thalamus. Functional analysis of identified and unidentified parasubicular neurons shows strong theta rhythmicity of spiking, a large fraction of head-direction selectivity (50%, 34 of 68), and spatial responses (grid, border and irregular spatial cells, 57%, 39 of 68). Parasubicular output preferentially targets patches of calbindin-positive pyramidal neurons in layer 2 of medial entorhinal cortex, which might be relevant for grid cell function. These findings suggest the parasubiculum might shape entorhinal theta rhythmicity and the (dorsoventral) integration of information across grid scales.

Key words: anatomy; border cell; head-direction cell; medial entorhinal cortex; parasubiculum; spatial navigation

Significance Statement

Grid cells in medial entorhinal cortex (MEC) are crucial components of an internal navigation system of the mammalian brain. The parasubiculum is a major input structure of layer 2 of MEC, where most grid cells are found. Here we provide a functional and anatomical characterization of the parasubiculum and show that parasubicular neurons display unique features (i.e., strong theta rhythmicity of firing, prominent head-direction selectivity, and output selectively targeted to layer 2 pyramidal cell patches of MEC). These features could contribute to shaping the temporal and spatial code of downstream grid cells in entorhinal cortex.

Introduction

The analysis of spatial discharge patterns in hippocampal and parahippocampal brain regions is a remarkable success story (Moser et al., 2008; Moser and Moser, 2013; Burgess, 2014). Extracellular recordings revealed an astonishing degree of complexity, abstractness, but also identified clear behavioral correlates of discharge patterns, such as place, head-direction, border, and grid cells. Along with the exploration of discharge properties, anatomists delineated in great detail the basic circuitry of the

Received Oct. 13, 2015; revised Jan. 11, 2016; accepted Jan. 13, 2016.

Author contributions: Q.T., A.B., C.L.E., J.I.S.-S., and M.B. designed research; Q.T., A.B., C.L.E., J.I.S.-S., H.S., J.J.T., R.N., S.R., P.P.-F., D.S., and M.B. performed research; Q.T., A.B., C.L.E., J.I.S.-S., H.S., J.J.T., R.N., S.R., P.P.-F., D.S., and M.B. analyzed data; Q.T., A.B., C.L.E., J.I.S.-S., H.S., J.J.T., R.N., S.R., P.P.-F., D.S., and M.B. wrote the paper.

This work was supported by Humboldt-Universität zu Berlin, BCCN Berlin (German Federal Ministry of Education and Research BMBF, Förderkennzeichen 01GQ1001A), NeuroCure, Neuro-Behavior ERC Grant, Deutsche Forschungsgemeinschaft Gottfried Wilhelm Leibniz Prize, and the Werner Reichardt Centre for Integrative Neuroscience at the Eberhard Karls University of Tübingen. The Centre for Integrative Neuroscience is an Excellence Cluster funded by the Deutsche Forschungsgemeinschaft within the framework of the Excellence Initiative (EXC 307). We thank Moritz von Heimendahl for programming; Falko Fuhrmann and Stefan Remy for generous donations of PV-Cre mice and help with the AAV injections; Susanne Schoch (University of Bonn) for providing the virus; and Andreea Neukirchner, Juliane Steger, Alexandra Eritja, Susanne Rieckmann, and Undine Schneeweiß for outstanding technical assistance.

The authors declare no competing financial interests.

*Q.T., A.B., C.L.E., and J.I.S.-S. contributed equally to this work.

Correspondence should be addressed to either of the following: Dr. Andrea Burgalossi, Werner Reichardt Centre for Integrative Neuroscience, Otfried-Müller-Str. 25, 72076 Tübingen, Germany, E-mail: andrea.burgalossi@cin.uni-tuebingen.de; or Dr. Michael Brecht, Bernstein Center for Computational Neuroscience, Humboldt Universität zu Berlin, Philippstr. 13, Haus 6, 10115 Berlin, Germany, E-mail: michael.brecht@bccn-berlin.de.

R. Naumann's current address: Max-Planck-Institute for Brain Research, Max-von-Laue-Str. 4, 60438 Frankfurt am Main, Germany.

DOI:10.1523/JNEUROSCI.3749-15.2016

 0270-6474/16/362289-13$15.00/0

hippocampal formation (Amaral and Witter, 1989; van Strien et al., 2009).

The detailed data available about certain parts of the hippocampal formation, such as dorsal CA1 in the rodent, should not blind us for gaps in our knowledge about less "classic" hippocampal processing nodes. The parasubiculum is one such structure that lies beyond the classic trisynaptic hippocampal loop (Andersen et al., 1971) and has been investigated relatively little. This parahippocampal region provides massive input to layer 2 of medial entorhinal cortex (van Groen and Wyss, 1990; Caballero-Bleda and Witter, 1993, 1994) and shows prominent expression of markers for cholinergic activity (Slomianka and Geneser, 1991). Early physiological analysis described a small fraction of place-responsive cells in the parasubiculum (Taube, 1995), and subsequent extracellular recordings have also identified head-direction, border, and grid responses among parasubicular neurons (Cacucci et al., 2004; Boccara et al., 2010).

From both a physiological and an anatomical perspective, the parasubiculum is somewhat difficult to study. First, the small size of the parasubiculum complicates recordings and tracer injections. Second, the parasubicular position (on the caudal edge of the parahippocampal lobe wrapping around entorhinal cortex, which goes along with a strong bending of the cortical sheet) greatly complicates the delineation of the parasubiculum. Here we aimed for a comprehensive description of parasubicular circuits by a combined anatomical and functional approach (Burgalossi et al., 2011; Tang et al., 2014a). Specifically, we were interested in how parasubicular circuits relate to pyramidal and stellate neuron microcircuits in layer 2 of medial entorhinal cortex (MEC) (Ray et al., 2014; Tang et al., 2014b).

In our current analysis, we investigate four issues: First, we delineate the location, shape, laminar organization, and internal structure of parasubiculum. Second, we investigate the sources of parasubicular inputs, as well as the targets of parasubicular outputs. Third, we assess spatial discharge patterns of parasubicular neurons by juxtacellular recording/labeling and tetrode recordings in freely moving rats. Fourth, we assess the temporal discharge patterns of identified and unidentified parasubicular neurons, and how this might relate to anatomical connectivity.

Materials and Methods

All experimental procedures were performed according to the German guidelines on animal welfare under the supervision of local ethics committees.

Brain tissue preparation. For anatomy experiments, male and female Wistar rats (150–400 g) were anesthetized by isoflurane and then killed by an intraperitoneal injection of 20% urethane or sodium pentobarbital. They were then perfused transcardially with 0.9% PBS solution, followed by 4% PFA in 0.1 M phosphate buffer (PB). After perfusion, brains were removed from the skull and postfixed in PFA overnight. They were then transferred into a 10% sucrose solution in PB and left overnight, and subsequently immersed in 30% sucrose solution for at least 24 h for cryoprotection. The brains were embedded in Jung Tissue Freezing Medium and subsequently mounted on the freezing microtome to obtain 20- to 60-μm-thick sagittal sections or tangential sections (parallel to the pial surface of the MEC). Tangential sections were obtained by removing the cerebellum, visually identifying the pial surface of the MEC (Ray et al., 2014; their Fig. 1*A*), and making a cut 3 mm anterior and parallel to the pial surface of the medial entorhinal cortex. The tissue was then frozen and positioned with the pial side to the block face of the microtome.

Tissue from PV-Cre mice, expressing Cre recombinase under the parvalbumin (PV) promoter (B6;129P2-Pvalbtm1(cre)Arbr/J mice, stock #008069, The Jackson Laboratory), was prepared using similar methods, except that the sections were cut on a standard microtome (nominal thickness 100 μm, horizontal) right after overnight fixation in PFA.

Histochemistry and immunohistochemistry. Acetylcholinesterase activity was visualized according to previously published procedures (Ray et al., 2014). After washing brain sections in a solution containing 1 ml of 0.1 M citrate buffer, pH 6.2, and 9 ml 0.9% NaCl saline solution (CS), sections were incubated with CS containing 3 mM $CuSO_4$, 0.5 mM $K_3Fe(CN)_6$, and 1.8 mM acetylthiocholine iodide for 30 min. After rinsing in PB, reaction products were visualized by incubating the sections in PB containing 0.05% 3,3′- DAB and 0.03% nickel ammonium sulfate. Immunohistochemical stainings were performed according to standard procedures. Briefly, brain sections were preincubated in a blocking solution containing 0.1 M PBS, 2% BSA, and 0.5% Triton X-100 (PBS-X) for an hour at room temperature. Following this, primary antibodies were diluted in a solution containing PBS-X and 1% BSA. We used primary antibodies against the calcium binding protein Calbindin (1:5000), the DNA binding neuron-specific protein NeuN (1:1000), and, for the mice, against GFP. Incubations with primary antibodies were allowed to proceed for at least 24 h under mild shaking at 4°C in free-floating sections. Incubations with primary antibodies were followed by detection with secondary antibodies coupled to different fluorophores (Alexa-488 and Alexa-546). Secondary antibodies were diluted (1:500) in PBS-X, and the reaction was allowed to proceed for 2 h in the dark at room temperature. For multiple antibody labeling, antibodies raised in different host species were used. After the staining procedure, sections were mounted on gelatin-coated glass slides with Mowiol or Vectashield mounting medium. In a subset of experiments, primary antibodies were visualized by DAB staining. For this purpose, endogenous peroxidases were first blocked by incubating brain tissue sections in methanol containing 0.3% hydrogen peroxide in the dark at room temperature for 30 min. The subsequent immunohistochemical procedures were performed as described above, with the exception that detection of primary antibodies was performed by biotinylated secondary antibodies and the ABC detection kit. Immunoreactivity was visualized using DAB staining.

The relative density of putative parvalbuminergic fibers in PV-Cre mice in hippocampus CA1–3, presubiculum, parasubiculum, and medial entorhinal cortex was estimated by manually outlining these four areas (Paxinos and Franklin, 2012) in epifluorescence images (2.5×) from horizontal sections (estimated depth 3 mm relative to bregma) and then measuring mean fluorescence signals in each area with the ImageJ software. For comparison between brains, these values were then normalized to the mean hippocampal value in each brain ($n = 3$).

Anterograde and retrograde neuronal labeling. Anterograde or retrograde tracer solutions containing biotinylated dextrane amine (BDA) (10% w/v; 3000 or 10,000 molecular weight) were injected in juvenile rats (~150 g) under ketamine/xylazine anesthesia. Briefly, a small craniotomy was opened above the parasubiculum/medial entorhinal cortex. Before injection, the parasubiculum was localized by electrophysiological recordings, based on cortical depth, characteristic signatures of the local field potential theta oscillations, and neuronal spiking activity. Glass electrodes with a tip diameter of 10–20 μm, filled with BDA solution, were then lowered into the target region. Tracers were either pressure-injected (10 injections using positive pressure of 20 psi, 10–15 s injection duration) or iontophoretically injected (7 s on/off current pulses of 1–5 mA for 15 min). After the injections, the pipettes were left in place for several minutes and slowly retracted. The craniotomies were closed by application of silicone and dental cement. The animals survived for 3–7 d before being transcardially perfused.

Viral injections and quantification of anterorgradely traced axons. PV-Cre mice, expressing Cre recombinase under the PV promoter (B6;129P2-Pvalbtm1(cre)Arbr/J mice, stock #008069, The Jackson Laboratory) were injected with AAV-Ef1a-dbf-hChR2(H134R)-EYFP-WPRE (serotype 1/2) ~6 weeks before perfusion. The medial septum was targeted under stereotaxic guidance: starting from the pial surface at 1 mm anterior, 0.7 mm right lateral to bregma, a 34-gauge NanoFil needle (WPI) was advanced at an angle of 10° in the coronal plane for 4200 and 4600 μm, where we injected 1 μl each (100 nl/s), waiting 5 min after each injection before moving the needle. The AAV virus was generously provided to us by Susanne Schoch (University of Bonn).

Fluorescence signals were normalized to dentate gyrus intensity levels and quantified. Briefly, regions of interests from horizontal sections (at a depth of ~3.5 mm ventral to bregma) (Paxinos and Franklin, 2012) were manually outlined and the mean fluorescence intensity for each area quantified using the ImageJ software ($n = 3$ mice).

Juxtacellular recordings. Juxtacellular recordings and tetrode recordings in freely moving animals were obtained in male Wistar and Long–Evans rats (150–250 g). Experimental procedures were performed as recently described (Tang et al., 2014a, b, 2015). Briefly, rats were maintained in a 12 h light/dark phase and were recorded in the dark phase. Glass pipettes with resistance 4–6 MΩ were filled with extracellular Ringer's solution containing (in mM) the following: 135 NaCl, 5.4 KCl, 5 HEPES, 1.8 $CaCl_2$, and 1 $MgCl_2$, pH 7.2, and Neurobiotin (1%–2%). Animal implantations were performed as previously described (Tang et al., 2014a). To target the parasubiculum, a plastic ring was placed 0.2–0.5 mm anterior to the transverse sinus and 4.0–4.5 mm lateral to the midline. After implantation, rats were allowed to recover from the surgery and were habituated to head fixation for 3–5 d. Rats were trained in the experimental arena (70 × 70 cm or 1 × 1 m square black box, with a white cue card on the wall) for 3–7 d. Juxtacellular recordings and labeling were essentially performed as previously described (Tang et al., 2014a; Pinault, 1996). Unidentified recordings in parasubiculum were either lost before the labeling could be attempted, or the recorded neurons could not be unequivocally identified; but either pipette tracks or dendritic processes were found in the parasubiculum. After the experiment, the animals were killed with an overdose of ketamine, urethane, or sodium pentobarbital, and perfused transcardially with 0.1 M PB followed by 4% PFA solution, shortly after the labeling protocol. The juxtacellular signals were amplified by the ELC-03XS amplifier (NPI Electronics) and sampled at 20 kHz by a data-acquisition interface under the control of PatchMaster 2.20 software (HEKA). The animal's location and head-direction were automatically tracked at 25 Hz by the Neuralynx video-tracking system and two head-mounted LEDs. MEC data for comparison have been published previously (Ray et al., 2014; Tang et al., 2014b, 2015). One head-direction cell recorded and identified in the parasubiculum has been shown in a previous paper (Tang et al., 2014a).

Tetrode recordings. Tetrode recordings from parasubiculum were essentially performed as recently described (Tang et al., 2014b, 2015). Tetrodes were turned from 12.5-μm-diameter nichrome wire (California Fine Wire) and gold plated to ~250 kΩ impedance. Spiking activity and local field potential were recorded at 32 kHz (Neuralynx; Digital Lynx). The local field potential was recorded from the same tetrode as single units and referenced to a superficial silent neocortical tetrode or to the rat ground. All recordings were performed following behavioral training, as specified above for juxtacellular procedures. The animal's location and head-direction were automatically tracked at 25 Hz by video tracking and head-mounted LEDs, as described above. After recordings, tetrodes were retracted from the parahippocampal areas, and multiple lesions were performed at distinct sites along the individual tetrode tracks, thereby allowing unequivocal assignment of the different tetrode tracks. Following perfusion, brains were sectioned tangentially and recording sites assigned by histology. Spikes were preclustered using KlustaKwik (K.D. Harris, Rutgers University) and manually using MClust (A.D. Redish, University of Minnesota). Cluster quality was assessed by spike shape, ISI-histogram, L-ratio, and isolation distance.

Neurobiotin labeling and calbindin immunohistochemistry. For histological analysis of juxtacellularly labeled neurons, Neurobiotin was visualized with streptavidin conjugated to Alexa-546 (1:1000). Subsequently, immunohistochemistry for Calbindin was performed, as previously described (Ray et al., 2014), and visualized with AlexaFluor-488. After fluorescence images were acquired, the Neurobiotin staining was converted into a dark DAB reaction product. Neuronal morphologies were reconstructed by computer-assisted manual reconstructions (Neurolucida).

Analysis of theta rhythmicity. Theta rhythmicity of spiking discharge was determined from the Fast Fourier Transform-based power spectrum of the spike-train autocorrelation functions of the neurons, binned at 10 ms. To measure modulation strength in the theta band (4–12 Hz), a theta power was computed, defined as the average power within 1 Hz of the maximum of the autocorrelation function in the theta rhythm (4–12 Hz). This is referred to here as theta rhythmicity. Only neurons with mean firing rate >0.5 Hz were included in the theta analysis. Statistical significance between groups was assessed by two-tailed Mann–Whitney nonparametric test with 95th confidence intervals.

Analysis of theta locking. For all neurons, we calculated the locking to theta phase based on spiking discharge in relation to theta rhythm in the local field potential. The local field potential was zero phase bandpass filtered (4–12 Hz), and a Hilbert transform was used to determine the instantaneous phase of the theta wave. In line with previous studies (Mizuseki et al., 2009), the theta phase locking strength, S, and the preferred phase angle, φ, were defined as the modulus and argument of the Rayleigh average vector of the theta phase for all spikes. The theta phase locking strength value can vary between 0 (uniform distribution of spikes over the theta cycle) and 1 (all spikes have the same theta phase). Only spikes during running (speed cutoff = 1 cm/s for juxtacellular signals, 5 cm/s for tetrode recordings) were included in the analysis. Only neurons with mean firing rate ≥0.5 Hz were included in the analysis. For comparison to MEC L2 data, both the analysis procedures and the juxtacellular dataset correspond to our recent publications (Ray et al., 2014; Tang et al., 2014b, 2015).

Analysis of spatial modulation. The position of the rat was defined as the midpoint between two head-mounted LEDs. A running speed threshold (see above) was applied for isolating periods of rest from active movement. Color-coded firing maps were plotted. For these, space was discretized into pixels of 2.5 cm × 2.5 cm, for which the occupancy z of a given pixel x was calculated as follows:

$$z(x) = \sum_t w(|x - x_t|)\Delta t$$

where x_t is the position of the rat at time t, Δt the interframe interval, and w a Gaussian smoothing kernel with $\sigma = 5$ cm.

Then, the firing rate r was calculated as follows:

$$r(x) = \frac{\sum_i w(|x - x_i|)}{z}$$

where x_i is the position of the rat when spike i was fired. The firing rate of pixels, whose occupancy z was <20 ms, was considered unreliable and not shown.

To determine the spatial periodicity of juxtacellularly recorded neurons, we determined spatial autocorrelations. The spatial autocorrelogram was based on Pearson's product moment correlation coefficient as follows:

$$r(\tau_x, \tau_y) = \frac{n\sum f(x, y) f(x - \tau_x, y - \tau_y) - \sum f(x, y)\sum f(x - \tau_x, y - \tau_y)}{\sqrt{n\sum f(x, y)^2 - \left(\sum f(x, y)\right)^2} \times \sqrt{n\sum f(x - \tau_x, y - \tau_y)^2 - \left(\sum f(x - \tau_x, y - \tau_y)\right)^2}}$$

where $r(\tau_x, \tau_y)$ the autocorrelation between pixels or bins with spatial offset τ_x and τ_y. f is the image without smoothing or the firing rate map after smoothing, n is the number of overlapping pixels or bins. Autocorrelations were not estimated for lags of τ_x and τ_y, where $n < 20$. For spatial and head-directional analysis, both a spatial (>50% spatial coverage) and a firing rate inclusion criterion (>0.5 Hz) were applied. Spatial coverage was defined as the fraction of visited pixels (bins) in the arena to the total pixels.

Analysis of spatial information. For all neurons, we calculated the spatial information rate, I, from the spike train and rat trajectory as follows:

$$I = \frac{1}{T}\int r(x)\log_2\frac{r(x)}{\bar{r}}\, o(x)dx$$

where $r(x)$ and $o(x)$ are the firing rate and occupancy as a function of a given pixel x in the rate map. $\bar{r}$ is the overall mean firing rate of the cell, and T is the total duration of a recording session (Skaggs et al., 1993). A cell was determined to have a significant amount of spatial information if the observed spatial information rate exceeded the 95th percentile of a distribution of values of I obtained by circular shuffling. Shuffling was performed by a circular time-shift of the recorded spike train relative to the rat trajectory by a random time $t' \in [0, T]$ for 1000 permutations (von Heimendahl et al., 2012; Bjerknes et al., 2014).

Analysis of border cells. To determine the modulation of a cell firing along a border, we determined border scores (Solstad et al., 2008). Border fields were identified from a collection of neighboring pixels having a firing rate >0.3 times the maximum firing rate and covering an area of at least 100 cm (Sargolini et al., 2006). The coverage (Cm) along a wall was defined as the maximum length of a putative border field parallel to a boundary, divided by the length of the boundary. The mean firing distance (Dm) of a field was defined as the sum of the square of its distance from the boundary, weighted by the firing rate (Solstad et al., 2008). The distance from a boundary was defined as the exponential of the square of the distance in pixels from the closest boundary, normalized by half the length of the boundary. Border scores were defined as the maximum difference between Cm and Dm, divided by their sum, and ranged from −1 to 1.

Analysis of grid cells. Grid scores were calculated, as previously described (Barry et al., 2012), by taking a circular sample of the autocorrelogram, centered on, but excluding the central peak. The Pearson correlation of this circle with its rotation for 60 degrees and 120 degrees was obtained (on peak rotations) and also for rotations of 30, 90, and 150 degrees (off peak rotations). Gridness was defined as the minimum difference between the on-peak rotations and off-peak rotations. To determine the grid scores, gridness was evaluated for multiple circular samples surrounding the center of the autocorrelogram with circle radii increasing in unitary steps from a minimum of 10 pixels more than the width of the radius of the central peak to the shortest edge of the autocorrelogram. The radius of the central peak was defined as the distance from the central peak to its nearest local minima in the spatial autocorrelogram. The radius of the inner circle was increased in unitary steps from the radius of the central peak to 10 pixels less than the optimal outer radius. The grid score was defined as the best score from these successive samples. Grid scores reflect both the hexagonality in a spatial field and also the regularity of the hexagon. To disentangle the effect of regularity from this index and consider only hexagonality, we transformed the elliptically distorted hexagon into a regular hexagon and computed the grid scores (Barry et al., 2012). A linear affine transformation was applied to the elliptically distorted hexagon, to stretch it along its minor axis, until it lay on a circle, with the diameter equal to the major axis of the elliptical hexagon. The grid scores were computed on this transformed regular hexagon (Barry et al., 2012).

Analysis of head-directionality. Head-direction tuning was measured as the eccentricity of the circular distribution of firing rates. For this, firing rate was binned as a function of head-direction ($n = 36$ bins). A cell was said to have a significant head-direction tuning if the length of the average vector exceeded the 95th percentile of a distribution of average vector lengths calculated from shuffled data and had a Rayleigh vector length >0.3. Data were shuffled by applying a random circular time-shift to the recorded spike train for 1000 permutations.

Classification of cells into functional categories. Cells were classified as head-direction cells, grid cells, conjunctive cells, border cells, spatially irregular cells, and nonspatially modulated cells, based on their grid score, border score, spatial information, and significance of head-directionality according to the following criteria: head-direction cells, Rayleigh vector length >0.3, and significant head-direction tuning (Boccara et al., 2010); grid cells, grid score >0.3, and significant spatial information; border cells, border score >0.5, and significant spatial information (Solstad et al., 2008), or those who passed border test (Lever et al., 2009); spatially irregular cells, significant spatial information (Bjerknes et al., 2014), while not passing grid score or border score criteria; and nonspatially modulated cell, no significant spatial information.

Results

Geometry of the parasubiculum

In our initial analysis, we sought to determine the general organization of the parasubiculum. Tangential sections (parallel to the pial surface of the MEC; see Materials and Methods) of the cortical sheet stained for acetylcholine esterase activity (Fig. 1*A*, left) or calbindin immunoreactivity (Fig. 1*A*, right) provide a particularly clear overview of the spatial extent of the parasubiculum. Consistent with findings from previous studies (Geneser, 1986; Slomianka and Geneser, 1991), we find that the parasubiculum shows prominent acetylcholine esterase activity (Fig. 1*A*, left). The parasubiculum can also be identified by an absence of calbindin immunoreactivity (Fig. 1*A*, left) (Fujise et al., 1995; Boccara et al., 2010). Further subdivisions of the parasubiculum have been suggested (Blackstad, 1956). Our data refer to the calbindin free area surrounding the MEC outlined in Figure 1*A*, left and highlighted in light blue in Figure 1*B* [possibly related to "parasubiculum b" in the terminology of Blackstad (1956)]. Laterally contiguous to the parasubiculum one observes a thin strip of cortex containing numerous calbindin-positive neurons (Fig. 1*A*, right, *B*, red "calbindin stripe").

As shown in Figure 1*A*, *B* and quantified in Figure 1*C*, the parasubiculum forms a fairly narrow (310 ± 83 μm width, $N = 10$), but very elongated (5.190 ± 0.485 mm length, $N = 10$) continuous curved stripe, which flanks the medial entorhinal cortex from its medial to dorsolateral side. The lateral part of the parasubiculum, dorsal to the medial entorhinal cortex, is narrower than the medial part. This may explain why this part of the parasubiculum has not been classified as such in most previous studies (Boccara et al., 2010; Ding, 2013). Other histological markers, such as cytochrome-oxidase activity, or soma morphologies, as visualized from Nissl stains (Burgalossi et al., 2011), also delineated the parasubiculum in the same way as shown in Figure 1 (data not shown). Similarly, parasagittal sectioning angles delineate the same outlines of the parasubiculum. We conclude that the parasubiculum has a linear structure with a narrow width.

We also investigated the laminar structure of the parasubiculum. Consistent with our previous conclusions (Burgalossi et al., 2011), we did not find direct evidence for a clear association of deep layers with the parasubiculum. For example, following tracer injections in the superficial parasubicular layers, we did not observe back-labeled neurons in the adjacent deep layers, even when we observed back-labeled neurons as distant as the subiculum (data not shown). Hence, we speculate that deep layers close to the parasubiculum might not be part of this structure but could rather be associated with the neighboring medial entorhinal cortex or the presubiculum (Mulders et al., 1997).

Internal structure of the parasubiculum

Consistent with our previous observations (Burgalossi et al., 2011), we found the superficial parts of the parasubiculum (corresponding to layers 1 and 2) can be divided into ~15 large patches with a diameter ~500 μm each. These patches can be revealed in superficial tangential sections (Fig. 1*D*, left) by PV immunoreactivity and by cell density visualized by NeuN immunoreactivity (Fig. 1*D*, right). However, the deeper parts of the parasubiculum (corresponding to layer 3) were not obviously divided into patches (Fig. 1*D*).

Injections of the anterograde tracer BDA (3000 molecular weight) showed that parasubicular neurons extend long axons throughout the full length of the parasubiculum (Fig. 1*E*), consistent with previous evidence from single-cell microcircuits (Burgalossi et al., 2011). In the latter work, these axons were

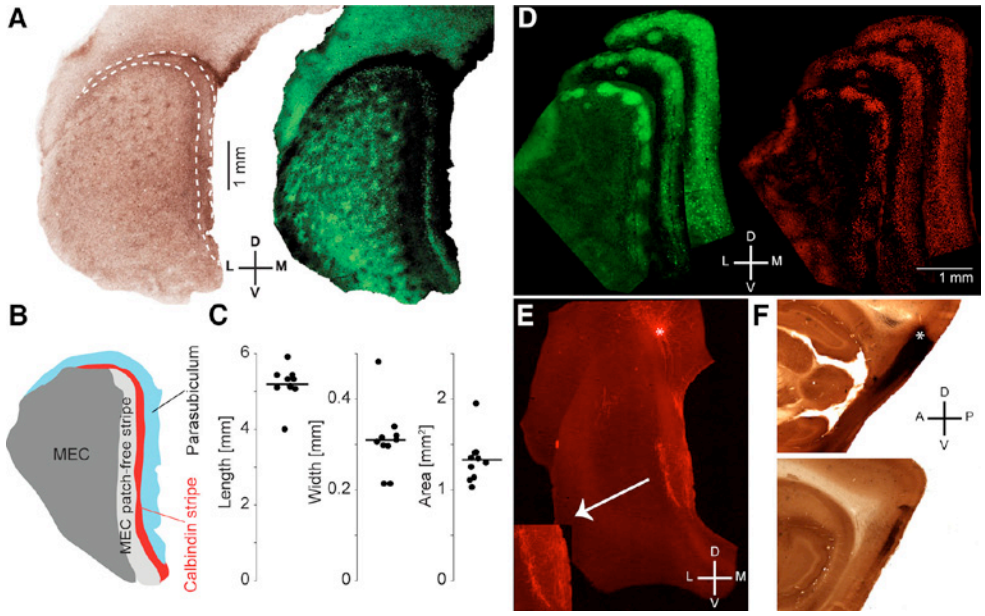

Figure 1. Shape and internal structure of the parasubiculum. ***A***, Left, Tangential section stained for acetylcholinesterase activity (dark precipitate). The shape of the parasubiculum is outlined (white dashed line) coinciding with high acetylcholinesterase activity. Right, Tangential section (same section as in ***A***, left) processed for calbindin immunoreactivity (green); the shape of the parasubiculum is negatively outlined by an absence of calbindin immunoreactivity. ***B***, Schematic of the parasubiculum (light blue) and adjacent MEC subdivisions. ***C***, Quantification of parasubiculum size in 10 hemispheres: length, width, and area. ***D***, Tangential sections stained for PV immunoreactivity (green, left) and NeuN immunoreactivity (red, right). The parasubiculum stands out by its intense staining. Three sections are shown: left, most superficial (closest to the pia); middle and right, progressively deeper. Note how the patchy structure of the superficial parasubiculum is replaced by a continuous cell band in deeper sections. ***E***, Tangential sections of the parasubiculum showing the injection site of BDA tracer (red fluorescence) and anterogradely traced circumcurrent axons (according to the terminology of Burgalossi et al., 2011), extending throughout the parasubiculum (see also magnified inset, left). *Injection site. ***F***, Parasagittal sections of the parasubiculum (top) and parasubiculum and MEC (bottom) after the injection of larger amounts of BDA (tracer, dark color). The tracer completely fills the parasubiculum and stains layer 2 of the MEC. *Injection site. ***A***, ***B***, Modified from Ray et al. (2014). D, Dorsal; L, lateral; M, medial; V, ventral; A, anterior; P, posterior.

termed "circumcurrent," as they appeared to interconnect parasubicular patches. As a consequence of this internal connectivity, a single tracer injection could label the full extent of the parasubiculum (Fig. 1*F*). This is a remarkable feature of the parasubiculum not seen in the medial entorhinal cortex. Thus, analysis of the internal structure of parasubiculum indicates both modularity and global connectivity.

Inputs to the parasubiculum

Of particular interest for hippocampal function are the inputs from the medial septum, which are of critical importance to grid cell activity (Brandon et al., 2011; Koenig et al., 2011). We first sought to determine the patterns of GABAergic inputs from the medial septum, which are thought to play a critical role in theta-rhythm generation (Mitchell et al., 1982; Buzsáki, 2002; Hangya et al., 2009; Brandon et al., 2011; Koenig et al., 2011). To this end, we performed viral injections in the medial septum in PV-Cre mice (see Materials and Methods) and expressed GFP selectively in GABAergic septal neurons (Fig. 2*A*,*B*). As shown in Figure 2*A*, the parasubiculum is an area within the hippocampal formation, which receives a comparatively dense innervation from GABAergic medial septal neurons (as quantified by normalized fluorescence levels, mean values [$n = 3$], parasubiculum $= 1.5 \pm 0.23$, MEC $= 1.0 \pm 0.05$, CA1–3 $= 1.2 \pm 0.06$, PreS $= 1.0 \pm 0.04$; Fig. 2*C*). As we already noted earlier, there is also a prominent expression of cholinergic activity markers (Figs. 1*A*, 2*D*) in line with *in vitro* work showing robust response of parasubicular neurons to muscarinic activation (Glasgow and Chapman, 2013). Together, these data point toward a strong medial septal drive to parasubicular neurons, likely contributing to strong theta rhythmicity in the parasubiculum (Burgalossi et al., 2011; see below).

By retrograde-tracer injections, we also identified parasubiculum-projecting neurons in the anterior thalamus, subiculum, and presubiculum. The findings are consistent with the earlier conclusions of previous authors (Köhler, 1985; van Groen and Wyss, 1992; Honda and Ishizuka, 2004) and are therefore not shown.

Outputs from the parasubiculum

Previous work showed that the parasubicular axons innervate layer 2 of the medial entorhinal cortex (van Groen and Wyss, 1990; Caballero-Bleda and Witter, 1993, 1994; but see Canto et al., 2012). Recent work showed that principal neurons in layer 2 of medial entorhinal cortex segregate into stellate and pyramidal cell subnetworks, which can be differentiated by the calbindin immunoreactivity of the pyramidal neurons (Varga et al., 2010). Layer 2 pyramidal neurons are arranged in a hexagonal grid, show strong theta-rhythmic discharges (Ray et al., 2014), and might preferentially contribute to the grid cell population (Tang et al., 2014b; but see Sun et al., 2015). To determine whether parasubicular inputs target a specific subpopulation of neurons in layer 2 of medial entorhinal cortex, we performed fine-scale injections of anterograde tracers in the dorsal parasubiculum, combined with visualization of calbindin patterns (Fig. 3). As shown in Figure 3, tangential sections through layer 2 with calbindin immunostaining revealed a regular organization of patches of pyramidal neurons (Ray et al., 2014). Surprisingly,

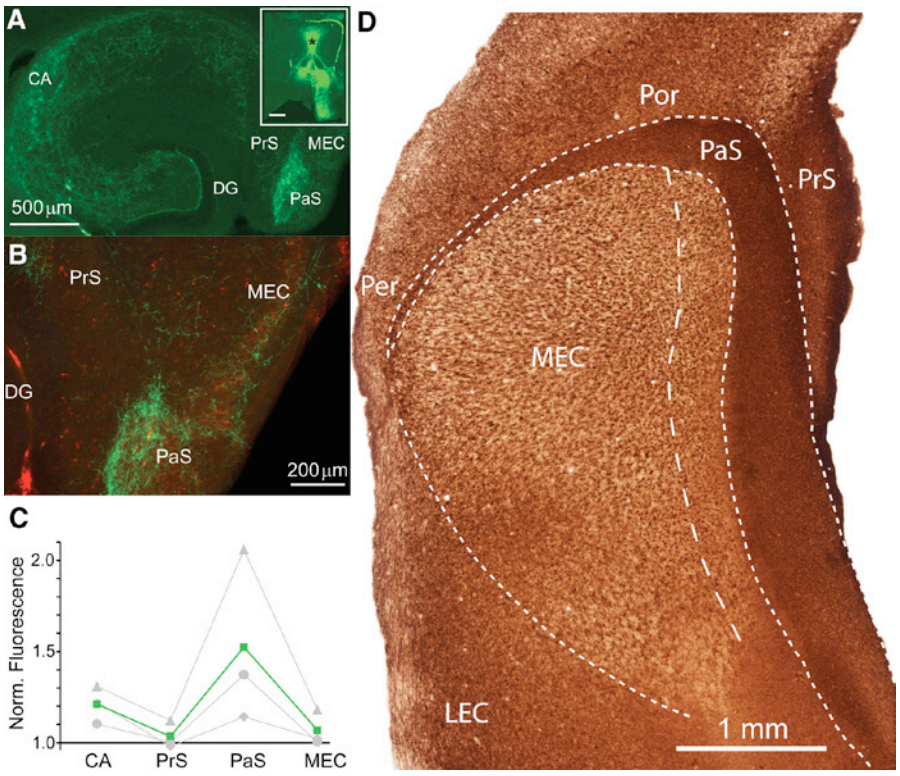

Figure 2. Parasubiculum receives GABAergic and cholinergic inputs. ***A***, Horizontal sections showing that the parasubiculum contains the densest projection in the hippocampal formation of GFP-positive, putative parvalbuminergic fibers deriving from injection of AAV into the medial septum (inset, asterisk) of mice expressing Cre recombinase under the PV promoter. This dense projection pattern was seen in 3 of 3 injected mice. In this brain, olfactory and accessory olfactory areas were also labeled unilaterally. ***B***, PV immunostaining (red) marks the extent of the parasubiculum (as shown in Fig. 1*D*, left). Note the higher density of GABAergic medial septal fibers (green) within the parasubiculum. ***C***, Normalized fluorescence intensity levels relative to dentate gyrus ($n = 3$ mice, different gray symbols represent the different mice). Green squares represent mean normalized fluorescence. ***D***, Tangential section showing high levels of acetylcholinesterase in the parasubiculum. PrS, Presubiculum; DG, dentate gyrus; LEC, lateral entorhinal cortex; PaS, parasubiculum; Por, postrhinal cortex; Per, perirhinal cortex; CA, cornus ammonis.

these patches were selectively innervated by parasubicular afferents (Fig. 3*A*,*B*), which targeted the center of patches (Fig. 3*C*). This indicates that parasubicular axons may preferentially target layer 2 pyramidal neurons of medial entorhinal cortex, which may in turn contribute to the strong theta rhythmicity in these neurons (Ray et al., 2014).

Identification of functional cell types in the parasubiculum

Compared with its major target structure (the entorhinal cortex), limited information is currently available about the spatial discharge properties in the parasubiculum (Taube, 1995; Cacucci et al., 2004; Boccara et al., 2010). To address this issue, we juxtacellularly recorded and labeled neurons ($n = 16$) in the parasubiculum of freely moving rats trained to explore 2D environments (Tang et al., 2014a) A representative recording from an identified parasubicular neuron is shown in Figure 4*A*. This neuron had divergent sideward-directed dendrites (seen from the top), was situated in the dorsal part of the parasubiculum (Fig. 4*A*, right), and discharged in spike bursts strongly entrained by the theta rhythm (Fig. 4*B*). Theta rhythmicity of spiking was revealed by the spiking autocorrelogram (Fig. 4*C*, left), and the spikes were also strongly locked to local theta oscillations (Fig. 4*C*, right). The neuron discharged along the border of the enclosure (Fig. 4*D*, left), a defining feature of border activity (Solstad et al., 2008), and showed head-direction selectivity (Fig. 4*D*, right).

In line with previous observations in linear mazes (Burgalossi et al., 2011), many juxtacellularly recorded neurons showed head-direction selectivity. A representative neuron is shown in Figure 4*E*. This neuron was situated in the medial part of the parasubiculum (Fig. 4*E*, right) and also discharged in bursts with strong theta rhythmicity (Fig. 4*F*, right). The spiking autocorrelogram also revealed a strong theta rhythmicity (Fig. 4*G*, left), and the spikes were strongly locked to local theta oscillations (Fig. 4*G*, right). Spikes were fired throughout the enclosure without obvious spatial modulation (Fig. 4*H*, left) but showed a clear head-direction preference (Fig. 4*H*, right).

Spatial firing properties of parasubicular neurons

By combining juxtacellularly recorded and identified parasubicular neurons with verified recording sites of single-cell and tetrode recordings (see Materials and Methods), we could provide a more comprehensive characterization of functional cell types in parasubiculum. In line with previous work (Boccara et al., 2010), we observed border discharges (9%, 6 of 68; Figs. 4*D*, 5*A*), grid discharges (9%, 6 of 68; Fig. 5*B*), strong head-direction selectivity (50%, 34 of 68; Figs. 4*H*, 5*C*), and a substantial proportion of irregular spatial discharges (40%, 27 of 68) (cells not shown). This last group contains cells with significant spatial information content (Skaggs et al., 1993; see Materials and Meth-

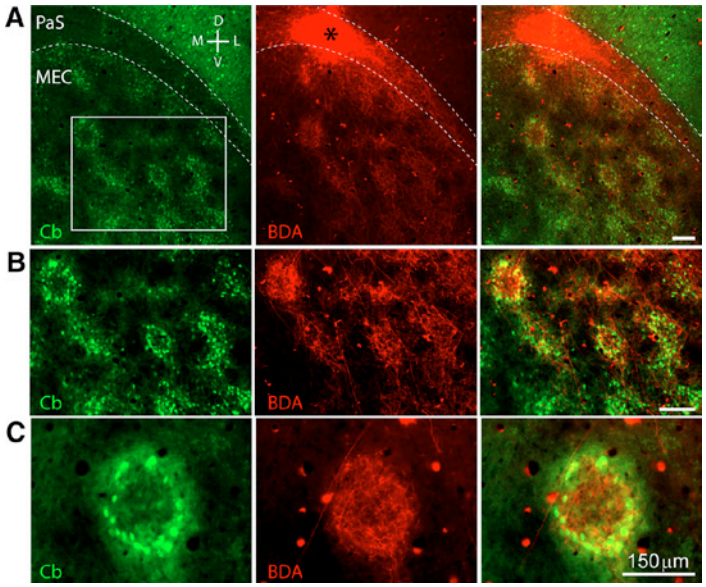

Figure 3. Parasubicular axons target layer 2 pyramidal cell patches in medial entorhinal cortex. ***A***, Left, Tangential section stained for calbindin (green) revealing patches of calbindin-positive pyramidal neurons. Middle, Same section as left processed to reveal the tracer BDA (red). *Location of the parasubicular injection site. Right, Overlay. Scale bar, 150 μm. ***B***, Same as ***A*** but at higher magnification. Scale bar, 150 μm. ***C***, High-magnification view of a single patch. D, Dorsal; L, lateral; M, medial; V, ventral.

ods) but that do not meet grid or border inclusion criteria (see Materials and Methods).

Next, we compared the spatial discharge properties of the parasubiculum with those of identified and putative MEC layer 2 pyramidal and stellate neurons (Tang et al., 2014b) as well as neurons recorded in MEC layer 3 (Tang et al., 2015). We found significantly more spatial responses in the parasubicular neurons than in the other cell types (Fig. 6*A*; all $p < 0.01$, χ^2 test with Bonferroni–Holm correction: 39 of 68 parasubiculum, $\chi^2 = 7.91$ vs 35 of 99 Pyr, $\chi^2 = 12.4$ vs 28 of 94 Stel, $\chi^2 = 11.1$ vs 19/66 L3). We also observed a strong head-directionality of parasubicular neurons, in line with previous observations from linear track recordings (Burgalossi et al., 2011). At the population level, the median head-direction vector of all parasubicular neurons was 0.31, much larger than in MEC layer 2 (0.12 in pyramidals; 0.14 in stellates) and layer 3 (0.09 in layer 3 cells; Fig. 6*B*; all $p < 0.001$, Mann–Whitney *U* tests with Bonferroni–Holm correction: z(Pyr) = 5.54, z(Stel) = 5.79, z(L3) = 7.01). Similarly, the proportion of neurons classified as head-direction cells was also considerably larger than in MEC layers 2 and 3 (Fig. 6*C*; all $p < 0.001$, χ^2 test with Bonferroni–Holm correction: χ^2(Pyr) = 17.7, χ^2(Stel) = 28.8, χ^2(L3) = 30.7)

Theta modulation of parasubicular neurons

As shown in representative neurons (Figs. 4, 5), the large majority of parasubicular neurons showed strong theta rhythmicity, as revealed by autocorrelation of spike trains (Fig. 7*A*) (Tang et al., 2014b, 2015). Parasubicular neurons were also strongly locked to local field potential theta oscillations, which is known to be in phase with MEC theta (Glasgow and Chapman, 2007) (Fig. 7*B*). On average, theta rhythmicity was stronger in parasubicular neurons than in identified layer 2 stellates and layer 3 neurons (both $p < 0.01$, Mann–Whitney *U* test, z(Stel) = 3.19, z(L3) = 8.39; Fig. 7*C*; MEC cells from Tang et al., 2014b and Tang et al., 2015). Identified parasubicular neurons tended to have a higher theta rhythmicity than identified layer 2 neurons (juxtacellularly recorded cells, $p = 0.0116$, Mann–Whitney *U* test), but this difference did not reach statistical significance when tetrode units were included in the sample of parasubicular neurons. Theta phase locking strength (mean (circular) vector length; see Materials and Methods) of parasubicular neurons was similar to that of MEC layer 2 pyramidal neurons ($p > 0.05$, Mann–Whitney *U* test: $z = -0.89$; Fig. 7*D*) and significantly stronger than that of layer 2 stellates and layer 3 neurons (both $p < 0.001$, Mann–Whitney *U* test: z(Stel) = 3.73, z(L3) = 7.83; Fig. 7*D*; MEC cells from Tang et al., 2014b, 2015).

Notably, at the population level, parasubicular and MEC layer 2 pyramidal and stellate neurons showed distinct preferred theta phases (all $p < 0.05$, Rayleigh test for nonuniformity: z(parasubiculum) = 29.5, z(Pyr) = 4.07, z(Stel) = 3.36; Fig. 7*E*; MEC cells from Tang et al., 2014b, 2015). When we compared the preferred phase of identified MEC layer 2 pyramids and identified parasubicular neurons, we found that the parasubicular neurons preferred an earlier theta phase (slightly before the trough; Fig. 7*F*, left; $p = 0.048$, Watson–Williams test for equal circular means: $F = 4.34$). When we included all nonidentified juxta and tetrode recordings of parasubicular and putative MEC layer 2 pyramidal neurons, this difference remained statistically significant (Fig. 7*F*, right; 155° vs 174°, $p = 0.0000085$, Watson–Williams test for equal circular means: $F = 22.7$). Because tetrode recordings of MEC layer 2 were assigned their putative cell identity based on their temporal spiking properties, we wondered whether this might have biased the comparison of preferred theta phase. However, two indications suggest that this was not the case: (1) in the identified dataset, we had not excluded any MEC layer 2 neurons, which locked before the trough (Tang et al., 2014b); and (2) even when we applied the same classifier to all parasubicular neurons and only compared MEC layer 2 putative pyramids with parasubicular neurons, which would have been classified as putative pyramids, the difference in preferred phase was still trending toward significance ($p = 0.076$, Watson–Williams test for equal circular means: $F = 3.21$).

The strong theta phase locking strength and theta rhythmicity of both parasubicular neurons and layer 2 pyramidal (but not stellate) neurons, as well as the preference of parasubicular neurons to fire at a slightly earlier theta phase (~19° phase angle, i.e., ~7 ms, assuming an 8 Hz theta rhythm) than layer 2 pyramidal neurons, are consistent with the idea that parasubicular neurons might impose a feedforward theta-modulated drive onto layer 2 pyramidal neurons.

Discussion

Unique features of the parasubiculum

The parasubiculum is distinct from other parahippocampal structures. The elongated shape of the parasubiculum and an almost linear arrangement of neurons differ from other (para)hippocampal structures, such as dentate gyrus, CA3, CA2, CA1, subiculum, pre-

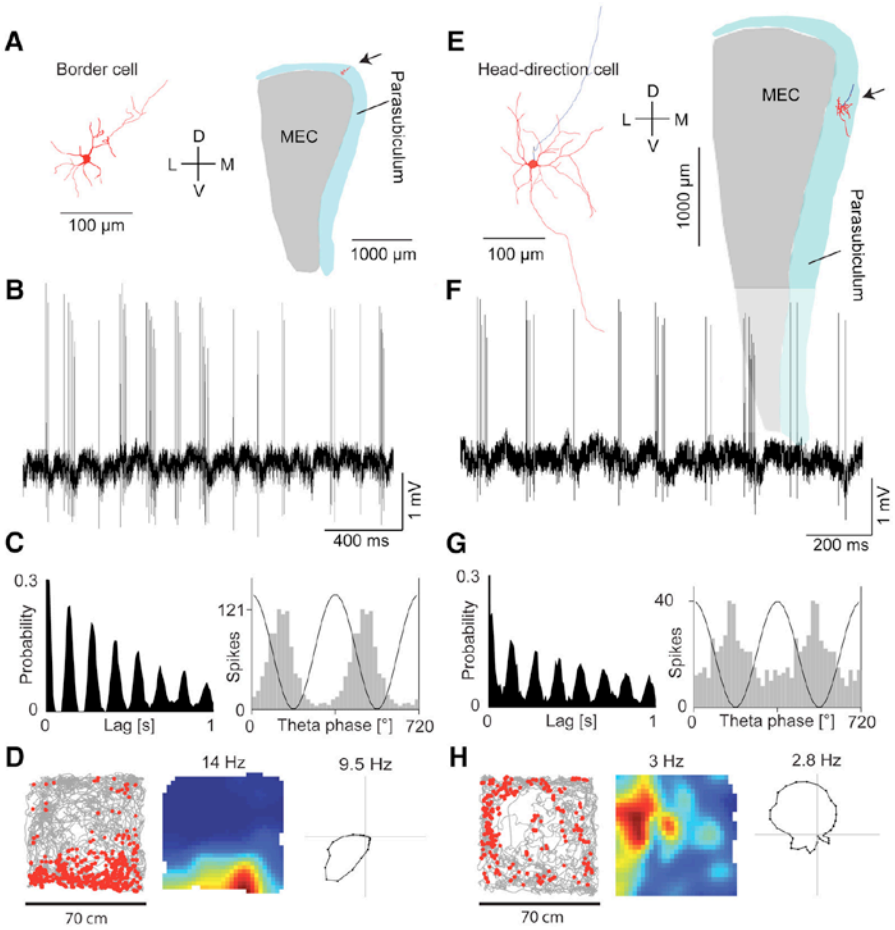

Figure 4. Physiology of identified parasubicular neurons. ***A***, Left, Reconstruction of a border cell juxtacellularly recorded and identified in a rat exploring a 2D environment (70 × 70 cm). Red and blue represent reconstructed dendrites and axon, respectively. Scale bar, 100 μm. Right, Schematic of the location of the cell in the parasubiculum (arrow). The cell is located in the dorsal band of the parasubiculum (blue), close to medial entorhinal cortex (gray). Scale bar, 1000 μm. ***B***, Representative raw traces of the recorded cell shown in ***A***. Note the prominent theta rhythm in LFP and theta-modulated firing of the recorded cell. ***C***, Left, Autocorrelogram of spike discharges for the cell shown in ***A***. Right, theta phase histogram of spikes for the cell shown in ***A***. For convenience, two repeated cycles are shown. The black sinusoid is a schematic local field potential theta wave for reference. ***D***, Spike-trajectory plot (left) and rate map (middle) revealing the border firing. Spike-trajectory plot, Red dots indicate spike locations. Gray lines indicate the rat trajectory. Rate map, Red represents maximal firing rate, value noted above. For this cell, the border score is 0.86. Right, Polar plot of the cell's head-direction tuning. Value indicates maximum firing rate to the preferred direction. ***E–H***, Same as ***A–D*** for an identified head-direction cell. D, Dorsal; L, lateral; M, medial; V, ventral.

subiculum, and medial or lateral entorhinal cortex (Amaral and Witter, 1989; Cenquizca and Swanson, 2007). Further, absence of directly associated deep layers distinguishes the parasubiculum from the surrounding entorhinal, retrosplenial, and presubicular cortices. The "circumcurrent" axons (as defined by Burgalossi et al., 2011) (Fig. 1*E*,*F*) that traverse the parasubiculum and could thus establish a "global" connectivity are also a unique feature of parasubicular anatomy. Furthermore, the parasubiculum is a preferred target of medial septal inputs and provides the major input to pyramidal neuron patches in layer 2 of medial entorhinal cortex. We observed a larger fraction of spatial and head-directional responses in the parasubiculum than in the adjacent medial entorhinal cortex (Solstad et al., 2008; Tang et al., 2014b).

Comparison with previous work

Our anatomical analysis agrees with earlier descriptions that large parts of the parasubiculum are situated between the medial entorhinal cortex and the presubiculum (Amaral and Witter, 1989; Cenquizca and Swanson, 2007). We provide evidence that the parasubiculum extends further laterally than previously thought (van Strien et al., 2009; Boccara et al., 2010) and that this structure might lack direct association with deep layers. The idea that the parasubiculum extends dorsolaterally from the medial entorhinal cortex is based on three observations: (1) staining of cholinergic markers, calbindin immunoreactivity, or cytochrome oxidase activity all delineate a continuous band, which extends dorsolaterally; similarly, both (2) the modular structure of the "large patches" and (3) "circumcurrent" axons extend as a continuous dorsolateral band (Fig. 1) (Burgalossi et al., 2011). Our conclusion that the parasubiculum extends dorsolaterally is strongly supported by recent high-resolution mapping of gene expression in parahippocampal cortices (Ramsden et al., 2015). The authors not only observed that this dorsolateral part is different from medial entorhinal cortex but also showed that it

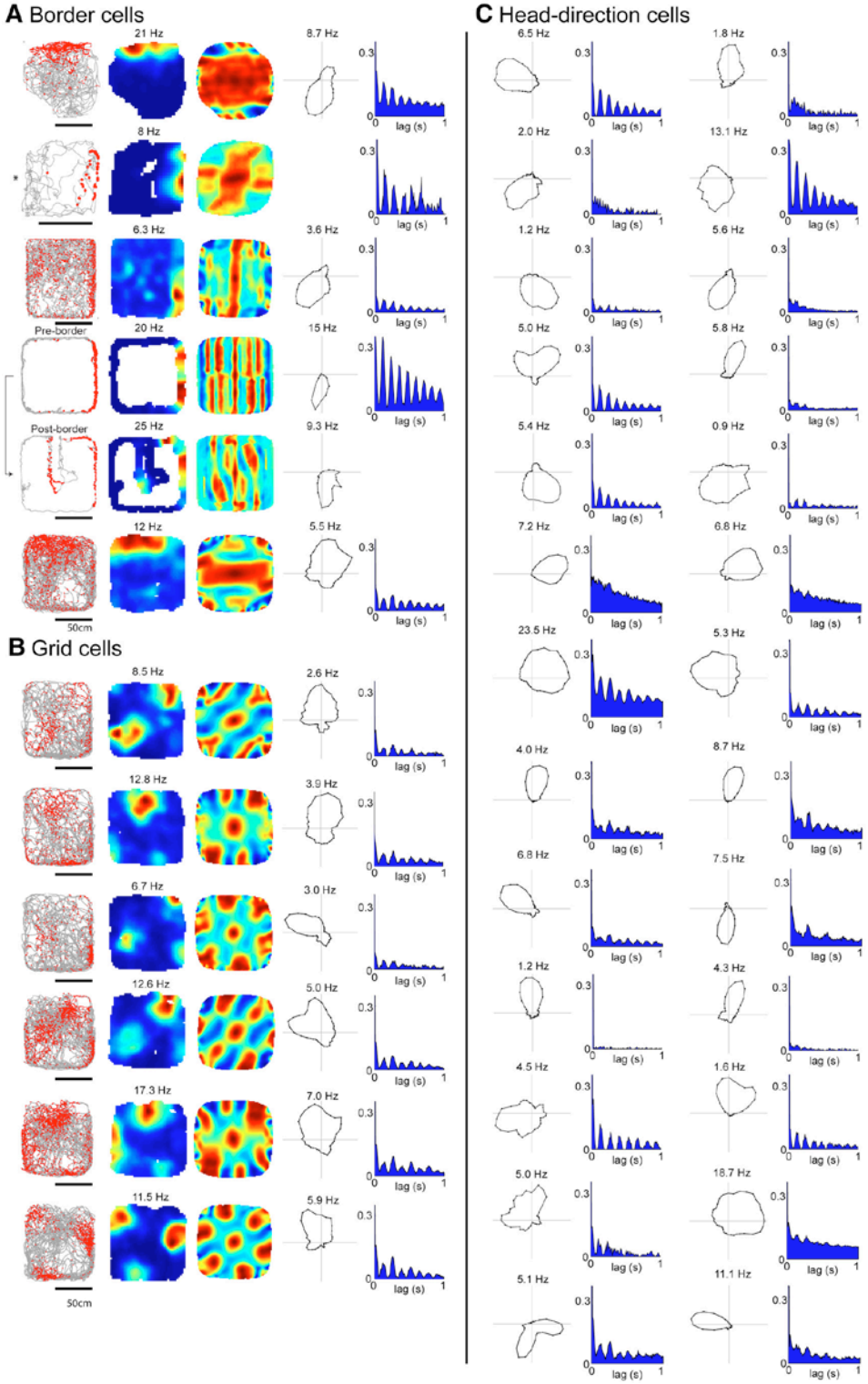

Figure 5. Border, grid, and head-direction firing properties of parasubicular neurons. ***A***, Parasubicular neurons classified as border cells. Left to right, Spike-trajectory plot, rate map, 2D spatial autocorrelation, angular tuning (shown only for head-direction selective cells), and spike autocorrelogram. Numbers above the rate map indicate maximum (*Figure legend continues.*)

shares patterns of gene expression with the "classical" medial parasubiculum (Ramsden et al., 2015). The extent to which deep layers were assigned to the parasubiculum varies in the literature. Whereas some studies assigned deep layers to the parasubiculum (Funahashi and Stewart, 1997; Glasgow and Chapman, 2007; Boccara et al., 2010), other work found it difficult to assign adjacent deep layers to either the presubiculum or the parasubiculum based solely on cytoarchitectonic criteria (Mulders et al., 1997). Our assessment that these deep layer neurons should not be viewed as part of the parasubiculum is based on three observations: (1) the shape of dorsal part of the parasubiculum, as revealed by cholinergic markers, calbindin immunoreactivity, or cytochrome oxidase activity, delineates only a "superficial-layer structure" encompassing layers 1–3 (Burgalossi et al., 2011); (2) we did not observe axons from the superficial parasubiculum into adjacent deep cortical layers; and (3) we did not observe axons from the adjacent deep cortical layers into the superficial parasubiculum. The idea that large parts of the parasubiculum lack deep layers is again supported by the gene expression analysis of Ramsden et al. (2015).

Our results agree with previous extracellular recording data that also revealed the presence of spatially modulated neurons in the parasubiculum (Taube, 1995; Cacucci et al., 2004; Boccara et al., 2010; Burgalossi et al., 2011). The present data are also consistent with the study of Boccara et al. (2010), where the authors described grid, border, and head-direction responses in the parasubiculum. Notably, the strong head-direction tuning in the parasubiculum is also consistent with previous (Fyhn et al., 2008; Wills et al., 2010) and more recent work (Giocomo et al., 2014), where sharply tuned head-direction neurons were recorded "near" the dorsalmost border medial entorhinal cortex, hence compatible with a parasubicular origin of these signals (Fig. 1) (Burgalossi et al., 2011). Extracellular recordings have also identified both theta-rhythmic and non–theta-rhythmic border cells in this dorsalmost region of MEC (Solstad et al., 2008), where the parasubiculum extends in a narrow stripe above MEC (Fig. 1*A*). We found that parasubicular border cells lock strongly to the theta rhythm, whereas border cells in MEC layer 2 show only weak entrainment by theta oscillations (Tang et al., 2014b). Our results show a substantial proportion of spatially irregular cells, in line with previous work (Krupic et al., 2012), which also showed a larger percentage of nongrid, spatially modulated cells in the parasubiculum compared with adjacent MEC. Spatially irregular cells could provide sufficient spatial information for coding the animal's position in space (Zhang et al., 1998; Zhang and Sejnowski, 1999).

Parasubicular discharge properties mirror those of its input structures

Parasubicular response properties match well with the properties of its inputs. Parasubicular head-direction selectivity is in line with its inputs from anterior thalamus and presubiculum (Taube, 2007). The border responses observed here are in line with subicular inputs, as numerous boundary-vector cells have been observed there (Lever et al., 2009). A prominent aspect of

←

(*Figure legend continued.*) firing rate. Numbers above the angular tuning map indicate maximum firing rate at the preferred direction. Scale bar (below the spike trajectory plot), 50 cm. *Border cell recorded in a 70 × 70 cm arena. Preborder and Postborder refer to the border test (recording of the same cell before and after the introduction of an additional wall into the arena). ***B***, Parasubicular neurons classified as grid cells (same panels as in ***A***). ***C***, Parasubicular neurons classified as head-direction cells (see Materials and Methods). Left, Angular tuning. Right, Spike autocorrelogram. Conventions as in ***A***.

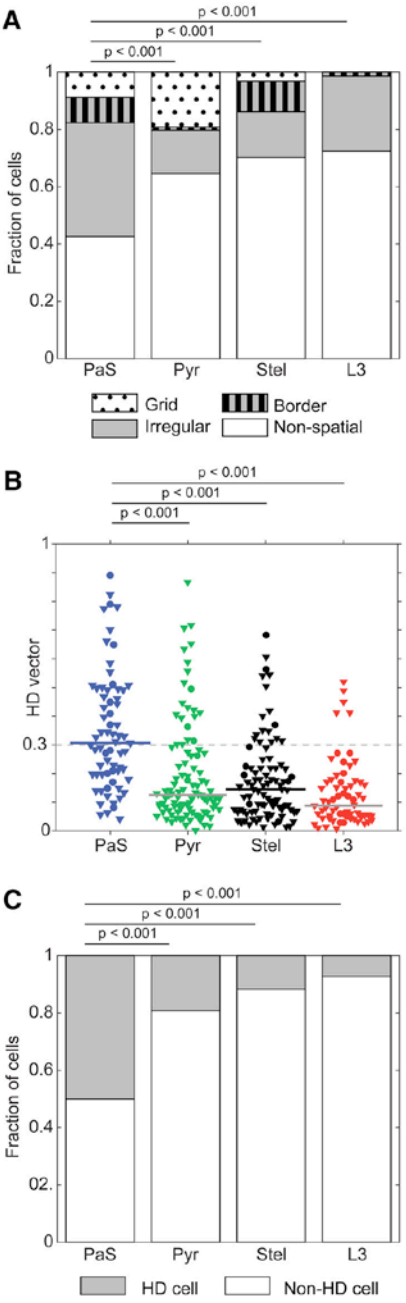

Figure 6. Border and head-direction (HD) firing properties of parasubicular neurons. Data from layers 2 and 3 of MEC come from the work of Tang et al. (2014b, 2015) and are shown for comparison. ***A***, Comparison of fractions of spatial discharges for parasubiculum, MEC L2 pyramidal, MEC L2 stellate, and MEC L3 neurons. Parasubicular neurons show large fraction of significantly spatially modulated cells: grid cells, border cells, and spatially irregular cells (χ^2 test with Bonferroni–Holm correction). ***B***, Comparison of HD vector lengths for parasubiculum (blue), MEC L2 pyramidal (green), MEC L2 stellate (black), and MEC L3 (red) neurons. Parasubicular neurons show significantly higher average HD vector length than all others (Mann–Whitney *U* tests with Bonferroni–Holm correction). Lines indicate medians. Horizontal dotted line at 0.3 indicates the threshold for HD classification. ***C***, Comparison of fractions of HD cells for parasubiculum, MEC L2 pyramidal, MEC L2 stellate, and MEC L3 neurons. Parasubicular neurons show significantly higher percentage of HD cells (χ^2 test with Bonferroni–Holm correction).

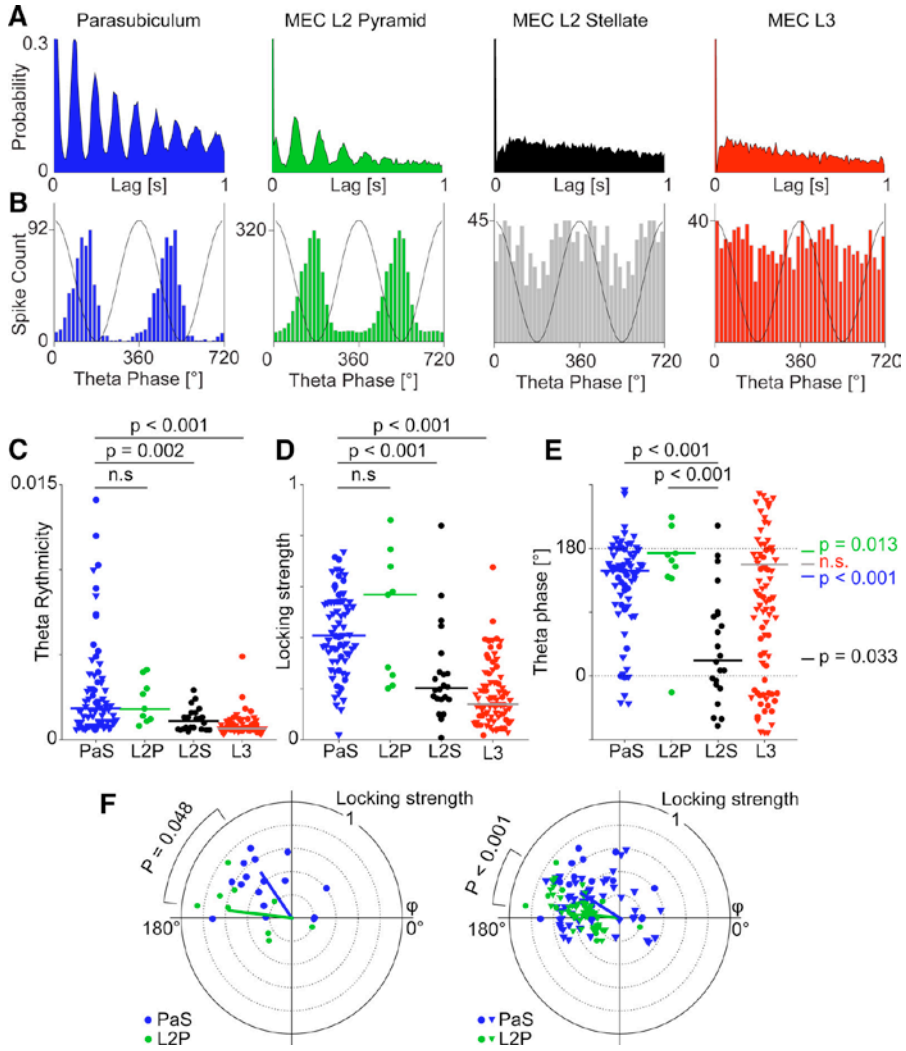

Figure 7. Theta modulation of parasubicular neurons compared with superficial medial entorhinal cortex. Data from layers 2 and 3 of MEC come from the work of Tang et al. (2014b, 2015) and are shown here for comparison. ***A***, Representative autocorrelograms of spike discharges of identified neurons recorded from parasubiculum (blue), MEC L2 pyramidal (L2P, green), MEC L2 stellate (L2S, black) and MEC L3 (red) neurons. ***B***, Theta phase histogram of spikes for the neurons shown in ***A***. For convenience, two theta cycles are shown. The black sinusoid is a schematic local field potential theta wave for reference. ***C***, Comparison of the power of theta rhythmicity in parasubiculum (blue), MEC L2 pyramid (L2P, green), MEC L2 stellate (L2S, black), and MEC L3 (L3, red) neurons. Parasubiculum neurons show significantly stronger theta rhythmicity than MEC L2 stellate and MEC L3 neurons (Kruskal–Wallis test with Bonferroni correction). Lines indicate medians. ***D***, Comparison of the theta phase locking strength (abbreviated in the figure as "Locking strength") for the neurons shown in ***C***. Parasubicular and MEC L2 pyramidal neurons show significantly higher theta phase locking than MEC L2 stellate and MEC L3 neurons (Kruskal–Wallis test with Bonferroni–Holm correction; significant differences between L2P and L2S have been shown in Ray et al., 2014). Lines indicate medians. ***E***, Comparison of the preferred theta phase for the neurons shown in ***C***. Parasubicular and MEC L2 neurons show significant preferred theta phases, whereas MEC L3 neurons do not (Rayleigh test for nonuniformity with Bonferroni–Holm correction: colored *p* values on the right side; Watson–Williams test for equal means with Bonferroni–Holm correction: black lined *p* values, top). Colored lines indicate circular means. ***F***, Polar plots of preferred theta phase (theta peak = 0°) and theta phase locking strength (Rayleigh vector, 0–1) for parasubiculum (blue) and MEC L2 pyramidal (green). Left, Only identified neurons. Right, Identified neurons and tetrode recordings. Dots represent identified neurons. Triangles represent tetrode units. Line indicates mean direction, median strength of locking.

parasubicular activity is the strong theta phase locking and theta rhythmicity of spike discharges. Large membrane-potential theta oscillations have also been recorded from parasubicular neurons in awake animals (Domnisoru et al., 2013). Such strong entrainment may result from the massive septal GABAergic innervation (Fig. 3*A*,*B*) because GABAergic neurons in the medial septum are known to be a key theta pacemaker (Buzsáki, 2002; Hangya et al., 2009; Brandon et al., 2011; Koenig et al., 2011). Cholinergic innervation may also drive parasubicular neurons to depolarized states promoting theta oscillations (Glasgow and Chapman, 2007, 2013).

Does the parasubiculum provide input to the grid system?

Our data suggest a relationship between the parasubiculum and layer 2 of medial entorhinal cortex grid cells (Sargolini et al., 2006; Boccara et al., 2010). Grid cells in the medial entorhinal cortex show strong theta rhythmicity of spiking (Boccara et al., 2010). It is therefore most interesting that the strongly theta-

rhythmic parasubicular neurons project selectively into layer 2 pyramidal cell patches, where neurons show strong entrainment by the theta rhythm (Ray et al., 2014) and where most grid cells might be located (Tang et al., 2014b). The discharge timing is consistent with an activation/entrainment of layer 2 pyramidal neurons by parasubicular inputs. Parasubicular neurons discharge on average at an earlier theta phase (~19° phase angle, i.e., ~7 ms) than layer 2 pyramidal neurons (Fig. 7*E*,*F*). The parasubicular input to layer 2 pyramidal neurons is also remarkable, in light of the sparse excitatory connectivity within layer 2 of medial entorhinal cortex (Couey et al., 2013; Pastoll et al., 2013). Parasubicular inputs could be important for three aspects: (1) for imposing theta rhythmicity on grid responses, and possibly also contributing to their temporal spiking dynamics (Hafting et al., 2008; Mizuseki et al., 2009; Ray et al., 2014; Tang et al., 2014b). (2) Parasubicular head-directional responses could be causally related to downstream grid activity in layer 2 of MEC. Indeed, grid cells have been shown to receive head-directional inputs, and disruptions of head-direction signals also impaired grid cell firing (Bonnevie et al., 2013; Winter et al., 2015). The parasubiculum might be the source of this input, given the large fraction of head-direction cells and the selective output to MEC layer 2 (Fig. 3). (3) Parasubicular border activity could be needed for anchoring entorhinal layer 2 grids to environmental boundaries (Hardcastle et al., 2015). Interestingly, direct projections from border to grid cells have been recently postulated, which might be responsible for determining grid orientation, ellipticity, and stability (Kruge et al., 2014; Hardcastle et al., 2015; Krupic et al., 2015; Stensola et al., 2015). The parasubiculum might be one source of border signals into the entorhinal grid system.

Functional considerations

What does the parasubiculum do? It seems likely that the parasubiculum plays a role in determining spike timing of downstream neurons relative to theta oscillations. The massive internal connectivity of the parasubiculum by circumcurrent axons is rather unique. These axons connect along the dorsoventral axis of the parahippocampal cortex. As different spatial scales are mapped onto the dorsoventral axis of the medial entorhinal cortex (Brun et al., 2008), we wonder whether these axons ensure that those parasubicular neurons along the dorsoventral axis signaling the same positions (at different spatial scales) fire at the same time relative to the theta cycle. Another peculiar aspect of parasubicular anatomy is the lack of strong direct hippocampal connections (van Strien et al., 2009). Together with the absence of deep layers (the recipient of CA1/subicular back projections in the medial entorhinal cortex) and a thinner layer 1, it seems that the parasubiculum is only poorly connected to the "trisynaptic memory loop" (reciprocal connections between the parasubiculum and postrhinal cortex could, however, provide an indirect pathway) (Agster and Burwell, 2013). We envision that the parasubiculum may function more for providing online spatial information like a pointer ("where am I?") rather than for long-term storage of information ("where was I?"). This pointer hypothesis is consistent with disruption of place cell activity (Liu et al., 2004) and working memory deficits after parasubicular lesions (Kesner and Giles, 1998).

References

Agster KL, Burwell RD (2013) Hippocampal and subicular efferents and afferents of the perirhinal, postrhinal, and entorhinal cortices of the rat. Behav Brain Res 254:50–64. CrossRef Medline

Amaral DG, Witter MP (1989) The three-dimensional organization of the hippocampal formation: a review of anatomical data. Neuroscience 31: 571–591. CrossRef Medline

Andersen P, Bliss TV, Skrede KK, Lomo T, Olsen LI (1971) Lamellar organization of hippocampal excitatory pathways. Exp Brain Res 13:222–238. Medline

Barry C, Ginzberg LL, O'Keefe J, Burgess N (2012) Grid cell firing patterns signal environmental novelty by expansion. Proc Natl Acad Sci U S A 109:17687–17692. CrossRef Medline

Bjerknes TL, Moser EI, Moser MB (2014) Representation of geometric borders in the developing rat. Neuron 82:71–78. CrossRef Medline

Blackstad TW (1956) Commissural connections of the hippocampal region in the rat, with special reference to their mode of termination. J Comp Neurol 105:417–537. CrossRef Medline

Boccara CN, Sargolini F, Thoresen VH, Solstad T, Witter MP, Moser EI, Moser MB (2010) Grid cells in pre- and parasubiculum. Nat Neurosci 13:987–994. CrossRef Medline

Bonnevie T, Dunn B, Fyhn M, Hafting T, Derdikman D, Kubie JL, Roudi Y, Moser EI, Moser MB (2013) Grid cells require excitatory drive from the hippocampus. Nat Neurosci 16:309–317. CrossRef Medline

Brandon MP, Bogaard AR, Libby CP, Connerney MA, Gupta K, Hasselmo ME (2011) Reduction of theta rhythm dissociates grid cell spatial periodicity from directional tuning. Science 332:595–599. CrossRef Medline

Brun VH, Solstad T, Kjelstrup KB, Fyhn M, Witter MP, Moser EI, Moser MB (2008) Progressive increase in grid scale from dorsal to ventral medial entorhinal cortex. Hippocampus 18:1200–1212. CrossRef Medline

Burgalossi A, Herfst L, von Heimendahl M, Förste H, Haskic K, Schmidt M, Brecht M (2011) Microcircuits of functionally identified neurons in the rat medial entorhinal cortex. Neuron 70:773–786. CrossRef Medline

Burgess N (2014) The 2014 Nobel Prize in Physiology or Medicine: a spatial model for cognitive neuroscience. Neuron 84:1120–1125. CrossRef Medline

Buzsáki G (2002) Theta oscillations in the hippocampus. Neuron 33: 325–340. CrossRef Medline

Caballero-Bleda M, Witter MP (1993) Regional and laminar organization of projections from the presubiculum and parasubiculum to the entorhinal cortex: an anterograde tracing study in the rat. J Comp Neurol 328: 115–129. CrossRef Medline

Caballero-Bleda M, Witter MP (1994) Projections from the presubiculum and the parasubiculum to morphologically characterized entorhinal-hippocampal projection neurons in the rat. Exp Brain Res 101:93–108. Medline

Cacucci F, Lever C, Wills TJ, Burgess N, O'Keefe J (2004) Theta-modulated place-by-direction cells in the hippocampal formation in the rat. J Neurosci 24:8265–8277. CrossRef Medline

Canto CB, Koganezawa N, Beed P, Moser EI, Witter MP (2012) All layers of medial entorhinal cortex receive presubicular and parasubicular inputs. J Neurosci 32:17620–17631. CrossRef Medline

Cenquizca LA, Swanson LW (2007) Spatial organization of direct hippocampal field CA1 axonal projections to the rest of the cerebral cortex. Brain Res Rev 56:1–26. CrossRef Medline

Couey JJ, Witoelar A, Zhang SJ, Zheng K, Ye J, Dunn B, Czajkowski R, Moser MB, Moser EI, Roudi Y, Witter MP (2013) Recurrent inhibitory circuitry as a mechanism for grid formation. Nat Neurosci 16:318–324. CrossRef Medline

Ding SL (2013) Comparative anatomy of the prosubiculum, subiculum, presubiculum, postsubiculum, and parasubiculum in human, monkey, and rodent. J Comp Neurol 521:4145–4162. CrossRef Medline

Domnisoru C, Kinkhabwala AA, Tank DW (2013) Membrane potential dynamics of grid cells. Nature 495:199–204. CrossRef Medline

Fujise N, Hunziker W, Heizmann CW, Kosaka T (1995) Distribution of the calcium binding proteins, calbindin D-28K and parvalbumin, in the subicular complex of the adult mouse. Neurosci Res 22:89–107. CrossRef Medline

Funahashi M, Stewart M (1997) Presubicular and parasubicular cortical neurons of the rat: functional separation of deep and superficial neurons in vitro. J Physiol 501:387–403. CrossRef Medline

Fyhn M, Hafting T, Witter MP, Moser EI, Moser MB (2008) Grid cells in mice. Hippocampus 18:1230–1238. CrossRef Medline

Geneser FA (1986) Distribution of acetylcholinesterase in the hippocampal region of the rabbit: I. Entorhinal area, parasubiculum, and presubiculum. J Comp Neurol 254:352–368. CrossRef Medline

Giocomo LM, Stensola T, Bonnevie T, Van Cauter T, Moser MB, Moser EI

(2014) Topography of head-direction cells in medial entorhinal cortex. Curr Biol 24:252–262. CrossRef Medline

Glasgow SD, Chapman CA (2007) Local generation of theta-frequency EEG activity in the parasubiculum. J Neurophysiol 97:3868–3879. CrossRef Medline

Glasgow SD, Chapman CA (2013) Muscarinic depolarization of layer II neurons of the parasubiculum. PLoS One 8:e58901. CrossRef Medline

Hafting T, Fyhn M, Bonnevie T, Moser MB, Moser EI (2008) Hippocampus-independent phase precession in entorhinal grid cells. Nature 453:1248–1252. CrossRef Medline

Hangya B, Borhegyi Z, Szilágyi N, Freund TF, Varga V (2009) GABAergic neurons of the medial septum lead the hippocampal network during theta activity. J Neurosci 29:8094–8102. CrossRef Medline

Hardcastle K, Ganguli S, Giocomo LM (2015) Environmental boundaries as an error correction mechanism for grid cells. Neuron 86:827–839. CrossRef Medline

Honda Y, Ishizuka N (2004) Organization of connectivity of the rat presubiculum: I. Efferent projections to the medial entorhinal cortex. J Comp Neurol 473:463–484. CrossRef Medline

Kesner RP, Giles R (1998) Neural circuit analysis of spatial working memory: role of pre- and parasubiculum, medial and lateral entorhinal cortex. Hippocampus 8:416–423. CrossRef Medline

Koenig J, Linder AN, Leutgeb JK, Leutgeb S (2011) The spatial periodicity of grid cells is not sustained during reduced theta oscillations. Science 332:592–595. CrossRef Medline

Köhler C (1985) Intrinsic projections of the retrohippocampal region in the rat brain: I. The subicular complex. J Comp Neurol 236:504–522. CrossRef Medline

Kruge IU, Waaga T, Wernle T, Moser EI, Moser MB (2014) Grid cells require experience with local boundaries during development: 2014 Neuroscience Meeting Planner (online 94.01/SS21). Washington, DC: Society for Neuroscience.

Krupic J, Burgess N, O'Keefe J (2012) Neural representations of location composed of spatially periodic bands. Science 337:853–857. CrossRef Medline

Krupic J, Bauza M, Burton S, Barry C, O'Keefe J (2015) Grid cell symmetry is shaped by environmental geometry. Nature 518:232–235. CrossRef Medline

Lever C, Burton S, Jeewajee A, O'Keefe J, Burgess N (2009) Boundary vector cells in the subiculum of the hippocampal formation. J Neurosci 29:9771–9777. CrossRef Medline

Liu P, Jarrard LE, Bilkey DK (2004) Excitotoxic lesions of the pre- and parasubiculum disrupt the place fields of hippocampal pyramidal cells. Hippocampus 14:107–116. CrossRef Medline

Mitchell SJ, Rawlins JN, Steward O, Olton DS (1982) Medial septal area lesions disrupt theta rhythm and cholinergic staining in medial entorhinal cortex and produce impaired radial arm maze behavior in rats. J Neurosci 2:292–302. Medline

Mizuseki K, Sirota A, Pastalkova E, Buzsáki G (2009) Theta oscillations provide temporal windows for local circuit computation in the entorhinal-hippocampal loop. Neuron 64:267–280. CrossRef Medline

Moser EI, Moser MB (2013) Grid cells and neural coding in high-end cortices. Neuron 80:765–774. CrossRef Medline

Moser EI, Kropff E, Moser MB (2008) Place cells, grid cells, and the brain's spatial representation system. Annu Rev Neurosci 31:69–89. CrossRef Medline

Mulders WH, West MJ, Slomianka L (1997) Neuron numbers in the presubiculum, parasubiculum, and entorhinal area of the rat. J Comp Neurol 385:83–94. CrossRef Medline

Pastoll H, Solanka L, van Rossum MC, Nolan MF (2013) Feedback inhibition enables theta-nested gamma oscillations and grid firing fields. Neuron 77:141–154. CrossRef Medline

Paxinos G, Franklin KBJ (2012) Paxinos and Franklin's the mouse brain in stereotaxic coordinates. San Diego: Academic.

Pinault D (1996) A novel single-cell staining procedure performed in vivo under electrophysiological control: morpho-functional features of juxtacellularly labeled thalamic cells and other central neurons with biocytin or Neurobiotin. J Neurosci Methods 65:113–136. CrossRef Medline

Ramsden HL, Sürmeli G, McDonagh SG, Nolan MF (2015) Laminar and dorsoventral molecular organization of the medial entorhinal cortex revealed by large-scale anatomical analysis of gene expression. PLoS Comput Biol 11:e1004032. CrossRef Medline

Ray S, Naumann R, Burgalossi A, Tang Q, Schmidt H, Brecht M (2014) Grid-layout and theta-modulation of layer 2 pyramidal neurons in medial entorhinal cortex. Science 343:891–896. CrossRef Medline

Sargolini F, Fyhn M, Hafting T, McNaughton BL, Witter MP, Moser MB, Moser EI (2006) Conjunctive representation of position, direction, and velocity in entorhinal cortex. Science 312:758–762. CrossRef Medline

Skaggs WE, McNaughton BL, Gothard KM, Markus EJ (1993) An information-theoretic approach to deciphering the hippocampal code. In: Advances in neural processing systems, Vol. 5 (Hanson SJ, Cowan JD, Giles CL, eds). San Mateo, CA: Morgan Kaufmann.

Slomianka L, Geneser FA (1991) Distribution of acetylcholinesterase in the hippocampal region of the mouse: I. Entorhinal area, parasubiculum, retrosplenial area, and presubiculum. J Comp Neurol 303:339–354. CrossRef Medline

Solstad T, Boccara CN, Kropff E, Moser MB, Moser EI (2008) Representation of geometric borders in the entorhinal cortex. Science 322:1865–1868. CrossRef Medline

Stensola T, Stensola H, Moser MB, Moser EI (2015) Shearing-induced asymmetry in entorhinal grid cells. Nature 518:207–212. CrossRef Medline

Sun C, Kitamura T, Yamamoto J, Martin J, Pignatelli M, Kitch LJ, Schnitzer MJ, Tonegawa S (2015) Distinct speed dependence of entorhinal island and ocean cells, including respective grid cells. Proc Natl Acad Sci U S A 112:9466–9471. CrossRef Medline

Tang Q, Brecht M, Burgalossi A (2014a) Juxtacellular recording and morphological identification of single neurons in freely moving rats. Nat Protoc 9:2369–2381. CrossRef Medline

Tang Q, Burgalossi A, Ebbesen CL, Ray S, Naumann R, Schmidt H, Spicher D, Brecht M (2014b) Pyramidal and stellate cell specificity of grid and border representations in layer 2 of medial entorhinal cortex. Neuron 84:1191–1197. CrossRef Medline

Tang Q, Ebbesen CL, Sanguinetti-Scheck JI, Preston-Ferrer P, Gundlfinger A, Winterer J, Beed P, Ray S, Naumann R, Schmitz D, Brecht M, Burgalossi A (2015) Anatomical organization and spatiotemporal firing patterns of layer 3 neurons in the rat medial entorhinal cortex. J Neurosci 35:12346–12354. CrossRef Medline

Taube JS (1995) Place cells recorded in the parasubiculum of freely moving rats. Hippocampus 5:569–583. CrossRef Medline

Taube JS (2007) The head-direction signal: origins and sensory-motor integration. Annu Rev Neurosci 30:181–207. CrossRef Medline

van Groen T, Wyss JM (1990) The connections of presubiculum and parasubiculum in the rat. Brain Res 518:227–243. CrossRef Medline

van Groen T, Wyss JM (1992) Projections from the laterodorsal nucleus of the thalamus to the limbic and visual cortices in the rat. J Comp Neurol 324:427–448. CrossRef Medline

van Strien NM, Cappaert NL, Witter MP (2009) The anatomy of memory: an interactive overview of the parahippocampal-hippocampal network. Nat Rev Neurosci 10:272–282. CrossRef Medline

Varga C, Lee SY, Soltesz I (2010) Target-selective GABAergic control of entorhinal cortex output. Nat Neurosci 13:822–824. CrossRef Medline

von Heimendahl M, Rao RP, Brecht M (2012) Weak and nondiscriminative responses to conspecifics in the rat hippocampus. J Neurosci 32:2129–2141. CrossRef Medline

Wills TJ, Cacucci F, Burgess N, O'Keefe J (2010) Development of the hippocampal cognitive map in preweanling rats. Science 328:1573–1576. CrossRef Medline

Winter SS, Clark BJ, Taube JS (2015) Disruption of the head-direction cell network impairs the parahippocampal grid cell signal. Science 347:870–874. CrossRef Medline

Zhang K, Sejnowski TJ (1999) Neuronal tuning: to sharpen or broaden? Neural Comput 11:75–84. CrossRef Medline

Zhang K, Ginzburg I, McNaughton BL, Sejnowski TJ (1998) Interpreting neuronal population activity by reconstruction: unified framework with application to hippocampal place cells. J Neurophysiol 79:1017–1044. Medline

6. Cell Type-Specific Differences in Spike Timing and Spike Shape in the Rat Parasubiculum and Superficial Medial Entorhinal Cortex

This manuscript was published as:
Ebbesen, C.L., Reifenstein, E.T., Tang, Q., Burgalossi, A., Ray, S., Schreiber, S., Kempter, R. & Brecht, M. (2016) Cell type-specific differences in spike timing and spike shape in rat parasubiculum and superficial medial entorhinal cortex. **Cell Reports** 16(4):1005-1015.

Article

Cell Reports

Cell Type-Specific Differences in Spike Timing and Spike Shape in the Rat Parasubiculum and Superficial Medial Entorhinal Cortex

Graphical Abstract

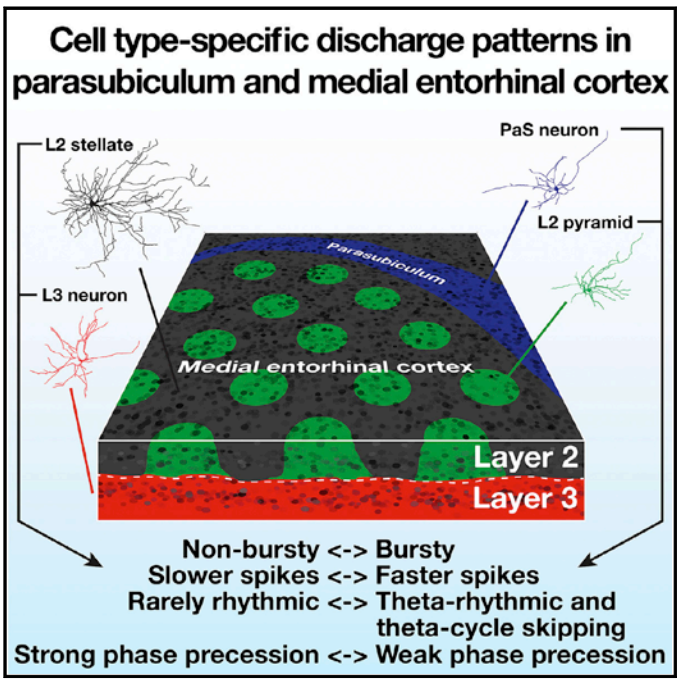

Highlights

- We find cell type-specific differences in spike shape, burstiness, and phase precession
- In vivo cell type specificity does not match predictions from previous in vitro studies
- Anatomical identity is a major determinant of spike patterns in the parahippocampal cortex

Authors

Christian Laut Ebbesen, Eric Torsten Reifenstein, Qiusong Tang, ..., Susanne Schreiber, Richard Kempter, Michael Brecht

Correspondence

michael.brecht@bccn-berlin.de

In Brief

Neurons in the parahippocampal cortex discharge in elaborate spatiotemporal firing patterns. Ebbesen et al. use juxtacellular recordings to show that the neuronal cell type is a major determinant of temporal discharge patterns such as bursting and phase precession.

Ebbesen et al., 2016, Cell Reports *16*, 1005–1015
July 26, 2016
http://dx.doi.org/10.1016/j.celrep.2016.06.057

Cell Reports
Article

OPEN ACCESS
CellPress

Cell Type-Specific Differences in Spike Timing and Spike Shape in the Rat Parasubiculum and Superficial Medial Entorhinal Cortex

Christian Laut Ebbesen,[1,2] Eric Torsten Reifenstein,[1,3] Qiusong Tang,[1] Andrea Burgalossi,[4] Saikat Ray,[1] Susanne Schreiber,[1,3] Richard Kempter,[1,3] and Michael Brecht[1,*]
[1]Bernstein Center for Computational Neuroscience, Humboldt Universität zu Berlin, Philippstr. 13, Haus 6, 10115 Berlin, Germany
[2]Berlin School of Mind and Brain, Humboldt Universität zu Berlin, 10115 Berlin, Germany
[3]Institute for Theoretical Biology and Department of Biology, Humboldt Universität zu Berlin, 10115 Berlin, Germany
[4]Werner Reichardt Centre for Integrative Neuroscience, Otfried-Müller-Strass 25, 72076 Tübingen, Germany
*Correspondence: michael.brecht@bccn-berlin.de
http://dx.doi.org/10.1016/j.celrep.2016.06.057

SUMMARY

The medial entorhinal cortex (MEC) and the adjacent parasubiculum are known for their elaborate spatial discharges (grid cells, border cells, etc.) and the precessing of spikes relative to the local field potential. We know little, however, about how spatio-temporal firing patterns map onto cell types. We find that cell type is a major determinant of spatio-temporal discharge properties. Parasubicular neurons and MEC layer 2 (L2) pyramids have shorter spikes, discharge spikes in bursts, and are theta-modulated (rhythmic, locking, skipping), but spikes phase-precess only weakly. MEC L2 stellates and layer 3 (L3) neurons have longer spikes, do not discharge in bursts, and are weakly theta-modulated (non-rhythmic, weakly locking, rarely skipping), but spikes steeply phase-precess. The similarities between MEC L3 neurons and MEC L2 stellates on one hand and parasubicular neurons and MEC L2 pyramids on the other hand suggest two distinct streams of temporal coding in the parahippocampal cortex.

INTRODUCTION

The discovery of grid cells in the medial entorhinal cortex (MEC) (Hafting et al., 2005) has been a major advance in cortical physiology (Burgess 2014). The assessment of single-unit activity in rats running in boxes has led to the discovery of a plethora of "functional" cell types in the MEC: conjunctive (head-directional) grid cells (Sargolini et al., 2006), border cells (Solstad et al., 2008), boundary vector cells (Koenig et al., 2011), speed cells (Kropff et al., 2015), and cue cells (Kinkhabwala et al., 2015, J Neurosci., conference). Grid and border cells also exist in areas neighboring the entorhinal cortex, such as the subiculum and pre- and parasubiculum (Lever et al., 2009; Boccara et al., 2010; Tang et al., 2016).

Computational models propose many different mechanisms to explain how grid cell discharges come about (Giocomo et al., 2011; Zilli 2012). A better knowledge of the anatomy and spatio-temporal firing patterns of defined cell types is needed to constrain models and help prune the forest of different models. Two aspects of the temporal firing patterns were highlighted in recent work: burstiness and theta cycle skipping. Burstiness has been shown to be associated with grid cell firing (Newman and Hasselmo, 2014; Latuske et al., 2015) and might serve important functions in parahippocampal microcircuits (Welday et al., 2011; Sheffield and Dombeck, 2015). Burstiness has also been linked to differences in extracellular spike shape (Newman and Hasselmo, 2014; Latuske et al., 2015). Theta cycle skipping might be related to the computation of head-directional information and grid firing (Brandon et al., 2013).

Previous investigations of burstiness and theta cycle skipping have analyzed mixed extracellular recordings from both the superficial medial entorhinal cortex and the parasubiculum (Brandon et al., 2013; Newman and Hasselmo, 2014; Latuske et al., 2015). It has thus remained unclear whether burstiness and theta cycle skipping map onto anatomical categories or whether bursty and non-bursty neurons are simply intermingled (Latuske et al., 2015). Stellate cells (Stel) in layer 2 (L2) of the medial entorhinal cortex show a tendency to fire bursts of action potentials upon membrane depolarization in vitro (Alonso and Klink, 1993; Pastoll et al., 2012; Alessi et al., 2016; Fuchs et al., 2016). Such findings led to the hypothesis that stellate cells might display bursty firing patterns in vivo (Newman and Hasselmo, 2014; Latuske et al., 2015).

Entorhinal grid cells phase-precess; i.e., they shift spike timing in a systematic way relative to the field potential during firing field transversals (Hafting et al., 2008; Jeewajee et al., 2013; Newman and Hasselmo 2014). Based on a pooled run analysis, it has been found that MEC L2 cells phase-precess more strongly than MEC layer 3 (L3) cells (Hafting et al., 2008; Mizuseki et al., 2009). This difference between MEC layers 2 and 3 has not been seen at the single run level; however, it may arise because MEC L3 cells are less correlated between runs (Reifenstein et al., 2012, 2014). Recently, a single run analysis of phase precession revealed differences between pyramidal and stellate neurons in MEC L2 (Reifenstein et al., 2016). Parasubicular neurons provide specific input to MEC L2 pyramidal neurons (Pyr) (Tang et al., 2016), but it is unknown whether parasubicular neurons phase-precess.

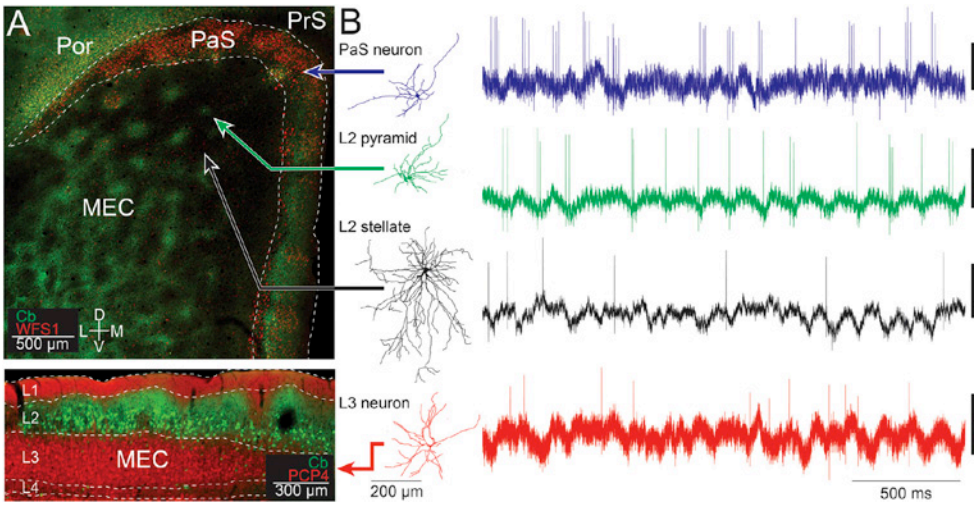

Figure 1. Parasubicular and Superficial Medial Entorhinal Cortex Neuron Types

(A) Top: tangential section of the parasubiculum (PaS) and layer 2 of the medial entorhinal cortex (MEC) stained for calbindin (Cb, green channel) and wolframin (WFS1, red channel). Bottom: parasagittal section of the MEC stained for Cb (green channel) and PCP4 (red channel). Also visible are the presubiculum (PrS) and postrhinal cortex (Por).

(B) Left: reconstructions (from tangential cortical sections; neurons are seen from the top) of examples of the four neuron types: a PaS neuron (blue), an MEC L2 pyramidal neuron (green), an MEC L2 stellate cell (black), and an MEC L3 neuron (red), corresponding to the anatomical cell types marked by arrows in (A). Right: juxtacellular recording traces of the reconstructed cells. The spiking of the parasubicular neuron and the MEC L2 pyramid is bursty and theta-modulated. Scale bars, 1 mV. Cell reconstructions were adapted from Tang et al. (2014a, 2015, 2016).

Here we analyze juxtacellular recordings from the medial entorhinal cortex (Ray et al., 2014; Tang et al., 2014a, 2015) and the parasubiculum (Tang et al., 2016). Juxtacellular data offer two advantages (Pinault 1996; Herfst et al., 2012). First, cells can often be anatomically identified. Second, juxtacellular recording of the local field potential (LFP) and spikes has a very high temporal resolution and signal-to-noise ratio, which is crucial for investigating temporal patterns such as burstiness. We ask the following questions. Does burstiness differ between parasubicular neurons, MEC L2 pyramids, MEC L2 stellates, and MEC L3 neurons? Are MEC L2 stellates actually bursty in vivo? Do differences in extracellular spike shape reflect burstiness or anatomical category? Does theta cycle skipping map onto anatomical categories? Does burstiness predict theta rhythmicity and theta locking? How does phase precession differ among cell types?

RESULTS

Overview of Anatomical Cell Types in the Parahippocampal Cortex

The parahippocampal cortex has a modular architecture. L2 of the MEC contains patches of calbindin-positive pyramidal neurons arranged in a hexagonal grid (Ray et al., 2014; Figure 1A, top) that are surrounded by calbindin-negative stellate cells (Figure 1A, top, black background). The parasubiculum (PaS) is a thin elongated structure that wraps around the MEC mediodorsally and has high wolframin expression (WFS1-positive cells; Figure 1A, top; Tang et al., 2016). Axons from the parasubiculum specifically target the patches of MEC L2 pyramidal cells (Burgalossi et al., 2011; Tang et al., 2016). MEC L3 neurons are not arranged in a hexagonal grid but are visible as a homogenous band of Purkinje cell protein 4 (PCP4)-positive cells below layer 2 (L3; red band in Figure 1A, bottom). Figure 1B, left, shows reconstructions of example cells of the four neuron types: a parasubicular neuron (blue), a MEC L2 pyramidal neuron (green), a MEC L2 stellate cell (black), and an MEC L3 pyramidal neuron (red), all recorded in freely moving rats. We use these colors throughout the manuscript. All reconstructions are from tangential sections (i.e., a "top view" of the morphology). In addition to the morphology, we also show juxtacellular recording traces from the reconstructed example cells (Figure 1B, right). Two signals are visible in the recordings: the spikes of the identified cells and the prominent theta rhythm in the LFP.

Analysis of Burstiness

To determine whether a neuron was discharging in a bursty pattern, we analyzed the interspike interval (ISI) histogram using a similar approach as Latuske et al. (2015). ISIs below 60 ms were binned in 2-ms bins (normalized to area = 1 to generate a probability distribution), which revealed that our dataset contained both non-bursty and bursty cells (Figure 2A). We performed a principal component analysis on a matrix of the ISI probability distributions of all neurons and found that the first three principal components (PCs; Figure 2B, bottom) explained 69% of the variance in the data. In agreement with Latuske et al. (2015), we found that, when the first two principal components were plotted against each other, the neurons formed a

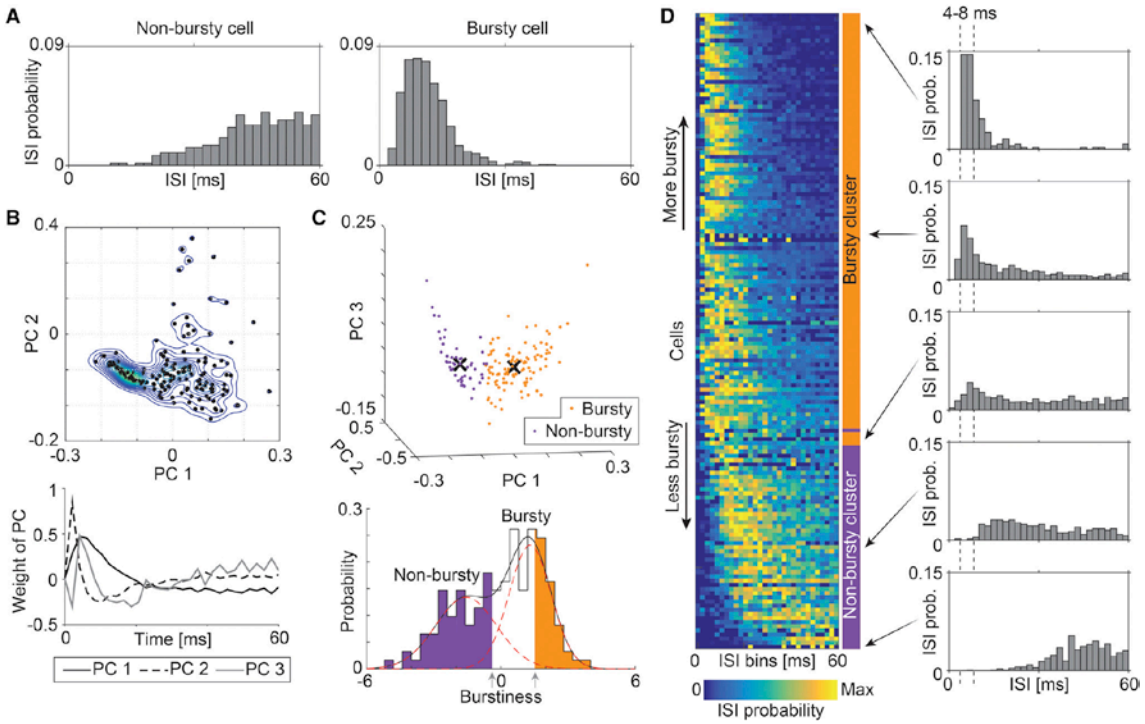

Figure 2. Classification of Bursty and Non-bursty neurons

(A) Example ISI distribution of a bursty (left) and non-bursty (right) juxtacellularly recorded neuron (bin width, 2 ms).

(B) Top: scatterplot of the first two principal components (PC1 and PC2) obtained from a PCA of ISI distributions (black dots). The neurons form a C-shaped structure, as described by Latuske et al. (2015) (2D kernel smoothed density estimate indicated by lines). Bottom: the first three PCs of the ISI histograms.

(C) Top: 3D scatterplot of the first three PCs, assigned to two clusters using a *k*-means clustering algorithm. Center-of-mass of bursty neurons (orange) and non-bursty neurons (purple) are indicated by black crosses. Bottom: projection of ISI distributions onto the optimal linear discriminant (the burstiness) of the two clusters revealed a bimodal distribution of bursty (orange) and non-bursty (purple) neurons.

(D) Left: ISI histograms of all classified neurons, sorted by burstiness (scaled to maximum probability for each neuron for visibility). Right: example ISI histograms of neurons at the edges and in the middle of the clusters. Bursty neurons tend to fire burst at 125–250 Hz (4- to 8-ms intervals).

C-shaped structure, indicative of a bimodal distribution (Figure 2B, top).

We assigned the neurons to two clusters using a *k*-means clustering algorithm on the first three principal components (Figure 2C, top). The two clusters were well separated with little overlap (Figure 2D). To assess the separation quality of the two clusters, we calculated the projection of the neurons onto Fisher's linear discriminant. We can interpret the linear discriminant as a measure of "burstiness" because it is places the cells along an axis from non-bursty to bursty based on the shape of the ISI histogram. We plotted all cells sorted according to burstiness, and, in agreement with Latuske et al. (2015), we found that bursty neurons were distinguished by a tendency to fire bursts at ~125–250 Hz (4- to 8-ms bins; Figure 2D).

To investigate differences in burstiness among cell types, we plotted the median ISI histogram of all recorded cells, resolved by cell type. The median ISI histograms of parasubicular as well as MEC L2 pyramidal neurons indicated very bursty cells (Figure 3A, top). The median ISI histograms of MEC L2 stellate and MEC L3 neurons were flat with no obvious burstiness (Figure 3A, bottom). To assess whether this difference was statistically significant, we performed two tests: one based on categorical classifications of cells as "non-bursty" and "bursty" with a guard zone (Experimental Procedures; Latuske et al., 2015) and another one where we directly compared burstiness among the neuron types.

When we compared the proportions of non-bursty, guard-zoned, and bursty cells among neuron types, we found no significant difference between parasubicular neurons and MEC L2 pyramids, which both contained predominantly bursty cells (PaS versus Pyr, bursty/guard/non-bursty: 11/11/0 versus 15/15/1, $p > 0.05$, χ^2 test; Figure 3B). We also found no difference between MEC L2 stellate cells and MEC L3 cells (Stel versus L3, bursty/guard/non-bursty: 9/25/34 versus 3/5/24, $p > 0.05$, χ^2 test; Figure 3B), which were both predominantly non-bursty. Both parasubicular neurons and MEC L2 pyramids contained significantly different proportions of bursty and non-bursty cells in comparison with both MEC L2 stellates and MEC L3 neurons (all $p < 0.001$, χ^2 tests; Figure 3B).

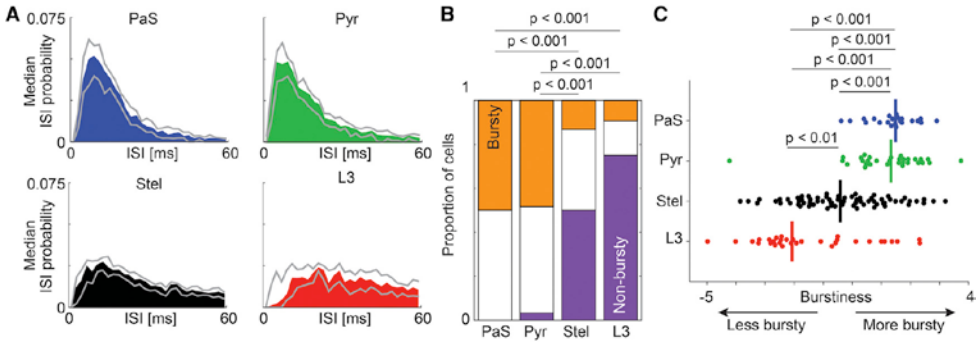

Figure 3. Burstiness in the Parasubiculum and Superficial Medial Entorhinal Cortex

(A) Median ISI histogram (bin width, 2 ms) of all neurons recorded in the PaS (blue), identified and putative MEC L2 pyramidal neurons (green), identified and putative MEC L2 stellate cells (black), and MEC L3 neurons (red). Grey lines indicate 95% confidence intervals of the median.

(B) Comparison of the proportions of the numbers of bursty (orange) and non-bursty (purple) neurons for the four different neuron types defined in (A). White areas denote cells that fall in the ambiguous zone between non-bursty and bursty (χ^2 tests of equal proportions among cell types).

(C) Comparison of the burstiness for the four different neuron types defined in (A). Vertical lines indicate medians (Mann-Whitney *U* tests).

Using a categorical classifier with a guard zone has potential problems. The width and placement of the guard zone is estimated from the bimodal fit, and thus the guard zone depends on the relative abundance of bursty and non-bursty cells, which is evidently not the same among neuron types; i.e., the guard zone might be either too wide or too narrow. The guard zone also discards information telling us whether a neuron is near the guard zone or closer to the extremes. These problems may inflate our estimated differences in burstiness among cell types. To make sure that no spurious results were imposed by the guard zone, we directly compared the burstiness of the neuron types and included all cells. In agreement with the estimations based on comparisons of the proportions, we found that the burstiness of parasubicular neurons and MEC L2 pyramids was significantly higher than the burstiness in both MEC L2 stellates and MEC L3 neurons (all $p < 0.001$, Mann-Whitney *U* tests; Figure 3C). Again, we did not find a significant difference between parasubicular neurons and MEC L2 pyramids ($p > 0.05$, Mann-Whitney *U* test; Figure 3C), but we did find that MEC L3 neurons had a significantly lower burstiness than MEC L2 stellates ($p = 0.0036$, Mann-Whitney *U* test; Figure 3C).

Thus, parasubicular neurons and MEC L2 pyramids are generally bursty, whereas MEC L2 stellates and MEC L3 neurons are generally non-bursty (Figures 3A and 3B). Furthermore, within the non-bursty neuron types, MEC L3 neurons are more strictly non-bursty than MEC L2 stellates (Figure 3C). It should be noted, however, that even though there are large and highly significant differences in burstiness among cell types, the distributions of burstiness among cell types are overlapping. For example, a minority of L2 stellate cells and L3 neurons assume firing patterns that are otherwise classically parasubicular/pyramid-like.

Our dataset includes MEC L2 neurons that were classified as putatively pyramidal or stellate based on theta strength and preferred theta phase (Tang et al., 2014a; Figure S1). We therefore also checked whether there was any correlation between burstiness and theta strength because such a correlation might introduce "artifactual" cell type differences in burstiness as a result of the classification method. First we used a statistical method. We fitted three generalized linear models to investigate whether burstiness might be related to theta strength (model 1, burstiness~strength; Figure S3A, left), putative cell type (model 2, burstiness~type; Figure S3A, middle), or both (model 3, burstiness~type + strength; Figure S3A, right). Both comparisons of the Akaike information criterion (AIC; Akaike, 1974) and likelihood ratio tests of nested models indicated that model 2 is superior to the other models (Figure S3B); i.e., the burstiness depends only on putative cell type (model 2, $P_{Type} = 0.0000076$; Figure S3C, middle) and not on theta strength (model 2 versus model 3, $p = 0.54$, likelihood ratio test; Figure S3B). Second, we plotted the burstiness among cell types twice: once where we include the classified MEC L2 cells (Figure S3D, left) and once where we only include identified MEC L2 cells (Figure S3D, right). The pattern of burstiness among cell types remained the same when we only included the identified cells (Figure S3D). We thus conclude that cell type-specific differences in burstiness are not an artifact of our classification approach.

Analysis of Spike Shape

In tetrode recordings of parasubicular and MEC L2/3 neurons, differences in spike shape have been linked to burstiness (Latuske et al., 2015) and theta phase preference of grid cells (Newman and Hasselmo, 2014). We therefore investigated whether there was a difference in spike shape among our four anatomical categories of neurons. First we removed a subset of cells for which the signal-to-noise ratio of spike waveforms was insufficient to reliably assess the spike shape. Second, we removed spikes that happened within 100 ms of the previous spike to disregard potential effects of spike shape adaptation during bursts (Experimental Procedures). In Figure 4A, we plot the remaining spike shapes (normalized for display; Experimental Procedures) for all four neuron types. We did not find any differences among neuron types in spike amplitude, peak-to-trough ratio, or spike half-width (all $p > 0.05$, Kruskal-Wallis test). This

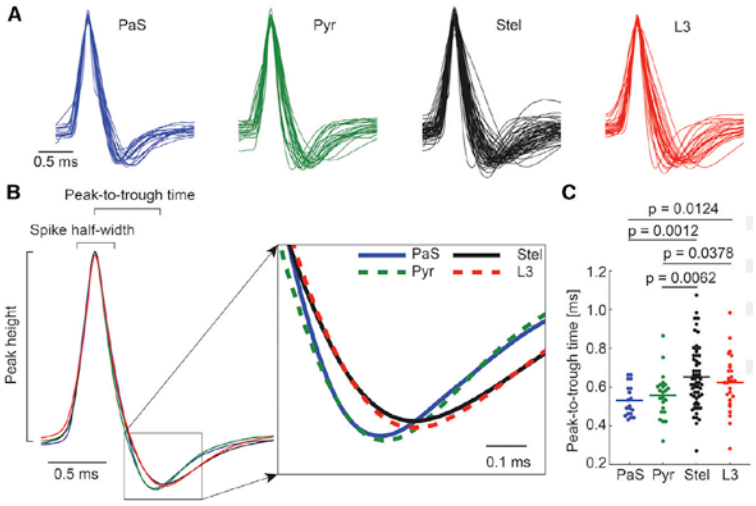

Figure 4. Spike Shapes in the Parasubiculum and Superficial Medial Entorhinal Cortex

(A) Peak-aligned and voltage-scaled spike shapes of cells in the PaS (blue), identified and putative MEC L2 pyramidal neurons (green), identified and putative MEC L2 stellate cells (black), and MEC L3 neurons (red).

(B) Left: mean spike shapes of the four neuron types in (A) show differences in peak-to-trough time. Right: close-up of the trough of the mean spike shapes.

(C) Comparison of peak-to-trough times of neurons as defined in (A) (Mann-Whitney *U* test; horizontal lines indicate means).

was expected for two reasons: Overall spike amplitude depends strongly on the particular recording pipette and relation to the soma (Gold et al., 2009), and narrow spikes and a small peak-to-trough ratio are indicative of interneurons (Mountcastle et al., 1969; Csicsvari et al., 1999), and we consider here four types of excitatory principal cells.

We noticed, however, a large variability in the repolarization phase of the cell type: Parasubicular neurons and MEC L2 pyramids contained many cells that quickly reached the trough and repolarized, whereas MEC L2 stellates and MEC L3 neurons reached the trough more slowly (Figure 4A). This tendency was also evident in the mean spike shape of the four neuron types (Figure 4B). When we compared the peak-to-trough time of the cell types, we found significant differences ($p = 0.0014$, Kruskal-Wallis test). Parasubicular neurons and MEC L2 pyramids had significantly shorter peak-to-trough times than both MEC L2 stellates and MEC L3 neurons (all $p < 0.05$, Mann-Whitney *U* test; Figure 4C).

Is Spike Shape a Reflection of Burstiness or Cell Type?

Because parasubicular neurons and MEC L2 pyramids have faster peak-to-trough times and are also the most bursty cell types, we wondered whether, as has been suggested (Latuske et al., 2015), the burstiness of the cell predicts the spike shape. Alternatively, the spike shape might simply be different among neuron types, or it might depend on neuron types as well as burstiness. To figure this out, we decided to employ a generalized linear regression approach. Because peak-to-trough time cannot assume negative values, we modeled peak-to-trough time as a gamma-distributed variable (Experimental Procedures). We selected the appropriate model using the following approach: We first modeled peak-to-trough time as a function of only burstiness (GLM1, peak-to-trough ~1 + burstiness) and found a significant dependence (ANOVA, $p_{Burstiness} = 0.0087$; Figure S4A, dashed gray line). This result is in agreement with Latuske et al. (2015). Also, when we modeled peak-to-trough time as a function of only neuron type (GLM2, peak-to-trough ~1 + type), we also found a significant dependence on neuron type (ANOVA, $p_{Type} = 0.0015$; Figure S4A, solid lines). However, when we modeled peak-to-trough time as a function of both burstiness and neuron type (GLM3, peak-to-trough ~1 + burstiness + type), we found that the dependency on type but not the dependency on burstiness remained significant (ANOVA, $p_{Burstiness} = 0.22$, $p_{Type} = 0.017$; Figure S4C). We also fitted a model where we allowed for interactions between burstiness and type (GLM4, peak-to-trough ~1 + burstiness + type + burstiness*type), where all effects became non-significant (ANOVA, all $p > 0.05$; Figure S4C). To determine which model best explains the data, we calculated the AIC of all models and found that, despite the four fitted parameters, GLM2 had the lowest AIC, indicating that the peak-to-trough time depends on neuron type, but not on burstiness (Figure S4B). Similarly, when comparing nested models, we found that GLM3 better explains the data than GLM1 ($p = 0.0023$, likelihood ratio test; Figure S4B); i.e., including neuron type as a predictor makes the model better. We did not find that GLM3 explains the data better than GLM2 ($p = 0.32$, likelihood ratio test; Figure S4B); i.e., it is unnecessary to include burstiness as a predictor in addition to neuron type. We thus infer that the differences in spike shape primarily reflect the anatomical type and not the burstiness of the neuron.

Analysis of Rhythmicity and Theta Cycle Skipping

To determine whether a neuron was theta cycle-skipping, we used a maximum likelihood estimation (MLE) of a parametric model of the ISI histogram (Climer et al., 2015; Experimental Procedures). Our dataset contained neurons that showed no theta modulation and also neurons that had strong rhythmic components (Figure 5A). For every cell, we fitted three models to the ISI distribution: a "flat" model with no rhythmic components (Figure 5A, left), a "rhythmic, non-skipping" model with a theta-rhythmic modulation of the ISI histogram (Figure 5A, middle), and a "rhythmic, cycle-skipping" model with a theta-rhythmic modulation of the ISI histogram and a second parameter introducing theta cycle skipping (i.e., a higher amplitude of every other peak in the ISI histogram; Figure 5A, right). The three fitted models were compared using the appropriate χ^2 statistic

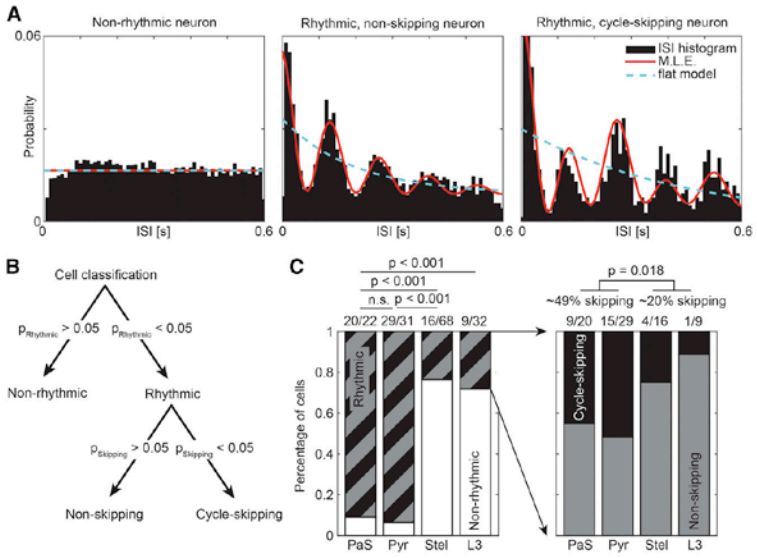

Figure 5. Theta Rhythmicity and Theta Cycle Skipping in the Parasubiculum and Superficial Medial Entorhinal Cortex

(A) Example ISI histograms (black bars) of non-rhythmic (left), rhythmic and non-skipping (middle), and rhythmic but theta cycle-skipping (right) juxtacellularly recorded neurons. Solid red lines show maximum likelihood estimates of the ISI, and dashed blue lines indicate a flat model (no rhythmicity or cycle skipping). Bin width, 1 ms.

(B) Flow diagram of the cell classification procedure. First we checked for rhythmicity and then for cycle skipping.

(C) Left: comparison of the proportions of non-rhythmic and rhythmic neurons recorded in the PaS, identified and putative MEC L2 pyramidal neurons, identified and putative MEC L2 stellate cells, and MEC L3 neurons. Right: comparison of the proportions of rhythmic, non-cycle-skipping and rhythmic, theta cycle-skipping neurons recorded in the four neuron types. The generally rhythmic cell types (PaS and Pyr) have a larger proportion of theta cycle-skipping neurons than the generally non-rhythmic cell types (Stel and L3).

(calculated from the maximum log likelihood of the models) to generate two p values: $p_{rhythmic}$ (comparing the flat and the rhythmic, non-skipping models) and $p_{skipping}$ (comparing the rhythmic, non-skipping and the rhythmic, cycle-skipping models). The cells were classified using a two-level classification (Figure 5B): First, we determined whether a cell was "rhythmic" ($p_{rhythmic} < 0.05$) or "non-rhythmic" ($p_{rhythmic} > 0.05$). Then we classified the rhythmic cells as either rhythmic, cycle-skipping ($p_{skipping} < 0.05$) or rhythmic, non-skipping ($p_{skipping} > 0.05$).

Using the MLE approach, we found that parasubicular neurons and MEC L2 pyramids were overwhelmingly rhythmic (~93%; PaS, 20/22; Pyr, 29/31; Figure 5C, left). MEC L2 stellates and MEC L3 neurons were rarely rhythmic (~26%; Stel, 16/68; L3, 9/32), both significantly less rhythmic than both parasubicular neurons and MEC L2 pyramids (all $p < 0.001$, χ^2 tests; Figure 5C, left). This is in agreement with previous observations in which evaluated spike train rhythmicity of cell types using a "theta index" was used (Ray et al., 2014; Tang et al., 2014a, 2016). We found that the generally rhythmic cell types were also significantly more likely to also be theta cycle-skipping than the generally non-rhythmic cell types ($p = 0.018$, mixed-effects logistic regression; Figure 5C, right; Experimental Procedures): Approximately 49% of the rhythmic parasubicular neurons and rhythmic MEC L2 pyramids were also theta cycle-skipping (PaS, 9/20; Pyr, 15/29; Figure 5C, right). Of the MEC L2 stellates and MEC L3 neurons, which were classified as rhythmic using the MLE approach, only ~20% were also theta cycle-skipping (Stel, 4/16; L3, 1/9; Figure 5C, right).

Our dataset includes MEC L2 neurons that were classified as putatively pyramidal or stellate based on theta strength and preferred theta phase (Tang et al., 2014a; Figure S1). Obviously, we expect a correlation between the theta rhythmicity (which is calculated from the ISI distribution) and the theta strength (locking to the LFP theta rhythm). However, the MLE approach of Climer et al. (2015) returns a p value of the rhythmicity per cell and is sensitive to very low amounts of rhythmicity, which could potentially have been present in, e.g., putative stellates with a low locking strength and locking to the peak of the LFP theta rhythm (Figure S1; Climer et al., 2015; Tang et al., 2014a). More importantly, our classification procedure considers simply strength of locking to the local LFP, and there is no way of distinguishing a simply theta-rhythmic cell from a rhythmic and cycle-skipping cell based on theta strength because they might show equally strong locking. To be sure that the cell type differences were not an artifact of including the classified cells, we plotted the burstiness among cell types twice: once where we included the classified MEC L2 cells (Figure S5A, left) and once where we only included identified MEC L2 cells (Figure S5A, right). The proportions among cell types remained the same when restricting the analysis to identified cells only (Figure S5A).

Single Run Analysis of Phase Precession

To compare the magnitude of phase precession among cell types at the single-run level, we first selected single runs of high firing based on the firing rate (Figures 6A, top, and 6B; Experimental Procedures). From these single runs, we determined the slope and range of phase precession by a circular-linear fit of time and theta phase angle of the spikes in each run (Figure 6A, bottom; Experimental Procedures). Figure 6C shows example single runs from example cells of the four neuron types. The example MEC L2 stellate and L3 neurons have steep phase precession slopes and cover larger ranges of theta phase angles during a single run. In contrast, the example parasubicular neuron and MEC L2 pyramid only weakly phase-precess. Across the population, we found the same result: First, identified and putative MEC L2 stellate and L3 neurons had approximately 3-fold steeper phase precession slopes than parasubicular neurons and identified and putative MEC L2 pyramids (Figure 6D;

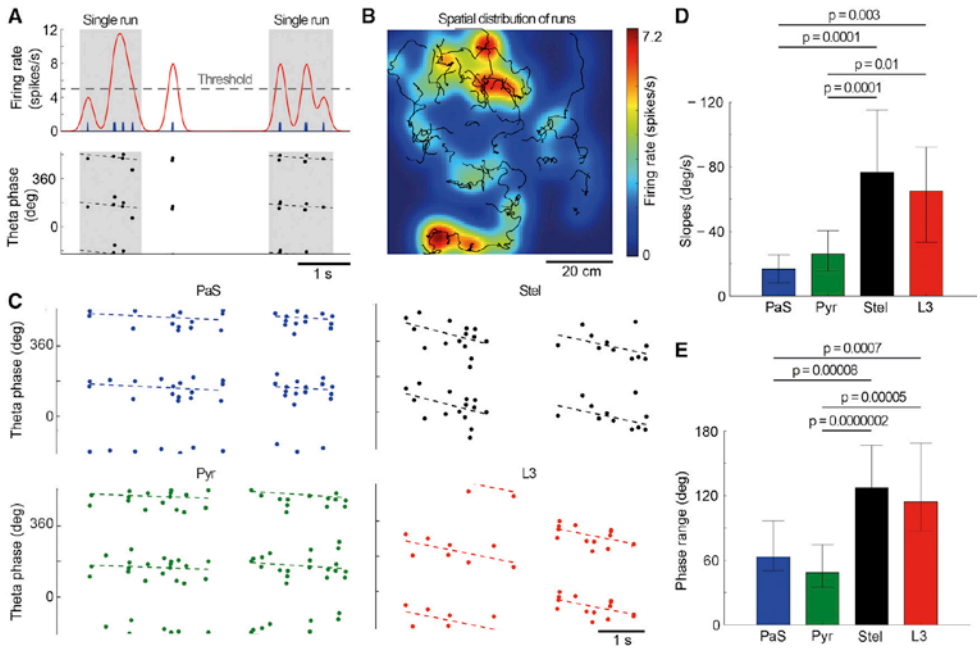

Figure 6. Phase Precession Slopes and Ranges in the Parasubiculum and Superficial Medial Entorhinal Cortex

(A) Detection of single runs. Top: firing rate (red line) is estimated by convolving spikes (blue ticks) with a Gaussian kernel. Detected runs are indicated by gray shading. Bottom: theta phase of spikes as a function of time (black dots). Phase precession slopes and ranges of single runs are estimated by circular-linear fits (dashed lines).

(B) Temporally defined single runs (black lines) match regions of elevated firing rate (color coded). Data are from the neuron shown in (A).

(C) Examples of single-run phase precession for parasubicular (blue dots), identified MEC L2 pyramidal (green dots), identified MEC L2 stellate (black dots), and MEC L3 (red dots) neurons. Each dot represents the theta phase angle of a spike as a function of time. Dashed lines depict circular-linear fits.

(D) Median single-run phase precession slopes for the four neuron types defined in (C). Single-run slopes are significantly larger in MEC L2 stellate and MEC L3 neurons than in parasubicular and MEC L2 pyramidal neurons (whiskers indicate 95% confidence intervals of the median).

(E) Median single-run phase precession ranges among the four neuron types as defined in (C) and (D). Single-run phase ranges are significantly larger in MEC L2 stellate and MEC L3 neurons than in parasubicular and MEC L2 pyramidal neurons (whiskers indicate 95% confidence intervals of the median).

median slopes: PaS/Pyr/Stel/L3 = −16.7/−25.9/−76.7/−64.8 degrees/s; p(PaS versus Stel) = 0.0001; p(PaS versus L3) = 0.003; p(Pyr versus Stel) = 0.0001; p(Pyr versus L3) = 0.01; Mann-Whitney *U* tests). Second, identified and putative MEC L2 stellate and L3 neurons covered a much larger range of theta phase angles per run than parasubicular neurons and identified and putative MEC L2 pyramids (approximately 2-fold; Figure 6E; median ranges: PaS/Pyr/Stel/L3 = 63.2/48.7/127.5/114.2 degrees; p(PaS versus Stel) = 0.00008; p(PaS versus L3) = 0.0007; p(Pyr versus Stel) = 0.0000002; p(Pyr versus L3) = 0.00005; Mann-Whitney *U* tests). We did not find any differences in the circular-linear correlation coefficient among the cell types (p = 0.38, Kruskal-Wallis test).

DISCUSSION

We used advanced statistical techniques to tease apart how differences in burstiness, spike shape, theta modulation (rhythmicity, locking, skipping), and phase precession map onto regular spiking layer 3 medial entorhinal neurons, layer 2 medial entorhinal pyramidal neurons, layer 2 medial entorhinal stellate neurons, and parasubicular regular spiking cells.

Cell Type-Specific Differences and Their Origin

We found significant differences in spike shape, burstiness, theta modulation (rhythmicity, locking, cycle skipping, phase precession), and theta phase precession between the four groups of cells investigated. Thus, our data suggest that cell type is a major determinant of discharge patterns in the rat parasubiculum and superficial medial entorhinal cortex. Although our data emphasize the significance of cell types, the discharge patterns we observed do not directly match what is expected based on the analysis of intrinsic properties of these neurons in vitro. In vitro recordings of parasubicular neurons have suggested an intrinsic disposition for theta rhythmicity (Glasgow and Chapman, 2008). It is known that in vitro measurements of L2 MEC cell properties are very sensitive to recording conditions (Alonso and Klink, 1993; Pastoll et al., 2012). However, MEC L2 stellates often display some intrinsic burstiness in vitro (Alonso and Klink, 1993; Pastoll et al., 2012; Alessi et al., 2016; Fuchs et al., 2016), but they are generally not very bursty in vivo (Ray

et al., 2014; Figure 2). Thus, it is probably incorrect to assume that bursty cells recorded extracellularly in the superficial MEC and the parasubiculum are MEC L2 stellates (Newman and Hasselmo, 2014; Latuske et al., 2015) because we show that bursty cells are more likely to be MEC L2 pyramids or parasubicular neurons.

Cell Type Specificity of Phase Precession

Although phase precession is arguably the most intensely studied example of temporal coding in the brain, its underlying mechanism is still a matter of debate. Parasubicular neurons, which show only weak phase precession, project to pyramidal cells in MEC L2 (Tang et al., 2016). Also, these MEC L2 pyramidal cells express only a low degree of phase precession. Conversely, stellate cells in MEC L2 and pyramidal cells in MEC L3 phase precess with steep slopes. The latter finding is somewhat surprising because it challenges the long-held belief that cells in MEC L3 do not phase-precess (Hafting et al., 2008; Mizuseki et al., 2009). However, differences in methodology might reconcile the different findings. Previous studies investigated MEC L3 phase precession in pooled run data. In contrast to that, we analyzed phase precession in single runs (Schmidt et al., 2009). We argue that the single-run approach is more appropriate because the animal needs to process information online and does not have the opportunity to pool over trials. Our finding of substantial MEC L3 phase precession is in line with a previous single-run account (Reifenstein et al., 2014). MEC L2 stellate cells project to the dentate gyrus, whereas MEC L2 pyramidal cells send output to CA1 (Varga et al., 2010; Kitamura et al., 2014; Ray et al., 2014). Because MEC L2 pyramidal cells show only weak phase precession, it seems unlikely that they substantially contribute to CA1 phase precession. Therefore, CA1 either generates phase precession de novo or inherits phase-precessing inputs via the strongly precessing stellate cells in MEC L3 (Jaramillo et al., 2014).

Whether Cell Types Show Specific Spatial Discharge Patterns Is Currently Unresolved

It is presently unknown how the functional categories (grid cells, border cells, speed cells, cue cells, etc.) map onto the anatomy. For example, it is unknown whether MEC L2 grid cells are predominantly pyramidal cells (Tang et al., 2014a) or stellate cells (Domnisoru et al., 2013) or whether they show no preference for either cell type (Sun et al., 2015). Similarly, some authors have reported that about a third to half of MEC L3 neurons are grid cells (Sargolini et al., 2006; Boccara et al., 2010), whereas others have estimated that if L3 grid cells exists, then they must be rare (~1%; Tang et al., 2015).

Relation between Temporal Spiking Features and Spatial Responses

Parasubicular neurons and MEC L2 pyramids are more bursty, have narrower spikes, and are more likely to be theta-rhythmic, theta-locked, and theta cycle-skipping than MEC L2 stellates and MEC L3 neurons. These differences remain even when we statistically control for interactions between spike shape, burstiness, and rhythmicity. Some studies have tried to elucidate the grid cell generation mechanism by characterizing the firing properties of the entorhinal network. From these studies we know that grid cells are bursty whereas border cells are not (Newman and Hasselmo 2014; Latuske et al., 2015). It has also been shown that theta cycle skipping is somehow necessary for maintaining grid cell firing (Brandon et al., 2013). In agreement with Tang et al. (2014a, 2016), we conclude that, based on burstiness and theta cycle skipping, parasubicular neurons and MEC L2 pyramids are likely to play a key role in generating grid cell activity in the parasubiculum and superficial medial entorhinal cortex.

Cell Type-Specific Differences in Spike Shape

In line with the differences in temporal discharge patterns, we observed that parasubicular and MEC L2 pyramidal cells had shorter spike durations than MEC L2 stellates and MEC L3 neurons. Several previous studies have noticed significant differences between MEC L2 pyramidal and MEC L2 stellate cells, most notably, that stellate cells have larger depolarizing afterpotentials (Alonso and Klink 1993; Alessi et al., 2016; Fuchs et al., 2016). In in vivo recordings, it was generally observed that stellate cells had a shorter spike duration than pyramidal cells (Alonso and Klink, 1993). Interestingly, however, it was also found that the spike duration of both pyramidal and stellate cells varied depending on the depolarizing current pulse (Alonso and Klink, 1993). Thus, the juxtacellularly observed differences in spike shape are probably not primarily a reflection of differences in intrinsic cell properties. Cell type differences in spike duration are statistically significant. However, the distributions of spike durations are largely overlapping (Figure 4C), probably precluding a classification of extracellularly recorded MEC L2 regular spiking neurons into pyramidal and stellate cells based purely on spike shape.

Do Layer 3 Cells and Layer 2 Stellate Cells, on One Hand, and Parasubiculum and Layer 2 Pyramids, on the Other Hand, Form Two Distinct Processing Systems?

We observed a strong similarity between spike shapes and firing patterns of parasubicular neurons and MEC L2 pyramids. These two neuron groups were different in spike shapes and firing patterns from layer 3 cells and layer 2 stellate cells, which were similar to each other, however. It turns out that these neurons groups share even more similarities and differences. Parasubicular axons specifically target patches of MEC L2 pyramidal cells (Tang et al., 2016), which might be a pathway for head-directional information from the medial septum to reach the grid cell system (Winter et al., 2015; Unal et al., 2015; Tang et al., 2016). L3 cells and layer 2 stellate cells provide a massive direct (L3) and indirect input to the hippocampus, whereas projections from both layer 2 pyramids and the parasubiculum are minor or absent (Varga et al., 2010; Ray et al., 2014; Kitamura et al., 2014). Thus, analysis of spike shapes and firing patterns, direct connectivity, and projection targets supports the distinction of layer 3 cells and layer 2 stellate cells on one hand and parasubiculum and layer 2 pyramids on the other hand as two distinct processing systems.

Possible Anatomical Origin of Firing Patterns

Layer 2 pyramids and parasubicular cells are anatomically similar. They both express wolframin (Ray and Brecht, 2016),

and, in the early development stages, they also express calbindin (Ray and Brecht, 2016). Likewise, layer 3 neurons and layer 2 stellate cells also have an anatomical likeliness in their protein expression profile, with both expressing Reelin in adult rats (Ray and Brecht, 2016). This might allude to the electrophysiological and functional characteristics of these two groups being perhaps somewhat genetically determined, with the protein expression profiles of these respective cell groups shaping their inputs and outputs.

Grid Cell Models

Our results will constrain future modeling of network activity in the hippocampus and para-hippocampal cortices. Because different anatomical cell types have different projection patterns, burstiness, and theta rhythmicity/skipping might be passed on differentially to hippocampal subfields like the dentate gyrus, which receives massive MEC L2 stellate input (Varga et al., 2010), and CA1, which receives some MEC L2 pyramidal input (Kitamura et al., 2014). Some grid cell models suggest that grid cells are generated by network mechanisms where a large number of similar (stellate) cells self-organize to generate symmetrical firing patterns either via continuous attractors or via oscillatory interference (for reviews, see Giocomo et al., 2011; Zilli 2012). Others have suggested mechanisms based on anatomical microcircuits (Brecht et al., 2013). Our results do not resolve this question, but we add to the picture that the network mechanism distributes firing patterns differentially according to cell type.

Conclusions

We conclude that the anatomical identity of the neuron is a strong determinant of the firing pattern. Analysis of burstiness, theta cycle skipping, and phase precession jointly suggest similarities between layer 3 cells and layer 2 stellate cells on one hand and layer 2 pyramidal cells and parasubicular cells on the other hand.

EXPERIMENTAL PROCEDURES

All experimental procedures were performed according to the German guidelines on animal welfare under the supervision of local ethics committees.

Juxtacellular Recordings and Immunohistochemistry

In this paper, we analyzed a dataset of juxtacellular recordings from the superficial medial entorhinal cortex and the parasubiculum that we have published previously (Ray et al., 2014; Tang et al., 2014a, 2015, 2016). Detailed descriptions of recording procedures (Pinault, 1996; Lee et al., 2006; Herfst et al., 2012; Tang et al., 2014b), quality control (Joshua et al., 2007), tissue preparation, immunohistochemistry, and image acquisition (Naumann et al., 2016; Ray and Brecht, 2016), can be found in these papers and in the Supplemental Experimental Procedures.

Classification of Non-identified Layer 2 Neurons

In addition to labeled cells, we included a number of unlabeled, regularly spiking cells from MEC L2 in our analysis. These cells were assigned as either putatively calbindin-positive (pCb+) pyramidal cells or putatively calbindin-negative (pCb−) stellate cells based on their theta strength and preferred theta phase angle using the classification approach of Tang et al. (2014a); i.e., based on the theta strength and preferred theta phase angle of spiking activity. As in Tang et al. (2014a), we used a 0.1 guard zone and found that the cells were well separated with no cells in the guard zone (Figure S1). In the manuscript, we refer to the pooled groups of identified and putative calbindin-positive pyramidal cells simply as "MEC L2 pyramids" and identified putative calbindin-negative stellate cells as "MEC L2 stellates." When we show example cells of the four cell types (Figures 1A and 1B and 6A–6C), we show only identified Cb+/− cells. In Figures S3 and S5, we show analysis of a dataset where we only included identified cells.

Analysis of Burstiness

To determine whether a neuron was discharging in a bursty pattern, we analyzed the ISI histogram using a similar approach as Latuske et al. (2015). ISIs below 60 ms were binned in 2-ms bins and normalized to area = 1 to generate a probability distribution (Figure 2A). A principle component analysis (PCA) was done on a matrix of the ISI probability distribution of all neurons ("pca" in MATLAB, MathWorks). For plotting, the density of cells in this space was estimated with a 2D Gaussian kernel density estimator ("kde2d"; Botev et al., 2010). The neurons were assigned to two clusters using a *k*-means clustering algorithm on the first three principal components ("kmeans"; MATLAB; Figure 2C, top). To assess the separation quality of the two clusters, we calculated the projection of the neurons onto Fisher's linear discriminant (the burstiness, using "LDA" from Scikit-Learn in Python) and found that the two clusters (non-bursty and bursty) were well separated with little overlap (Figure 2C, top). To check whether the distribution of burstiness was bimodal, thus reflecting two distinct classes of ISI histograms, we fitted probability density functions for Gaussian mixture models with between one and three underlying Gaussians and compared the models using the Akaike information criterion (Akaike 1974; AIC from "gmdistribution.fit" in MATLAB). A bimodal distribution best explained the data ($AIC_{unimodal}$ = 622.7, $AIC_{bimodal}$ = 609.6, $AIC_{trimodal}$ = 614.7). Based on the mean and variance of the two Gaussian distributions underlying the observed distribution of burstiness (Figure 2C, bottom, dashed red lines), we estimated that excluding cells where $-0.4 <$ burstiness < 1.5 would yield >95% correct labeling of non-bursty and bursty neurons in the non-bursty and bursty categories and used this as a guard zone (Latuske et al., 2015).

Analysis of Spike Shape

During recording, the juxtacellular traces were digitized at 20 kHz. To analyze the spike shapes, we first zero-phased high pass-filtered the raw signal at 100 Hz with a finite impulse response filter of order 2^8 ("fir1" in MATLAB). The spike times were detected by thresholding the filtered signal and saving each threshold crossing ± 2.5 ms. Spike sorting based on the first principal components was performed on these 5-ms snippets to remove any threshold crossings because of artifacts in the signal (Tang et al., 2014a). To align the spike shapes optimally after spike sorting, the 5-ms snippets were oversampled at five times their original sampling rate using a spline interpolation ("interp1" in MATLAB) and were then aligned to the peak sample. To ensure that we were only analyzing shapes free of distortions because of drift of the pipette and that the spikes were well above the noise floor, we only analyzed spikes for which the spike amplitude was in the top 60^{th}-90^{th} percentile and where the *Z* score of the spike amplitude was >17. The noise floor was defined as the mean of the first and last 0.5 ms of each 5-ms spike snippet. We also removed any spikes where there was another spike in the preceding 100 ms. In the four cell groups, there were only a few cells where the spikes did not have sufficient quality to analyze the spike shape, and we could analyze 19/22 parasubicular cells, 24/31 MEC L2 pyramidal cells, 58/68 MEC L2 stellate cells, and 27/32 MEC L3 cells. We calculated the mean spike shape of every cell and determined the spike features from these traces. For plotting the comparison between cells and for illustrating the differences in peak-to-trough time (Figures 4A and 4B), we normalized the spike shape by subtracting the noise floor, dividing the mean spike by the peak-to-trough height, and setting the peak height to 1.

Analysis of Theta Rhythmicity and Theta Cycle Skipping

To determine whether a neuron was rhythmic and theta cycle-skipping, we used an MLE of a parametric model of the ISI histogram ("mle_rhythmicity"; Climer et al., 2015). For every cell, we fitted three models to the ISI distribution: a flat model with no rhythmic components, a rhythmic, non-skipping model with a rhythmic modulation of the ISI histogram, and a rhythmic, cycle-skipping

model with a rhythmic modulation of the ISI histogram and a second parameter introducing theta cycle skipping (i.e., a higher amplitude of every other peak in the ISI histogram). When fitting the models, we searched for a rhythmic component with a theta frequency between 5 and 13 Hz and for cycle skippings >0.01. The three fitted models were compared using the appropriate χ^2 statistic (calculated from the maximum log likelihood of the models) to generate two p values: $p_{rhythmic}$ (comparing the flat and the rhythmic, non-skipping models) and $p_{skipping}$ (comparing the rhythmic, non-skipping and the rhythmic, cycle-skipping models). The cells were classified using a two-level classification (Figure 5B). First we determined whether a cell was rhythmic ($p_{rhythmic} < 0.05$) or non-rhythmic ($p_{rhythmic} > 0.05$). Then we classified the rhythmic cells as either rhythmic, cycle-skipping ($p_{skipping} < 0.05$) or rhythmic, non-skipping ($p_{skipping} > 0.05$).

To statistically assess whether theta cycle skipping cells were rarer among rhythmic cells in the generally non-rhythmic cell types (MEC L2 stellates and MEC L3 neurons) than in the generally rhythmic cell types (parasubicular neurons and MEC L2 pyramids), we fitted a mixed-effects logistic regression. We constructed a vector, isGenRhytm (which takes the value 1 for parasubicular neurons and MEC L2 pyramids and the value 0 for MEC L2 stellates and MEC L3 neurons). We also constructed a vector type that simply dummy-coded the four neuron types from 1, 2, 3, and 4. We dummy-coded when the neuron was theta cycle-skipping in the vector isSkipping. We then modeled the probability of being rhythmic as a function of being generally rhythmic while controlling for the different number of cells in the four categories of neurons: "isSkipping~isGenRhytm + (1|type)" using "fitglme" in MATLAB (Aarts et al., 2014).

In addition to the MLE approach, we also calculated the theta strength and preferred theta phase of every cell. The local field potential was bandpass-filtered in the theta range (4–12 Hz), and a Hilbert transform was used to determine the instantaneous phase of the theta wave for every spike. The theta locking strength and the preferred phase angle were calculated as the modulus and argument of the Rayleigh average vector of the theta phase at all spike times.

Statistical Modeling

Statistical modeling (generalized linear models) was done in MATLAB using the "glmefit" function. We modeled burstiness as a function of theta strength as a normally distributed variable (Figures S3A–S3C). We modeled the peak-to-trough time as a gamma-distributed variable with a reciprocal link function in MATLAB because it can only assume positive values (Figures S4A–S4C). To compare models, we either calculated and compared the AIC (Akaike, 1974) or, in the case of nested models, calculated the p value from likelihood ratio tests. In the manuscript, we describe all statistical models using standard Wilkinson notation (Wilkinson and Rogers, 1973).

Analysis of Phase Precession

To identify coherent periods of elevated firing ("single runs"), we follow a previously applied strategy based on the temporal structure of the recorded spike trains (Reifenstein et al., 2016). Briefly, we convolved the spike train with a Gaussian kernel to estimate the instantaneous firing rate. We then used a firing rate threshold to locate periods of elevated firing (Figure 6A, top). For each of the single runs, the times and theta phases of all spikes were used to assess phase precession. We quantified phase precession by calculating the slope, phase range, and circular-linear correlation coefficient of the circular-linear regression line (Figure 6A, bottom; Kempter et al., 2012; Reifenstein et al., 2012, 2014, 2016).

SUPPLEMENTAL INFORMATION

Supplemental Information includes Supplemental Experimental Procedures and five figures and can be found with this article online at http://dx.doi.org/10.1016/j.celrep.2016.06.057.

AUTHOR CONTRIBUTIONS

C.L.E. analyzed burstiness, spike shape, theta rhythmicity, and cycle skipping. E.T.R. analyzed phase precession. Q.T. and A.B. provided access to juxtacellular data and assisted with data analysis. S.R. performed immunohistochemistry and microscopy. S.S., R.K., and M.B. provided expertise and feedback on the analysis and supervised the project. C.L.E. conceived the study and wrote the first version of the manuscript. All authors provided feedback and contributed to writing the manuscript.

ACKNOWLEDGMENTS

This work was supported by the Humboldt Universität zu Berlin, BCCN Berlin (German Federal Ministry of Education and Research BMBF, Förderkennzeichen 01GQ1001A, 01GQ0901, 01GQ1403, and 01GQ0972), NeuroCure, the Neuro-Behavior ERC grant, and the Gottfried Wilhelm Leibniz Prize of the DFG. We thank Andreea Neukirchner, Juliane Steger, and Undine Schneeweiß for technical assistance.

Received: March 30, 2016
Revised: May 4, 2016
Accepted: June 12, 2016
Published: July 14, 2016

REFERENCES

Aarts, E., Verhage, M., Veenvliet, J.V., Dolan, C.V., and van der Sluis, S. (2014). A solution to dependency: using multilevel analysis to accommodate nested data. Nat. Neurosci. *17*, 491–496.

Akaike, H. (1974). A new look at the statistical model identification. IEEE Trans. Automat. Contr. *19*, 716–723.

Alessi, C., Raspanti, A., and Magistretti, J. (2016). Two Distinct Types of Depolarizing Afterpotentials are Differentially Expressed in Stellate and Pyramidal-like Neurons of Entorhinal-Cortex Layer II. Hippocampus.

Alonso, A., and Klink, R. (1993). Differential electroresponsiveness of stellate and pyramidal-like cells of medial entorhinal cortex layer II. J. Neurophysiol. *70*, 128–143.

Boccara, C.N., Sargolini, F., Thoresen, V.H., Solstad, T., Witter, M.P., Moser, E.I., and Moser, M.B. (2010). Grid cells in pre- and parasubiculum. Nat. Neurosci. *13*, 987–994.

Botev, Z.I., Grotowaki, J.F., and Kroese, D.P. (2010). Kernel density estimation via diffusion. Ann. Stat. *38*, 2916–2957.

Brandon, M.P., Bogaard, A.R., Schultheiss, N.W., and Hasselmo, M.E. (2013). Segregation of cortical head direction cell assemblies on alternating θ cycles. Nat Neurosci. *16*, 739–748.

Brecht, M., Ray, S., Burgalossi, A., Tang, Q., Schmidt, H., and Naumann, R. (2013). An isomorphic mapping hypothesis of the grid representation. Philos. Trans. R. Soc. Lond. B Biol. Sci. *369*, 20120521.

Burgalossi, A., Herfst, L., von Heimendahl, M., Förste, H., Haskic, K., Schmidt, M., and Brecht, M. (2011). Microcircuits of functionally identified neurons in the rat medial entorhinal cortex. Neuron *70*, 773–786.

Burgess, N. (2014). The 2014 Nobel Prize in Physiology or Medicine: a spatial model for cognitive neuroscience. Neuron *84*, 1120–1125.

Climer, J.R., DiTullio, R., Newman, E.L., Hasselmo, M.E., and Eden, U.T. (2015). Examination of rhythmicity of extracellularly recorded neurons in the entorhinal cortex. Hippocampus *25*, 460–473.

Csicsvari, J., Hirase, H., Czurkó, A., Mamiya, A., and Buzsáki, G. (1999). Oscillatory coupling of hippocampal pyramidal cells and interneurons in the behaving Rat. J. Neurosci. *19*, 274–287.

Domnisoru, C., Kinkhabwala, A.A., and Tank, D.W. (2013). Membrane potential dynamics of grid cells. Nature *495*, 199–204.

Fuchs, E.C., Neitz, A., Pinna, R., Melzer, S., Caputi, A., and Monyer, H. (2016). Local and Distant Input Controlling Excitation in Layer II of the Medial Entorhinal Cortex. Neuron *89*, 194–208.

Giocomo, L.M., Moser, M.-B., and Moser, E.I. (2011). Computational models of grid cells. Neuron *71*, 589–603.

Glasgow, S.D., and Chapman, C.A. (2008). Conductances mediating intrinsic theta-frequency membrane potential oscillations in layer II parasubicular neurons. J. Neurophysiol. *100*, 2746–2756.

Gold, C., Girardin, C.C., Martin, K.A., and Koch, C. (2009). High-amplitude positive spikes recorded extracellularly in cat visual cortex. J. Neurophysiol. *102*, 3340–3351.

Hafting, T., Fyhn, M., Molden, S., Moser, M.B., and Moser, E.I. (2005). Microstructure of a spatial map in the entorhinal cortex. Nature *436*, 801–806.

Hafting, T., Fyhn, M., Bonnevie, T., Moser, M.B., and Moser, E.I. (2008). Hippocampus-independent phase precession in entorhinal grid cells. Nature *453*, 1248–1252.

Herfst, L., Burgalossi, A., Haskic, K., Tukker, J.J., Schmidt, M., and Brecht, M. (2012). Friction-based stabilization of juxtacellular recordings in freely moving rats. J. Neurophysiol. *108*, 697–707.

Jaramillo, J., Schmidt, R., and Kempter, R. (2014). Modeling inheritance of phase precession in the hippocampal formation. J. Neurosci. *34*, 7715–7731.

Jeewajee, A., Barry, C., Douchamps, V., Manson, D., Lever, C., and Burgess, N. (2013). Theta phase precession of grid and place cell firing in open environments. Philos. Trans. R Soc. Lond. B Biol. Sci. *369*, 20120532.

Joshua, M., Elias, S., Levine, O., and Bergman, H. (2007). Quantifying the isolation quality of extracellularly recorded action potentials. J. Neurosci. Methods *163*, 267–282.

Kempter, R., Leibold, C., Buzsáki, G., Diba, K., and Schmidt, R. (2012). Quantifying circular-linear associations: hippocampal phase precession. J. Neurosci. Methods *207*, 113–124.

Kinkhabwala AA, Aronov D, Tank DW (2015) Visual cue-related activity of MEC cells during navigation in virtual reality. Program No. 632.21/CC2. 2015 Neuroscience Meeting Planner. Washington, DC: Society for Neuroscience, 2015. Online.

Kitamura, T., Pignatelli, M., Suh, J., Kohara, K., Yoshiki, A., Abe, K., and Tonegawa, S. (2014). Island cells control temporal association memory. Science *343*, 896–901.

Koenig, J., Linder, A.N., Leutgeb, J.K., and Leutgeb, S. (2011). The spatial periodicity of grid cells is not sustained during reduced theta oscillations. Science *332*, 592–595.

Kropff, E., Carmichael, J.E., Moser, M.B., and Moser, E.I. (2015). Speed cells in the medial entorhinal cortex. Nature *523*, 419–424.

Latuske, P., Toader, O., and Allen, K. (2015). Interspike Intervals Reveal Functionally Distinct Cell Populations in the Medial Entorhinal Cortex. J. Neurosci. *35*, 10963–10976.

Lee, A.K., Manns, I.D., Sakmann, B., and Brecht, M. (2006). Whole-cell recordings in freely moving rats. Neuron *51*, 399–407.

Lever, C., Burton, S., Jeewajee, A., O'Keefe, J., and Burgess, N. (2009). Boundary vector cells in the subiculum of the hippocampal formation. J. Neurosci. *29*, 9771–9777.

Mizuseki, K., Sirota, A., Pastalkova, E., and Buzsáki, G. (2009). Theta oscillations provide temporal windows for local circuit computation in the entorhinal-hippocampal loop. Neuron *64*, 267–280.

Mountcastle, V.B., Talbot, W.H., Sakata, H., and Hyvärinen, J. (1969). Cortical neuronal mechanisms in flutter-vibration studied in unanesthetized monkeys. Neuronal periodicity and frequency discrimination. J. Neurophysiol. *32*, 452–484.

Naumann, R.K., Ray, S., Prokop, S., Las, L., Heppner, F.L., and Brecht, M. (2016). Conserved size and periodicity of pyramidal patches in layer 2 of medial/caudal entorhinal cortex. J. Comp. Neurol. *524*, 783–806.

Newman, E.L., and Hasselmo, M.E. (2014). Grid cell firing properties vary as a function of theta phase locking preferences in the rat medial entorhinal cortex. Front. Syst. Neurosci. *8*, 193.

Pastoll, H., Ramsden, H.L., and Nolan, M.F. (2012). Intrinsic electrophysiological properties of entorhinal cortex stellate cells and their contribution to grid cell firing fields. Front. Neural Circuits *6*, 17.

Pinault, D. (1996). A novel single-cell staining procedure performed in vivo under electrophysiological control: morpho-functional features of juxtacellularly labeled thalamic cells and other central neurons with biocytin or Neurobiotin. J. Neurosci. Methods *65*, 113–136.

Ray, S., and Brecht, M. (2016). Structural development and dorsoventral maturation of the medial entorhinal cortex. eLife *5*, 13343.

Ray, S., Naumann, R., Burgalossi, A., Tang, Q., Schmidt, H., and Brecht, M. (2014). Grid-layout and theta-modulation of layer 2 pyramidal neurons in medial entorhinal cortex. Science *343*, 891–896.

Reifenstein, E.T., Kempter, R., Schreiber, S., Stemmler, M.B., and Herz, A.V. (2012). Grid cells in rat entorhinal cortex encode physical space with independent firing fields and phase precession at the single-trial level. Proc. Natl. Acad. Sci. USA *109*, 6301–6306.

Reifenstein, E., Stemmler, M., Herz, A.V.M., Kempter, R., and Schreiber, S. (2014). Movement dependence and layer specificity of entorhinal phase precession in two-dimensional environments. PLoS ONE *9*, e100638.

Reifenstein, E.T., Ebbesen, C.L., Tang, Q., Brecht, M., Schreiber, S., and Kempter, R. (2016). Cell-Type Specific Phase Precession in Layer II of the Medial Entorhinal Cortex. J. Neurosci. *36*, 2283–2288.

Sargolini, F., Fyhn, M., Hafting, T., McNaughton, B.L., Witter, M.P., Moser, M.B., and Moser, E.I. (2006). Conjunctive representation of position, direction, and velocity in entorhinal cortex. Science *312*, 758–762.

Schmidt, R., Diba, K., Leibold, C., Schmitz, D., Buzsáki, G., and Kempter, R. (2009). Single-trial phase precession in the hippocampus. J. Neurosci. *29*, 13232–13241.

Sheffield, M.E.J., and Dombeck, D.A. (2015). The binding solution? Nat. Neurosci. *18*, 1060–1062.

Solstad, T., Boccara, C.N., Kropff, E., Moser, M.B., and Moser, E.I. (2008). Representation of geometric borders in the entorhinal cortex. Science *322*, 1865–1868.

Sun, C., Kitamura, T., Yamamoto, J., Martin, J., Pignatelli, M., Kitch, L.J., Schnitzer, M.J., and Tonegawa, S. (2015). Distinct speed dependence of entorhinal island and ocean cells, including respective grid cells. Proc. Natl. Acad. Sci. USA *112*, 9466–9471.

Tang, Q., Burgalossi, A., Ebbesen, C.L., Ray, S., Naumann, R., Schmidt, H., Spicher, D., and Brecht, M. (2014a). Pyramidal and stellate cell specificity of grid and border representations in layer 2 of medial entorhinal cortex. Neuron *84*, 1191–1197.

Tang, Q., Brecht, M., and Burgalossi, A. (2014b). Juxtacellular recording and morphological identification of single neurons in freely moving rats. Nat. Protoc. *9*, 2369–2381.

Tang, Q., Ebbesen, C.L., Sanguinetti-Scheck, J.I., Preston-Ferrer, P., Gundlfinger, A., Winterer, J., Beed, P., Ray, S., Naumann, R., Schmitz, D., et al. (2015). Anatomical Organization and Spatiotemporal Firing Patterns of Layer 3 Neurons in the Rat Medial Entorhinal Cortex. J. Neurosci. *35*, 12346–12354.

Tang, Q., Burgalossi, A., Ebbesen, C.L., Sanguinetti-Scheck, J.I., Schmidt, H., Tukker, J.J., Naumann, R., Ray, S., Preston-Ferrer, P., Schmitz, D., and Brecht, M. (2016). Functional Architecture of the Rat Parasubiculum. J. Neurosci. *36*, 2289–2301.

Unal, G., Joshi, A., Viney, T.J., Kis, V., and Somogyi, P. (2015). Synaptic Targets of Medial Septal Projections in the Hippocampus and Extrahippocampal Cortices of the Mouse. J. Neurosci. *35*, 15812–15826.

Varga, C., Lee, S.Y., and Soltesz, I. (2010). Target-selective GABAergic control of entorhinal cortex output. Nat. Neurosci. *13*, 822–824.

Welday, A.C., Shlifer, I.G., Bloom, M.L., Zhang, K., and Blair, H.T. (2011). Cosine directional tuning of theta cell burst frequencies: evidence for spatial coding by oscillatory interference. J. Neurosci. *31*, 16157–16176.

Wilkinson, G.N., and Rogers, C.E. (1973). Symbolic Description of Factorial Models for Analysis of Variance. J. R. Stat. Soc. Ser. C Appl. Stat. *22*, 392–399.

Winter, S.S., Clark, B.J., and Taube, J.S. (2015). Spatial navigation. Disruption of the head direction cell network impairs the parahippocampal grid cell signal. Science *347*, 870–874.

Zilli, E.A. (2012). Models of grid cell spatial firing published 2005-2011. Front. Neural Circuits *6*, 16.

Cell Reports, Volume *16*

Supplemental Information

Cell Type-Specific Differences in Spike Timing and Spike Shape in the Rat Parasubiculum and Superficial Medial Entorhinal Cortex

Christian Laut Ebbesen, Eric Torsten Reifenstein, Qiusong Tang, Andrea Burgalossi, Saikat Ray, Susanne Schreiber, Richard Kempter, and Michael Brecht

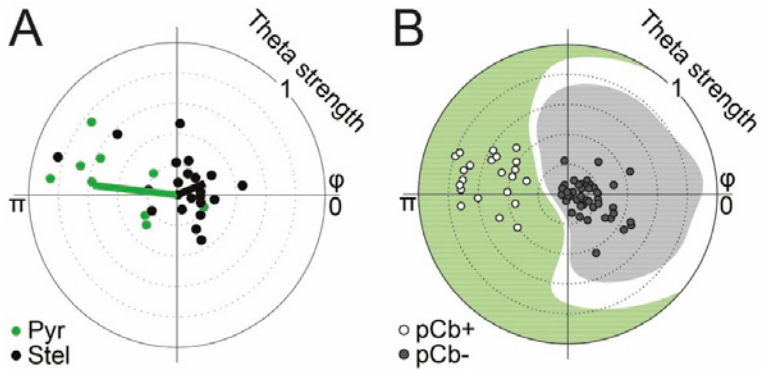

Figure S1: Classification of medial entorhinal cortex layer 2 neurons, Related to Figure 1.

(A) Polar plot of theta strength and theta phase angle, ϕ, of the spiking activity of calbindin+ pyramidal cells (Pyr, green dots) and calbindin- stellate cells (Stel, black dots) identified in freely moving rats. Lines indicate mean theta phase angle and median theta strength.

(B) Polar plot of theta strength and preferred theta phase angle, ϕ, for nonidentified MEC L2 cells, which were classified as putative calbindin+ cells (pCb+, white dots) and putative calbindin- cells (pCb-, dark grey dots). The background colors indicate the two classification groups (light green and light grey for putative calbindin+ (pCb+) and putative calbindin- (pCb-)) and the guard zone around the classification boundary (white). No nonidentified cell fell within the guard zone.

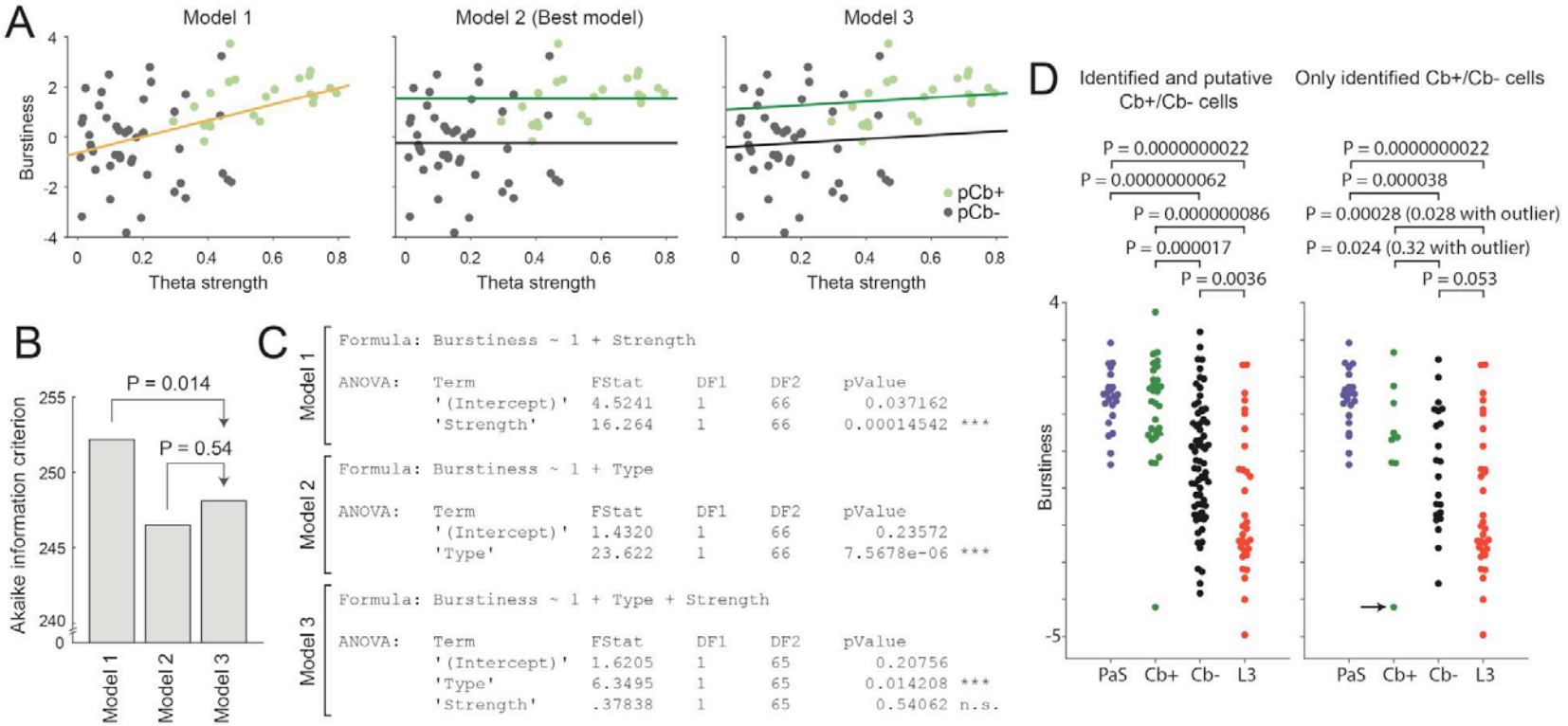

Figure S3: Classification of medial entorhinal cortex layer 2 cells does not explain cell-type specific differences in burstiness, Related to Figure 3.

(Legend on next page)

Figure S3: Classification of medial entorhinal cortex layer 2 cells does not explain cell-type specific differences in burstiness, Related to Figure 3

(A) Graphical representation of three fitted generalized linear models to investigate if burstiness is related to theta strength (Model 1), putative cell type (Model 2) or both (Model 3).

(B) Comparison of the Akaike information criterion ('AIC') of the three models. P-values indicate theoretical likelihood ratio tests between nested models. Both the AIC and the likelihood ratio tests suggest that Model 2 is superior to the other models.

(C) ANOVA tables with F-statistics for the three fitted models. Model 1 indicates a significant relationship between theta strength and burstiness ($P_{Strength} = 0.00015$), but this effect disappears when we add cell type as another independent variable (Model 3: $P_{Type} = 0.014$, $P_{Strength} = 0.54$). The best model depends only on cell type (Model 2: $P_{Type} = 0.0000076$).

(D) Left: Comparison of the burstiness for the four different neuron types as in Figure 3C, i.e. including MEC L2 cells classified as putatively pyramidal and putatively stellates (Same as Fig 3C). Right: Same plot, but only including identified MEC L2 cells. P-values indicate results of t-tests (assuming equal (Cb- vs. L3) or unequal (PaS, Cb+ vs. Cb-, L3) variances). Due to the low number of Cb+ cells, we report the P-value both with and without the statistical outlier (indicated by arrow).

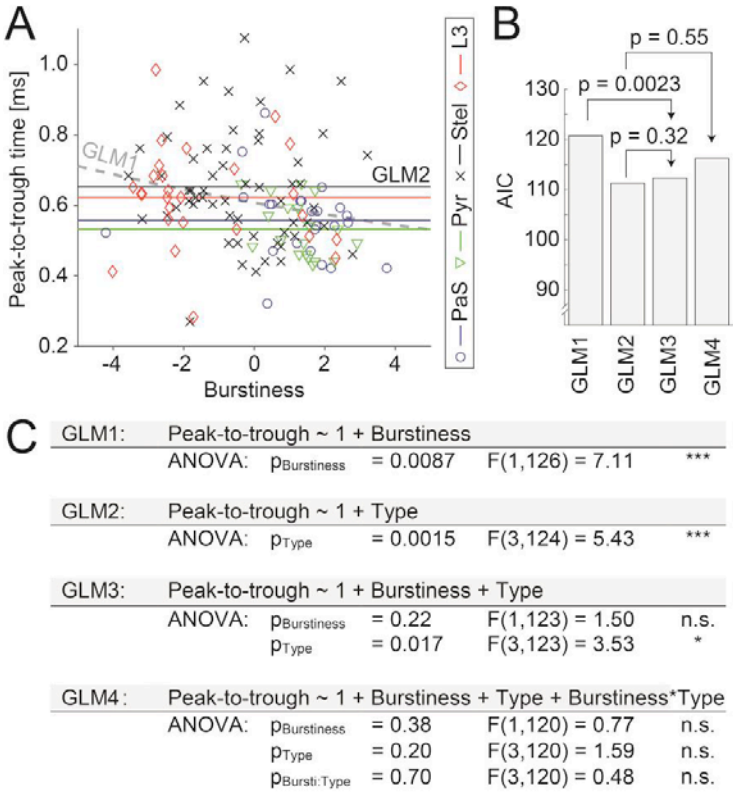

Figure S4. Spike shape is a feature of cell type rather than burstiness, Related to Figure 4.

(A) Scatterplot of the peak-to-trough time as a function of burstiness for the four neuron types defined in Fig. 4A; symbols indicated by legend. Lines indicate the estimated peak-to-trough times as a function of burstiness and cell type from the generalized linear model 1 (GLM1, dashed grey line) and GLM2 (best model, four solid horizontal lines, color code as for symbols).

(B) Comparison of degrees of freedom ("params") and Akaike information criterion (AIC) for four GLMs in (A). P-values indicate theoretical likelihood ratio tests for nested models. According to the AIC, the best model is GLM2 (Peak-to-trough time depends only on neuron type, not on burstiness). Similarly, a likelihood ratio test rejects the inclusion of burstiness as an extra predictor variable (p = 0.32 for GLM2 vs. GLM3). There is no indication of a statistical interaction between cell type and burstiness (GLM4).

Ebbesen et al. *MEC Cell Type, Spike Shape & Discharge Timing* Supplemental 5

(C) Results of ANOVA for four statistical models relating the spike peak-to-trough time to cell type and burstiness.

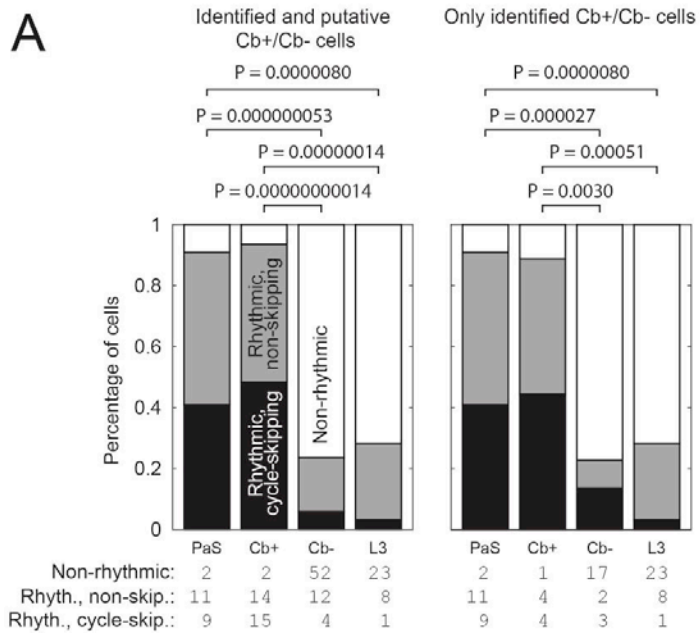

Figure S5. Comparison of rhythmicity and cycle-skipping with and without including classified medial entorhinal cortex layer 2 cells show similar patterns, Related to Figure 5.

(A) Left: Same plot as Figure 5C, proportions (above) and counts (below) of non-rhythmic, rhythmic and cycle-skipping neurons among the cell types, i.e. including MEC L2 cells classified as putatively pyramidal and putatively stellate. Right: Same plot, but only including identified MEC L2 cells. (P values indicate χ^2 tests of equal proportions among cell types).

Ebbesen et al. *MEC Cell Type, Spike Shape & Discharge Timing* Supplemental 7

Supplemental experimental procedures

Juxtacellular recordings

In this paper, we analyzed a data set of juxtacellular recordings from the superficial medial entorhinal cortex and the parasubiculum which we have previously published (Ray et al. 2014, Tang et al. 2014, Tang et al. 2015, Tang et al. 2016). Below, we present a summary of the recording procedure from these previous papers.

Juxtacellular recordings and tetrode recordings in freely moving animals were obtained in male Wistar and Long-Evans rats (150-250 g). Experimental procedures were essentially performed as recently described (Tang et al., 2014a; Tang et al., 2014b). Briefly, for juxtacellular recordings, glass pipettes with resistance 4-6 MΩ were filled with extracellular (Ringer) solution containing (in mM) NaCl 135, KCl 5.4, HEPES 5, $CaCl_2$ 1.8, and $MgCl_2$ 1 (pH = 7.2) and Neurobiotin (1-2%). The glass recording pipette was advanced into the brain by means of a miniaturized micromanipuator (Tang et al 2014b) while rats explored open field arenas (70 x 70 cm or 1 x 1 m square black box, with a white cue card on the wall). Juxtacellular labeling was attempted at the end of the recording session according to standard procedures (Pinault, 1996). Unidentified recordings in parasubiculum and MEC were either lost before the labeling could be attempted, or the recorded neurons could not be unequivocally identified, as described in Tang et al., 2014a, Tang et al 2015, Tang et al., 2016. After the experiment, the animals were euthanized with an overdose of ketamine, urethane or pentobarbital, and perfused transcardially with 0.1 M phosphate buffer followed by 4% paraformaldehyde solution. The juxtacellular signals were amplified by the ELC-03XS amplifier (NPI Electronics, Tamm, Germany) and sampled at 20 kHz by a data-acquisition interface under the control of PatchMaster 2.20 software (HEKA, Ludwigshafen, Germany). The animal's location and head-direction was automatically tracked at 25 Hz by the Neuralynx video tracking system and two head-mounted LEDs.

Tissue preparation, immunohistochemistry, and image acquisition

Rats were anaesthetized by isoflurane and euthanized by an intraperitoneal injection of 20% urethane. Animals were then transcardially perfused with 0.9% phosphate-buffered saline, followed by PFA.

Subsequently, brains were removed from the skull and postfixed in PFA overnight. Brains were then immersed in 10% sucrose and then in 30% sucrose for at least one night for cryoprotection. The brains were embedded in Jung tissue Freeing Medium (Leica Microsystems Nussloch, Germany), and mounted on a freezing microtome (Leica 2035 Biocut) to obain tangential and parasaggital sections at 60 microns.

Tangential sections of the medial entorhinal cortex and parasubiculum were obtained as previously described (Ray et al., 2014; Naumann et al., 2016) by separating the entorhinal cortex from the remaining hemisphere by a cut parallel to the face of the medial entorhinal cortex (Ray & Brecht, 2016) and sectioning with the surface of the entorhinal cortex attached to the block face of the microtome.

Immunohistochemical stains were performed on tangential and sagittal sections. The sections were pre-incubated in a blocking solution containing 0.1 M PBS, 2% Bovine Serum Albumin (BSA) and 0.5% Triton X-100 (PBS-X) for an hour at room temperature (RT). Following this, primary antibodies were diluted in a solution containing PBS-X and 1% BSA. Primary antibodies against the calcium binding proteins Calbindin (Swant: CB300, CB 38; 1:5000), the transmembrane protein Wolframin (Proteintech: 11558-1-AP; 1:200), and the calmodulin binding protein Purkinje cell protein 4 (Sigma: HPA005792; 1:200) were used. Sections were incubated in primary antibodies for at least 24 hours under mild shaking at 4 degrees centigrade. Subsequently sections were incubated in secondary antibodies coupled to different fluorophores (Alexa 488, 546; Invitogen; 1:500). For multiple antibody labelling, antibodies raised in different host species were used.

Images were acquired with a Leica DM5500B epifluorescence microscope with a Leica DFC345 FX camera. Alexa fluorophores were excited using the appropriate filters (Alexa 488- L5; Alexa 546- N3). Fluorescent images were acquired in monochrome, and color maps were applied to the images post acquisition. Post hoc linear brightness and contrast adjustment were applied uniformly to the image under analysis.

Quality control across juxtacellular recordings

We checked explicitly for systematic differences in LFP power across recordings. First, we calculated the global theta power in the LFP of all recordings, defined as the mean power spectral density of the theta-peak in the LFP spectrogram ± 0.3 Hz. We did not find any significant differences in LFP theta power among cell types ($P > 0.05$, one-way ANOVA). We also did not find any correlation between the LFP theta power and burstiness in our data ($P > 0.05$, Spearman correlation).

If spikes are missed during bursts, this would bias a recording towards low burstiness. Under the juxtacellular recording configuration, however, spikes are well above the noise level (signal-to-noise typically an order of magnitude higher than tetrode recordings) and thus unlikely to fall below the detection threshold. It is the case, however, juxtacellular recordings might potentially be more disruptive for the recorded neurons due to the close proximity of the glass tip and the membrane; recordings (or portions of recordings) where signs of cellular damage were observed (e.g. action-potential broadening, increase in firing rate; see Pinault et al., 1996; Herfst et al., 2012) were excluded from the analysis. As a measure of 'recording quality', we estimated the signal-to-noise ratio of the spikes (Joshua et al. 2007), and we found no difference between cell types ($P > 0.05$, Kruskal-Wallis test). We also found no correlation between recording quality and burstiness, spike shape or phase precession (all $P > 0.05$, Spearman correlations).

Supplemental references

Herfst L, Burgalossi A, Haskic K, Tukker JJ, Schmidt M, Brecht M. (2012) Friction-based stabilization of juxtacellular recordings in freely moving rats. J Neurophysiol. (2):697-707.

Joshua M, Elias S, Levine O, Bergman H. (2007) Quantifying the isolation quality of extracellularly recorded action potentials. J Neurosci Methods. 163(2):267-82.

Naumann, RK, Ray, S, Prokop, S, Las, L, Heppner, FL, Brecht M. (2016) Conserved size and periodicity of pyramidal patches in layer 2 of medial/caudal entorhinal cortex. J Comp. Neurol. 524:783-806

Pinault D. (1996) A novel single-cell staining procedure performed in vivo under electrophysiological control: morpho-functional features of juxtacellularly labeled thalamic cells and other central neurons with biocytin or Neurobiotin. J Neurosci Methods; 65(2):113-36.

Ray, S., Naumann, R., Burgalossi, A., Tang, Q., Schmidt, H., Brecht, M. (2014) Grid-layout and theta-modulation of layer 2 pyramidal neurons in medial entorhinal cortex. Science 343, 891–6.

Ray S, Brecht M (2016) Structural development and dorsoventral maturation of the medial entorhinal cortex. eLife. e13343.

Tang, Q., Burgalossi, A., Ebbesen, C.L., Ray, S., Naumann, R., Schmidt, H., Spicher, D., Brecht, M. (2014a) Pyramidal and Stellate Cell Specificity of Grid and Border Representations in Layer 2 of Medial Entorhinal Cortex. Neuron 84, 1191–1197.

Tang, Q., Brecht, M., Burgalossi, A. (2014b) Juxtacellular recording and morphological identification of single neurons in freely moving rats. Nat Protoc. 9(10), 2369-81.

Tang, Q., Ebbesen, C.L., Sanguinetti-Scheck, J.I., Preston-Ferrer, P., Gundlfinger, A., Winterer, J., Beed, P., Ray, S., Naumann, R., Schmitz, D., Brecht, M., Burgalossi, A. (2015) Anatomical Organization and Spatiotemporal Firing Patterns of Layer 3 Neurons in the Rat Medial Entorhinal Cortex. J. Neurosci. 35(36), 12346–12354.

Tang, Q., Burgalossi, A., Ebbesen, C.L., Sanguinetti-Scheck, J.I., Schmidt, H., Tukker, J.J., Naumann, R., Ray, S., Preston-Ferrer, P., Schmitz, D., Brecht, M. (2016) Functional Architechture of the Rat Parasubiculum. J. Neurosci. 36(7):2289-301

7. Vibrissa motor cortex activity suppresses contralateral whisking behavior

This manuscript was published as:
Ebbesen, C.L., Doron, G., Lenschow, C., & Brecht, M. (2017). Vibrissa motor cortex activity suppresses contralateral whisking behavior. **Nature Neuroscience** 20(1):82-89
This is the author's version of this work, reprinted with permission from Nature Pub. Group

Figure 10: Our suggested cover image, based on the article: A Wistar rat it reins. The reins symbolize the suppressive effect of motor cortex, which is "reining in" the behavior of the rat. The rat, grass and flowers is a 3d model by Shimpei Ishiyama.

A preliminary subset of the data presented in this article were shown in my M.Sc. thesis (2013).

Vibrissa motor cortex activity suppresses contralateral whisker touch

by

Christian Laut Ebbesen[1,2], Guy Doron[1,3], Constanze Lenschow[1] and Michael Brecht[1].

[1]Bernstein Center for Computational Neuroscience Berlin, Humboldt-Universität zu Berlin, Berlin, Germany

[2]Berlin School of Mind and Brain, Humboldt-Universität zu Berlin, Berlin, Germany

[3]Current Address: NeuroCure Cluster of Excellence, Humboldt-Universität zu Berlin, Berlin, Germany

Anatomical[1,2], stimulation[1–8] and lesion data[9,10] point to a role of vibrissa motor cortex in the control of whisker movement. Motor cortex is classically thought to play a key role in movement generation[11–13], but most studies have found only weak correlations between vibrissa motor cortex activity and whisking[14–17]. The exact role of vibrissa motor cortex in motor control remains unknown. To address this question we recorded vibrissa motor cortex neurons during various forms of vibrissal touch, all of which were associated with increased movement and forward positioning of whiskers. Free whisking, palpation of objects and social touch all resulted in similar vibrissa motor cortex responses: *(i)* Population activity decreased. *(ii)* The vast majority (~80%) of significantly modulated single cells decreased their firing. *(iii)* Rate-decreasing cells were the most strongly modulated cells. To understand the cellular basis of this decrease of activity, we performed juxtacellular recordings, nanostimulation and *in vivo* whole-cell recordings in head-fixed animals. Social facial touch – a strongly engaging stimulus[18–20] – resulted in decreased spiking activity, decreased cell excitability and a ~1.5 mV hyperpolarization in vibrissa motor cortex neurons. High-speed videography and generalized linear modeling of the spiking patterns of identified deep layer output neurons during social facial touch episodes revealed that the observed suppression of VMC activity is likely due to nose-to-nose touch and whisker protraction. To assess how activation of vibrissa motor cortex impacts whisking behavior we performed intra-cortical microstimulation, which led to whisker retraction, as if to abort vibrissal touch. Finally, we blocked vibrissa motor cortex. A variety of inactivation protocols resulted in an increase of contralateral whisker movements and contralateral whisker protraction, as if to engage in vibrissal touch. These observations suggest that the role of vibrissa motor cortex is not restricted to movement generation. Instead, the data collectively point to movement suppression as a prime function of vibrissa motor cortex activity.

Vibrissa motor cortex (VMC, Fig 1a) is a cortical vibrissa representation originally identified by a variety of stimulation techniques[1–8]. The huge size of this representation possibly reflects the great ecological relevance of vibrissa movements for rats[21,22]. In contrast to classic studies on primate primary motor cortex (M1) activity[11,12], VMC population activity is only weakly correlated with movement[14–17]. It is not entirely clear why the correlation between whisker movement and VMC activity is weak, but we note that most of what we know about VMC activity during whisking comes from recordings in animals simply whisking in air[14–17]. Studies on primate motor cortex have shown, that besides the musculotopic representation of body movements[12,13], the motor cortex might also represent a map of ecologically relevant behaviors[23]. The information about VMC activity during self-initiated, ecologically relevant behaviors is still limited and it remains unclear how VMC contributes to motor control during such behaviors. This prompted us to pose the following questions about VMC function: (1) How is the activity of the VMC "output layers"[1] modulated, when rats engage in various ecologically relevant whisking behaviors? (2) What are the cellular mechanisms, which contribute to the modulation of VMC activity? (3) How does an increase of VMC activity by microstimulation during whisking affect ongoing whisking movements? (4) How does a decrease of VMC activity by pharmacological blockade affect whisking movements?

RESULTS:

Vibrissa motor cortex firing decreases during various forms of vibrissal touch

We investigated VMC modulation by three self-initiated rat whisker behaviors (Fig. 1b): free whisking (explorative whisking bouts in air), object touch (whisking onto objects) and social touch (whisking onto conspecifics)[19]. All whisker-behaviors were compared to rest (animal not whisking). Single unit activity was recorded from VMC layer 5 using tetrodes. With high-speed videography, we quantified the whisker set angle and whisking power during the various behaviors (Fig. 1c). We found that during all whisker behaviors the whiskers were held at a more protracted set angle than at rest, on average by 19° (Fig. 1d top, $P < 0.001$, one-way ANOVA, all $P < 0.001$, unpaired t-tests). By definition, during all whisking behaviors, the whisking power was higher than at rest (Fig. 1d bottom).

In Fig. 1e, we show a raster plot and a peri-stimulus time histogram (PSTH) of an example layer 5 cell aligned to the beginning of free whisking. The PSTH shows the predominant response pattern: a decrease in firing rate during free whisking. We observed a large variability of responses (Fig. 1e, top). Some cells increased their firing, some were not modulated and some decreased their firing rate, but as a whole the population activity was significantly decreased during free whisking (Fig. 1f top, median 2.31/2.05 Hz Baseline/free whisking, Slope = 0.812, $P = 0.00010$, N = 158 cells, Mann-Whitney U-test). We assessed the significance of firing rate changes by a bootstrapping procedure and found that 80% of significantly modulated cells decreased their activity in free whisking ($P = 0.000041$, two-tailed binomial test for equal proportions). We restricted our analysis to cells with a firing rate below 10 Hz to reduce the proportion of interneurons (see Methods). In the small subset of cells with firing rates > 10 Hz (14% of cells) we found no significant rate changes (All $P > 0.05$, Mann-Whitney U-test). Inclusion of high-firing cells did not change the results. To quantify the modulation of single cells, we calculated a modulation index (see Methods) and found that the most strongly modulated cells were the cells that decreased their firing rate (Fig. 1f bottom, $P < 0.05$, Mann-Whitney U-test). We wondered, if the firing rate decrease is also to be seen in more challenging forms of vibrissal touch. For both object touch (Fig. 1g,h top, median 2.20/1.65 Hz Baseline/Touch, Slope = 0.749, $P = 0.023$, N = 122 cells, Mann-Whitney U-test) and for social facial touch (Fig. 1i,j top, median 2.26/1.87 Hz Baseline/Touch, Slope = 0.806 $P = 0.00018$, N = 156 cells, Mann-Whitney U-test), neurons also decreased their firing rate. Specifically, we observed a decrease in 88% of the cells significantly modulated by object touch (Fig. 1h bottom) and in 78% of the cells significantly modulated by social touch, (Fig. 1j bottom, both $P < 0.05$, two-tailed binomial tests). As during free whisking, the most strongly modulated cells were the cells that decreased their firing rate (Fig. 1h,j bottom, both $P < 0.05$, Mann-Whitney U-test).

Cellular mechanisms of vibrissa motor cortex suppression

Thus, the transition from rest (retracted whiskers, no movement) to whisker behaviors (protracted whiskers, whisking) leads to a decrease of VMC activity. In cortical physiology, this is a highly unusual result. In the somatosensory system and the visual system, relevant stimuli lead to an increase in population activity[24]. To explore the cellular basis of the decrease of VMC activity during whisking, we habituated rats to head-fixation and performed juxtacellular recording, nanostimulation and whole-cell recordings from VMC putative layer 5 neurons,

the output layer[1]. We focused on social touch, an engaging stimulus[18], which strongly activates primary somatosensory cortex (S1)[19,20] and medial prefrontal cortex[25]. During recordings, we staged facial interactions of the head-fixed rats with stimulus rats in front of them (Fig. 2a). In agreement with the recordings in freely moving rats, we found that VMC activity strongly decreased during social facial touch episodes. As shown in Fig. 2b the rat protracted the whiskers during nose-to-nose touch and a juxtacellularly recorded neuron discharged fewer APs than at baseline. Across the population of neurons, we found a significant decrease of spiking during social facial touch compared to baseline (Fig 2c, median 2.5/2.0 Hz, baseline/social touch, $P = 0.0079$, $N = 21$ cells, Wilcoxon signed-rank test). To investigate if the decrease in spiking was due to a decrease in cell excitability, we evoked APs in single layer 5 neurons at baseline and during social touch episodes, using a nanostimulation protocol (Fig. 2d, see Methods). Across the population, we found that layer 5 neurons were indeed much less excitable during social facial touch than during baseline (Fig. 2e, median evoked rate 14.6/4.8 Hz, baseline/social touch, $P = 0.0125$, $N = 15$, Wilcoxon signed-rank test). To investigate the underlying intracellular signals, we targeted whole-cell patch-clamp recordings to the deep layers of VMC during social facial touch (Fig. 2f). In agreement with the reduced excitability, we found that the neurons were slightly but significantly more hyperpolarized during social facial touch than at baseline, on average by 1.5 mV (Fig. 1f, $P = 0.0171$, $N = 10$ cells, paired t-test). Some cells showed a reduction in the membrane potential coefficient of variation during social touch (e.g. Fig. 1e), but across the population, there was no significant change ($P > 0.05$, $N = 10$ cells, paired t-test). Both the dampening of spiking evoked by juxtasomal nanostimulation and the observed hyperpolarization point to increased somatic inhibition in VMC during whisker movement.

Whisker protraction and social touch drive suppression of vibrissa motor cortex

Even though social facial touch is generally associated with whisker movement and whisker protraction (Fig 1d), there is a large variability in the whisking between touch episodes[18,19,26]. We decided to exploit this fact to disentangle whether the suppression of VMC activity during social facial touch (Fig. 2b) was due to the nose-to-nose touch, the coincidental whisker protraction and increased whisking amplitude, or perhaps a combination thereof. To this end, we juxtacellularly recorded an additional set of cells during social facial touch episodes, where we now also simultaneously recorded and tracked the whisker angle of the contralateral whiskers using high-speed videography, using a robust method which captures most aspects of the whisker movements (see Methods). We then used likelihood maximization to fit a Poisson model (with 1-ms bins) to the spike trains[27], where the instantaneous firing rate depends linearly on nose-to-nose touch (a binary variable), the whisker angle and the whisking amplitude by the coefficients β_{Nose}, β_{Angle} and β_{Ampl} (Fig. 3a-b, see Methods). After recording, we labeled and recovered cells, both Ctip2-positive cells (putative thick-tufted pyramidal tract (PT-type) neurons[28], Fig 3a-b) and Ctip2-negative cells (putative thin-tufted intratelencephalic (IT-type) neurons, example Fig. S3d-e). Across all cells, we found that the cells were suppressed by both nose touch (Fig. 3c, median $\beta_{Nose} = -0.60$, $P = 0.0067$, $N = 32$ cells, Wilcoxon signed-rank test) and by whisker protraction (Fig. 3c, median $\beta_{Angle} = -0.026\ (°)^{-1}$, $P = 0.020$, $N = 32$ cells, Wilcoxon signed-rank test). We did not find a systematic dependence on the whisking amplitude across the population (median $\beta_{Ampl} = -0.026\ (°)^{-1}$, $P > 0.05$, $N = 32$ cells, Wilcoxon signed-rank test). When we used a likelihood ratio test to select single cells, which were significantly modulated by amplitude (at $P < 0.05$, see Methods), the results were

also mixed (Fig S3b): 10 cells were significantly suppressed, 6 cells were significantly activated, and 16 cells were not significantly modulated. However, we note suppressed cells were more strongly modulated that the activated cells: (median $|\beta_{Ampl}| = 0.221/0.128$ for suppressed/activated cells, P = 0.00025, Mann-Whitney U-test). In our subset of labeled cells, we did not find indications, that PT or IT type cells had different response patterns; both cell types were generally suppressed by nose touch and whisker protraction (data not shown). To control for possible collinearity, we also fitted a model, where we performed stepwise orthogonalization of the predictor vectors 'nose touch', 'angle' and 'amplitude' using the Gram-Schmidt algorithm. In this case, we found the same pattern: the β_{Nose}'s and the β_{Angle}'s were significantly negative (Fig. S3f)

Since each cell is associated with an individual estimate of the baseline firing rate and dependence on nose touch and whisker protraction, we could evaluate our model for all cells to estimate the population activity during various whisker behaviors. We first compared the baseline firing rate ($\lambda_{rest} = \exp(\beta_0)$) to the firing rate during nose touch ($\lambda_{touch} = \exp(\beta_0 + \beta_{Nose})$). In agreement with Fig. 2c, we found that the population activity is suppressed during nose touch (Fig dc, median 1.69/1.15 Hz, baseline/nose touch, P = 0.036, N = 32 cells, paired t-test), even in the absence of whisker protraction. When we calculated the modulation index resulting from comparing rest to nose touch (Fig 3e, left, median index: −0.29, P = 0.0067, N = 32 cells, Wilcoxon signed-rank test), comparing rest to 15° whisker protraction (Fig 3e, middle, median index: −0.19, P = 0.020, N = 32 cells, Wilcoxon signed-rank test) and from comparing rest to nose touch coinciding with 15° whisker protraction (Fig 3e, right, median index: −0.40, P = 0.00041, N = 32 cells, Wilcoxon signed-rank test), we found that all conditions lead to a suppression of the population activity. We conclude, that the suppression of activity during exploratory whisking in air and during social facial touch, which we observe in behaving animals (Fig 1 & 2), likely results from a suppression due to both nose touch and coincidental whisker protraction (Fig 3c).

Activation of vibrissa motor cortex by microstimulation

In order to better understand the role of VMC activity in control of contralateral movement during ongoing whisking, we decided to test the effect of increasing VMC activity by intracortical microstimulation at a behavioral time scale in the range where we observed modulation of VMC activity[23]. To this end, we unilaterally microstimulated VMC deep layer cells during bouts of free whisking using 1 s long stimulation pulse trains randomly preceded or followed by a 1 s long break ("sham stimulation") (Fig. 4a, see Methods). The dominant effect of such stimulation was the retraction of the contralateral whiskers (Fig. 4b, 1.2 ± 0.7°/s vs. –2.4 ± 1.5°/s, sham vs. stimulation, P = 0.0000245, paired t-test). We also observed a small increase in the contralateral whisking power during the stimulation pulses, suggesting that we induced extra movement of the contralateral whiskers (11% increase, Fig. 4c, 194 ± 64(°)^2 vs. 216 ± 64(°)^2, P = 0.0151, paired t-test). We wondered, if the extra induced backwards movement might be enough to influence social touch behavior, so we also performed a set of experiments, where we unilaterally microstimulated VMC deep layers during social facial touch episodes. When comparing the duration of social facial touch episodes from first to last whisker touch, we found that microstimulation significantly shortens the whisker touches (Figure S4, mean duration 0.692/0.973 s, stimulation/sham, P = 0.0000011, LME

198 model), consistent with the finding that VMC activation induces whisker retraction to abort
199 social facial touch.

200

Blockade of vibrissa motor cortex

We wondered, how whisking would be affected by VMC inactivation and therefore pharmacologically blocked VMC deep layer activity unilaterally by injection of lidocaine. As shown in an example experiment prior to lidocaine injection, the rat's whiskers were positioned symmetrically (Fig. 5a left). After lidocaine injection, the whiskers were asymmetric and more protracted contralaterally (Fig. 5a right). Similarly, the rat whisked with equal whisking amplitude ipsilaterally and contralaterally prior to lidocaine injection (Fig. 5b, left), but whisked with much larger amplitude on the contralateral side than on the ipsilateral side after blockade (Fig. 5b right). The same observations were made across a series of experiments. Injection of lidocaine solution (Fig. 5c left, $P = 0.0052$, $N = 10$, paired t-test) but not of ringer solution (Fig. 5c right) led to a significant increase in the contralateral whisking power. Similarly, injection of lidocaine but not of ringer solution led to a protraction of the contralateral whiskers by an average of 21° (Fig. 5d, $-7.0 \pm 16.3°$ vs. $14.2 \pm 7.3°$, $P = 0.0012$, $N = 10$, paired t-test). Neither injection of ringer nor lidocaine had an effect on the set angle of the ipsilateral whiskers. When we unilaterally blocked excitatory currents in the VMC by superfusion of APV (an NMDA antagonist) and NBQX (an AMPA antagonist) in lightly anaesthetized rats (Figure S5, $N = 3$ rats), and when we blocked VMC activity by injection of muscimol (a $GABA_A$ agonist) in lightly anaesthetized mice (Figure S6, $N = 4$ mice), we saw the same effects: protraction of contralateral whiskers and increased contralateral whisker movements.

DISCUSSION:

Summary

Most work on the mammalian motor cortex has focused on a role of this cortical area in movement generation[11,12]. It is therefore surprising that our observations coherently indicate that a prime function of VMC activity might be to suppress behavior: *(i)* When the rat engages in whisker-related behavior (protracted whiskers, whisker movements), we see a decrease in spiking activity in the VMC output layers (Fig. 1-3). *(ii)* VMC microstimulation leads to retractive movements, as if to abort behavior (Fig. 4). *(iii)* VMC blockade disinhibits contralateral whisker movements and leads to contralateral whisker protraction, as if to engage in behavior (Fig. 5). Our observations are difficult to reconcile with the classic model, where the prime role of VMC activity is whisker protraction and the generation of movement[8]. Instead the data support a model where VMC activity suppresses whisker behavior, perhaps by gating a downstream whisking central pattern generator[7,15,29,30].

Relation to previous vibrissa motor cortex studies

The whisker motor plant[31,32] and vibrissa motor neurons[33] are laid out for the fine control of individual whisker protraction. This is in line with a prime function of vibrissal touch in palpation of objects, obstacles and conspecifics in front of the animal[21,22]. In light of the specialization of the motor plant and motor neurons for whisker protraction, our observation that VMC deep layer microstimulation leads to whisker retraction is quite surprising. This retraction result is in agreement with previous studies, which have all reported that VMC microstimulation[2–6], single-cell stimulation[7] and optogenetic stimulation[8] elicit with few exceptions[5,8] whisker retraction. The retraction movements let it appear unlikely that an increase in VMC activity drives vibrissal touch (which is associated with whisker protraction, Fig. 1d). Rather, it suggests, that the role of VMC is to abort undesired whisking behavior. This idea is also supported by the unexpected increase of contralateral whisking following acute VMC blockade. Our observation that a reduction in motor cortex activity increases movement is consistent with observations on whisking patterns after VMC lesions: Whisking persists after VMC ablation[21] and blockade[8,34], VMC ablation spares large-amplitude whisking, but reduces small whisker movements[9], and unilateral VMC lesions increases contralateral whisking power[10].

While the bulk of our data point to motor suppressive effects of VMC activity, some of our results also point to a role of VMC cells in movement generation. Thus, a small subset of VMC cells weakly increased their firing rate during movements (Fig 1-2). Further, generalized linear modeling of VMC activity revealed, that the relationship between VMC activity and whisking amplitude was mixed with no obvious pattern (Fig 3). This is consistent with previous studies, which have reported both negative and positive correlations between activity of single VMC cells and whisking power[14–17]. A novelty of our study is that we used statistical modeling to analyze all spikes and relate them to naturalistic behavior (whisker angle, amplitude and social touch episodes), i.e. we did not only analyze whisking in air[14–17] and we did not exclude periods, where the amplitude was low[15] (breaks in whisking are also a part of natural whisking patterns). Speaking more generally, movement suppression and movement generation are probably inseparable aspects of motor control.

Is the functional output of vibrissa motor cortex a decrease in spikes to downstream targets?

The output of vibrissa motor cortex is thought to play two major roles: First, it is supposed to control whisker movement, presumably by gating a downstream whisking central pattern generator in the brainstem (PT-type neurons)[15,29,30]. Secondly, it is supposed to transmit an efferent, internal signal to sensory cortices, so they can disentangle afferent sensory signals due to touch stimulation of the whiskers from sensory signals due to self-generated whisker movement (IT-type neurons)[22,35,36]. Previous investigations of the relationship between VMC activity and whisking have found that the overall modulation of VMC activity due to whisking is weak, although single cells exist which correlate with the whisking amplitude[14–17] and the whisker angle[15]. These single cells have previously been found in roughly equal proportions, and it has remained unclear what the prime 'functional' output of the VMC might be[15,17].

In neurophysiology we normally observe that cells respond to behavior with an increase of activity. This is the case in the somatosensory system[37] and the visual system[38], and has been proposed to be a governing principle for cortical information processing[24]. Thus, our observation that the 'functional' response of VMC cells during various whisker behaviors is a *decrease* in spiking is highly surprising. The whisker motor plant is laid out for controlled forward movement, yet we found that VMC activity decreases with whisker protraction (Fig. 1,3). Social facial touch is a very engaging stimulus, where correct sensorimotor computation is of high ecological importance[18], yet we robustly see a decrease in VMC activity and a decrease in VMC excitability during social touch episodes (Fig 1-3). For comparison, previous studies have found that social facial touch very strongly activates primary somatosensory cortex (S1)[19,20] and medial prefrontal cortex[25]. Cells, where the functional response is a hyperpolarization, are rare but not unknown (e.g. the photoreceptor of the mammalian eye[39]), yet our findings are very unusual for a primary cortical area.

Motor suppressive effects of motor cortex

Motor effects of motor cortex lesions in rats are subtle, as many simple behaviors (e.g. locomotion) persist after decortication[40]. Motor cortex lesions are associated with performance deficits in several movement related tasks, but at least some of these deficits are not primarily due to deficits in the generation of movement, but to deficits in the control and suppression of movement[40]. For instance, rats can perform long sequences of skilled, learned motor behaviors after motor cortex ablation, but motor cortex is required for them to learn a task of behavioral inhibition (they must learn to postpone lever presses)[41]. When swimming, intact rats hold their forelimbs still and swim with only their hindlimbs. After forelimb motor cortex lesions, however, rats swim with their forelimbs also[42]. After learning a go/no-go whisker task, where mice must lick to receive a water reward, motor cortex inactivation does not significantly decrease the licking at correct times, but massively increases the 'false alarm' licking rate (where licking should be suppressed)[34,43]. Human patients with frontal lesions are notorious for their lack of behavioral control and do things, they should not do[40], rodents with lesions in motor cortex often perform movements, that should rather be suppressed.

Motor-suppressive effects are impossible to detect in classic motor mapping experiments in lightly anaesthetized animals[1–7,44], but human patients report an inability to move as a prominent effect of intra-operative stimulation of motor cortex[45–50]. The existence of these negative motor areas (NMAs) in M1 where stimulation elicit an inhibition of movement is a robust

result, but even in humans there has historically been a strong bias towards the study of positive motor effects of M1 stimulation, and consequently the function of NMAs in the inhibitory control of movement is still poorly understood[46]. Furthermore, a complication is that NMA stimulation can elicit positive movements with an increasing stimulation current[50], and may as such simply be missed, if only positive stimulation effects are evaluated[46].

Is rat vibrissa motor cortex different from primate motor cortex?

Our observation that a decrease in VMC activity leads to whisker protraction is incompatible with a model where VMC PT-type neurons synapse directly onto whisker motor neurons in the facial nucleus. This direct wiring pattern from motor cortex to motor neurons is famously present in primate hand motor cortex[51], where overwhelming evidence suggests, that in contrast to our observations of rat VMC, activity mainly correlates positively with movement[11,52]. Indeed, there is only a very sparse direct projection from VMC to the whisker motor neurons[53] with the vast majority of VMC PT-type neurons targeting brainstem interneurons[54,55].

It is worth noting, that even in primates, the predominant wiring pattern of corticobulbar and corticospinal projections from M1 is to brainstem and spinal interneurons[51]. The monosynaptic projections from M1 to motor neurons innervating distal limb muscles is an exception, which evolved in primates in parallel with the evolution of skilled digit movements[51]. Spike-triggered averaging techniques used in monkeys have all showed that M1 neuron spikes can predict both EMG peaks and troughs, which suggest that M1 neurons commonly have suppressive effects on motorneuronal pools[56–58]. Recent single-cell recordings in monkeys have shown, that also in primates, some M1 cells correlate negatively with movement: Both premotor neurons[59] and indeed M1[60] and M1 pyramidal tract neurons[61,62] respond with mirror neuron activity to the observation of actions, even when the monkey is not moving, a kind of "monkey see, monkey *not* do" response[63]. Similarly, although some muscle weakness is a symptom in patients with M1 or pyramidal tract lesions, the prominent symptoms are ataxia (loss of control over movements), spasticity, clonus, hyperexcitability of reflexes[64]. Spastic paralysis can be managed by high doses of muscle relaxants to reduce the output from the spinal cord or by sectioning the dorsal roots, suggesting that it represents an abnormal increase in muscular input from the spinal cord due to a net loss of descending inhibition from M1[64].

Conclusion

Action suppression is vital for behavior and numerous studies point to a frontal cortical location of this important cognitive capacity[40]. Our observations suggest that the classic work on the role of motor cortex in movement generation should be complemented by a more extensive investigation of motor suppressive functions of motor cortices.

348 **REFERENCES**

349 1. Neafsey, E. J. *et al.* The organization of the rat motor cortex: A microstimulation
350 mapping study. *Brain Res. Rev.* **11,** 77–96 (1986).

351 2. Brecht, M. *et al.* Organization of rat vibrissa motor cortex and adjacent areas according
352 to cytoarchitectonics, microstimulation, and intracellular stimulation of identified cells.
353 *J. Comp. Neurol.* **479,** 360–373 (2004).

354 3. Hall, R. D. & Lindholm, E. P. Organization of motor and somatosensory neocortex in
355 the albino rat. *Brain Res.* **66,** 23–38 (1974).

356 4. Gioanni, Y. & Lamarche, M. A reappraisal of rat motor cortex organization by
357 intracortical microstimulation. *Brain Res.* **344,** 49–61 (1985).

358 5. Haiss, F. & Schwarz, C. Spatial segregation of different modes of movement control in
359 the whisker representation of rat primary motor cortex. *J. Neurosci.* **25,** 1579–1587
360 (2005).

361 6. Tandon, S., Kambi, N. & Jain, N. Overlapping representations of the neck and
362 whiskers in the rat motor cortex revealed by mapping at different anaesthetic depths.
363 *Eur. J. Neurosci.* **27,** 228–237 (2008).

364 7. Brecht, M., Schneider, M., Sakmann, B. & Margrie, T. Whisker movements evoked by
365 stimulation of single pyramidal cells in rat motor cortex. **427,** (2004).

366 8. Matyas, F. *et al.* Motor control by sensory cortex. *Science* **330,** 1240–1243 (2010).

367 9. Semba, K. & Komisaruk, B. R. Neural substrates of two different rhythmical vibrissal
368 movements in the rat. *Neuroscience* **12,** 761–774 (1984).

369 10. Gao, P., Hattox, A. M., Jones, L. M., Keller, A. & Zeigler, H. P. Whisker motor cortex
370 ablation and whisker movement patterns. *Somatosens. Mot. Res.* **20,** 191–198 (2003).

371 11. Georgopoulos, A. P., Schwartz, A. B. & Kettner, R. E. Neuronal population coding of
372 movement direction. *Science (80-.).* **233,** 1416–1419 (1986).

373 12. Lemon, R. The output map of the primate motor cortex. *Trends Neurosci.* **11,** 501–506
374 (1988).

375 13. Asanuma, H. Recent developments in the study of the columnar arrangement of
376 neurons within the motor cortex. *Physiol. Rev.* **55,** 143–156 (1975).

377 14. Carvell, G. E., Miller, S. A. & Simons, D. J. The relationship of vibrissal motor cortex
378 unit activity to whisking in the awake rat. *Somatosens. Mot. Res.* **13,** 115–127 (1996).

379 15. Hill, D. N., Curtis, J. C., Moore, J. D. & Kleinfeld, D. Primary motor cortex reports
380 efferent control of vibrissa motion on multiple timescales. *Neuron* **72,** 344–356 (2011).

381 16. Friedman, W. A., Zeigler, H. P. & Keller, A. Vibrissae motor cortex unit activity
382 during whisking. *J. Neurophysiol.* **107,** 551–563 (2012).

383 17. Gerdjikov, T. V, Haiss, F., Rodriguez-Sierra, O. E. & Schwarz, C. Rhythmic whisking
384 area (RW) in rat primary motor cortex: an internal monitor of movement-related
385 signals? *J. Neurosci.* **33,** 14193–204 (2013).

386 18. Wolfe, J., Mende, C. & Brecht, M. Social facial touch in rats. *Behav. Neurosci.* **125,**
387 900–910 (2011).

388 19. Bobrov, E., Wolfe, J., Rao, R. P. & Brecht, M. The representation of social facial touch
389 in rat barrel cortex. *Curr. Biol.* **24,** 109–115 (2014).

390 20. Lenschow, C. & Brecht, M. Barrel Cortex Membrane Potential Dynamics in Social
391 Touch. *Neuron* **85,** 718–725 (2015).

21. Welker, W. I. Analysis of Sniffing of the Albino Rat. *Behaviour* **22,** 223–244 (1964).

22. Kleinfeld, D., Ahissar, E. & Diamond, M. E. Active sensation: insights from the rodent vibrissa sensorimotor system. *Curr. Opin. Neurobiol.* **16,** 435–444 (2006).

23. Graziano, M. S. a, Taylor, C. S. R., Moore, T. & Cooke, D. F. The cortical control of movement revisited. *Neuron* **36,** 349–362 (2002).

24. Mountcastle, V. *An organizing principle for cerebral function: the unit model and the distributed system*. *The Mindful Brain* (1978).

25. Lee, E. *et al.* Enhanced Neuronal Activity in the Medial Prefrontal Cortex during Social Approach Behavior. **36,** 6926–6936 (2016).

26. Lenschow, C. & Brecht, M. Membrane potential dynamics of barrel cortex neurons during staged episodes of active social touch. 45 (2012).

27. MacDonald, C. J., Lepage, K. Q., Eden, U. T. & Eichenbaum, H. Hippocampal 'time cells' bridge the gap in memory for discontiguous events. *Neuron* **71,** 737–749 (2011).

28. Schiemann, J. *et al.* Cellular Mechanisms Underlying Behavioral State-Dependent Bidirectional Modulation of Motor Cortex Output. *Cell Rep.* (2015). doi:10.1016/j.celrep.2015.04.042

29. Moore, J. D. *et al.* Hierarchy of orofacial rhythms revealed through whisking and breathing. *Nature* **497,** 205–210 (2013).

30. Deschênes, M. *et al.* Inhibition, Not Excitation, Drives Rhythmic Whisking. *Neuron* **90,** 374–387 (2016).

31. Dörfl, J. The musculature of the mystacial vibrissae of the white mouse. *J. Anat.* **135,** 147–154 (1982).

32. Haidarliu, S., Simony, E., Golomb, D. & Ahissar, E. Muscle architecture in the mystacial pad of the rat. *Anat. Rec.* **293,** 1192–1206 (2010).

33. Herfst, L. J. & Brecht, M. Whisker movements evoked by stimulation of single motor neurons in the facial nucleus of the rat. *J. Neurophysiol.* **99,** 2821–32 (2008).

34. Huber, D. *et al.* Multiple dynamic representations in the motor cortex during sensorimotor learning. *Nature* **484,** 473–478 (2012).

35. Diamond, M. E. & Arabzadeh, E. Whisker sensory system - From receptor to decision. *Prog. Neurobiol.* **103,** 28–40 (2013).

36. Kleinfeld, D. & Deschênes, M. Neuronal basis for object location in the vibrissa scanning sensorimotor system. *Neuron* **72,** 455–468 (2011).

37. Talbot, W. H., Darian-Smith, I., Kornhuber, H. H. & Mountcastle, V. B. The sense of flutter-vibration: comparison of the human capacity with response patterns of mechanoreceptive afferents from the monkey hand. *J. Neurophysiol.* **31,** 301–334 (1968).

38. HUBEL, D. H. & WIESEL, T. N. Receptive fields of single neurones in the cat's striate cortex. *J. Physiol.* **148,** 574–91 (1959).

39. Cao, L.-H., Luo, D.-G. & Yau, K.-W. Light responses of primate and other mammalian cones. *Proc. Natl. Acad. Sci. U. S. A.* **111,** 2752–7 (2014).

40. Kolb, B. Functions of the frontal cortex of the rat: a comparative review. *Brain Res.* **320,** 65–98 (1984).

41. Kawai, R. *et al.* Motor Cortex Is Required for Learning but Not for Executing a Motor Skill. *Neuron* 800–812 (2015). doi:10.1016/j.neuron.2015.03.024

436 42. Stoltz, S., Humm, J. L. & Schallert, T. Cortical injury impairs contralateral forelimb
437 immobility during swimming: a simple test for loss of inhibitory motor control. *Behav.*
438 *Brain Res.* **106,** 127–32 (1999).

439 43. Zagha, E., Ge, X. & McCormick, D. A. Competing Neural Ensembles in Motor Cortex
440 Gate Goal-Directed Motor Output. *Neuron* **88,** 565–577 (2015).

441 44. Berg, R. W. & Kleinfeld, D. Vibrissa movement elicited by rhythmic electrical
442 microstimulation to motor cortex in the aroused rat mimics exploratory whisking. *J.*
443 *Neurophysiol.* **90,** 2950–2963 (2003).

444 45. Penfield, W. & Rasmussen, T. *The Cerebral Cortex of Man*. (The Macmillan
445 Company, 1952). doi:10.1212/WNL.1.1.96

446 46. Filevich, E., Kühn, S. & Haggard, P. Negative motor phenomena in cortical
447 stimulation: Implications for inhibitory control of human action. *Cortex* **48,** 1251–1261
448 (2012).

449 47. Ikeda, A. *et al.* Movement-related potentials associated with bilateral simultaneous and
450 unilateral movements recorded from human supplementary motor area.
451 *Electroencephalogr. Clin. Neurophysiol.* **95,** 323–34 (1995).

452 48. Lüders, H. O., Dinner, D. S., Morris, H. H., Wyllie, E. & Comair, Y. G. Cortical
453 electrical stimulation in humans. The negative motor areas. *Adv. Neurol.* **67,** 115–29
454 (1995).

455 49. Nii, Y., Uematsu, S., Lesser, R. P. & Gordon, B. Does the central sulcus divide motor
456 and sensory functions? Cortical mapping of human hand areas as revealed by electrical
457 stimulation through subdural grid electrodes. *Neurology* **46,** 360–7 (1996).

458 50. Mikuni, N. *et al.* Evidence for a wide distribution of negative motor areas in the
459 perirolandic cortex. *Clin. Neurophysiol.* **117,** 33–40 (2006).

460 51. Kuypers, H. G. J. M. A New Look at the Organization of the Motor System. *Prog.*
461 *Brain Res.* **57,** 381–403 (1982).

462 52. Lemon, R. N., Mantel, G. W. & Muir, R. B. Corticospinal facilitation of hand muscles
463 during voluntary movement in the conscious monkey. *J. Physiol.* **381,** 497–527 (1986).

464 53. Grinevich, V., Brecht, M. & Osten, P. Monosynaptic pathway from rat vibrissa motor
465 cortex to facial motor neurons revealed by lentivirus-based axonal tracing. *J. Neurosci.*
466 **25,** 8250–8258 (2005).

467 54. Sreenivasan, V., Karmakar, K., Rijli, F. M. & Petersen, C. C. H. Parallel pathways
468 from motor and somatosensory cortex for controlling whisker movements in mice. *Eur.*
469 *J. Neurosci.* **41,** 354–367 (2015).

470 55. Takatoh, J. *et al.* New modules are added to vibrissal premotor circuitry with the
471 emergence of exploratory whisking. *Neuron* **77,** 346–60 (2013).

472 56. Buys, E. J., Lemon, R. N., Mantel, G. W. & Muir, R. B. Selective facilitation of
473 different hand muscles by single corticospinal neurones in the conscious monkey. *J.*
474 *Physiol.* **381,** 529–49 (1986).

475 57. Cheney, P. D. & Fetz, E. E. Functional classes of primate corticomotoneuronal cells
476 and their relation to active force. *J. Neurophysiol.* **44,** 773–791 (1980).

477 58. Davidson, A. G., Chan, V., O'Dell, R. & Schieber, M. H. Rapid changes in throughput
478 from single motor cortex neurons to muscle activity. *Science* **318,** 1934–7 (2007).

479 59. Bonini, L., Maranesi, M., Livi, A., Fogassi, L. & Rizzolatti, G. Ventral premotor
480 neurons encoding representations of action during self and others' inaction. *Curr. Biol.*

24, 1611–1614 (2014).

60. Dushanova, J. & Donoghue, J. Neurons in primary motor cortex engaged during action observation. *Eur. J. Neurosci.* **31,** 386–398 (2010).

61. Vigneswaran, G., Philipp, R., Lemon, R. N. & Kraskov, A. M1 corticospinal mirror neurons and their role in movement suppression during action observation. *Curr. Biol.* **23,** 236–243 (2013).

62. Kraskov, A. *et al.* Corticospinal mirror neurons. *Philos. Trans. R. Soc. Lond. B. Biol. Sci.* **369,** 20130174 (2014).

63. Schieber, M. H. Mirror neurons: reflecting on the motor cortex and spinal cord. *Curr. Biol.* **23,** R151–2 (2013).

64. Purves, D. *Neuroscience Third Edition*. *Vascular* **3,** (2004).

Acknowledgements We thank Brigitte Geue, Undine Schneeweiß and Juliane Diederichs for technical assistance and Viktor Bahr and Falk Mielke for assistance with programming. We thank Maria Rüsseler for assistance with video tracking and Rajnish P. Rao and Evgeny Bobrov for sharing tracked whisker traces of behaving rats. We thank Andreea Neukirchner, Edith Chorev, Saikat Ray, Peter Bennett and Ann Clemens for comments on the manuscript. We thank Sara Helgheim Tawfiq for behavior drawings. This work was supported by Humboldt-Universität zu Berlin, the Bernstein Center for Computational Neuroscience Berlin, the German Federal Ministry of Education and Research (BMBF, Förderkennzeichen 01GQ1001A) and NeuroCure. M.B. was a recipient of a European Research Council grant and the Gottfried Wilhelm Leibniz Prize.

Competing interests statement The authors declare that they have no competing financial interests.

Correspondence and requests for materials should be addressed to M.B. (michael.brecht@bccn-berlin.de).

Contributions C.L.E, G.D. and C.L. performed experiments and analysis. M.B. supervised the study. All authors contributed to writing the manuscript.

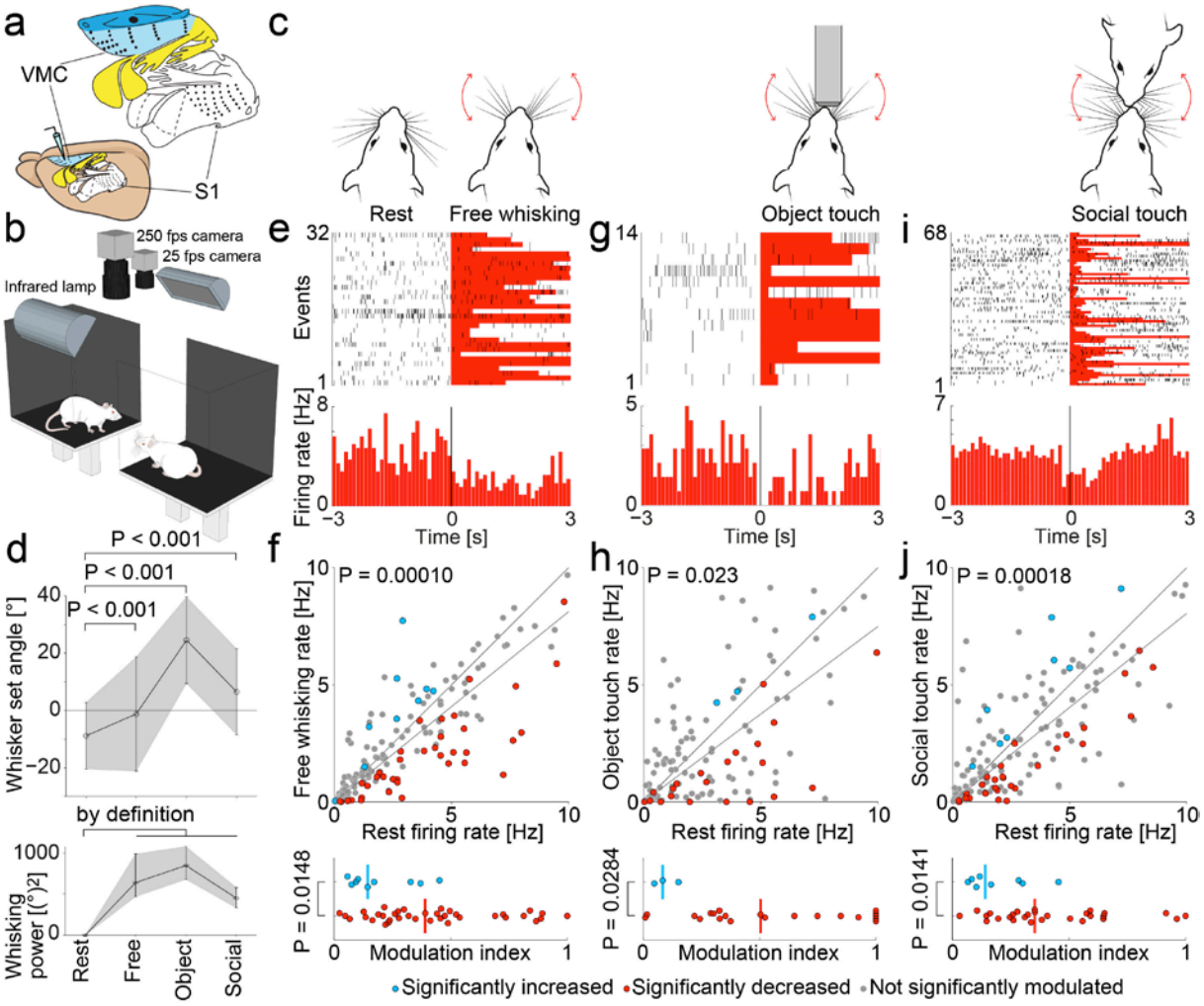

FIGURE 1: Decrease of vibrissa motor cortex activity during vibrissal touch

(a) The vibrissa motor cortex ("VMC", light blue color) is a large frontal area. Somatosensory ("S1", white) and motor (colored) ratunculus shown above.

(b) Experimental setup ('Social gap paradigm', Wolfe et al. 2011) for recording VMC activity during social facial interactions in freely moving rats: A stimulus rat and a rat with implanted tetrodes for recording are placed on two platforms (25 x 30 cm), separated by a gap (~20 cm, varied slightly according to the individual size of the rats). All experiments were performed in darkness, under infrared illumination.

(c) Sketches of four whisking patterns: rest (whiskers not moving), free whisking (self-initiated exploratory whisking in air), object touch (whisking onto objects) and social touch (social touch of a conspecific).

(d) Top: Comparison of whisking set angle during rest to free whisking, object touch and social touch (All $P < 0.001$, t-tests, plot shows mean ± SD). Bottom: Same for whisking power (plot shows median ± 25% and 75% quartiles).

(e) PSTH of activity of a layer 5 VMC neuron aligned to the onset of free whisking. A significant firing rate-decrease is observed.

Correction: The correct label for the x axes in Figure 1e,g,i is "Time (s)"; not "Time (Hz)." Also, the correct P value in Figure 1j is 0.00018; not 0.00018.

(f) Top: Scatterplot of the firing rate during rest vs. free whisking for VMC layer 5 cells. The population activity is lower during free whisking (P = 0.00010, Wilcoxon signed-rank test, dark grey line indicates slope). Cells with significantly decreased activity during free whisking (red dots), cells with significantly increased activity during free whisking (blue dots), cells not significantly modulated (gray dots). Bottom: Modulation index of significantly rate-increasing and rate-decreasing cells. Rate-decreasing cells are more strongly modulated (P = 0.0148, Mann-Whitney U-test).

(g,h) Same as (e,f) for rest vs. object touch.

(i,j) Same as (e,f) for rest vs. social touch.

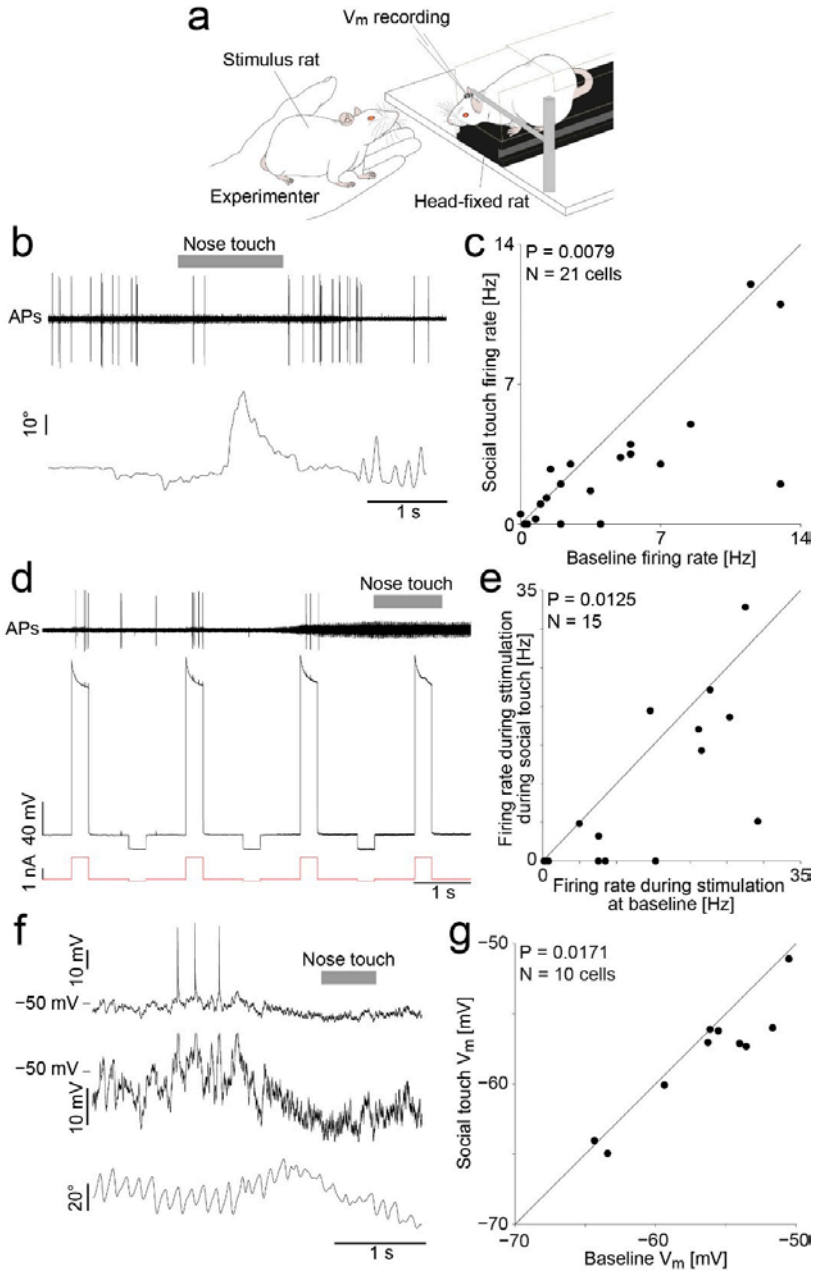

FIGURE 2: Decreased activity, decreased excitability and hyperpolarization of vibrissa motor cortex during social touch

(a) VMC recording and nanostimulation in head-fixed rats during staged social touch.
(b) Top: Example juxtacellular recording in a VMC layer 5 neuron during a social facial interaction, showing a reduction in APs during social touch (nose-to-nose touch indicated by grey bar). Bottom: Angle of contralateral whisker (C2, protraction plotted upwards).

547 (c) Scatterplot of firing rate of VMC layer 5 cells during social facial touch and baseline
548 (P = 0.0079, Wilcoxon signed-rank test).
549 (d) Assessment of cell excitability by nanostimulation. Top: Filtered voltage trace of a
550 VMC layer 5 cell. The evoked firing rate during nanostimulation is higher at baseline,
551 than during social touch (indicated by grey bar). Middle: Unfiltered voltage trace. Bot-
552 tom: Nanostimulation current steps.
553 (e) Scatterplot of the firing rate of VMC layer 5 cells when stimulated during social facial
554 touch and baseline (P = 0.0125, Wilcoxon signed-rank test).
555 (f) Top: Example whole-cell patch clamp recording from a VMC layer 5 cell showing a
556 hyperpolarization of the membrane potential during social facial touch (duration of
557 nose-to-nose touch indicated by grey bar). Middle: Zoom of the above trace (Spikes
558 clipped). Bottom: Angle of contralateral whisker (C2).
559 (g) Scatterplot of the membrane potential (V_m) of VMC layer 5 cells during social facial
560 touch and baseline (P = 0.0171, paired t-test).

561

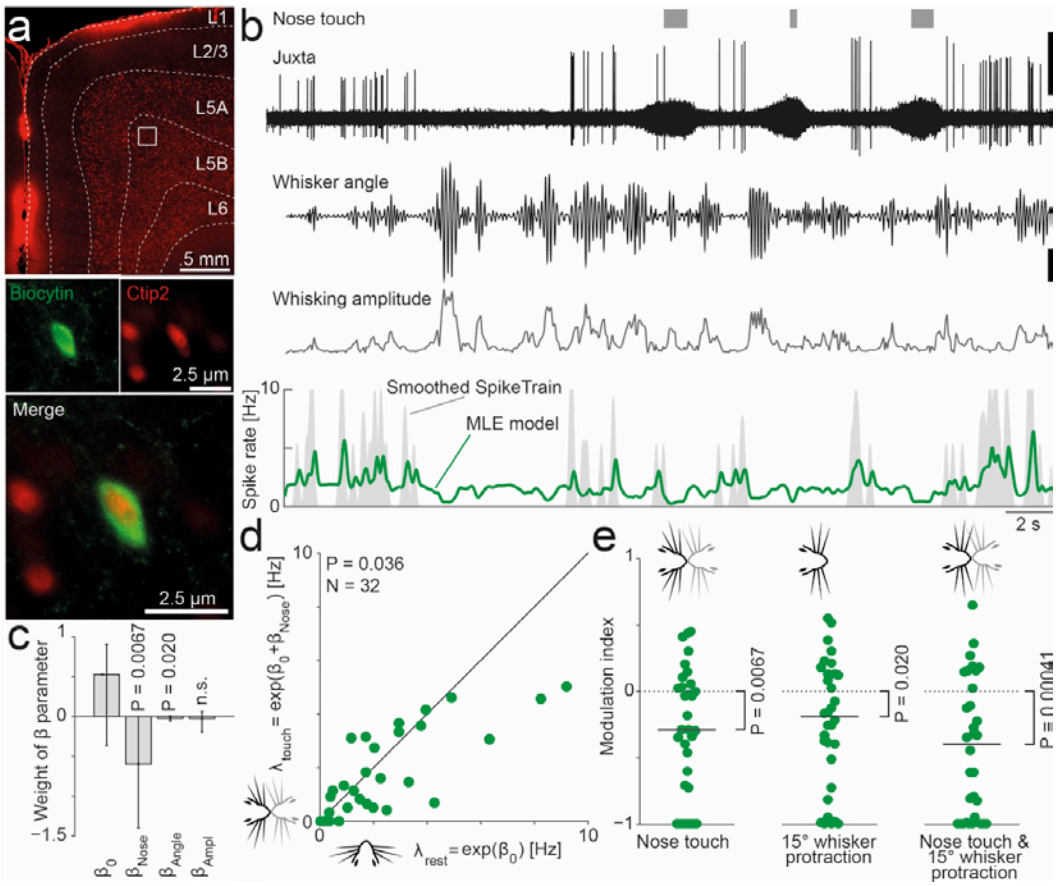

FIGURE 3: Vibrissa motor cortex activity is additively suppressed by both nose-to-nose touch and whisker protraction.

(a) Example soma of a juxtacellularly labeled neuron in layer 5B of VMC. Top: Overview of coronal section of the VMC showing a wide layer 5, which contains a large fraction of Ctip2-positive, putative thick-tufted pyramidal tract (PT-type) neurons (Red channel = Ctip2, white lines indicate layer boundaries traced on brightfield image, white square indicates location of labeled soma: 1.25mm deep, 1.21 mm medial, uncorrected for shrinkage). Bottom: Close up image of the juxtacellularly recorded soma (labeled by biocytin filling, green channel), which is Ctip2-positive (red channel).

(b) Example recorded data and fitted model from the neuron shown in (a). The top traces show the occurrence of nose-no-nose touches (grey bars), the juxtacellular recording trace with spikes (high-pass filtered at 300 Hz, top trace, scale bar = 1 mV) and the whisker angle and whisking amplitude (tracked by high-speed videography, scale bar = 5°). Below we show the estimate of the instantaneous firing rate of the best fitted model ('MLE model', green line, smoothed with a Gaussian with σ = 75 ms for plotting, real model is run with 1-ms bins) plotted on top of an estimate of the observed firing rate ('Smoothed SpikeTrain', grey area, calculated by convolving the spike train with a Gaussian with σ = 75 ms, clipped at 10 Hz for plotting). This cell was suppressed by nose touch, whisker protraction and by increased whisking amplitude (maximum likelihood estimates: $\beta_0 = 0.68$, $\beta_{Nose} = -1.40$, $\beta_{Angle} = -0.06$ $(°)^{-1}$, $\beta_{Ampl} = -0.20$ $(°)^{-1}$)

584 (c) Across the population, VMC activity is significantly suppressed by nose-no-nose
585 touch and whisker protraction (median $\beta_{Nose} < 0$, $\beta_{Ampl} < 0$, both $P < 0.05$), but not sig-
586 nificantly modulated by changes in whisking amplitude.
587 (d) Evaluating the MLE model to estimate the firing rate at rest ($\lambda_{rest} = \exp(\beta_0)$) and dur-
588 ing nose touch ($\lambda_{touch} = \exp(\beta_0 + \beta_{Nose})$) recapitulates the finding from Fig 2c: nose-
589 to-nose touch suppresses VMC activity.
590 (e) Evaluating the MLE model during three behavioral states to demonstrate, that the sup-
591 pression due to nose touch and whisker protraction is additive: nose touch in the ab-
592 sence of whisker protraction (left), 15° whisker protraction in absence of nose touch
593 (middle) and nose touch coinciding with 15° whisker protraction (right) all suppress
594 VMC activity compared to rest.

595

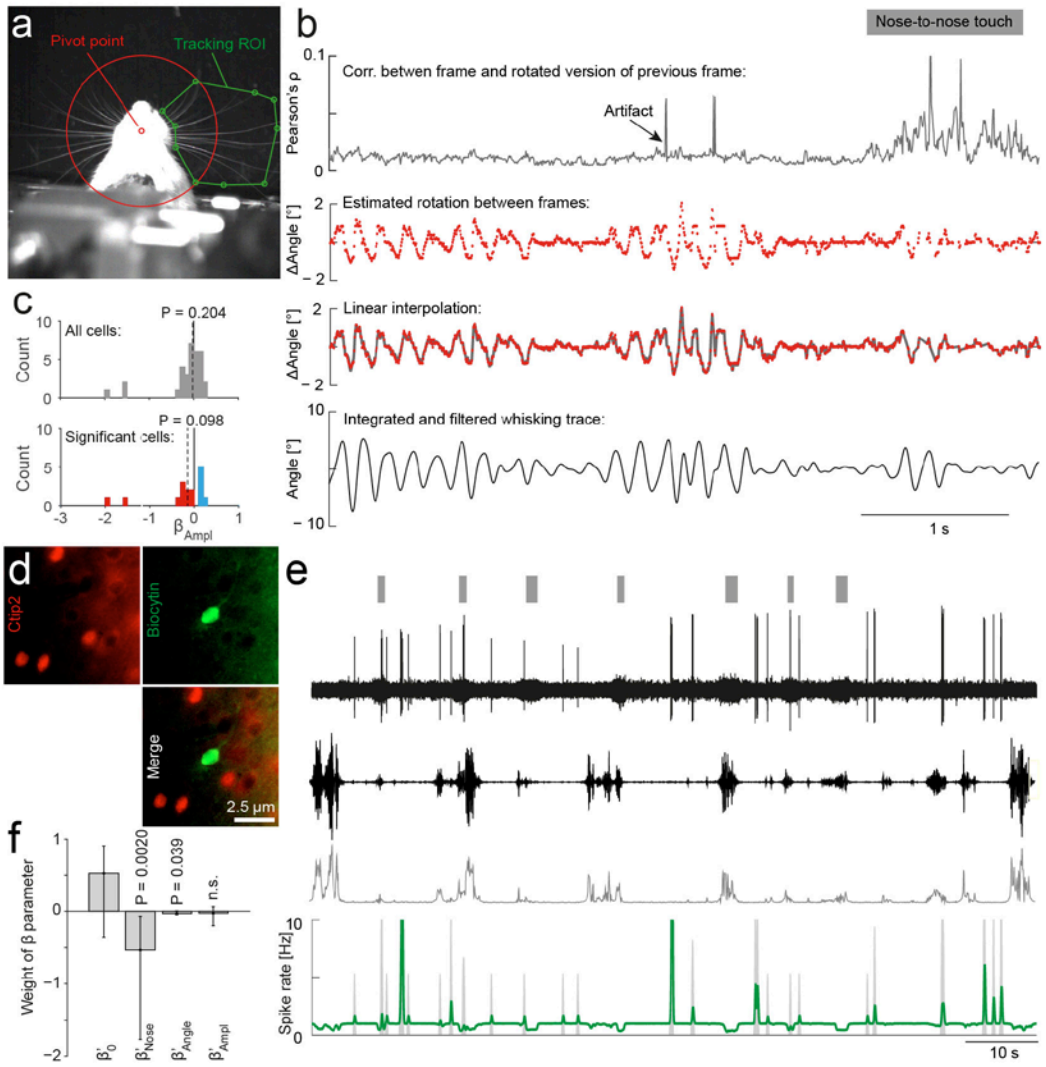

596

597 **FIGURE S3: Whisker tracking procedure and additional modeling**

598 (a) Example high-speed (250 frames/s) video frame showing whiskers of a head-fixed rat
599 during a juxtacellular recording experiment. The pivot point (red dot) and the whisker
600 tracking ROI (green dots) are manually clicked for tracking each video.
601 (b) Example traces demonstrating the tracking procedure. We rotated adjacent frames
602 around the pivot point shown in (a) to maximize the correlation between the frames
603 within the whisking ROI ('Pearson's ρ', top trace) and estimated the mean change in
604 angles between adjacent frames ('ΔAngle', middle traces). Datapoints with sudden
605 spikes in the correlation between frames due to video artifacts were removed from the
606 traces (example marked by black arrow). To estimate the whisking angle, we linearly
607 interpolated, numerically integrated and band-pass filtered the change in angle be-
608 tween frames ('Angle', bottom trace). Grey bar indicates a nose-to-nose touch.
609 (c) Top: Distribution of β_{Ampl} for all cells is not different from zero (P = 0.204, Wilcoxon
610 signed-rank test, also shown in Fig 3c). Bottom: When we plot only significant cells
611 (assessed by a likelihood ratio test), the pattern is mixed: 10 cells are suppressed (red
612 bars) and 6 cells are activated (blue bars). As a population, they are not different from

zero (P = 0.098, Wilcoxon signed-rank test), but we note that the suppressed cells tend to be more strongly modulated that the activated cells: (median$\left|\beta_{Ampl}\right| = 0.221/0.128$ for suppressed/activated cells, P = 0.00025, Mann-Whitney U-test).

(d) Soma of example juxtacellularly labeled Ctip2-negative cell.

(e) Example recorded data and fitted model from the neuron shown in (d). The top traces show the occurrence of nose-no-nose touches (grey bars), the juxtacellular recording trace with spikes (high-pass filtered at 300 Hz, top trace) and the whisker angle and whisking amplitude (tracked by high-speed videography). Below we show the estimate of the instantaneous firing rate of the best fitted model (green line, smoothed with a Gaussian with σ = 75 ms) plotted on top of an estimate of the observed firing rate (grey area, calculated by convolving the spike train with a Gaussian with σ = 75 ms, clipped at 10 Hz for plotting). This cell was suppressed by nose touch, whisker protraction and by increased whisking amplitude (maximum likelihood estimates: β_0 = 0.03, $\beta_{Nose} = -0.70$, $\beta_{Angle} = -0.30\ (°)^{-1}$, $\beta_{Ampl} = -0.38\ (°)^{-1}$)

(f) Fitted betas, when we run the model shown in Fig 3 on stepwise orthogonalized data. In this model, β'_{Nose} measures how the spike rate depends on nose touch, β'_{Angle} measures how the spike rate depends on 'the variation in whisker angle, which is orthogonal to variations in nose touch', and β'_{Ampl} measures how the spike rate depends on 'the variation in whisking amplitude, which is orthogonal to variations in nose touch and variations in whisker angle'.

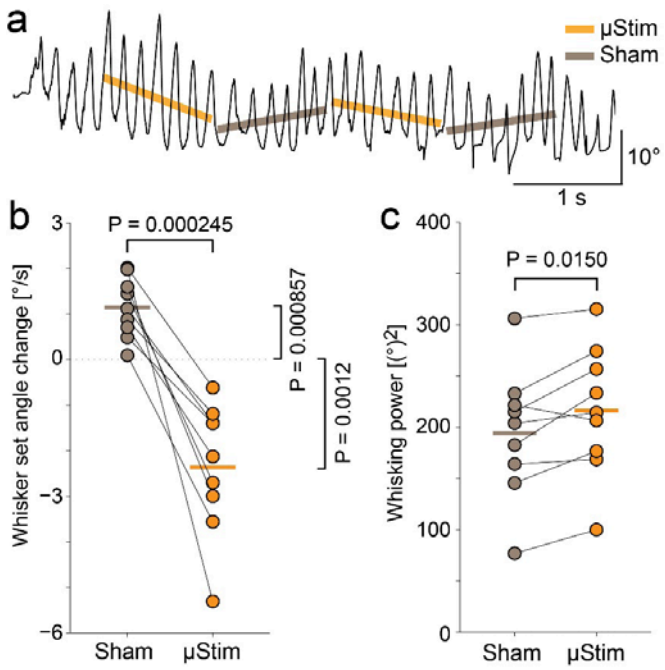

635

636 **FIGURE 4: Unilateral microstimulation of vibrissa motor cortex in awake rats leads to**
637 **contralateral whisker retraction.**

638 (a) Trace of rat whisking during a microstimulation experiment (C2, protraction plotted
639 upwards). Stimulation is delivered in 1 s long pulse trains ("μStim", slope denoted by
640 orange line) alternating with 1 s pauses ("Sham", slope denoted by grey line).
641 (b) Comparison of whisker set angle change during periods of sham stimulation (grey
642 dots) and microstimulation (orange dots, vertical lines indicate means) (P = 0.0002,
643 paired t-test).
644 (c) Same as (b) for whisking power (P = 0.0150, paired t-test).

645

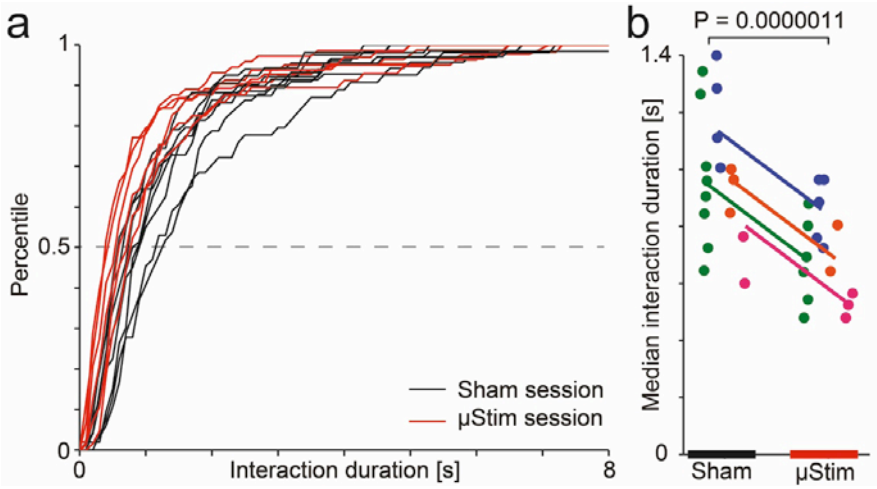

FIGURE S4: Unilateral microstimulation of vibrissa motor cortex shortens social facial touch episodes.

(a) Cumulative histograms of the duration of social facial interactions (from first to last whisker-to-whisker touch) on days with VMC microstimulation during interactions (red lines) and days with sham stimulation during interactions (black lines) for one example rat.

(b) Interactions are shorter with VMC microstimulation than during sham stimulation (N = 4 rats, dots indicate median interaction duration, lines indicate rat-specific slope from LME model, colors indicate rats).

663 **FIGURE 5: Unilateral blockade of vibrissa motor cortex increases contralateral whisker**
664 **movement and protraction.**

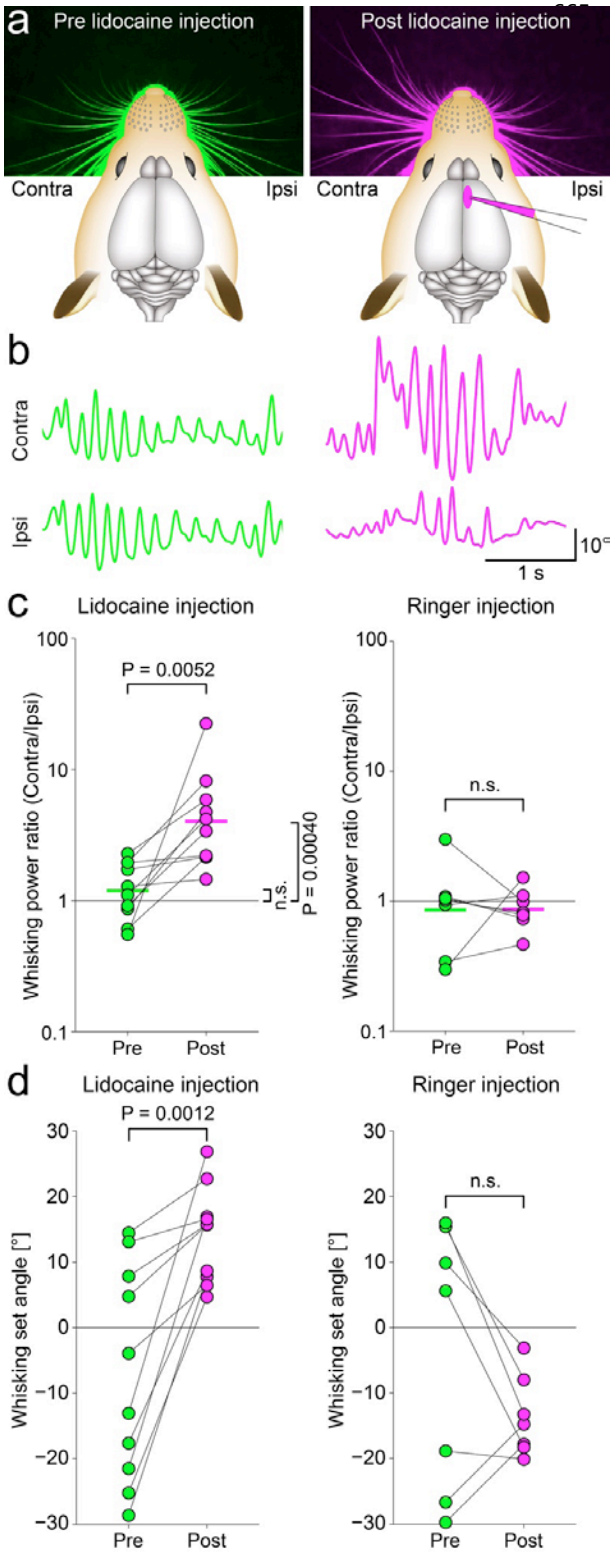

(a) Left: Rat whisker set angles at rest before unilateral lidocaine injection (green color). Right: whisker set angles after unilateral lidocaine injection (pink color) in deep layers of VMC. Lidocaine injection leads to a protraction of the contralateral whiskers.

(b) Ipsilateral and contralateral whisker traces prior to (green color) and after (pink color) lidocaine injection (protraction plotted upwards). Prior to injection, whisking is similar on both sides, after injection the contralateral whiskers move more.

(c) Left: bilaterally symmetric whisking during baseline (contralateral and ipsilateral whisking power ratio ≈1, green dots) changes to a predominance of contralateral whisking after lidocaine injection into VMC deep layers (pink dots, P = 0.0052, paired t-test, lines indicate means). Right: Control injections of ringer have no such effect, (P > 0.05, paired t-test).

(d) Same as (c) for whisking set angle. Lidocaine injection results in contralateral protraction (Ringer: P > 0.05, Lidocaine: P = 0.0012, paired t-tests).

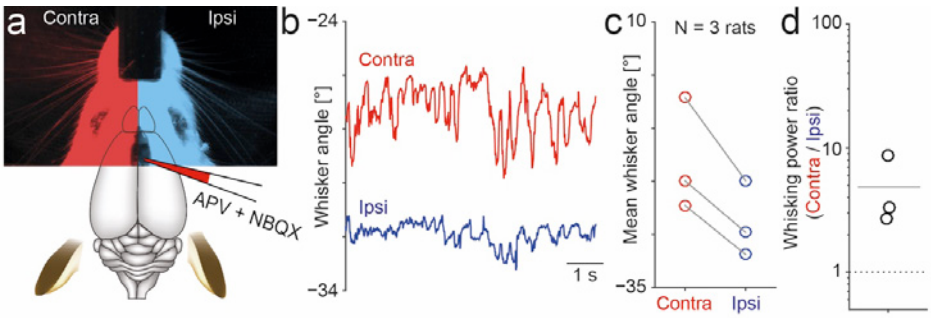

FIGURE S5: Unilateral blockade of vibrissa motor cortex (by AMPA & NMDA antagonists) increases contralateral whisker movement and protraction.

(a) Example image of anaesthetized rat after unilateral VMC blockade (right hemisphere) by superfusion of APV (an NMDA antagonist) and NBQX (an AMPA antagonist).

(b) Example ipsilateral (blue) and contralateral (red) whisking traces of whisker micromovements, which escape light anaesthesia (Whisker arc 1). The contralateral whiskers are more protracted (~27° vs. ~32°) and the contralateral micromovements have a larger amplitude.

(c) After VMC blockade, the whisker set point is higher contralaterally (red markers) than ipsilaterally (blue markers) to the blocked hemisphere (N = 3 rats).

(d) After VMC blockade, the whisking power is much higher (~5 fold) in the contralateral whiskers than in the ipsilateral whiskers (Markers indicate ratio of contralateral to ipsilateral whisker power).

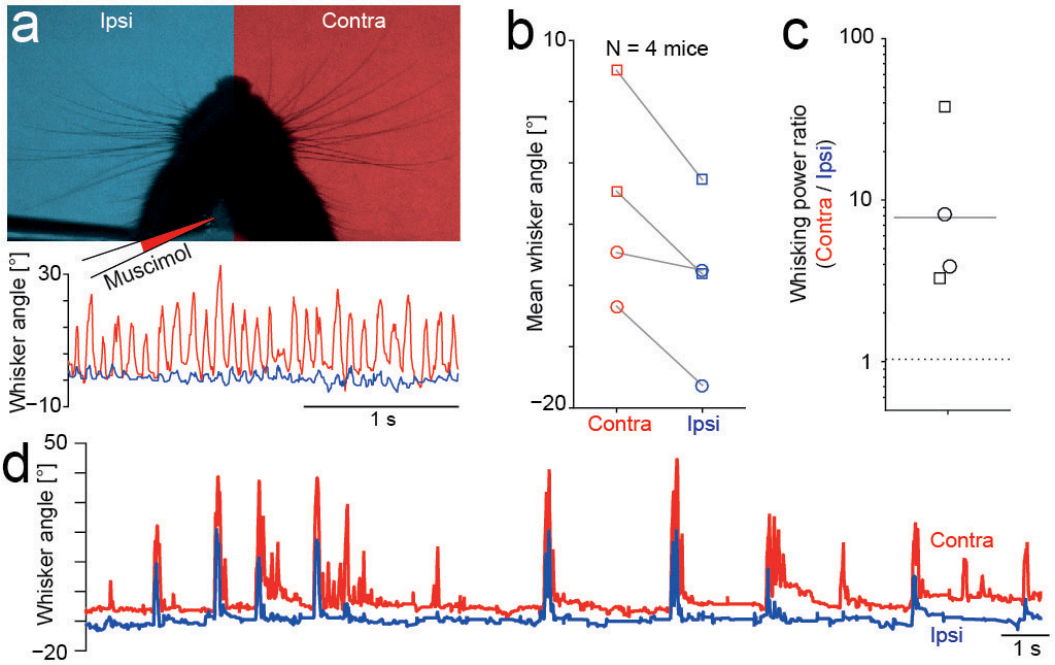

FIGURE S6: Unilateral blockade of vibrissa motor cortex (by muscimol injection) increases contralateral whisker movement and protraction.

(a) Top: Example image of lightly anaesthetized mouse after unilateral VMC blockade (left hemisphere) by muscimol injection, showing protraction of contralateral whiskers. Bottom: Example whisking pattern from the same mouse showing large whisker movements contralaterally, and smaller whisker movements ipsilaterally.

(b) After VMC blockade, the whisker set point is higher contralaterally (red markers) than ipsilaterally (blue markers) to the blocked hemisphere (N = 4 mice). Round markers indicate that only deep VMC was blocked, square markers indicate that both deep and superficial VMC was blocked.

(c) After VMC blockade, the whisking power is much higher (~8 fold) in the contralateral whiskers than in the ipsilateral whiskers (Markers indicate ratio of contralateral to ipsilateral whisker power). Round markers indicate that only deep VMC was blocked, square markers indicate that both deep and superficial VMC was blocked.

(d) Example ipsilateral (blue) and contralateral (red) whisking traces of whisker micromovements which escape light anaesthesia (Whisker arc 1) in another mouse, showing the whisking patterns at a longer time scale.

732 **METHODS:**

733 **Animal welfare**

734 All experimental procedures were performed according to German animal welfare law under
735 the supervision of local ethics committees (Permit no. G0259/09, G0193/14). Wistar rats were
736 purchased from Harlan (Eystrup, Germany). Stimulus animals were housed socially in same-
737 sex cages, and post-surgery implanted animals were housed in single animal cages, but were
738 in visual, olfactory and auditory contact other rats. All animals were kept on a 12h:12h re-
739 versed light/dark cycle with lights off at 8:00 a.m., so that all experiments were performed in
740 the rats' dark phase. Rats had ad libitum access to food and water.

741 **Whisker behavior**

742 Behavioral experiments were done using the "social gap paradigm"[18,19,65]. The experimental
743 paradigm consists of two elevated platforms, 30 cm long and 25 cm wide surrounded by walls
744 on 3 sides, positioned approximately 20 cm apart. The distance between platforms was varied
745 slightly depending on the size of the rats. The platforms and platform walls were covered with
746 soft black foam mats to provide a dark and nonreflective background and to reduce mechani-
747 cal artifacts in electrophysiological recordings and ultrasound recordings. All experiments
748 were performed in (visual spectrum) darkness or in dim light, and behavior was monitored by
749 monochrome video recording obtained under illumination with infrared light, not visible to
750 the rats. The implanted rat was placed on one platform, and on the other platform we either
751 presented various objects or conspecific rats. The implanted rats were not trained, but would
752 spontaneously engage in investigation of the objects or social facial interactions with conspe-
753 cifics.

754 The rat behavior was recorded at low speed from above with a 25 Hz digital camera, synchro-
755 nized to the electrophysiological data acquisition using TTL pulses to trigger each frame. Ad-
756 ditional 250 Hz high-speed recordings were performed, when the rats were freely whisking
757 over the gap, socially interacting or investigating objects. Typically, recording sessions were
758 performed in four to eight 15 min blocks, where we would present either objects or conspecif-
759 ics (of both sexes) in each block, randomly. The video frames of the 25 Hz videos were la-
760 belled in four categories: "Free whisking" (Animal freely whisking into air), "Object touch"
761 (animal touching an object with its nose), "Social touch" (animal touching a conspecific nose-
762 to-nose) and "Rest" (animal not whisking). Videos were labeled blind to the spike data.

763 In our assessment of the whisker set angle and whisker power during the various whisker be-
764 haviors, we included a large dataset of already-tracked whisker traces, some of which have
765 previously been published in Bobrov et al. 2014[19] and Rao et al. 2014[65].

766 To quantify the whisking behavior, the whisker traces were tracked from the 250 Hz video
767 frames, as previously described[18,19,65]. We first band-pass filtered the raw tracked whisker
768 trace to remove jitter due to the tracking (2^{nd} order Butterwoth filter from 0.25 to 12.5 Hz).
769 The whisking power was calculated from a spectrogram constructed by performing a Stock-
770 well transform from 0-20 Hz (frequency steps of 0.1 Hz)[66], and by integrating the absolute
771 value of the power spectral density in the 0-20 Hz band over time to calculate an average
772 power. The set angle was estimated by calculating the average angle of the whisker trace.

773 **Tetrode recording of vibrissa motor cortex activity in freely moving animals**

774 In tetrode recording experiments, we used p60 Wistar rats (N = 5, 3 male, 2 female), which
775 were handled for 2-3 days, before being implanted with a tetrode microdrive over the vibrissa
776 motor cortex (centered on 1.5 mm anterior, 1.5 mm lateral from bregma). Before surgery, the
777 rats were briefly anesthetized with isoflurane and then injected i.p. with a dose of 100 mg/kg
778 ketamine and 7.5 mg/kg xylazine. During the surgery, the anesthesia depth was monitored by
779 watching the rat respiration rate, testing the pinch reflex and monitoring whisker micromove-
780 ment. If the rat appeared to be entering a lighter state of anaesthesia, additional alternating
781 doses of 25% of the initial dose in ketamine/xylazine amount or 25% of the corresponding
782 ketamine dose alone were given. Typically, this was needed 1 h after the first injection. Dur-
783 ing the surgery, the rat was placed on a heating pad and was kept at approximately 35°C using
784 a feedback system attached to a rectal temperature probe (Stoelting, Wood Dale, IL, USA). 10
785 mins before the first incision, the scalp was locally anaesthetized by injection of a 1% lido-
786 caine solution. Then the rat was placed in a stereotax, the scalp was cut and the tissue on the
787 skull removed.

788 The implanted microdrive had eight separately movable tetrodes driven by screw microdrives
789 (Harlan 8-drive; Neuralynx, Bozeman, MT, USA). The tetrodes were twisted from 12.5 µm
790 diameter nichrome wire coated with polymide (California Fine Wire Company), cut and ex-
791 amined for quality using light microscopy and gold-plated to a resistance of ca. 300 kOhm in
792 the gold-plating solution using an automatic plating protocol ("nanoZ", Neuralynx). For tet-
793 rode recordings, a craniotomy of 1x2 mm was made 0.75-2.75 mm anterior and 1-2 mm lat-
794 eral to bregma, corresponding to the coordinates of VMC. Steel screws for stability and two
795 gold screws for grounding the headstage PCB were drilled and inserted into the skull, and the
796 gold screws were soldered and connected to the headstage PCB using silver wire. After fixa-
797 tion of all screws, the dura was removed, the implant fixated in the craniotomy, the cranioto-
798 my sealed with 0.5% agarose and the tetrode drive fixed in place with dental cement (Herae-
799 us). Outer polyimide guiding tubes were arranged in a 2-by-4 grid (d ≈ 500 µm) and contained
800 smaller polyimide tubes, which in turn contained the tetrode wires. Neural signals were rec-
801 orded through a unity-gain headstage preamp and transmitted via a soft tether cable to a digi-
802 tal amplifier and A/D converter (Digital Lynx SX; Neuralynx). The spike signals were ampli-
803 fied by a factor of 10 and then digitized at 32 kHz. The digital signal was bandpass filtered
804 between 600 Hz and 6 kHz. Spike events were detected by crossing of a threshold (typically
805 ~50 µV) and recorded for 1 ms (23 samples - 250 µs before voltage peak and 750 µs after
806 voltage peak). At the end of the experiment, animals were again anaesthetized with a mix of
807 ketamine and xylazine, and the single tetrode tracks were labelled using small electrolytic
808 lesions made by injecting current through the tetrode wire (10 µA for 10 s, tip-negative DC).
809 After lesioning, animals were perfused with phosphate buffer followed by a 4% paraformal-
810 dehyde solution (PFA). Brains were stored overnight in 4% PFA before preparing 150 µm
811 coronal sections. Sections were stained for cytochrome oxidase to reveal the areal and laminar
812 location of tetrode recording sites, which could be calculated from the location of tetrode
813 tracks and lesions. We only analyzed data from recording sites, where the lesion pattern could
814 unanimously identify the tetrode and the recording sites.

815 All spike analysis was done in Matlab (MathWorks, Natick, MA, USA). Spikes were preclus-
816 tered off-line on the basis of their amplitude and principal components by means of a semiau-
817 tomatic clustering algorithm (KlustaKwik by K. D. Harris, Rutgers University). After preclus-
818 tering, the cluster quality was assessed and the clustering refined manually using MClust (A.

D. Redish, University of Minnesota). The spike features used for clustering were energy and the first principle component of the waveform. To be included in the analysis as a single unit, clusters had to fulfill the following criteria: first, the L-ratio, a measure of distance between clusters[67], was below 0.5. Second, the histogram of inter-spike intervals (ISIs) had to have a shape indicating the presence of a refractory time of 1-2 ms, or have the appearance of a bursty cell (many short ISIs). Flat ISI histograms were indicative of multi-unit activities, and these units were not included. Further requirements were that the firing of the cluster was stable over the course of the recordings and that the cluster did not appear to be ”cut” - that is, so close to noise that many spikes were not detected as spike events.

Since we wanted to investigate the contribution of VMC to motor control, we were interested in the spiking activity of the pyramidal projection neurons in layer 5[1]. Due to the different morphology and ion channel populations in the cell membrane, interneurons and pyramidal cells can sometimes be separated based on the shape of the extracellular spike waveform[68]. We tried various combinations of spike shape parameters such as spike-width, peak-to-trough time, shape of after-hyperpolarization, but none yielded convincingly bimodal distributions which allowed separation of cells into regular-spiking putative pyramids and fast-spiking putative interneurons (data not shown). This may relate to the fact that motor cortex projection neurons have exceedingly narrow spikes[69]. Since separation by spike shape was not feasible, we instead reduced the number of fast-spiking interneurons by simply excluding very-high firing cells (mean rate during whole recording session above 10 Hz) from the analysis.

In the case of all three behaviors, we compared the firing rate during the behavior to the firing rate during ”Rest”, defined as when the rats were not moving the whiskers. To statistically asses, if single cells were significantly modulated by whisker behaviors, we used a bootstrap method: First, we calculated a modulation index: $Idx = (R_{behavior} - R_{baseline})/(R_{behavior} + R_{baseline})$ where $R_{behavior}$ and $R_{baseline}$ is the average firing rate at baseline and during the behavior (e.g. during social touch), respectively. In the bootstrapping, we avoided bias by having a balanced baseline design, where the baseline was defined to be segments of time of equal lengths to the nose-to-nose touches, just prior to the beginning of nose-to-nose touches. We generated a distribution of 10.000 bootstrapped dummy modulation indices by preserving the lengths of the nose-to-nose touches, but randomly placing the start-times within the recordings. If the real modulation index was below the 2.5th or above the 97.5th percentile of the bootstrapped dummy indices (i.e. a two-tailed test at $\alpha = 0.05$), the cell was taken to be significantly modulated.

After having assessed that a cell was significantly modulated, we compared significantly modulated cells to ”Rest”. Here we calculated a similar modulation index: Modulation index $= (R_{behavior} - R_{rest})/(R_{behavior} + R_{rest})$, where $R_{behavior}$ and R_{rest} is the average firing rate at ”Rest” and during the behavior of interest (e.g. during social touch), respectively. The response index is symmetric and can take on values between -1 (cell only spikes at ”Rest”) and +1 (cell only spikes during behavior). Thus, cells with negative indices are suppressed during behavior and cells with positive indices are spiking more during behavior. To compare the modulation strength of suppressed and increased cells, we compared the absolute value of this response index.

Head-fixed juxtacellular and whole cell patch-clamp recordings in the vibrissa motor cortex

In juxtacellular recording experiments, rats were between 35 and 40 days old. Whole cell patch clamp recordings were made in younger animals, aged between P25-P30 at the day of the final experiments. All Wistar rats (male) were handled for 2-3 days, before being implanted with a head-fixation post and a recording chamber over the vibrissa motor cortex (1.5 mm anterior, 1.5 mm lateral from bregma). The surgery procedure including anesthesia and preparation of the skull were the same as described above. The head-fixation post and recording chamber were fixed to the skull using a UV-curable adhesive (Kerr) and dental cement (Heraeus). After the first surgery, animals were given 2 days of rest and then habituated to head-fixation over several days. The rat was first head-fixed for 5 minutes in the first head-fixation session, then for an additional 10 minutes with each succeeding session until the rat was comfortable with head-fixation for 60 minutes. During the habituation procedure, the rat was also accustomed to the experimental setup (e.g. microscope light turning on and off, noise from the micromanipulator etc.). Habituation to head-fixation took 2-4 days on average, depending on the rat's behavior. After the habituation procedure a second surgery was performed, during which a craniotomy was drilled inside the recording chamber. In the case of patch-clamp recordings the dura was removed using a bent syringe. The preparation was covered with silicone (Kwik-Cast, World Precision Instruments) and additionally protected by a lid closing the cylinder. After the second surgery, the animals recovered for one day before the recording sessions started.

Juxtacellular and whole-cell patch-clamp recordings were made using glass electrodes made of borosilicate glass tubes (Hilgenberg) pulled to have a resistance of 4 to 6 MΩ. Pipettes were lowered into the cortex with positive pressure (200- 300bar). In both cases, the pipettes was filled with intracellular solution of 135 mM K-gluconate; 10 mM HEPES; 10 mM Na_2-phosphocreatine; 4 mM KCl; 4 mM MgATP; and 0.3 mM Na_3GTP (pH 7.2). After the pipette reached 150-200µm below the surface the following steps were different depending on the recording type. For juxtacellular recordings a nanostimulation protocol was performed and the pipette was lowered stepwise through the cortex (step size: 3µm) until a cell could be detected by excitability (as previously described[70]). In the case of patched cells, the positive pressure in the pipette was lowered to 30 bars to search for cells and the pipette was lowered with a step size of 3µm through the cortex. When the pipette resistance increased, suction was applied to establish a gigaohm seal and achieve the whole-cell configuration. The recorded signal was amplified and low-pass filtered at 3 kHz by a patch-clamp amplifier (Dagan) and sampled at 25 kHz by a Power1401 data acquisition interface under the control of Spike2 software (CED). All head-fixed recording and stimulation experiments were performed at a depth reading of 1423 ± 512 µm (mean ± SD) from the pia, corresponding to putative layer 5 of VMC. Only regular spiking, putative pyramidal neurons were included in the analysis.

During head-fixed recording sessions, stimulus rats, hand held by the experimenter, were presented in front of the head-fixed rat the rats were allowed to socially interact. To monitor social interactions, 25 Hz and 250 Hz digital video synchronized to the electrophysiology data was recorded from above by triggering frames and recording from a Spike2 script. The whisker movements were tracked from the 250 Hz videos using a custom written computer software for whisker tracking (Viktor Bahr, adapted from Clack et al. 2012[71]). Behavioral events (beginning and end of nose touches) were labeled in the 25 Hz videos. All video analysis was performed blind to the electrophysiology data.

To estimate the firing rate change during social facial touch in the head-fixed animals, we computed the average firing rate during 1 second preceding start of social facial touch (begin-

ning of nose-to-nose touch), this we used as a baseline firing rate. Firing rates during social facial touch were computed by averaging the firing rate in a 1 s response window after the onset of nose-to-nose touch. In this analysis, we included both juxtacellularly recorded cells, and patched cells which were spiking. To estimate the change in cell excitability, we calculated the average firing rate from juxtacellularly nano-stimulated cells during positive stimulation pulses, where the rat was not engaging in social facial touch (the baseline). This we compared to the average firing rate during stimulation pulses that happened during a social facial episode (i.e. while the rats were touching nose-to-nose). To estimate the hyperpolarization of the patched cells during social facial touch episodes, we clipped the spikes from the membrane potential and compared the average membrane potential during social facial touch episodes to the average membrane potential during 1 second preceding start of social facial touch (the baseline).

Automatic whisker tracking in socially interacting, head-fixed animals

We used a correlation-based algorithm to automatically track the whisking during juxtacellular recordings in head-fixed rats, all males. We filmed the rats from above using a high-speed camera (250 frames/s, Figure S3a). For each tracked video, we manually clicked a pivot point on the center of the whisker pad and drew a tracking region of interest (ROI) around the whiskers contralateral to the recording craniotomy. To estimate the change in mean whisker angle ('ΔAngle') between two adjacent video frames, we calculated the correlation between the two frames within the tracking ROI (Pearson's ρ calculated between the greyscale values of the pixels) and rotated the previous frame around the pivot point (with nearest-neighbor interpolation), so that the correlation was maximized. This method was very robust, since it considers many whiskers simultaneously, and also worked during nose-to-nose touch episodes, where a few whiskers of the stimulus rat might enter the tracking ROI (Figure S3b, middle). Artifacts from badly tracked video frames were detected as sudden spikes in the correlation (Figure S3b, top) and the corresponding estimated values of ΔAngle were removed (by a threshold of $\rho > 0.03$). To estimate the mean whisker angle ('Angle', Figure S3b, bottom), we linearly interpolated, numerically integrated and bandpass filtered ΔAngle. For filtering, we used a bandpass IIR filter from 5-15 Hz in Matlab, to remove low-frequency drift stemming from the discrete integration. Since our tracking method considers all whiskers within the whisking ROI, our calculated whisker angle should be thought of as the mean deviation from the mean set angle of the whiskers, i.e. Angle = 10° corresponds to a mean-field, net 10° degrees whisker protraction, not an absolute whisker angle of 10°.

Maximum likelihood modeling

We used maximum likelihood modeling to estimate the dependence of VMC activity on the three covariates nose-to-nose touch, whisker angle and whisking amplitude, by fitting a Poisson model to the spike trains[27]. First, we binned the spike train in 1 ms bins. We assume, that the discharge of spikes within one time bin is generated by a homogenous Poisson point process, so that the probability of observing y spikes in a time bin is:

$$p(y|\lambda) = \frac{(\lambda\Delta)^y}{y!}\exp(-\lambda\Delta)$$

where $\Delta = 1$ ms is the width of the time bin and $\lambda > 0$ s^{-1} is the expected discharge rate of the cell. If we assume, that each time bin is independent, the probability of the entire spike train, $\bar{y}$ is:

$$p(\bar{y}|\bar{\lambda}) = \prod_i \frac{(\lambda_i \Delta)^{y_i}}{y_i!} \exp(-\lambda_i \Delta)$$

where y_i, λ_i is the observed number of spikes and the expected discharge rate in the *i*'th time bin, respectively. If we model the expected discharge rate, $\bar{\lambda}$, so that it depends on some parameters, $\bar{\beta}$, we have the log-likelihood function:

$$\mathcal{L}(\bar{\beta}) = \log p\left(\bar{y}\middle|\bar{\lambda}(\bar{\beta})\right) = \sum_i y_i \log \lambda_i + \sum_i y_i \log \Delta - \sum_i \log y_i! - \Delta \sum_i \lambda_i$$

For our purpose, we model $\bar{\lambda}$ so that it depends on the spike history and linearly on a 1-ms interpolated vector indicating nose touch, $\overline{Nose}$ (either 0 or 1), a vector of the whisker angle, $\overline{Angle}$, and a vector of the whisking amplitude, $\overline{Ampl}$ (calculated by quadratically splining the local maxima of the rectified whisker angle). Due to the refractory period of the cell, it is not correct to assume, that all time bins are statistically independent, so following MacDonald et al. 2011[27], we also include 11 spike history parameters, $h_1 \ldots h_{11}$, to model the interspike interval distribution of the cell. The spike history term is binned to 11 successive bins, five 1-ms bins (vectors $\bar{n}_1 \ldots \bar{n}_5$: no. of spikes in the previous 0-1 ms, 1-2 ms, 2-3 ms, 3-4 ms, 4-5 ms,) and six 25-ms bins (vectors $\bar{n}_6 \ldots \bar{n}_{11}$: no. of spikes in the previous 5-30 ms, 30-55 ms, 55-80 ms, 80-105 ms, 105-130 ms, 130-155 ms). We thus have:

$$\lambda_i = \exp\left(\beta_0 + \beta_{Angle} \cdot Angle_i + \beta_{Ampl} \cdot Ampl_i + \beta_{Nose} \cdot Nose_i + \sum_{j=1}^{5} h_j \cdot n_{i,j}^{1ms\ bin} + \sum_{j=6}^{11} h_j \cdot n_{i,j}^{25ms\ bin}\right)$$

For each cell, we fit the model by adjusting the parameters $\beta_0, \beta_{Angle}, \beta_{Ampl}, \beta_{Nose}, h_1 \ldots h_{11}$ so that we maximize the log-likelihood function (using 'fminunc' in Matlab).

Since we did not find a dependence of the population activity on whisking amplitude, we also fitted a reduced model to the spike train, which does not depend on the whisking amplitude:

$$\lambda_i^{reduced} = \exp\left(\beta_0 + \beta_{Angle} \cdot Angle_i + \beta_{Nose} \cdot Nose_i + \sum_{j=1}^{5} h_j \cdot n_{i,j}^{1ms\ bin} + \sum_{j=6}^{11} h_j \cdot n_{i,j}^{25ms\ bin}\right)$$

We then used a likelihood ratio test between the full model and the reduced model to estimate if single cells are significantly modulated by the whisking amplitude. Since there is one less fitted parameter in the reduced model, the log-likelihood ratio:

$$LLRT = -2\log\left(\frac{likelihood\ of\ simpler\ model}{likelihood\ of\ model\ with\ additional\ terms}\right) = 2(\mathcal{L}^{full} - \mathcal{L}^{reduced})$$

follows a χ^2-distribution with one degree of freedom ($\nu = 1$). The p-value of the increase in likelihood due to including whisking amplitude in the model can thus be evaluated using the 'chi2cdf' function in Matlab. We classified cells with $p < 0.05$ as significantly modulated (Figure S3c).

Vibrissa motor cortex microstimulation

Animals were surgically prepared and habituated to head-fixation as described above. The microstimulation[72] was done with 0.3 ms, 50μA unipolar negative-tip current pulses at 100 Hz through a tungsten microelectrode in deep layers (putative layer 5) of the VMC (depth = 1500 μm from the dura). Current pulses were delivered from a stimulus isolator (World precision instruments, Sarasota, USA), gated by TTL pulses sent from a CED Power1401 by protocols written in Spike2 (Cambridge Electronic Design, Cambridge). The stimulation paradigm was blocks of 1 s long stimulation trains interspersed with 1 s long pauses in stimulation ("sham stimulation"). We observed the rats, and when the rats were whisking, we performed the microstimulation protocol during the ongoing whisking. A random number generator ensured that the stimulation would either start with stimulation or with sham stimulation, as not to bias the experiment. Synchronized 250 Hz digital high-speed video was recorded by triggering frames and recording from a Spike2 script. The whisker movements were tracked using a custom written computer software for whisker tracking (Viktor Bahr, adapted from Clack et al. 2012). Whisker tracking was done blind to the timing of stimulation and sham stimulation.

To quantify the change in whisking power due to microstimulation, we filtered the trace to remove jitter and calculated the whisking power as described above. To quantify the change in whisker set angle during the 1 s stimulation periods, and 1 s sham periods, we fitted straight lines to the whisker trace during each 1 s period. We took the slope of these straight lines to be a measure of the average change of whisker set angle per time (°/s), and averaged across these slopes for each experimental session.

For microstimulation in awake, socially interaction rats in the social gap paradigm, we used the same microstimulation train as above, but the microstimulation was applied to deep layer VMC through the tetrode wires, implanted for recording (see above). Stimulation sites were conformed post-hoc by histology. In these experiments, the stimulation was triggered by the experimentor, who was watching the infrared video whenever the rats started socially interacting. The duration of social facial touch was quantified from the 25 frames/s video from the first to last whisker touch of the implanted rat. Since we had a varying number of data points pr. rat (depending on how many days the stimulation sites were found to be in VMC layer 5), we compared the differences between median social facial interaction duration between the stimulated and sham stimulated by fitting a linear mixed effects model (LME model) assuming a gaussian error distribution, with a random rat-specific intercept ('Length ~isStim + (1| Rat)') to account for mean differences among rats[73].

Vibrissa motor cortex blockade in awake rats

Animals were surgically prepared and habituated to head-fixation as described above. Borosilicate injection pipettes (Hirschmann Laborgeräte, Eberstadt, Germany) were pulled to an sharp tip and backfilled with Ringer or a 2% lidocaine solution[74] (bela-pharm, Vechta, Germany). 250 nL Lidocaine was slowly pressure-injected into deep layers (putative layer 5) of the VMC (depth = 1500 μm from the dura) at two injection sites: (1.75 mm anterior, 1.5 mm lateral to bregma) and (1.25 mm anterior, 1.5 mm lateral to bregma), ~2-5 min pr. injection. Based on measurements on the spatial spread of injection of 2% lidocaine in cortex[74], we estimate that the injection of 250 nL lidocaine inactivated an area around the injection site define by a sphere with a radius of 390 μm (which is given simply by the volume equation of the sphere ($V_{inactivated} \approx \frac{4}{3}\pi R^3_{inactivated}$). 250 Hz digital video was recorded by triggering

frames and recording from a Spike2 script and the whisker movements were tracked using a custom written computer software for whisker tracking (Viktor Bahr, adapted from Clack et al. 2012[71]). The whisking was filmed just following the lidocaine injections (i.e. in the few minutes range), where the inactivation by 2% lidocaine injection is largest, and before the cell activity recovers (which happens slowly in the 10-40 min post injection range)[74]. Whisker tracking was done blind to the injected solution (Ringer or lidocaine).

The whisker trace was filtered, and whisking power and whisker set angle was calculated as described above. The ratio of the contralateral whisking power to the ipsilateral whisking power was found to be log-normally distributed (assessed with a Lilliefors test), so we performed log-normal t-tests instead of non-parametric tests to assess statistical significance of the ratios.

Vibrissa motor cortex blockade in anaesthetized rats

Rats were anaesthetized and prepared for head-fixation as described above. A square craniotomy was microdrilled above VMC, 0.5 mm - 4.5 mm anterior bregma and 0.5 mm - 2.0 mm lateral. After dura removal, VMC was superfused with 30 µL blocking solution. The blocking solution was made from 500 µL 1 mM APV suspended in 0.1 M PBS, 50 µL 100 µM NBQX suspended in 0.1 M PBS and 500 µL Ringer's solution. After superfusion of blocking solution, the rat was intraperitoneally injected with 0.1 mL 0.1 mg/mL acepromazine. The animal was monitored until anaesthesia was light and whisker micromovements were observed (typically ~ 60 mins post first ketamine/xylazine dose), and kept in light anaesthesia by additional alternating doses of 5% of the initial dose in ketamine/xylazine amount or 5% of the corresponding ketamine dose alone, respectively. As soon as whisker movements were observed, 250 Hz high-speed videos of the whiskers were recorded at 10 min intervals until 160 mins post blocking. In one rat, the time course of the blocking of excitatory transmission in VMC was monitored with a field electrode, and found to be extinguished in deeper cortical layers of VMC ~ 100 mins post blocking. Whisker movements were tracked from the 250 Hz video and analyzed as described above.

Vibrissa motor cortex blockade in anaesthetized mice

Mice were anaesthetized and prepared for head-fixation as described above, but given 100 mg/kg ketamin, 15 mg/kg xylazine. A square craniotomy was microdrilled above one hemisphere centered on VMC, 0.8 mm anterior bregma, 1.0 mm lateral. The mice supplemented with 0.01, 0.2 mg/mL acepromazine and a head-fixation post was applied to the skull with cyanoacrylate glue. The mice were head-fixed and kept at body temperature with a heating pad. We waited until the anaesthesia became light and we saw whisker movements begin to emerge, then VMC activity was blocked by injection of 25 mM muscimol (a $GABA_A$ receptor agonist, Sigma-Aldrich) suspended in Ringer's solution at 10 nL/min (Huber et al. 2012) using a QSI stereotactic injector (Stoelting). In two mice, we only blocked deep VMC, by an injection of 50 nL muscimol solution 900 µm below the dura, an another two mice, we blocked both superficial and deep VMC by injecting 100 nL muscimol solution at 900 µm and another 50 nL muscimol solution at 500 µm. Injection pipettes (Drummond 5µL) were labeled with DiI and the injection sites were confirmed to be VMC be perfusing the mice and locating the DiI-labeled pipette tracks by fluorescence microscopy. Whisker movements were tracked from the 250 Hz video and analyzed as described above.

Methods references

65. Rao, R. P., Mielke, F., Bobrov, E. & Brecht, M. Vocalization–whisking coordination and multisensory integration of social signals in rat auditory cortex. *Elife* **3,** 1–20 (2014).

66. Stockwell, R. G. Localization of the Complex Spectrum: The S Transform. *IEEE Trans. Signal Process.* **44,** 998–1001 (1996).

67. Schmitzer-Torbert, N., Jackson, J., Henze, D., Harris, K. & Redish, a. D. Quantitative measures of cluster quality for use in extracellular recordings. *Neuroscience* **131,** 1–11 (2005).

68. Barthó, P. *et al.* Characterization of neocortical principal cells and interneurons by network interactions and extracellular features. *J. Neurophysiol.* **92,** 600–608 (2004).

69. Vigneswaran, G., Kraskov, A. & Lemon, R. Large Identified Pyramidal Cells in Macaque Motor and Premotor Cortex Exhibit 'Thin Spikes': Implications for Cell Type Classification. **31,** 14235–14242 (2011).

70. Houweling, A. R., Doron, G., Voigt, B. C., Herfst, L. J. & Brecht, M. Nanostimulation: manipulation of single neuron activity by juxtacellular current injection. *J. Neurophysiol.* **103,** 1696–704 (2010).

71. Clack, N. G. *et al.* Automated tracking of whiskers in videos of head fixed rodents. *PLoS Comput. Biol.* **8,** e1002591 (2012).

72. Tehovnik, E. J., Tolias, A. S., Sultan, F., Slocum, W. M. & Logothetis, N. K. Direct and indirect activation of cortical neurons by electrical microstimulation. *J. Neurophysiol.* **96,** 512–521 (2006).

73. Aarts, E., Verhage, M., Veenvliet, J. V, Dolan, C. V & van der Sluis, S. A solution to dependency: using multilevel analysis to accommodate nested data. *Nat. Neurosci.* **17,** 491–6 (2014).

74. Tehovnik, E. J. & Sommer, M. A. Effective spread and timecourse of neural inactivation caused by lidocaine injection in monkey cerebral cortex. *J. Neurosci. Methods* **74,** 17–26 (1997).

8. Motor cortex – To act or not to act?

This manuscript was submitted as:
Ebbesen, C.L., & Brecht, M. (2017) Motor cortex – To act or not to act? (submitted to **Nature Reviews Neuroscience** on 21.0.3.2017), subsequently published as **Ebbesen, C.L.**, & Brecht, M. (2017) Motor cortex – To act or not to act? (2017) **Nature Reviews Neuroscience** 18(1):694-705-
This is the author's version of this work, reprinted with permission from Nature Pub. Group

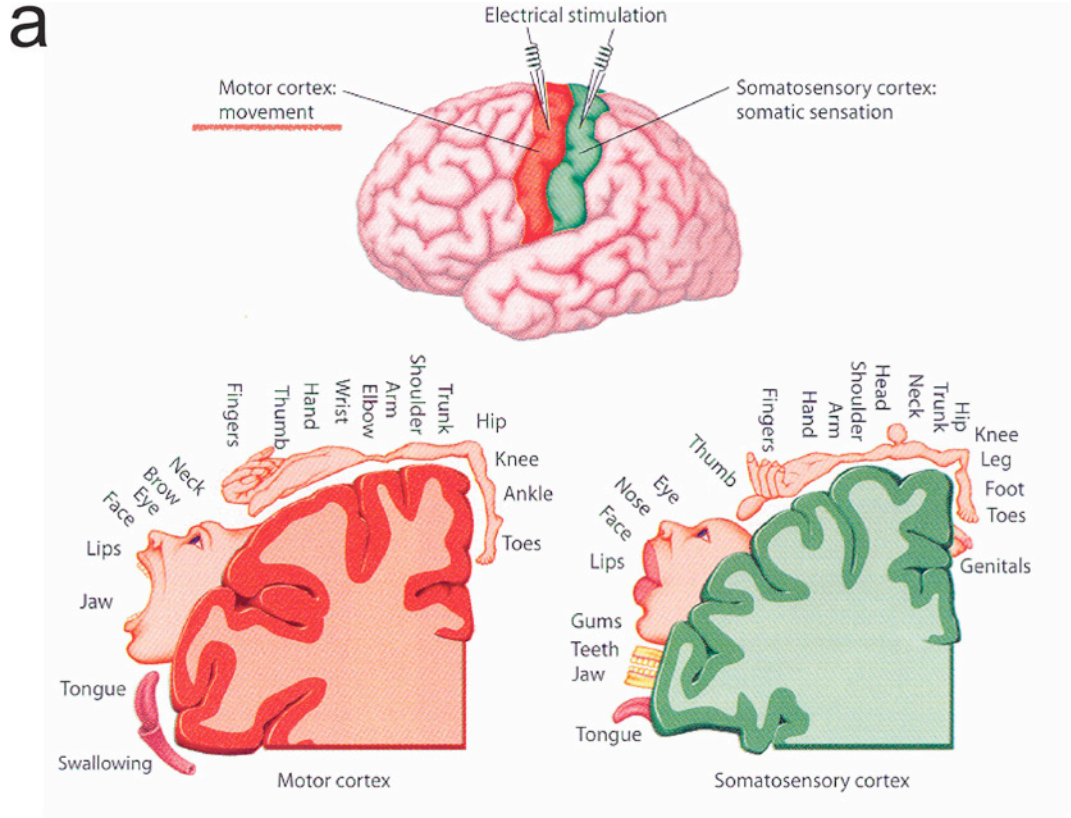

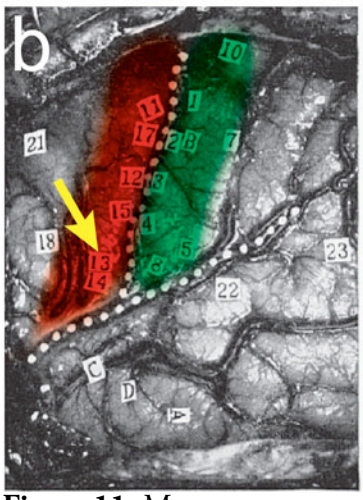

13 (1½v)—Repeated, while patient was squeezing Dr. Stephen's hand. After it was over he said, "I could not do it." The hand had relaxed instantly when stimulation was carried out. When stimulation was withdrawn, he squeezed the hand again.

14 (1½v)—Patient said, "Yes, it felt like a paralysis going down my right leg." When asked again he said that it felt like a numbness.

14 (1½v)—Restimulated while patient was carrying out voluntary movement of the foot. Movement relaxed during stimulation and came again when stimulation was withdrawn. [...]

13 (1½v)—Restimulated. "Oh, my right hand. I couldn't move it." When asked what attracted his attention to his hand, he said, "I had a sensation I wanted to move it."

14 (1½v)—Restimulated. Strange numbness in the right hand. No movement in the hand. No sensation in the arm, but it moved a little.

14 (1½v)—Restimulated 2 mm. lower, in edge of fissure of Sylvius. Sensation in foot, from the ankle down. A feeling of numbness as though he wanted to move it toward him, but he could not move it.

Figure 11: Movement suppression is under-represented in depictions of motor cortex (a) A textbook illustration of the human 'motor' (red) and somatosensory (green) cortex after the intraoperative stimulation experiments by Penfield & Rasmussen. The textbooks interpret human motor cortex as a 'motor homunculus', that is a muclelotopic motor map: "Motor cortex: movement" (red underscore, added). (b) Intraoperative photograph of an actual human motor (red, color added) and somatosensory cortex (green, color added) mapping experiment, as reported in the famous book by Penfield & Rasmussen (1952). Right, we see what the patient reports, when site 13 and 14 (yellow arrow, middle of motor cortex) are stimulated: a clear suppression of movement.

Motor cortex – To act or not to act?

by

Christian Laut Ebbesen[1,2] and Michael Brecht[1,3]

[1]Bernstein Center for Computational Neuroscience Berlin, Humboldt-Universität zu Berlin, Berlin, Germany

[2]Berlin School of Mind and Brain, Humboldt-Universität zu Berlin, Berlin, Germany

[3] NeuroCure Cluster of Excellence, Humboldt-Universität zu Berlin, Berlin, Germany

Correspondence should be addressed to M.B. (michael.brecht@bccn-berlin.de)

Article Format: Opinion

WORD COUNT:

Abstract: 240

Main text: 5870

Abstract

The motor cortex is a large frontal structure in the cerebral cortex of eutherian mammals. A vast array of evidence implicates the motor cortex in the volitional control of motor output, but how does the motor cortex exert this 'control'? Ideas regarding the motor cortex have historically been shaped by the discovery of cortical 'motor maps', i.e. ordered representations of stimulation-evoked movements in anaesthetized animals. Volitional control, however, entails the initiation of movements as well as the ability to suppress undesired movements and behave in a non-reflexive fashion. In this review, we highlight classic and recent findings which emphasize that motor cortex neurons not only initiate movement, but also contribute strongly to movement suppression. Motor cortical stimulation in awake subjects often leads to movement arrest and motor cortical inactivation often disinhibits movements which are normally suppressed. Similarly, there is an unusual predominance of suppression of motor cortical population activity during movement and an increase of motor cortical activity in tasks which require the withholding of motor output. Thus, stimulation, recording and inactivation studies suggest that the motor cortex – at least in some instances – exerts a negative control of movement. This type of control is rather different from the representation in sensory cortices, where sensory stimuli almost invariably drive population firing rate increases and sensations. Action suppression is critical for the strategic planning of behavior and numerous observations suggest that motor cortical activity contributes heavily to this important and understudied cognitive ability.

Introduction

The discovery of motor cortex as a 'motor map'

In the late 1860s, two young physicians conducted an experiment which defined our thinking about the brain and about motor control. Fritsch and Hitzig did not have laboratory working space and therefore went home, tied down their experimental animals on Fritsch's wife's dressing table, and performed one of the greatest neurophysiological experiments of all times: They used electrodes to electrically stimulate the surface of the cerebral cortex of anesthetized dogs (Figure 1a, left). They adjusted stimulation currents to evoke a tickling sensation when applied to their own tongues. When Fritsch and Hitzig applied the same currents to specific sites in the frontal cortex of their experimental animals, something very spooky happened: Currents evoked movements of the experimental animals, whereby the type of evoked movement varied with the cortical location of the stimulation site[1] (Figure 1a, right). The discovery of this 'motor map' paved the way for modern thinking about the cerebral cortex. Ferrier soon reproduced Fritsch and Hitzig's results in monkeys[2] and after years of careful experiments it gradually became clear that the cortical motor representation is highly somatotopic, with a fine-grained 2D map of the external body[3]. In later work, it became clear that long and more intense stimulation trains can activate very complex motor patterns[4]. Although early experiments demonstrated that surgically lesioning the frontal 'motor sites' did not abolish movements[1], these experiments indicated that a prime role of this cortical area must be movement generation, hence the name *motor* cortex.

The discovery of a 'movement suppression map' in human motor cortex

A major advance in our understanding of the motor cortex came when cortical mapping experiments were done in humans. The Canadian neurosurgeons Penfield and Rasmussen[5] mapped the cortex in awake patients during surgeries. This approach has an enormous advantage over anaesthetized animal experimentation: the experimenter can *ask* the patient how the cortical stimulation feels. These experiments yielded two insights: First, they confirmed that the human motor cortex contains a somatotopic map of the body, a motor 'homunculus' (Figure 1b, left). Secondly, the human patients often reported that motor cortex stimulation lead to movement inhibition and muscle relaxation. Upon stimulation of motor cortex sites, patients felt a sense of paralysis and numbness focal to specific body parts (Figure 1b, right, during motor cortex stimulation: *'I could not do it […] it felt like a paralysis' – 'Oh, my right hand. I couldn't move it.*'). The Penfield and Rasmussen

experiments demonstrated that the human motor cortex is not a pure 'motor map'[5], but also a map of movement suppression[6].

Several subsequent studies have made similar observations and shown that so-called negative motor areas (cortical areas where stimulation inhibits movement) are widespread across motor cortex[7–10] and premotor cortices[11]. Such movement-suppressive effects of motor cortex stimulation are impossible to discover in experiments on anaesthetized animals where only 'positive' motor effects can be evaluated. Interestingly, we know from animal experiments that many motor cortex stimulation sites produce no movements at all[12–14], but the 'motor maps' observed from stimulating motor cortex in anesthetized animals have dominated our thinking about motor cortex function[15]. A further complication lies in the fact that 'negative motor area' stimulation can be made to elicit positive movements (i.e. muscle twitches) with an increasing stimulation current[10], and may thus remain unnoticed if only positive stimulation effects are evaluated[11].

Is the motor cortex a brain structure for movement generation, a brain structure for withholding movements – or both? Below, we review these two complementary views of motor cortex function and highlight open questions.

From motor cortex to muscle output

What do we mean, when we say 'motor cortex'?

The motor cortex is a large frontal structure in eutherian mammals (Figure 2a). There are a number of ways to define primary motor cortex. As described above, the 'classic' definition of motor cortex is physiologically defined as the largest frontal area where e.g. electrical[1,2,6,12,16] or optogenetic[14,17] stimulation elicits somatotopically organized movements at low stimulation thresholds. In higher mammals, this 'body-map' of movements is adjacent to and is a mirror image of the body map in primary somatosensory cortex[12,16,18–21]. We suggest that these four criteria (low stimulation thresholds for movements, full body topography, adjacent to primary somatosensory cortex, mirror image topography of primary somatosensory cortex) identify a homologous area in eutherian mammals. By this definition, marsupials (an early branch of the mammalian tree) have only a large somatosensory representation, but no motor cortex[21–23] (Figure 2a, left). In rodents, the primary motor cortex is very large and takes up almost all of frontal cortex[12,16,24,25] (Figure 2a, middle). In primates, frontal cortex contains several specialized premotor and prefrontal structures and the primary motor cortex takes up (in relative terms), a much smaller area, a thin strip anterior to the rolandic fissure (Figure 2a, right)[2,3,5].

Other definitions of motor cortex rely on anatomical markers such as a thick layer 5b and a near-absent layer 4[26,27], the frontal area of origin of corticospinal projections[28,29] or the area of dense corticocortical innervation from primary somatosensory cortex[30,31]. Finally, some definitions are based on mixed criteria[32] and often rely on comparative anatomy to name motor structures in e.g. the rodent brain after their putative corresponding primate homologues[18,20,21,32]. The precise correspondence between primate and rodent motor cortex (and other premotor areas) is largely unknown and different ways of delineating motor cortex sometimes suggest conflicting naming schemes[33]. For example, the area of rat cortex which the physiological approach designates as primary vibrissa motor cortex[12,16,17,19], is referred to as secondary motor cortex ('M2', a putative homologue of primate supplementary motor areas) by the rat brain atlas[32] and some publications[34–39] and as frontal orientation field ('FOF', a putative homologue of primate frontal eye field) by others[40–43].

Parallel inhibitory and excitatory pathways from motor cortex to motoneurons

Motor cortical neurons do not innervate muscles directly. The most 'direct' pathways from motor cortex to muscles are from so-called pyramidal tract-type neurons, which have their

somata in layer 5 of motor cortex and send their axons through the pyramidal tract to target neurons in the spine and brainstem. Some pyramidal tract neurons synapse directly onto motor neurons which innervate muscles. This provides a straightforward circuit for motor control: if pyramidal tract neurons spike, downstream motoneurons depolarize and spike, which elicits muscle contraction[44]. This direct wiring pattern in mammals, however, appears to be the exception rather than the norm. In rodents[45–49] as well as primates[44,50], the predominant wiring pattern of corticobulbar and corticospinal projections from motor cortex is not directly to motoneurons, but rather to brainstem and spinal interneurons, many of which have inhibitory connections onto motor neurons[44,51] (Figure 2b, left). The monosynaptic projections from motor cortex to motor neurons in primates is a specialization of primate distal limb muscles, which seems to have evolved for dexterous and fractionated digit movements[50,52–54] (Figure 2b, right).

Anatomical loops via other motor centers

In addition to direct corticospinal projections from motor cortex, there are major projections from motor cortex to other cortical and subcortical motor structures, such as the somatosensory cortex, the basal ganglia, the motor thalamus, the brain stem and the cerebellum[55–57]. Like the motor cortex, the somatosensory cortex also directly innervates spinal and brain stem motor centers and can directly modulate muscle output[6,12,17,47]. Many motor cortical and pyramidal tract neurons send axon collaterals through the striatum and target neurons in the subcortical nuclei of the basal ganglia, which also contains circuits for both facilitation and suppression of muscle output. The basal ganglia circuitry is complex and not sharply dichotomous[58–61], but in the 'classic' model, the basal ganglia is separated into the so-called 'direct' and 'indirect' pathways[58,62]. The net effect of exciting striatal neurons through the direct pathway is a disinhibition of spinal motor centers, while the net effect of exciting neurons through the indirect pathway is an increase in inhibitory drive from the basal ganglia to downstream spinal motor centers.

Facilitation and suppression of muscle activity by motor cortical spikes

Through direct projections from motor cortex to spinal neurons and through indirect projections via other motor centers, parallel anatomical loops exist, by which motor cortical activity might potentially facilitate or suppress muscle activity. Spike-triggered averaging of muscle electromyography (EMG) signals reveals that spikes of single motor cortical pyramidal-tract neurons can predict both EMG peaks and EMG troughs[44,63–65]. In primates, monosynaptic excitatory connections between motor cortex neurons and spinal motoneurons

are abundant, and net inhibitory connections to motoneurons are multisynaptic via spinal interneuron microcircuits. Accordingly, peaks in the spike-triggered EMG (indicating muscle facilitation) are abundant (~24% of neurons), large and have a short latency. Troughs in the spike-triggered EMG, on the other hand, appear fewer in number (~2% of neurons) and are smaller, presumably due to the temporal noise induced by the many synapses between motor cortical spike and muscle contraction. This higher noise makes it likely that spike-triggered averaging underestimates the functional connectivity of motor cortical neurons that lead to net suppressive effects[63–65]. More generally, spike-triggered averaging techniques are only well suited to reveal oligosynaptic connections from motor cortex to motoneurons. During active behavior, it is possible that motor cortex may act to initiate[30] or to suppress[66] motor programs initiated reflexively from subcortical circuits including the basal ganglia and brainstem[49,67,68].

An alternative way of revealing the impact of motor cortical activity on muscle output is to relate EMG signals to intra-cortical microstimulation. Motor cortex microstimulation also causes increases and decreases in EMG signals and in the membrane potential of spinal motorneurons[64,65,69–71] (Figure 2c). In microstimulation experiments using brief stimulation trains (~few ms), net EMG-suppression is much more common than that EMG-facilitation[64,65], thus implicating motor cortical neurons in the suppression of muscular activity. In microstimulation experiments using longer stimulation trains (several hundred ms), it is possible to elicit coordinated sequences of muscle activation and inhibition towards a range of body postures[4,72].

Clearly, analyzing the relationship between motor cortex activity and muscle activity by either spike-triggered averaging techniques or by cortical microstimulation leads to very different conclusions. Intracortical microstimulation induces neural activity that is very different from 'natural' physiological patterns[73–75]. Thus, the fact that investigations of the functional connectivity from motor cortex to muscles suggest a substantial movement-suppressive role of motor cortex activity might be viewed simply as artificial effects, which are interfering with natural motor programs and have little physiological relevance. There is also evidence to suggest that the relationship between motor cortex and muscle activity is highly dynamic[71]. Additionally, even though the effects of microstimulation point to a substantial role of motor cortical activity in the suppression of muscle activity, suppression of muscle activity is not necessarily suppression of motor output. Initiation of most motor actions, such as reaching, involves both muscle excitation and inhibition. In the limb motor system there are agonist and antagonist muscles that span the various joints which must be coordinated to make a movement[65,76].

Motor cortex – to act? The physiology of action

In this section, we will review motor cortex activity patterns which are associated with action. Here, it is important to emphasize the immense diversity of motor cortex discharge patterns. Such response diversity might contribute to behavioral flexibility of motor outputs, but it limits the validity of general statements about motor cortex activity. In motor cortex – much like in other cortices – cellular responses greatly vary between cortical layers and cell types; the need for cell-specific readouts and unbiased population analysis is becoming increasingly recognized.

Distal limb movements in monkeys

A major share of what we know about how motor cortical activity correlates with movement comes from single-cell recordings in primates performed with reaching movements and hand-manipulations. Just as with the interpretation of stimulation effects, it is a caveat that an increase in motor cortical activity can be seen as facilitating movement in reference to the excitation of agonist muscles but also as inhibition in reference to the antagonists. However, even though some motor cortical neurons decrease their activity during such movements, the majority of motor cortical and pyramidal-tract neurons correlate positively with movement and force[77–82] (Figure 3a). Motor cortex recordings during arm movements in monkeys displayed peak firing rates just prior to movement onset and a cessation of activity before movement completion, suggesting a role of motor cortex in movement initiation[77].

Complex activity patterns during limb movements in non-primates

In other mammals, the relationship of motor cortical firing rates with limb movements is complex. In cats, for example, there is no overall modulation of motor cortical activity during locomotion compared to rest[83,84]. However, motor cortical activity increases with the 'difficulty' of the locomotion, when the animal must make precise, controlled steps, such as over obstacles or onto narrow steps of a ladder[84–86]. Most motor cortical neurons progressively increase their firing rate when the cat walks progressively slower to take smaller steps between barriers[87]. Motor cortical activity in cats is also related to phases of the step cycle, with more spiking during the swing phase (where the foot is not touching the ground) than during the stance phase (where the foot is applying force against the ground)[84–87].

With current techniques, it is now possible to investigate the relationship between motor cortical activity and motor output with high fidelity in rodents[88]. In contrast to the archetypal

increase of motor cortical activity with movement observed in most studies on primate motor cortex[77–82], there is a surprising predominance of suppression of rodent motor cortical activity during movement across several studies and several motor behaviors. For example, a recent study used extracellular recordings to investigate activity in deep layers of motor cortex in mice running freely on a treadmill. During locomotion, the average spike rate of neurons in deep layers of motor cortex decreased by 30% and single units, which discharged less spikes during locomotion (66% of neurons), were much more common than neurons which increased their firing rate during locomotion (34% of neurons)[89]. Further, the reduction in spike rate correlated with the spike width, such that units with wider spikes (putative principal cells[90], see[91–93]) showed the strongest suppression of activity[89].

In a similar study, the activity of layer 5b neurons during locomotion in mouse motor cortex was investigated with intracellular recordings[94]. In this study, there was also an unusual abundance of layer 5b motor cortical neurons which decreased their spike rate during locomotion (Figure 3c). Overall, there was no modulation of motor cortical firing, but at the single-cell level, there was a higher number of significantly activated (53%) compared to suppressed (38%) layer 5b neurons during locomotion[94].

Vibrissa motor cortex activity decreases during whisking

In the rodent whisker system, movements can be easily quantified. Similar to locomotion, but different from grasping and reaching, whisking movements are mediated by a subcortical central pattern generator. The whisker motor plan is laid out for highly controlled whisker protraction[95], which the animal uses to palpate objects in front of the nose[96,97]. Vibrissa motor cortex is huge (Figure 2a) and makes up approximately 6.5% of the whole cortical sheet[12,16,19,24,25]. Remarkably, vibrissa motor cortical neurons decrease spiking activity during various whisking behaviors. Several studies have examined the relationship between vibrissa motor cortex activity and whisking kinematics[67,98–100]. The exact relation between vibrissa motor cortex activity and whisker movement is still debated. An early study examined the relationship between vibrissa motor cortex activity and whisker pad EMG[98] and did not find *"any obvious correlation"*[101]. Several subsequent studies made similar observations and found no overall modulation of vibrissa motor cortex population activity by whisking[67,98–100], but this view has been challenged by two recent publications[30,66]. One investigation found that during whisking in head-fixed mice, there was a decrease in the firing rate of layer 2/3 and a more mixed response pattern in layer 5[30]. Specifically, there was a small increase in layer 5 activity around the onset of whisking and single cells displayed both firing rate decreases and

increases during whisking[30]. Similar to earlier conclusions from monkey motor cortex, such findings might indicate a role of vibrissa motor cortex in whisking initiation[30]. Another study also investigated activity in layer 5 of vibrissa motor cortex, but this time in freely moving rats during various forms of more naturalistic whisking behaviors. Exploratory whisking in air, whisking to palpate objects and social whisking during facial interactions with conspecifics[66] were associated with ~21% overall decrease in spike rates in layer 5 of vibrissa motor cortex. Further, intracellular recordings from layer 5 vibrissa motor cortex neurons in socially interacting rats revealed that social whisking was associated with reduced cellular excitability and membrane hyperpolarization[66].

Motor cortical inhibition during reaching movements

In a forelimb task, where head-fixed mice must push and pull a lever to receive a reward, various studies have also revealed suppressed motor cortical activity during forelimb movement: Across all layers of motor cortex, more putative pyramidal neurons were active during phases of non-movement than during the actual movement phases. Based on extracellular unit recordings across all layers, 43% of task-related neurons were active during movement, while 57% were active during non-movement[102] (Figure 3d). Juxtacellular recordings targeted to deep-layer neurons (> 900 μm) yielded a more mixed picture with an equal proportion of task-related neurons firing during movement and during non-movement. Interestingly, however, the vast majority (94%) of fast-spiking interneurons in motor cortex fired during the movement phase, suggesting that phases of forelimb movement are associated with greatly increased motor cortical inhibition[102].

Another study investigated motor cortical activity in mouse motor cortex during reaches, which were cued by a vibrotactile stimulus to the paw[103]. The response of regular spiking units during reaches was mixed with 20% of regular spiking units showing significantly decreased and 39% showing significantly increased spike rates. In agreement with high levels of motor cortical inhibition noted above, almost all parvalbumin positive interneurons increased their firing rates[103].

In primates, attempts have also been made to investigate how motor cortical activity patterns during reaching map onto principal and inhibitory cell types. One study used spike-width to identify putative inhibitory interneurons in motor cortex and found that in this subpopulation, firing rates tended to massively increase during movement, whereas the responses in putative principal neurons was more mixed and showed less of an increase in firing rates upon movement[82]. It should be noted, however, that some primate pyramidal cells in macaque

motor cortex have very narrow spikes[104] and a large subset of interneurons in monkey motor cortex have surprisingly wide spikes[105]; thus, this result should be taken with some caution[92].

Decreased corticospinal activity from rodent motor cortex during movement

We know relatively little about the activity patterns of identified corticospinal neurons in rodent motor cortex during movement. Studies with recordings from identified neurons during motor behavior have used immunohistochemistry techniques to assign projection targets to recovered cells, but this approach yields relatively low cell numbers[66,94]. Using retrograde labeling techniques combined with extracellular recordings[106] and calcium imaging[107], two studies investigated the activity of pyramidal-tract projecting neurons in mouse anterior-lateral motor cortex (a premotor structure involved in licking[108,109]) and primary motor cortex during tongue movements. The activity of pyramidal tract projecting neurons displayed complex temporal patterns in relation to tongue movements, showing both increases and decreases with movement and during a delay period[106,107]. These studies focused on differences in firing rate between tongue movements in ipsilateral and contralateral directions. While the population of pyramidal-tract neurons in anterior-lateral motor cortex as a whole, across all firing patterns, showed a contralateral firing rate bias during movement[106,107], pyramidal tract neurons in motor cortex showed no contralateral preference, but instead strong somatosensory responses[107]. Instead of comparing ipsilateral and contralateral trials, another recent study used calcium-imaging of motor cortex layer 5b dendrites to investigate the activity of identified corticospinal neurons in mouse motor cortex during a forelimb lever press task. This study found that two-thirds of movement-related layer 5b corticospinal neurons showed decreased activity during movement[110].

Inactivation studies: Acting without motor cortex

Movement patterns after motor cortex inactivation

Even the first experiments by Fritsch and Hitzig demonstrated that surgically lesioning the motor cortex did alter, but not abolish, movements in their experimental animals[1]. In most mammals the behavioral effects of motor cortical lesions are remarkably subtle[111]. Many simple behaviors (e.g. locomotion) persist even after total decortication[112,113] due to the fact that many complete neural circuits from sensory input to motor output are fully contained within the spinal cord[114–116]. For example, since locomotion is regulated by intrinsic pattern generators in the spinal cord[114,115], a decorticate cat can display a wide range of natural gait patterns when walking on a treadmill[117,118].

Symptoms of motor cortical lesions in humans and primates

Motor cortical lesions are associated with performance deficits in several movement related tasks and massive 'motor deficits'. The motor effects of motor cortical lesions greatly change over time and, hence, are not easily categorized. For example, while the acute effects of motor cortical lesions (muscle weakness and reduced, slowed-down movement) suggest that motor cortex contributes positively to intact movement patterns, the chronic effects (spasticity, clonus and hypertonia) point to a net loss of inhibitory control of motoneurons[119–121]. A prominent effect of motor cortical lesions in primates is a loss of fractionated movements and the ability to independently move one body part without others: Attempts at individuated movements of a given body part are accompanied by excessive, unintended motion of contiguous body parts[119,122–124]. These effects of motor cortex inactivation also suggest that a prime role of descending motor cortex activity may be to 'control' – i.e. suppress and inhibit – undesirable movements.

Non-primates: loss of movement suppression dominates

In many mammals, motor cortical inactivation leads to increases in movement. For example, as perhaps suggested by the surprising abundance of motor cortical suppression during whisking, locomotion and reaching (Figure 3b-d), the patterns of whisking and limb movements after motor cortical inactivation reveal surprising deficits in movement suppression and motor control.

Corresponding to the suppression of motor cortical activity during whisker movements (Figure 3b), unilateral lesioning[125] and unilateral inactivation[66] of rat vibrissa motor cortex

leads to protraction of the contralateral whiskers and increases the whisking power contralaterally (Figure 4a). Corresponding to the suppression of motor cortical activity during locomotion on a treadmill (in some cells) (Figure 3c), forelimb motor cortex lesions disinhibit limb movements: Swimming rats normally hold their forelimbs still and swim with only their hindlimbs, but after a unilateral forelimb motor cortex lesion, they start swimming with the contralateral forelimb as well[126] (Figure 4b). After motor cortex lesions, cats[127,128] and rats[129,130] perform poorly in tasks requiring reaching and gripping food rewards. Corresponding to the prevalence of suppressed neurons in a forelimb reaching task (Figure 3d), these deficits do not arise because the animals move too little, but because they lose individual digit movements (all digits move together) and because they cannot control their forelimb movements and 'over-reach' too far past their intended targets (Figure 4c).

Clearly, the interpretation of lesion-induced changes in behavior is complex. Several recent studies have used optogenetic techniques to rapidly and reversibly inactivate motor cortex during motor behavior and studies have made mixed observations. For example, in contrast to observations made after lesioning[131] or pharmacological inactivation of vibrissa motor cortex[66], optogenetic activation of inhibitory interneurons in motor cortex did not affect whisker set angle and reduced whisking amplitudes[30]. Similarly, in contrast to the overreaching induced by pharmacological motor cortical inactivation[127–130], optogenetic activation of inhibitory interneurons in motor cortex blocked initiation and freeze execution of reaches during a trained reaching task, but left untrained forelimb movements unaffected and had no effect on initiation or execution of tongue movements[132]. Perhaps the discrepancies between the apparent effects of motor cortical lesions and transient optogenetic inhibition can be at least partly explained by acute effects stemming from the rapid perturbance of the homeostasis[133], but this remains an open question[134].

Motor cortex lesions lead to impaired performance in several movement-related tasks. In many mammals, these deficits are not due to inability to generate movement, but to a lack of controlled movements and compromised movement inhibition.

Motor cortex – not to act?

The physiology of action suppression

Motor cortical neurons have usually been studied during motor performance. However, a few recent studies have investigated the activity of motor cortical neurons in animals performing tasks where withholding movement was required.

Several studies have investigated motor cortices using head-fixed experimental paradigms, where mice are trained to respond to sensory stimulation by tongue movements in a go/no-go paradigm: The animal must lick in response to the stimulus ('hit') and withhold licking to other stimuli ('correct rejection') [135,136] (Figure 5a, left). In trials where the mouse licked after the stimulus ('hit trials'), some layer 5 motor cortical neurons (41% 'enhanced neurons', with high baseline firing rates) increased their firing rate during licking, while others decreased their firing rate (20% 'suppressed neurons', with lower baseline firing rates) (Figure 5a, middle). However, when the authors investigated the activity in trials where the mouse did not lick after the sensory stimulation ('miss trials'), they found that while the 'enhanced neurons' were still increasing their firing rate, there was no modulation of the 'suppressed neurons'[135] (Figure 5a, right). The responses of 'enhanced neurons' was highly correlated with the sensory stimulation and only 500 ms after the stimulus (i.e. after or around the reaction time of the mouse), there was also a small difference between 'hit' and 'miss' trials in the 'enhanced' neurons[135]. In other words, the 'suppressed neurons' in layer 5b of motor cortex were strongly predictive of licking behavior (the actual motor output), whereas the 'enhanced neurons' showed firing rate increases both when the mouse did and did not lick. It remains an open question why 'enhanced neurons' relate so weakly to the actual movement output in such a go/no-go task, while the suppressed neurons show a tight correlation with movement, but it may be that enhanced neurons in motor cortex largely represent a sensory signal[107,135,136], where a late component has been shown to correlate with perception[137].

Motor cortex inactivation and action suppression

In such sensorimotor go/no-go tasks, inactivation of sensory cortices leads to a degradation of task performance because the licking 'hit rate' in go-trials is reduced. The animal correctly does not lick to the no-go cue, but also stops licking to the go-cue (where he should lick), as if he does not perceive the sensory stimuli. Motor cortex inactivation has the exact opposite behavioral phenotype: When motor cortex is inactivated (Figure 5b, left), the 'hit rate' licking remains high (the animal keeps licking to the go-cue) (Figure 5b, middle), but the animal also

starts licking in no-go trials, where licking is supposed to be suppressed and is punished by time-outs[135,136] (Figure 5b, right). Behavioral performance in such go/no-to paradigms is often quantified as *d' = Z(Hit rate)-Z(False alarm rate)* and thus the inactivation of both motor cortex and sensory cortex leads to a reduced 'task performance', but for opposite reasons.

The effect of optogenetic activation of inhibitory interneurons motor cortex mirror the effects of pharmacological blockade: one study found that motor cortical inactivation did not stop lick initiation or execution in a cued licking task[132] and another study found that optogenetic inactivation of motor cortex spared hit rate, but increased false alarm licking in a go/no-go task[135].

The fact that motor cortex inactivation does not reduce 'hit rate' licking, but disinhibits disadvantageous licking suggests that a prime role of motor cortex in such a task may not be the generation of licking, but rather withholding tongue movements.

Withholding movement and waiting for rewards

Rats can learn to solve a task where they must initiate trials by poking in a nose-port, and then wait for a reward, which arrives after a random time[35,36] (Figure 5c, left). When the time to reward is long, some rats will break the trial early and fail to receive the reward because of their 'impatience'. Recordings from motor cortex in rats solving such a 'waiting task' revealed that there were more neurons which suppressed, rather than enhanced, their firing rate when the rats moved away from the nose-port[35]. Further, a large fraction (18%) of motor cortical neurons showed activity just before or during the delay period, which was significantly related to the time, which the rat decided to spend waiting for rewards. While the response pattern of single neurons was mixed, the majority of these neurons showed positive correlations between firing rate and waiting time, such that higher motor cortical firing predicted longer waiting[35] (Figure 5c, right). It should be added, however, that many motor cortex cells showing delay activity also burst prior to movement onset. In a follow-up investigation, the authors used demixed principal component analysis to interrogate motor cortical activity for signals, which might be hidden in the 'mixed' population response. Across the population, the pattern was the same: just before and during the waiting period, the principal components of the population activity were positively correlated with waiting time[36]. Motor cortex inactivation disrupted performance in such a waiting task, for two major reasons: First, most rats became 'impatient' during nose-poke trials and were not able to wait long enough to receive the reward. Secondly, the rats spent more time moving, and less time receiving the reward[36].

It is a well-established finding across humans, monkeys and rodents that (pre)frontal cortical lesions are associated with deficits in behavioral inhibition[111,138–140], which manifests itself in impulsivity, "unrestrained and tactless" behavior and "fatuos jocularity and ill-timed bawdy and puerile jokes"[141]. In one rodent study, the authors examined how motor cortical activity is modulated when behavioral inhibition is impaired due to inactivation of frontal cortex[142]. Rats were trained to perform a task, where they had to press a lever to initiate a trail, hold the lever during a delay period of 1 second, and then release the lever to receive a reward. Pharmacological inactivation of dorsomedial prefrontal cortex impaired the task performance, due to a large increase in 'premature responding', i.e. the rats did not hold the lever down for the full delay period, but released the lever too early and failed to receive the reward. Interestingly, recordings from motor cortex revealed that the premature responding was not associated with an increase in motor cortical activity during the delay period. Rather, the inability to wait during the delay was associated with a decrease in motor cortical activity[142], suggesting that motor cortical activity might be important for the suppression of premature lever presses.

Motor cortex manipulation and waiting tasks

The interpretation that motor cortex plays an important role in the suppression of disadvantageous lever presses is supported by a recent study. The study investigated the effect of motor cortical inactivation in rats that were trained to press a lever twice to receive a reward[143] (Figure 5d, left). Both intact rats and rats with motor cortex lesions could learn to solve the task and press the lever twice. Intact rats could learn to postpone the second lever press to obtain a larger reward and once this had been learned, motor cortex ablation did not affect the stereotyped/learned motor sequence, which the rats used to time their lever pressing. Rats with motor cortex lesions, however, could not learn to postpone the second lever press and continued to receive only low rewards by pressing the lever in fast succession[143] (Figure 5d, right).

Conclusions

Summary

We have reviewed findings suggesting that, in addition to movement generation, motor cortex might contribute to movement suppression. The famous motor homunculus by Penfield & Rasmussen is frequently presented as a movement map, but the observed stimulation effects indicate a somatotopic organization of movement suppression (Figure 1). Motor cortical pyramidal tract neurons are often presented as heavily innervating spinal motoneurons, but this clear 'movement circuit' is an exceptional wiring pattern in mammals (Figure 2). In some preparations, motor cortical activity increases upon movement, but movement is also accompanied by a surprising prevalence of principal neuron suppression and increased motor cortical inhibition (Figure 3). Motor cortical lesions interfere with, but do not abolish movement and are often associated with impaired movement suppression (Figure 4). Motor cortex has mainly been investigated as a structure for movement generation, but several studies implicate motor cortex in the withholding of disadvantageous motor output (Figure 5).

A purely movement/action centered perspective does not capture motor cortical function

The activity patterns of motor cortical neurons during ongoing behavior are highly diverse. In addition to relationships with movement[30,66,67,76,89,94,98,100,102], neurons in the primary motor cortex have been implicated in choice, working memory and preparation of upcoming motor decisions[40,43,144,145], in decision making in relation to rewards and upcoming motor strategies[34–39], in 'mirror neuron'-like representations of actions[146–149] and in the representation of visual[150] and somatosensory[31,107,136,151] stimuli. Such diversity is probably functionally important[107,136,152] and it emphasizes the importance of unbiased analysis. Thus, rather than 'searching' for single cells with a-priori expected response pattern (e.g. positive correlation with limb movement), we must also focus on analysis of e.g. multi-electrode or imaging data to determine if systematic population responses exist and how archetypical activity patterns map onto specific cell types and projection patterns.

Motor suppressive functions of motor cortices have received much less attention than the role of motor cortex in movement generation, but these negative motor phenomena[11] deserve broader attention. Movement is often associated with a decrease in activity of principal neurons, increases in activity of fast-spiking neurons and large amounts of movement-related inhibition. This is an unexpected response pattern for a primary cortical area dedicated to movement, since cortical neurons most commonly respond to relevant stimuli with *increased*

activity. This is the case for sensory cortices[153,154], and has been proposed as a general principle for the flow of cortical information[155]. There are many ways to reconcile decreases in activity with a primarily movement-promoting function of motor cortical activity[76,81,156]. Nonetheless, because the population-firing-rate decrease to relevant stimuli is an unusual cortical response pattern, this deserves more attention.

Behavioral inhibition across frontal cortex

Numerous animal studies[111,157] and classic neuropsychological work (Phineas Gage[158,159]) point to a major role of frontal and prefrontal cortex in the inhibitory control of behavior[111,138–140]. Frontal cortices are relatively large in primates while the primary motor cortex is comparatively small[2,3,5], whereas in rodents, frontal cortex is almost entirely primary motor cortex[12,16,19,24,25]. In primates, several premotor structures have been shown to perform movement-suppressive functions in the executive control of behavior. For example, the primate frontal and cingulate cortex responses arising in the context of countermanding occulomotor movement and antisaccades have been described[160,161]. Similarly, both primate studies and observations on human patients point to a major role of the supplementary motor area in movement inhibition[162–164], and lesions to this area reveak involuntary, 'alien' movements[165].

We wonder, if rodent motor cortex might be more general and more 'frontal-like' than the potentially more movement-specialized primate motor cortex. Thus, while both the activity patterns during movement and the movement patterns after cortical blockade lets it appear likely that rodent motor cortex plays a major role in movement suppression, it needs to be checked by comparative analysis if this is an archetypical feature of motor cortex. For example, it would be interesting to see how marsupials perform on tasks of behavioral inhibition, such as the classic marshmallow test[166].

Outlook: A strategic function of motor cortex

Volitional control of motor output means deciding when to move and when *not* to move. Freud's notion of *Überich*[167] was based in a correct intuition about behavior: sometimes it is very important to repress the urge to act on immediate desires. Action suppression is critical to the strategic planning of motor behaviors, but we still know little about how motor cortex contributes to this important cognitive capacity. We need to get away from a 'movement' perspective, and further investigate motor cortex from a 'behavioral strategy' perspective. We propose that future investigations of motor cortex function should study both movement and

530 movement-suppression to elucidate how motor cortex allows mammals to behave in non-
531 reflexive ways.

References

1. Fritsch, G. & Hitzig, E. Ueber die elektrische Erregbarkeit des Grosshirns. *Arch. Anat. Physiol. wiss. Med.* **37,** 300–332 (1870).
2. Ferrier, D. Experiments on the Brain of Monkeys - No. I. *Proc. R. Soc. B Biol. Sci.* **23,** 409–430 (1874).
3. Leyton, A. S. F. S. F. & Sherrington, C. S. S. Observations on the excitable cortex of the chimpanzee, orang-utan, and gorilla. *Q. J. Exp. Physiol.* **11,** 135–222 (1917).
4. Graziano, M. S. a, Taylor, C. S. R. & Moore, T. Complex movements evoked by microstimulation of precentral cortex. *Neuron* **34,** 841–851 (2002).
5. Asanuma, H. & Rosén, I. Topographical organization of cortical efferent zones projecting to distal forelimb muscles in the monkey. *Exp. brain Res.* **14,** 243–56 (1972).
6. Penfield, W. & Rasmussen, T. *The Cerebral Cortex of Man*. (The Macmillan Company, 1952). doi:10.1212/WNL.1.1.96
7. Ikeda, A. *et al.* Movement-related potentials associated with bilateral simultaneous and unilateral movements recorded from human supplementary motor area. *Electroencephalogr. Clin. Neurophysiol.* **95,** 323–34 (1995).
8. Lüders, H. O., Dinner, D. S., Morris, H. H., Wyllie, E. & Comair, Y. G. Cortical electrical stimulation in humans. The negative motor areas. *Adv. Neurol.* **67,** 115–29 (1995).
9. Nii, Y., Uematsu, S., Lesser, R. P. & Gordon, B. Does the central sulcus divide motor and sensory functions? Cortical mapping of human hand areas as revealed by electrical stimulation through subdural grid electrodes. *Neurology* **46,** 360–7 (1996).
10. Mikuni, N. *et al.* Evidence for a wide distribution of negative motor areas in the perirolandic cortex. *Clin. Neurophysiol.* **117,** 33–40 (2006).
11. Filevich, E., Kühn, S. & Haggard, P. Negative motor phenomena in cortical stimulation: Implications for inhibitory control of human action. *Cortex* **48,** 1251–1261 (2012).
12. Neafsey, E. J. *et al.* The organization of the rat motor cortex: A microstimulation mapping study. *Brain Res. Rev.* **11,** 77–96 (1986).
13. Ayling, O. G. S., Harrison, T. C., Boyd, J. D., Goroshkov, A. & Murphy, T. H. Automated light-based mapping of motor cortex by photoactivation of channelrhodopsin-2 transgenic mice. *Nat. Methods* **6,** 219–24 (2009).
14. Harrison, T. C., Ayling, O. G. S. & Murphy, T. H. Distinct Cortical Circuit Mechanisms for Complex Forelimb Movement and Motor Map Topography. *Neuron* **74,** 397–409 (2012).
15. Lemon, R. N. An enduring map of the motor cortex. *Exp. Physiol.* **93,** 798–802 (2008).
16. Brecht, M. *et al.* Organization of rat vibrissa motor cortex and adjacent areas according to cytoarchitectonics, microstimulation, and intracellular stimulation of identified cells. *J. Comp. Neurol.* **479,** 360–373 (2004).

17. Matyas, F. *et al.* Motor control by sensory cortex. *Science* **330,** 1240–1243 (2010).

18. Molnár, Z. *et al.* Evolution and development of the mammalian cerebral cortex. *Brain. Behav. Evol.* **83,** 126–39 (2014).

19. Hall, R. D. & Lindholm, E. P. Organization of motor and somatosensory neocortex in the albino rat. *Brain Res.* **66,** 23–38 (1974).

20. Nudo, R. J. & Frost, S. B. 3 . 28 The Evolution of Motor Cortex and Motor Systems. (2007).

21. Kaas, J. H. Evolution of somatosensory and motor cortex in primates. *Anat. Rec. - Part A Discov. Mol. Cell. Evol. Biol.* **281,** 1148–1156 (2004).

22. Frost, S. B., Milliken, G. W., Plautz, E. J., Masterton, R. B. & Nudo, R. J. Somatosensory and motor representations in cerebral cortex of a primitive mammal (Monodelphis domestica): A window into the early evolution of sensorimotor cortex. *J. Comp. Neurol.* **421,** 29–51 (2000).

23. Karlen, S. J. & Krubitzer, L. The functional and anatomical organization of marsupial neocortex: Evidence for parallel evolution across mammals. *Prog. Neurobiol.* **82,** 122–141 (2007).

24. Gioanni, Y. & Lamarche, M. A reappraisal of rat motor cortex organization by intracortical microstimulation. *Brain Res.* **344,** 49–61 (1985).

25. Zilles, K. & Wree, A. in *The Rat Nevous System* (ed. Paxinos, G.) 649–685 (Academic Press, 1995).

26. Brodmann, K. *Vergleichende Lokalisationslehre der Großhirnrinde : in ihren Prinzipien dargestellt auf Grund des Zellenbaues*. (J.A.Barth, 1909).

27. Yamawaki, N. *et al.* A genuine layer 4 in motor cortex with prototypical synaptic circuit connectivity. *Elife* **4,** e05422 (2014).

28. Nudo, R. J. & Masterton, R. B. Descending pathways to the spinal cord, III: Sites of origin of the corticospinal tract. *J. Comp. Neurol.* **296,** 559–583 (1990).

29. Rathelot, J.-A. & Strick, P. L. Muscle representation in the macaque motor cortex: An anatomical perspective. *Proc. Natl. Acad. Sci.* **103,** 8257–8262 (2006).

30. Sreenivasan, V. *et al.* Movement Initiation Signals in Mouse Whisker Motor Cortex. *Neuron* **92,** 1368–1382 (2016).

31. Ferezou, I. *et al.* Spatiotemporal Dynamics of Cortical Sensorimotor Integration in Behaving Mice. *Neuron* **56,** 907–923 (2007).

32. Paxinos, G. & Watson, C. *The rat brain in stereotaxic coordinates*. (Academic Press, 1982).

33. Brecht, M. Movement, Confusion, and Orienting in Frontal Cortices. *Neuron* **72,** 193–196 (2011).

34. Barthas, F. & Kwan, A. C. Secondary Motor Cortex : Where ‘ Sensory ’ Meets ‘ Motor ’ in the Rodent Frontal Cortex. *Trends Neurosci.* **40,** 181–193 (2017).

35. Murakami, M., Vicente, M. I., Costa, G. M. & Mainen, Z. F. Neural antecedents of self-initiated actions in secondary motor cortex. *Nat. Neurosci.* **17,** 1574–1582 (2014).

36. Murakami, M., Shteingart, H., Loewenstein, Y. & Mainen, Z. F. Distinct Sources of Deterministic and Stochastic Components of Action Timing Decisions in Rodent Frontal Cortex. *Neuron* **94,** 908–919.e7 (2017).

37. Reep, R. L., Goodwin, G. S. & Corwin, J. V. Topographic organization in the corticocortical connections of medial agranular cortex in rats. *J. Comp. Neurol.* **294,** 262–280 (1990).

38. Reep, R. L., Corwin, J. V, Hashimoto, A. & Watson, R. T. Efferent connections of the rostral portion of medial agranular cortex in rats. *Brain Res. Bull.* **19,** 203–21 (1987).

39. Sul, J. H., Jo, S., Lee, D. & Jung, M. W. Role of rodent secondary motor cortex in value-based action selection. *Nat. Neurosci.* **14,** 1202–8 (2011).

40. Brody, C. D. & Hanks, T. D. Neural underpinnings of the evidence accumulator. *Curr. Opin. Neurobiol.* **37,** 149–157 (2016).

41. Hanks, T. D. *et al.* Distinct relationships of parietal and prefrontal cortices to evidence accumulation. *Nature* **520,** 220–223 (2015).

42. Erlich, J. C., Bialek, M. & Brody, C. D. A cortical substrate for memory-guided orienting in the rat. *Neuron* **72,** 330–343 (2011).

43. Erlich, J. C., Brunton, B. W., Duan, C. A., Hanks, T. D. & Brody, C. D. Distinct effects of prefrontal and parietal cortex inactivations on an accumulation of evidence task in the rat. 1–28 (2015). doi:10.7554/eLife.05457

44. Lemon, R. N. Descending Pathways in Motor Control. *Annu. Rev. Neurosci* **31,** 195–218 (2008).

45. O'Donoghue, D. L., Kartje-Tillotson, G. & Castro, a J. Forelimb motor cortical projections in normal rats and after neonatal hemicerebellectomy: an anatomical study based upon the axonal transport of WGA/HRP. *J. Comp. Neurol.* **256,** 274–283 (1987).

46. Grinevich, V., Brecht, M. & Osten, P. Monosynaptic pathway from rat vibrissa motor cortex to facial motor neurons revealed by lentivirus-based axonal tracing. *J. Neurosci.* **25,** 8250–8258 (2005).

47. Sreenivasan, V., Karmakar, K., Rijli, F. M. & Petersen, C. C. H. Parallel pathways from motor and somatosensory cortex for controlling whisker movements in mice. *Eur. J. Neurosci.* **41,** 354–367 (2015).

48. Rouiller, E. M., Moret, V. & Liang, F. Comparison of the connectional properties of the two forelimb areas of the rat sensorimotor cortex: support for the presence of a premotor or supplementary motor cortical area. *Somatosens. Mot. Res.* **10,** 269–289 (1993).

49. Deschênes, M. *et al.* Inhibition, Not Excitation, Drives Rhythmic Whisking. *Neuron* **90,** 374–387 (2016).

50. Kuypers, H. G. J. M. A New Look at the Organization of the Motor System. *Prog. Brain Res.* **57,** 381–403 (1982).

51. Fetz, E. E., Perlmutter, S. I. & Prut, Y. Functions of mammalian spinal interneurons during movement. *Curr. Opin. Neurobiol.* **10,** 699–707 (2000).

52. Rathelot, J.-A. & Strick, P. L. Subdivisions of primary motor cortex based on cortico-motoneuronal cells. *Proc. Natl. Acad. Sci. U. S. A.* **106,** 918–23 (2009).

53. Heffner, R. & Masterton, B. Variation in form of the pyramidal tract and its relationship to digital dexterity. *Brain. Behav. Evol.* **12,** 161–200 (1975).

54. Nakajima, K., Maier, M. A., Kirkwood, P. A. & Lemon, R. N. Striking differences in transmission of corticospinal excitation to upper limb motoneurons in two primate species. *J. Neurophysiol.* **84,** 698–709 (2000).

55. Osten, P. & Margrie, T. W. Mapping brain circuitry with a light microscope. *Nat. Methods* **10,** 515–523 (2013).

56. Hooks, B. M. *et al.* Organization of cortical and thalamic input to pyramidal neurons in mouse motor cortex. *J. Neurosci.* **33,** 748–60 (2013).

57. Jeong, M. *et al.* Comparative three-dimensional connectome map of motor cortical projections in the mouse brain. *Sci. Rep.* **6,** 20072 (2016).

58. Calabresi, P., Picconi, B., Tozzi, A., Ghiglieri, V. & Di Filippo, M. Direct and indirect pathways of basal ganglia: a critical reappraisal. *Nat. Neurosci.* **17,** 1022–1030 (2014).

59. Kress, G. J. *et al.* Convergent cortical innervation of striatal projection neurons. *Nat. Neurosci.* **16,** 665–667 (2013).

60. Cui, G. *et al.* Concurrent activation of striatal direct and indirect pathways during action initiation. *Nature* **494,** 238–42 (2013).

61. Tecuapetla, F., Jin, X., Lima, S. Q. & Costa, R. M. Complementary Contributions of Striatal Projection Pathways to Action Initiation and Execution. *Cell* **166,** 703–715 (2016).

62. Grillner, S. & Robertson, B. The basal ganglia downstream control of brainstem motor centres—an evolutionarily conserved strategy. *Curr. Opin. Neurobiol.* **33,** 47–52 (2015).

63. Cheney, P. D. & Fetz, E. E. Comparable patterns of muscle facilitation evoked by individual corticomotoneuronal (CM) cells and by single intracortical microstimuli in primates: evidence for functional groups of CM cells. *J. Neurophysiol.* **53,** 786–804 (1985).

64. Lemon, R., Muir, R. & Mantel, G. The effects upon the activity of hand and forearm muscles of intracortical stimulation in the vicinity of corticomotor neurones in the conscious monkey. *Exp. Brain Res.* **66,** 621–637 (1987).

65. Cheney, P. D., Fetz, E. E. & Palmer, S. S. Patterns of facilitation and suppression of antagonist forelimb muscles from motor cortex sites in the awake monkey. *J. Neurophysiol.* **53,** 805–820 (1985).

66. Ebbesen, C. L., Doron, G., Lenschow, C. & Brecht, M. Vibrissa motor cortex activity suppresses contralateral whisking behavior. *Nat. Neurosci.* **20,** 82–89 (2017).

67. Hill, D. N., Curtis, J. C., Moore, J. D. & Kleinfeld, D. Primary motor cortex reports efferent control of vibrissa motion on multiple timescales. *Neuron* **72,** 344–356 (2011).

68. Moore, J. D. *et al.* Hierarchy of orofacial rhythms revealed through whisking and breathing. *Nature* **497,** 205–210 (2013).

69. Buys, E. J., Lemon, R. N., Mantel, G. W. & Muir, R. B. Selective facilitation of different hand muscles by single corticospinal neurones in the conscious monkey. *J. Physiol.* **381,** 529–49 (1986).

70. Lemon, R. N., Mantel, G. W. & Muir, R. B. Corticospinal facilitation of hand muscles during voluntary movement in the conscious monkey. *J. Physiol.* **381,** 497–527 (1986).

71. Davidson, A. G., Chan, V., O'Dell, R. & Schieber, M. H. Rapid changes in throughput from single motor cortex neurons to muscle activity. *Science* **318,** 1934–7 (2007).

72. Ramanathan, D., Conner, J. M. & Tuszynski, M. H. A form of motor cortical plasticity that correlates with recovery of function after brain injury. *Proc. Natl. Acad. Sci. U. S. A.* **103,** 11370–11375 (2006).

73. Stoney, S. D., Thompson, W. D. & Asanuma, H. Excitation of pyramidal tract cells by intracortical microstimulation: effective extent of stimulating current. *J. Neurophysiol.* **31,** 659–669 (1968).

74. Tehovnik, E. J., Tolias, A. S., Sultan, F., Slocum, W. M. & Logothetis, N. K. Direct and indirect activation of cortical neurons by electrical microstimulation. *J. Neurophysiol.* **96,** 512–521 (2006).

75. Histed, M. H., Bonin, V. & Reid, R. C. Direct Activation of Sparse, Distributed Populations of Cortical Neurons by Electrical Microstimulation. *Neuron* **63,** 508–522 (2009).

76. Shenoy, K. V, Sahani, M. & Churchland, M. M. Cortical Control of Arm Movements: A Dynamical Systems Perspective. *Annu. Rev. Neurosci.* **36,** 337–359 (2013).

77. Georgopoulos, a P., Kalaska, J. F., Caminiti, R. & Massey, J. T. On the relations between the direction of two-dimensional arm movements and cell discharge in primate motor cortex. *J. Neurosci.* **2,** 1527–1537 (1982).

78. Kalaska, J. F., Cohen, D. a, Hyde, M. L. & Prud'homme, M. A comparison of movement direction-related versus load direction-related activity in primate motor cortex, using a two-dimensional reaching task. *J. Neurosci.* **9,** 2080–2102 (1989).

79. Evarts, E. V. Relation of pyramidal tract activity to force exerted during voluntary movement. *J. Neurophysiol.* **31,** 14–27 (1968).

80. Cheney, P. D. & Fetz, E. E. Functional classes of primate corticomotoneuronal cells and their relation to active force. *J. Neurophysiol.* **44,** 773–791 (1980).

81. Fetz, E. E. Are movement parameters recognizable coded in the activity of single neurons? *Behav. Brain Sci.* **15,** 679–690 (1992).

82. Kaufman, M. T., Churchland, M. M. & Shenoy, K. V. The roles of monkey M1 neuron classes in movement preparation and execution. *J. Neurophysiol.* **110,** 817–825 (2013).

83. Armstrong, D. M. & Drew, T. Discharges of pyramidal tract and other motor cortical neurones during locomotion in the cat. *J. Physiol.* **346,** 471–95 (1984).

84. Drew, T., Jiang, W. & Widajewicz, W. Contributions of the motor cortex to the control of the hindlimbs during locomotion in the cat. *Brain Res. Rev.* **40,** 178–191 (2002).

85. Beloozerova, I. N., Farrell, B. J., Sirota, M. G. & Prilutsky, B. I. Differences in movement mechanics, electromyographic, and motor cortex activity between accurate and nonaccurate stepping. *J. Neurophysiol.* **103,** 2285–2300 (2010).

86. Drew, T. Motor Cortical Activity During Voluntary Cat . I . Cells Re lated to he Forelimbs Gait Modifications in the. *J. Neurophysiol.* **70,** 179–99 (1993).

87. Beloozerova, I. N. & Sirota, M. G. The role of the motor cortex in the control of vigour of locomotor movements in the cat. *J. Physiol.* **461,** 27–46 (1993).

88. Ölveczky, B. P. Motoring ahead with rodents. *Curr. Opin. Neurobiol.* **21,** 571–8 (2011).

89. Fisher, S. P. *et al.* Stereotypic wheel running decreases cortical activity in mice. *Nat. Commun.* **7,** 13138 (2016).

90. Barthó, P. *et al.* Characterization of neocortical principal cells and interneurons by network interactions and extracellular features. *J. Neurophysiol.* **92,** 600–608 (2004).

91. Gentet, L. J., Avermann, M., Matyas, F., Staiger, J. F. & Petersen, C. C. H. Membrane Potential Dynamics of GABAergic Neurons in the Barrel Cortex of Behaving Mice. *Neuron* **65,** 422–435 (2010).

92. Sjulson, L. L. Reforming our ideas about cell types and spike waveforms. *J.Neurosci.* (2011). at <http://www.jneurosci.org/content/31/40/14235/tab-article-info#reforming-our-ideas-about-cell-types-and-spike-waveforms>

93. Suter, B. A., Migliore, M. & Shepherd, G. M. G. Intrinsic electrophysiology of mouse corticospinal neurons: A class-specific triad of spike-related properties. *Cereb. Cortex* **23,** 1965–1977 (2013).

94. Schiemann, J. *et al.* Cellular Mechanisms Underlying Behavioral State-Dependent Bidirectional Modulation of Motor Cortex Output. *Cell Rep.* **11,** 1319–1330 (2015).

95. Dörfl, J. The musculature of the mystacial vibrissae of the white mouse. *J. Anat.* **135,** 147–154 (1982).

96. Welker, W. I. Analysis of Sniffing of the Albino Rat. *Behaviour* **22,** 223–244 (1964).

97. Sachdev, R. N. S., Sato, T. & Ebner, F. F. Divergent movement of adjacent whiskers. *J. Neurophysiol.* **87,** 1440–8 (2002).

98. Carvell, G. E., Miller, S. A. & Simons, D. J. The relationship of vibrissal motor cortex unit activity to whisking in the awake rat. *Somatosens. Mot. Res.* **13,** 115–127 (1996).

99. Friedman, W. A., Zeigler, H. P. & Keller, A. Vibrissae motor cortex unit activity during whisking. *J. Neurophysiol.* **107,** 551–563 (2012).

100. Gerdjikov, T. V, Haiss, F., Rodriguez-Sierra, O. E. & Schwarz, C. Rhythmic whisking area (RW) in rat primary motor cortex: an internal monitor of movement-related signals? *J. Neurosci.* **33,** 14193–204 (2013).

101. Kleinfeld, D., Berg, R. W. & O'Connor, S. M. Anatomical loops and their electrical dynamics in relation to whisking by rat. *Somatosens. Mot. Res.* **16,** 69–88 (1999).

102. Isomura, Y., Harukuni, R., Takekawa, T., Aizawa, H. & Fukai, T. Microcircuitry coordination of cortical motor information in self-initiation of voluntary movements. *Nat. Neurosci.* **12,** 1586–1593 (2009).

103. Estebanez, L., Hoffmann, D., Voigt, B. C. & Poulet, J. F. A. Parvalbumin expressing GABA-ergic neurons in primary motor cortex signal reaching. *Cell Rep.* (2017).

104. Vigneswaran, G., Kraskov, A. & Lemon, R. Large Identified Pyramidal Cells in Macaque Motor and Premotor Cortex Exhibit 'Thin Spikes': Implications for Cell Type Classification. **31,** 14235–14242 (2011).

105. Zaitsev, A. V., Povysheva, N. V., Gonzalez-Burgos, G. & Lewis, D. A. Electrophysiological classes of layers 2-3 pyramidal cells in monkey prefrontal cortex. *J. Neurophysiol.* 595–609 (2012). doi:10.1152/jn.00859.2011

106. Li, N., Chen, T., Guo, Z. V, Gerfen, C. R. & Svoboda, K. A motor cortex circuit for motor planning and movement. *Nature* (2015). doi:10.1038/nature14178

107. Chen, T.-W., Li, N., Daie, K. & Svoboda, K. A Map of Anticipatory Activity in Mouse Motor Cortex. *Neuron* **94,** 866–879.e4 (2017).

108. Travers, J. B., Dinardo, L. A. & Karimnamazi, H. Motor and premotor mechanisms of licking. *Neurosci. Biobehav. Rev.* **21,** 631–647 (1997).

109. Guo, Z. *et al.* Flow of cortical activity underlying a tactile decision in mice. *Neuron* **81,** 179–194 (2014).

110. Peters, A. J., Lee, J., Hedrick, N. G., O'Neil, K. & Komiyama, T. Reorganization of corticospinal output during motor learning. *Nat. Neurosci.* (2017). doi:10.1038/nn.4596

111. Kolb, B. Functions of the frontal cortex of the rat: a comparative review. *Brain Res.* **320,** 65–98 (1984).

112. Franz, S. I. & Lashley, K. S. The retention of habits by the rat after destruction of the frontal portion of the cerebrum. *Psychobiology* 3–18 (1917).

113. Semba, K. & Komisaruk, B. R. Neural substrates of two different rhythmical vibrissal movements in the rat. *Neuroscience* **12,** 761–774 (1984).

114. Goulding, M. Circuits controlling vertebrate locomotion: moving in a new direction. *Nat. Rev. Neurosci.* **10,** 507–518 (2009).

115. Kiehn, O. Locomotor circuits in the mammalian spinal cord. *Annu. Rev. Neurosci.* **29,** 279–306 (2006).

116. Bourane, S. *et al.* Identification of a Spinal Circuit for Light Touch and Fine Motor Control. *Cell* **160,** 503–515 (2015).

117. Whelan, P. Control of Locomotion in the Decerebrate Cat. *Prog. Neurobiol.* **49,** 481–515 (1996).

118. Graham Brown, T. The Intrinsic Factors in the Act of Progression in the Mammal. (1911).

119. Schieber, M. H. & Poliakov, A. V. Partial inactivation of the primary motor cortex hand area: effects on individuated finger movements. *J. Neurosci.* **18,** 9038–9054 (1998).

120. Laplane, D., Talairach, J., Meininger, V., Bancaud, J. & Bouchareine, A. Motor consequences of motor area ablations in man. *J. Neurol. Sci.* **31,** 29–49

121. Barnes, M. P. & Johnson, G. R. *Upper Motor Neurone Syndrome and Spasticity*. *Clinical Management and Neurophysiology* (Cambridge University Press, 2008).

122. Sasaki, S. *et al.* Dexterous finger movements in primate without monosynaptic corticomotoneuronal excitation. *J. Neurophysiol.* **92,** 3142–3147 (2004).

123. Rouiller, E. M. *et al.* Dexterity in adult monkeys following early lesion of the motor cortical hand area: The role of cortex adjacent to the lesion. *Eur. J. Neurosci.* **10,** 729–740 (1998).

124. Lawrence, D. G. & Kuypers, H. G. J. M. The Functional Organization of the Motor System in the Monkey. *Brain* **91,** 1–14 (1968).

125. Gao, P., Hattox, A. M., Jones, L. M., Keller, A. & Zeigler, H. P. Whisker motor cortex ablation and whisker movement patterns. *Somatosens. Mot. Res.* **20,** 191–198 (2003).

126. Stoltz, S., Humm, J. L. & Schallert, T. Cortical injury impairs contralateral forelimb immobility during swimming: a simple test for loss of inhibitory motor control. *Behav. Brain Res.* **106,** 127–32 (1999).

127. Martin, J. H. & Ghez, C. Impairments in reaching during reversible inactivation of the distal forelimb representation of the motor cortex in the cat. *Neurosci. Lett.* **133,** 61–64 (1991).

128. Martin, J. H. & Ghez, C. Differential impairments in reaching and grasping produced by local inactivation within the forelimb representation of the motor cortex in the cat. *Exp. brain Res.* **94,** 429–43 (1993).

129. Castro, A. J. The effects of cortical ablations on digital usage in the rat. *Brain Res.* **37,** 173–85 (1972).

130. Alaverdashvili, M. & Whishaw, I. Q. Motor cortex stroke impairs individual digit movement in skilled reaching by the rat. *Eur. J. Neurosci.* **28,** 311–22 (2008).

131. Gao, P., Bermejo, R. & Zeigler, H. P. Whisker deafferentation and rodent whisking patterns: behavioral evidence for a central pattern generator. *J. Neurosci.* **21,** 5374–80 (2001).

132. Guo, J.-Z. *et al.* Cortex commands the performance of skilled movement. *Elife* **4,** 1–18 (2015).

133. Otchy, T. M. *et al.* Acute off-target effects of neural circuit manipulations. *Nature* **528,** 358–363 (2015).

134. Südhof, T. C. Reproducibility: Experimental mismatch in neural circuits. *Nature* **528,** 338–339 (2015).

135. Zagha, E., Ge, X. & McCormick, D. A. Competing Neural Ensembles in Motor Cortex Gate Goal-Directed Motor Output. *Neuron* **88,** 565–577 (2015).

136. Huber, D. *et al.* Multiple dynamic representations in the motor cortex during sensorimotor learning. *Nature* **484,** 473–478 (2012).

137. Sachidhanandam, S., Sreenivasan, V., Kyriakatos, A., Kremer, Y. & Petersen, C. C. H. Membrane potential correlates of sensory perception in mouse barrel cortex. *Nat. Neurosci.* **16,** 1671–7 (2013).

138. Dalley, J. W., Cardinal, R. N. & Robbins, T. W. Prefrontal executive and cognitive functions in rodents: Neural and neurochemical substrates. *Neurosci. Biobehav. Rev.* **28,** 771–784 (2004).

139. Kim, S. & Lee, D. Prefrontal Cortex and Impulsive Decision Making. *Biol. Psychiatry* **69,** 1140–1146 (2011).

140. Miller, E. K. The prefrontal cortex and cognitive control. *Nat. Rev. Neurosci.* **1,** 59–65 (2000).

141. Mayer-Gross, W., Slater, E. & Roth, M. *Clinical Psychiatry*. (Cassell & Co., 1954).

142. Narayanan, N. S. & Laubach, M. Top-Down Control of Motor Cortex Ensembles by Dorsomedial Prefrontal Cortex. *Neuron* **52,** 921–931 (2006).

143. Kawai, R. *et al.* Motor Cortex Is Required for Learning but Not for Executing a Motor Skill. *Neuron* **86,** 800–812 (2015).

144. Erlich, J. C., Bialek, M. & Brody, C. D. A Cortical Substrate for Memory-Guided Orienting in the Rat. *Neuron* **72,** 330–343 (2011).

145. Hanks, T. D. *et al.* Distinct relationships of parietal and prefrontal cortices to evidence accumulation. *Nature* **520,** 220–223 (2015).

146. Dushanova, J. & Donoghue, J. Neurons in primary motor cortex engaged during action observation. *Eur. J. Neurosci.* **31,** 386–398 (2010).

147. Tkach, D., Reimer, J. & Hatsopoulos, N. G. Congruent activity during action and action observation in motor cortex. *J. Neurosci.* **27,** 13241–13250 (2007).

148. Kraskov, a *et al.* Corticospinal mirror neurons Corticospinal mirror neurons. (2014).

149. Vigneswaran, G., Philipp, R., Lemon, R. N. & Kraskov, A. M1 corticospinal mirror neurons and their role in movement suppression during action observation. *Curr. Biol.* **23,** 236–243 (2013).

150. Goard, M. J., Pho, G. N., Woodson, J. & Sur, M. Distinct roles of visual, parietal, and frontal motor cortices in memory-guided sensorimotor decisions. *Elife* **5,** (2016).

151. Kleinfeld, D., Sachdev, R. N. S., Merchant, L. M., Jarvis, M. R. & Ebner, F. F. Adaptive filtering of vibrissa input in motor cortex of rat. *Neuron* **34,** 1021–1034 (2002).

152. Kilner, J. M. & Lemon, R. N. What We Know Currently about Mirror Neurons. *Curr. Biol.* **23,** R1057–R1062 (2013).

153. Mountcastle, V. Modalily and topographic properties of single neurons of cat's somatic sensory system. *J.Neurophysiol.* **20,** 408–434 (1956).

154. Hubel, D. H. & Wiesel, T. N. Receptive fields of single neurones in the cat's striate cortex. *J. Physiol.* **148,** 574–91 (1959).

155. Mountcastle, V. *An organizing principle for cerebral function: the unit model and the distributed system*. *The Mindful Brain* (MIT Press, 1978).

156. Sanes, J. N. & Donoghue, J. P. Plasticity and Primary Motor Cortex. *Annu. Rev. Neurosci.* **23,** 393–415 (2000).

157. Laubach, M., Caetano, M. S. & Narayanan, N. S. Mistakes were made: Neural mechanisms for the adaptive control of action initiation by the medial prefrontal cortex. *J. Physiol. Paris* **109,** 104–117 (2015).

158. Harlow, J. M. Rocovery from the passage of an iron bar through the head. *Publ. Massachusetts Med. Soc.* **2,** (1868).

159. Harlow, J. M. Passage of an iron rod through the head. *Bost. Med. Surg. J.* **39,** 281–283 (1848).

160. Shadmehr, R. Distinct neural circuits for control of movement vs. holding still. *J. Neurophysiol.* jn.00840.2016 (2017). doi:10.1152/jn.00840.2016

161. Schall, J. D., Stuphorn, V. & Brown, J. W. Monitoring and control of action by the frontal lobes. *Neuron* **36,** 309–22 (2002).

162. Wardak, C. The Role of the Supplementary Motor Area in Inhibitory Control in Monkeys and Humans. *J. Neurosci.* **31,** 5181–5183 (2011).

163. Nachev, P., Kennard, C. & Husain, M. Functional role of the supplementary and pre-supplementary motor areas. *Nat. Rev. Neurosci.* **9,** 856–869 (2008).

164. Filevich, E., Kühn, S. & Haggard, P. Intentional inhibition in human action: The power of 'no'. *Neurosci. Biobehav. Rev.* **36,** 1107–1118 (2012).

165. Brainin, M., Seiser, A. & Matz, K. The mirror world of motor inhibition: the alien hand syndrome in chronic stroke. *J. Neurol. Neurosurg. Psychiatry* **79,** 246–252 (2008).

166. Mischel, W., Ebbesen, E. B. & Raskoff Zeiss, A. Cognitive and attentional mechanisms in delay of gratification. *J. Pers. Soc. Psychol.* **21,** 204–218 (1972).

167. Freud, S. *Das Ich und das Es*. *Gesammelte Werke: XIII* (Internationaler Psychoanalytischer Verlag, 1923).

Acknowledgements

We thank James Poulet, Mikkel Vestergaard, Ann Clemens, Rajnish Rao and Andreea Neukirchner for valuable discussions and comments on the manuscript. This work was supported by Humboldt-Universität zu Berlin, BCCN Berlin (German Federal Ministry of Education and Research BMBF, Förderkennzeichen 01GQ1001A), NeuroCure, and the Gottfried Wilhelm Leibniz Prize of the DFG.

Competing interests statement

The authors declare no competing interests.

Figures

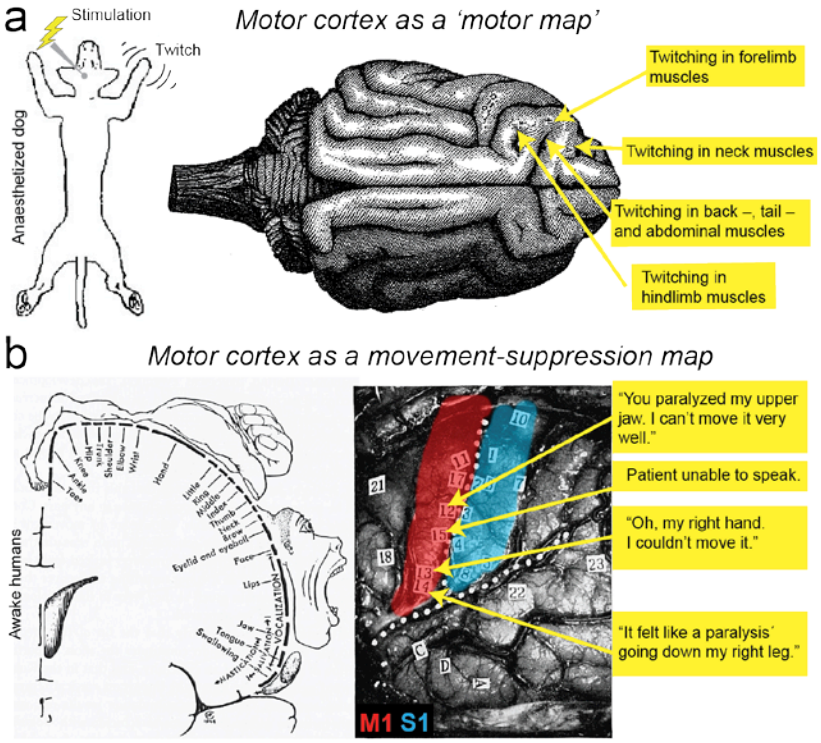

Figure 1: Two opposing views of the motor cortex.

(a) Discovery of motor cortex as a motor map. Left: Anaesthetized dog. Right: Sketch of dog brain with indications of the cortical sites where stimulation evoked movements (Fritsch and Hitzig)[1]. (Adapted with permission from ref. [1])

(b) Stimulation of human motor cortex often leads to movement suppression. Left: Penfield and Rasmussen's famous human motor homunculus. Right: Intra-operative photograph and reports made by a patient during stimulation of motor cortical sites (red color: M1, blue color: S1, white dots indicate rolandic and sylvian fissures)[5]. (Adapted with permission from ref.[5])

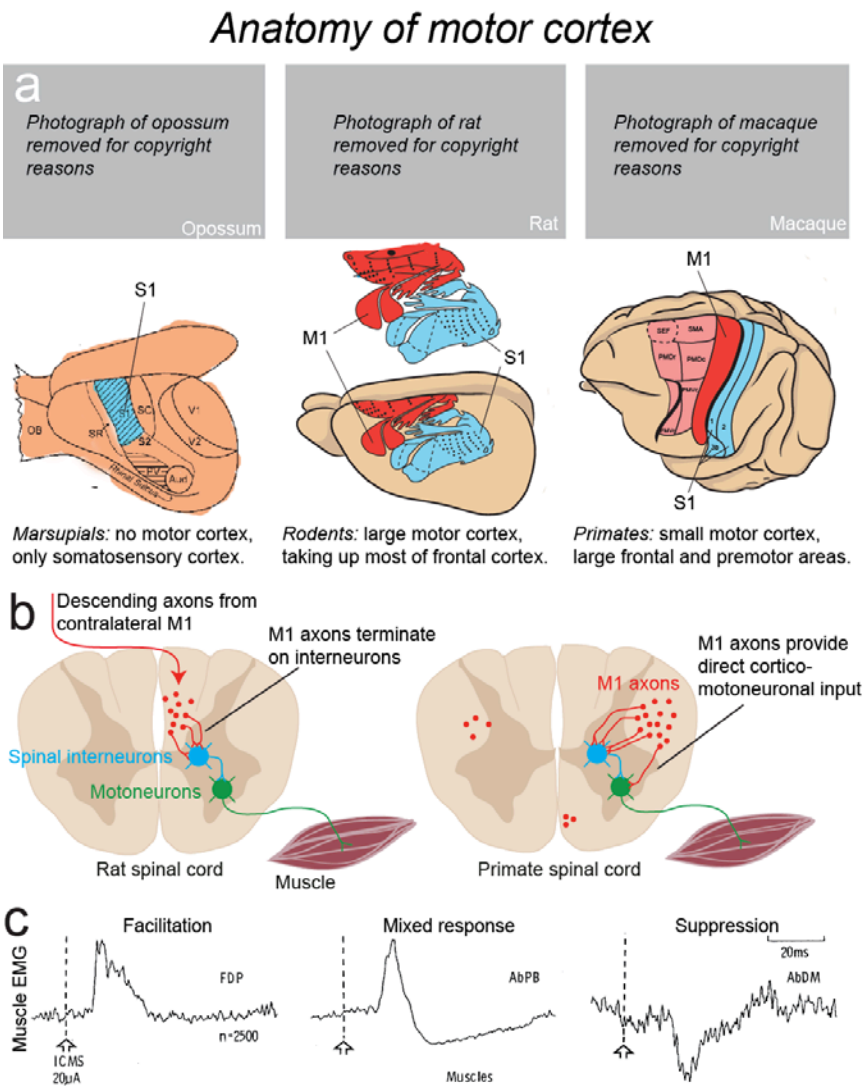

Figure 2: From motor cortex to muscle output: Anatomy and functional connectivity

(a) Motor cortex is a large frontal structure in eutherian mammals. *Left:* Marsupials have no motor cortex. *Middle:* In rodents, primary motor cortex takes up almost all of frontal cortex. *Right:* In primates, frontal cortex is compartmentalized into specialized pre-motor subfields (pale red), and the primary motor cortex (red) is comparatively small. (Adapted with permission from refs. [21,33])

(b) *Left:* Old wiring scheme. In most animals, motor cortical axons terminate on spinal interneurons, not directly on motoneurons (red dots indicate axons from M1). *Right:* Recent wiring scheme (distal limbs in primates, larynx in humans): Some motor cortex axons terminate directly on motoneurons.[44,52]. (Adapted with permission from ref. [44])

(c) Focal intra-cortical microstimulation reveals that motor cortical activity has both facilitating, mixed and – most commonly –suppressive effects on muscular activity (vertical lines indicate stimulation)[64]. (Reproduced with permission from ref. [64])

Permissions: (a,left) Wiley and Sons (a,mid,right) Elsevier (b) Annual Reviews (c) Springer

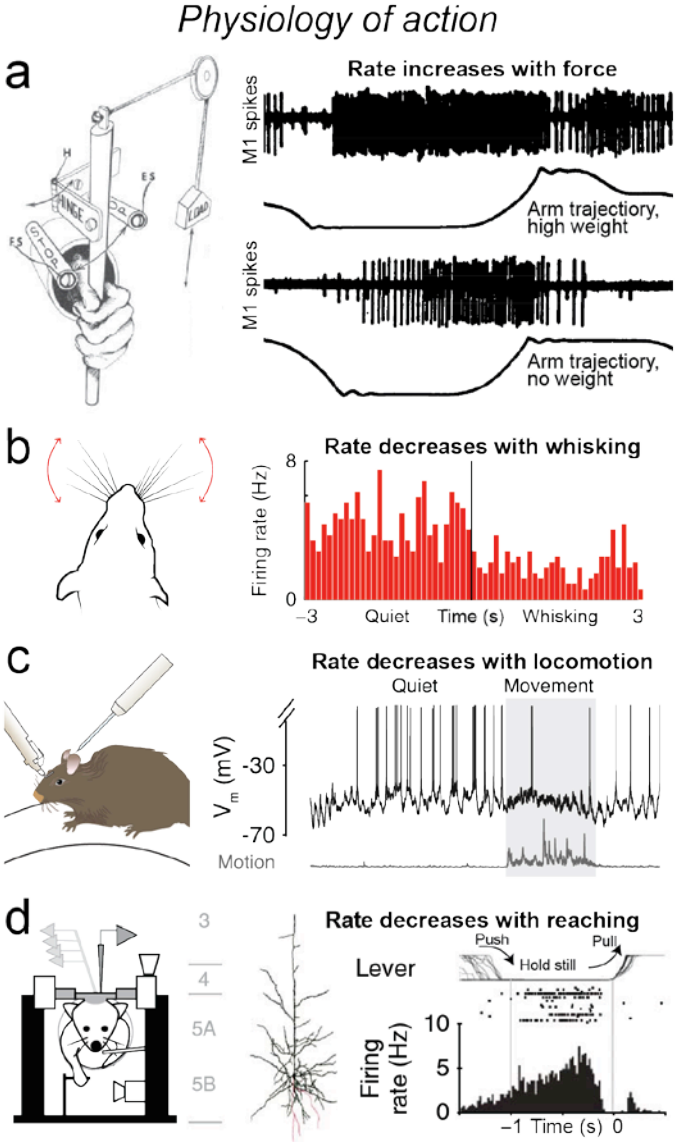

954

955 **Figure 3: *Motor cortex – to act*: Motor cortical activity during movement.**

956 (a) In primates, motor cortical firing rates increase with arm movements and force. *Left:*
957 In a classic experiment[79], a monkey moves a lever connected to a weight in order to
958 receive a reward. *Right:* Motor cortical activity and arm trajectory when the monkey is
959 lifting a high weight (top) and no weight (bottom). (Adapted with permission from ref.
960 [79])

961 (b) In rats, motor cortical activity decreases with whisking[66]. *Left:* A whisking rat. *Right:*
962 Peri-stimulus time histogram of a single unit in layer 5 of vibrissa motor cortex,
963 aligned to the beginning of whisking[66]. (Adapted with permission from ref. [66])

964 (c) In rats, motor cortical activity decreases with locomotion[89,94]. *Left:* A mouse running
965 on a treadmill. *Right:* Intra-cellular recording from neuron in layer 5b of motor cortex,
966 which is suppressed during locomotion[94]. (Adapted with permission from ref. [94])

Permissions: (a) Americal Phys. Soc. (b) own work / Nature Pub. Group (c) Elsevier (d) Nature Pub. Group

967 (d) In rats, motor cortical activity decreases with reaching movements[102]. *Left:* A mouse
968 performing a task, which requires pushing and pulling a lever. *Middle:* Identified
969 neuron in layer 5b of motor cortex. *Right:* Activity of the same neuron is suppressed
970 during reaching[102]. (Adapted with permission from ref. [102])

971

972

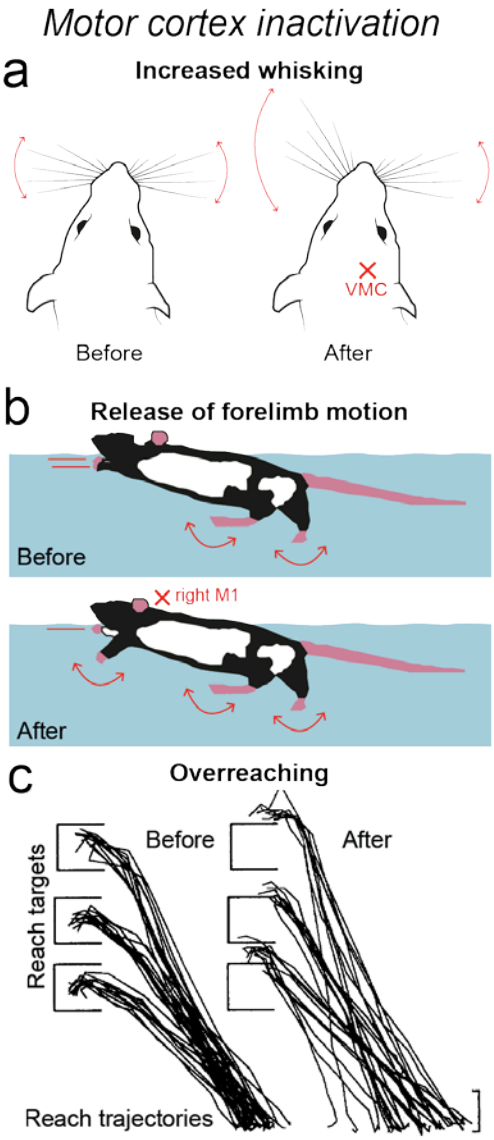

Figure 4: ***Acting without motor cortex:*** **Movement patterns after motor cortex inactivation.**

(a) *Left:* In intact rats, whisking is similar on both sides. *Right:* After unilateral vibrissa motor cortex blockade, contralateral whisker move forward and contralateral whisking power increases[66,125]. (Adapted with permission from ref. [66])

(b) *Top:* Swimming rats normally hold their forelimbs still and swim with only their hindlimbs. *Bottom:* After a unilateral forelimb motor cortex lesion, rats start swimming with the contralateral forelimb also[126]. (Adapted with permission from ref. [126])

(c) *Left:* Intact cats can be trained to reach for morsels of food inside small reaching targets. *Right:* After forelimb motor cortex inactivation, cats fail to receive the rewards because they move too much and over-reach the targets[127]. (Adapted with permission from ref. [127])

Permissions: (a) own work / Nature Pub. Group (b)

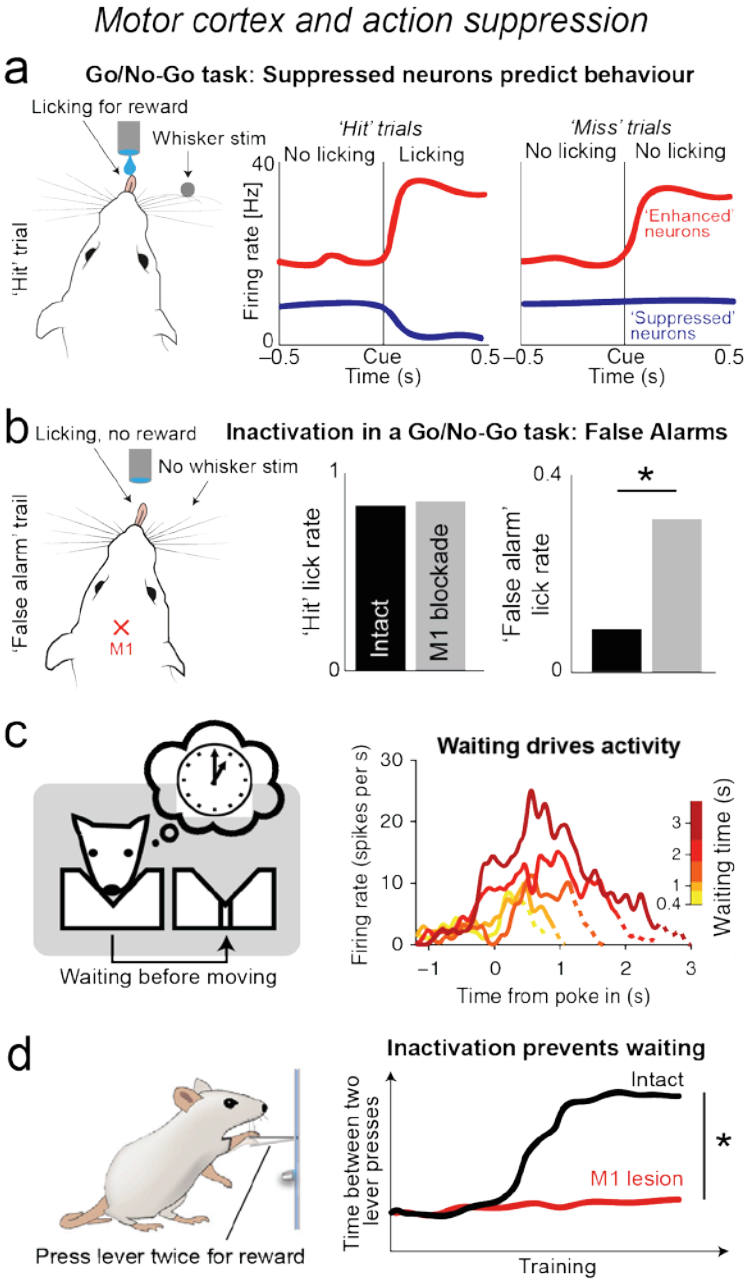

Figure 5: ***Motor cortex – not to act.*** **The neurophysiology of not moving.**

(a) *Left:* Example of a 'hit' trial in a sensorimotor go/no-go task: after a whisker stimulation, the mouse licks for a reward. *Middle:* In hit trials, a population of motor cortical neurons increase their firing rate ('enhanced neurons', red line) and another population decrease their firing rate ('suppressed neurons', blue line) upon stimulation and during licking. *Right:* In 'miss' trials, where the whiskers are stimulated, but the mouse does not lick, the population of 'enhanced neurons' respond nearly identically, but there is no response in the population of 'suppressed neurons'. (Adapted with permission from ref. [135])

Permissions: (a,mid-right) Elsevier (b,mid-right) Elsevier (c) Nature Pub. Group (d) Elsevier

997 (b) *Left:* Example of a 'false alarm' trial in a sensorimotor go/no-go task: the mouse licks
998 in the absence of whisker stimulation and is punished by a time out period. *Right:*
999 Motor cortical inactivation does not affect hit rate (where the rat must lick), but
1000 massively increases false alarm rate (where licking must be withheld)[135,136] (Adapted
1001 with permission from ref. [135])
1002 (c) *Left:* Rat waiting for a reward, which arrives after a random time. *Right:* Activity of a
1003 single motor cortical neuron while the rat is waiting. Longer waiting times (dark
1004 colors) are associated with higher motor cortical activity[35,36]. (Adapted with
1005 permission from ref. [35])
1006 (d) *Left:* Both intact rats and rats with motor cortex lesions can learn to solve a task,
1007 where they must press a lever twice to receive a reward. *Right:* Intact rats can learn to
1008 postpone the second lever press to receive a larger reward, but rats with motor cortex
1009 lesions cannot learn to postpone[143]. (Adapted with permission from ref. [143])

1010

9. General Discussion

9.1 Parahippocampal cortex and neural circuits underlying spatial exploration

9.1.1 Structure-function relationships in parahippocampal cortex

In the first part of this thesis I presented work, which showed that both spatial response patterns and temporal coding patterns map onto the anatomical structure of parahippocampal cortex with cell-type specificity. We found differences between neurons in parasubiculum and the superficial median entorhinal cortex (Chapters 5-6). Further, within the medial entorhinal cortex, we found differences between neurons in layer 3 and layer 2 (Chapter 5-6 and Tang et al., 2015). Finally, within layer 2 of the medial entorhinal cortex, we found differences between stellate neurons and pyramidal neurons (Chapter 4 and Reifenstein et al., 2016).

Before our work, it was already know that parahippocampal neurons show correlations between spatial and temporal response patters. For example, extracellular recordings had revealed that grid cells in layer 2 of medial entorhinal cortex were overwhelmingly theta-modulated neurons (Boccara et al., 2010). Based on intrinsic cell properties, stellate neurons show a higher tendency to discharge at theta frequencies in-vitro than pyramidal neurons (Alonso and Klink, 1993; Shay et al., 2015). Thus, based on in-vitro spike patterns and intrinsic properties, stellate neurons seemed the most likely candidates for grid cells (Latuske et al., 2015; Moser et al., 2008; Rowland et al., 2016). On the other hand, it was also known from extracellular recordings that grid cells were not uniformly distributed across layer 2 of the medial entorhinal cortex, but rather clustered in grid activity 'hot-spots' (Stensola et al., 2012) with a size and spacing corresponding to the anatomical clusters of pyramidal neurons (Ray et al., 2014). Thus, the anatomical distribution of grid cells rather pointed to the conclusion that grid cells might be pyramidal neurons (Brecht et al., 2014; Burgalossi and Brecht, 2014; Savelli and Knierim, 2014).

9.1.2 How are grid cells made?

We could show that differences between temporal spiking patterns of stellate and pyramidal neurons (Ray et al., 2014) suggested that grid cells were primarily pyramidal neurons and that border cells were primarily stellate neurons (Chapter 4). Obviously, this conclusion is indirect and rests on assumptions about the stationarity of theta modulation within and between neurons (Chapter 4 & 6). Thus, even though our observations were quite clear, our method cannot exclude that e.g. a small subpopulation of stellate neurons spike with otherwise pyramidal-typic theta modulation and a spatial grid pattern.

Interestingly, despite massive efforts by several groups, we still have only little data indicating if such a stellate-grid-cell subpopulation exists, if grid cells are primarily pyramidal neurons, or if grid cells are equally prevalent in both cell types. The paucity of data mainly stems from the fact that grid cells are not very abundant (~ 5-15% of principal neurons, Chapter 4) and must be recorded in animals exploring a full two-dimensional environment to be unequivocally identified. These factors contribute to making grid cells highly challenging to study, and thus much of our knowledge about structure-function relationships in parahippocampal cortex must be taken with important caveats. For example, in addition to entorhinal grid cells being theta-modulated (Boccara et al., 2010), Chapter 4), two studies found that across parahippocampal cortex, grid cells were also most often bursty neurons (Latuske et al., 2015; Newman and Hasselmo, 2014). According to our studies on cell-type differences in burstiness (Chapter 6), this suggests that parahippocampal grid cells are most likely either pyramidal neurons in layer 2 of medial entorhinal cortex or parasubicular neurons, with the caveat that we have to assume that temporal spike patterns map onto cell type in a well-behaved manner.

Another study made intracellular recordings from neurons in layer 2 of medial entorhinal cortex and assigned the neurons as pyramidal or stellate by their reconstructed morphology. This study found that stellate neurons, not pyramidal neurons, were most likely to be grid cells (Domnisoru et al., 2013). While the morphological and laminar assignment of these neurons was clear, the neurons were recorded in rats exploring a linear track (not a full two-dimensional environment). In such a setup, it is extremely difficult to distinguish a true grid cell from a neuron with another spatial, but 'non-grid' pattern (Yoon et al., 2016). Two recent studies used transgenic mice and viral techniques to restrict the expression of a calcium sensor and light-gated ion channels to pyramidal and stellate neurons. In one study, in-vivo imaging of calcium-activity suggested that the proportion of grid cells was remarkably similar in the two cell types (Sun et al., 2015). While this study had high certainty of the cellular identity (dentate gyrus-projecting 'stellate' versus wolframin-positive 'pyramidal' neurons), dorsal implantation of an endoscope for in-vivo imaging massively disrupts the tissue and impairs the ability to distinguish e.g. parasubicular and entorhinal neurons, which both express wolframin. Another study used optogenetic activation to identify extracellularly recorded stellate and pyramidal neurons and similarly found that grid cells were equally distributed across cell types (Toader, 2016), with the major caveat that due to the very low latencies of some synaptically activated neurons (Muñoz et al., 2014), such optogenetic tagging-studies are susceptible to high rates of false-positives, especially when optogenetcally activating excitatory cell types (Toader, 2016).

9.1.3 What does the grid cell system teach us about cortical computation?

Numerous anatomical studies have clearly shown that the cytoarchitechtonic structure of parahippocampal cortex is highly modular (Burgalossi and Brecht, 2014), comprising both the hexagonal arrangement of patches of pyramidal neurons in layer 2 of the medial entorhinal cortex ((Kitamura et al., 2014; Naumann et al., 2016; Ray et al., 2014), perhaps with further subdivisions (Fuchs et al., 2016)), but also other anatomical modules within layer 2 (Ray et al., 2017), layer 3 (Henn-Mike et al., 2016; Ray et al., 2017; Tang et al., 2015) and the adjacent presubiculum (Preston-Ferrer et al., 2016; Ray et al., 2017) and parasubiculum (Chapter 5, (Burgalossi et al., 2011; Ray et al., 2017)) (Figure 12). Our work suggests that both spatial and temporal temporal coding features are highly determined by these anatomical modules (Chapters 4,6).

There is a wealth of computational models, which propose mechanisms, which could generate spatial discharge patterns in parahippocampal neurons (Giocomo et al., 2011; Zilli, 2012). Models where the anatomical structure patterns the activity are rare (but see Brecht et al., 2014) and most models propose mechanisms by which networks of similar (most often stellate) neurons organize to generate e.g. periodic grid-cell-like spike patterns, commonly by oscillatory interference and/or by network attractor dynamics (but see e.g. Kerdels, 2016). Such models do not in their present form account for the stratified distribution of parahippocampal activity onto specific cellular ensembles with distinct archetypal temporal spike patterns (e.g. bursty, theta-rhythmic pyramidal neurons vs. non-bursty stellate neurons in layer 2

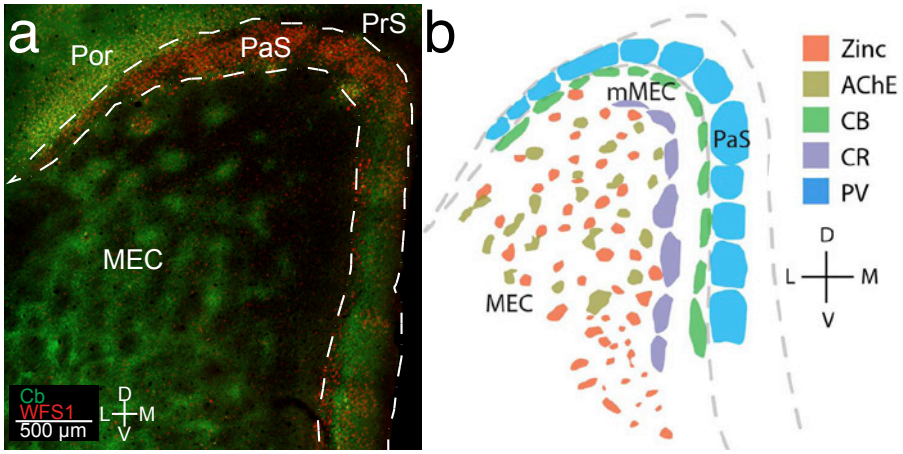

Figure 12: Modular cytoachitectonics of parahippocampal cortex.
(a) Tangential section of rat parahippocampal cortex through the presubiculum (PrS), parasubiculum (PaS), postrhinal cortex (Por) and layer 2 of the medial entorhinal cortex (MEC), stained for calbindin (Cb, green channel) and wolframin (WFS1, red channel). Clusters of calbindin-positive pyramidal neurons are visible in the medial entorhinal cortex. (Adapted from Ebbesen et al., 2016, Chap 4.)
(b) Schematic overview of modular structures in the superficial layers of MEC and the neighbouring medial-most MEC (mMEC), PaS, and PrS. Colored regions indicate anatomical 'modules' of neurons delineated by enrichment in synaptic Zinc activity (Zinc), enriched cholinergic activity (AChE) and expression of calbindin (Cb), calretinin (Cr) and parvalbumin (PV). (Adapted from Ray et al., 2017, with permission, Frontiers)

of medial entorhinal cortex, Chapter 6). Elucidating if and how the elaborate modular cytoarchitechtonics contribute to the generation of spatial responses in the parahippocampal region would be a major advance in our understanding of how anatomical microcircuits contribute to cortical computation and temporal coding in general.

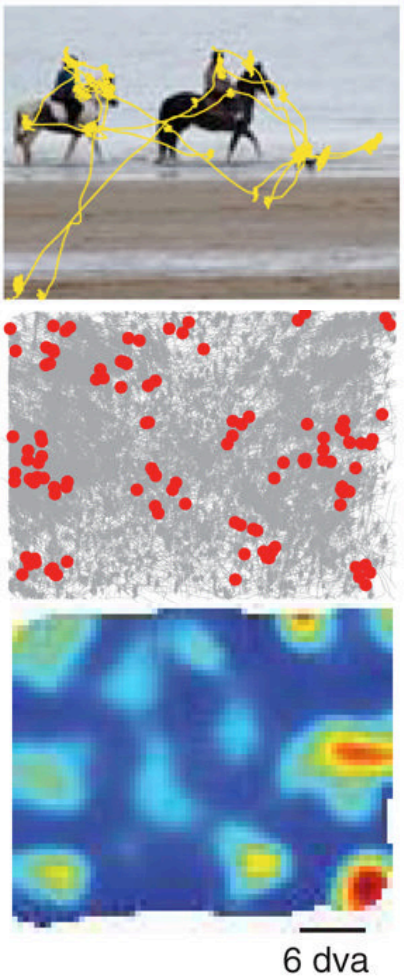

Figure 13: Grid-cell-like responses of entorhinal neurons to saccades across a visual scene. Top: Example 10-second saccade paths across a visual stimulus. Middle: Plots of eye position (gray) and spikes (red) reveal a grid-cell-like firing pattern (spikes only plotted at loci of above-average firing rates). Bottom: Spatial firing rate maps across visual scenes show multiple distinct firing fields (dva = degrees of visual angle). (Adapted from Killian et al., 2012, with permission, Nature NPG)

The striking spatial representations in the parahippocampal cortex present a rare opportunity to tie single cell cortical computation to the 'high-level' cognitive tasks, which the grid cell system is solving. As mentioned in the introduction, the fact that plotting the two-dimensional spike patterns of parahippocampal neurons produces enormously elegant patterns lets it appear likely that these neurons are involved in a cognitive task, which requires an 'encoding' of the environment. Interestingly, it remains an open question what these cognitive tasks might be. Early interpretations suggested that the grid cell system might be primarily for navigation, contributing to path integration of self-motion (Bush et al., 2015; McNaughton et al., 2006; Moser and Moser, 2008; Rowland et al., 2016). However, grid cells have several dynamic features, such as non-uniform expansion in novel environments (Barry et al., 2012; Hägglund et al., 2016), drift (Hardcastle et al., 2015) and distortions of the hexagonality (Krupic et al., 2015; Stensola et al., 2015). These dynamic features make grid cells less than ideal as the matric basis of an internal navigation system, since any read-out mechanism would need to track and correct for these dynamic effects (but on the other hand, mammals also generally perform poorly in path integration tasks (Etienne and Jeffery, 2004; Etienne et al., 1996)). Further, several studies have implicated neurons in superficial medial entorhinal cortex in distinctly 'non-navigation' tasks, such as memory consolidation (Kitamura et al., 2014, 2017), integration of sensory stimuli (timing lever presses in response to auditory cues, Aronov et al., 2017) and mapping of a visual scene (Killian et al., 2012, 2015). Intriguingly, in the latter case, the discharge pattern in response to saccades across the visual scene was both grid-cell-like and border-cell-like (Figure 13), suggesting that perhaps the spatial

fields are not strictly tied to allocentric space, but rather the signature of an abstract, general principle by which cortical neurons encode complex information (Kerdels, 2016; Kerdels and Peters, 2015). Answering these many open questions (Figure 14) and determining what the grid cell system is really 'doing' will be a major advance in our understanding of the cellular basis of cognition.

9.2 Motor cortex and neural circuits underlying social exploration

9.2.1 What is the function of rat vibrissa motor cortex?

The brain structure, which we refer to as 'vibrissa motor cortex' in Chapters 7-8, is anatomically delineated as an agranular area with a large layer 5b and an (almost) absence of layer 4 (Brecht et al., 2004; Yamawaki et al., 2014; Zilles and Wree, 1995). Classical cortical mapping studies clearly assign this area as the primary motor representation of the whiskers (Brecht et al., 2004; Hall and Lindholm, 1974; Matyas et al., 2010; Neafsey et al., 1986) and accordingly many studies have focused on the relation between neural activity in this area and the kinematics of whisker movements (Gerdjikov et al., 2013; Hill et al., 2011; Sreenivasan et al., 2016). However – as we discuss in Chapter 8 – this brain structure is referred to by many names (Brecht, 2011) and has been implicated in a range of functions. For example, some studies have investigated this cortical area as a frontal orientation field (i.e. a rodent homologue of primate frontal eye field) and implicated the area in choice, working memory and preparation of upcoming motor decisions (Brody and Hanks, 2016; Erlich et al., 2011, 2015; Hanks et al., 2015). Other studies have investigated this area as secondary motor cortex (i.e. a homologue of primate supplementary motor areas) and implicated the neurons in decision making in relation to rewards and upcoming motor strategies (Barthas and Kwan, 2017; Murakami et al., 2014, 2016, Reep et al., 1987, 1990; Sul et al., 2011).

In the second part of this thesis I presented a study where we investigated the activity patterns in vibrissa motor cortex during a range of 'naturalistic' whisking behaviors (Chapter 7). We can draw two major conclusions from our observations. The first major conclusion is that spike patterns, microstimulation and inactivation experiments point to a major role of this cortical structure in inhibitory control of behavior. In the manuscript presented in Chapter 8, we already discussed in detail how this observation aligns with other studies on motor cortex function across mammals. The second major conclusion is that neural activity in primary motor cortex is modulated by social touch, even when basic kinematic aspects of the whisker movement are regressed out (at least in our first-order generalized

linear modeling of the spike patterns). This point was not developed extensively in the manuscripts presented in Chapter 7-8, but it opens avenues for interesting follow-up studies investigating social computations in frontal cortex.

9.2.2 Social computations in sensorimotor cortex

Social interactions, such as play behavior and pair bond formation, are fundamental aspects of animal and human behavior. Despite this fact, we still know only very little about the cortical machinery for social cognition. The somatosensory cortex is a large cortical area, which contains a remarkably detailed, somatotopic representation of the body (Lenschow et al., 2016; Woolsey and Van der Loos, 1970) and is massively interconnected with motor cortex (Barth et al., 1990; Diamond et al., 2008; Feldmeyer et al., 2013; Hatsopoulos and Suminski, 2011; Smith and Alloway, 2013). It has long been known that neural activity in somatosensory cortex is critical for the perception of touch, i.e. sensing the body surface (Mountcastle, 1956). Surprisingly, recent evidence shows that activity in somatosensory cortex is also key for social cognition, i.e. 'thinking about' your own body and other bodies. For example, in rodents (Bobrov et al., 2014) and humans (Gazzola et al., 2012), neural activity in somatosensory cortex is different when touching male and a female conspecifics, even though the actual touch input is the same – a signature that these neurons encode 'social' categories. Similarly, somatosensory cortex is activated in a social context before any actual touch input (Lenschow and Brecht, 2015), when observing others in pain (Keysers et al., 2010) , and when simply imagining pleasant or sexual touch (Wise et al., 2016), so-called 'vicarious' touch responses. Human studies using trans-cranial magnetic stimulation to influence cortical activity have shown that these 'vicarious' responses in somatosensory cortex are actually causally involved in crucial aspects of healthy social cognition, such as empathy (Bolognini et al., 2013; Keysers et al., 2010) and deciphering the bodily and emotional states of conspecifics (Paracampo et al., 2016; Valchev et al., 2016).

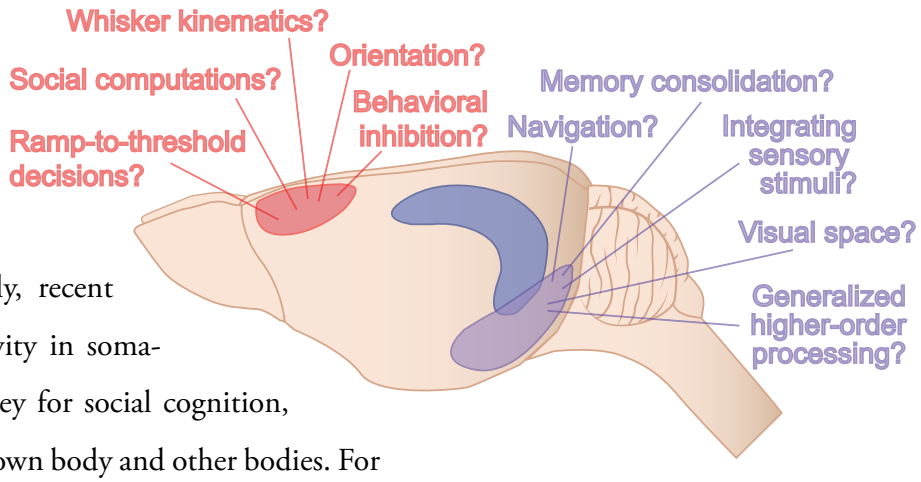

Figure 14: What are cortical neurons doing? Vibrissa motor cortex (red color) and parahippocampal cortex (purple color) has been implicated in a diverse range of functions across a variety of cognitive domains. (Adapted from Poucet & Sargolini, 2013, with permission, Nature Pub. Group)

To investigate if motor cortical activity is modulated by social covariates further studies might record vibrissa motor cortex of both male and female animals, across hormonal states, during social facial interactions with both male and female conspecifics to determine if performing the same whisker movements in different social contexts modulates neural activity differentially. While such a study is beyond the scope of this thesis, I already observed response patterns during my experiments presented in Chapter 7, which indicated that motor cortical activity is modulated by social covariates. For example, even though whisking patterns in male rats are very similar between interactions with male and female conspecifics (Wolfe et al., 2011), I recorded neurons in the vibrissa motor cortex of male rats, which showed markedly different responses to interacting with male and female conspecifics. We are currently investigating these observations further and comparing them to social signals in sensory cortices (Bobrov et al., 2014; Rao et al., 2014).

It is presently unknown how higher-order 'social' responses in somatosensory cortex are generated from afferent sensory information relayed to cortex from the sensory epithelium. We also do not know if these responses in social contexts are truly 'social' in the sense that they are specific to the social domain (as e.g. the macaque face patch systems seems specifically tuned to recognize conspecifics (Ghazanfar and Santos, 2004; Tsao and Livingstone, 2008; Tsao et al., 2006)), or if they are simply 'ordinary' responses to highly salient stimuli. Elucidating if and how activity patterns indicative of social computations (e.g. different responses to the same 'touch' from a male and female conspecific (Bobrov et al., 2014; Gazzola et al., 2012), modulation of these responses by the hormonal state of the animal (Bobrov et al., 2014)) extend to motor cortex could provide valuable information about how 'social' patterns of computation arise, how they propagate across neural circuits and what they contribute to the neural control of healthy social behavior.

9.3 References

Alonso, A., and Klink, R. (1993). Differential electroresponsiveness of stellate and pyramidal-like cells of medial entorhinal cortex layer II. J. Neurophysiol. 70, 128–143.

Aronov, D., Nevers, R., and Tank, D.W. (2017). Mapping of a non-spatial dimension by the hippocampal–entorhinal circuit. Nature 543, 719–722.

Barry, C., Ginzberg, L.L., O'Keefe, J., and Burgess, N. (2012). Grid cell firing patterns signal environmental novelty by expansion. Proc. Natl. Acad. Sci. U. S. A. 109, 17687–17692.

Barth, T.M., Jones, T. a., and Schallert, T. (1990). Functional subdivisions of the rat somatic sensorimotor cortex. Behav. Brain Res. 39, 73–95.

Barthas, F., and Kwan, A.C. (2017). Secondary Motor Cortex : Where " Sensory " Meets " Motor " in the Rodent Frontal Cortex. Trends Neurosci. 40, 181–193.

Bobrov, E., Wolfe, J., Rao, R.P., and Brecht, M. (2014). The representation of social facial touch in rat barrel cortex. Curr. Biol. 24, 109–115.

Boccara, C.N., Sargolini, F., Thoresen, V.H., Solstad, T., Witter, M.P., Moser, E.I., and Moser, M.-B. (2010). Grid cells in pre- and parasubiculum. Nat. Neurosci. 13, 987–994.

Bolognini, N., Rossetti, a, Convento, S., and Vallar, G. (2013). Understanding other's fellings: the role of the right primary somatosensory cortwx in encoding the affective valence of other's touch. J. Neurosci. 33, 4201–4205.

Brecht, M. (2011). Movement, Confusion, and Orienting in Frontal Cortices. Neuron 72, 193–196.

Brecht, M., Krauss, A., Muhammad, S., Sinai-Esfahani, L., Bellanca, S., and Margrie, T.W. (2004). Organization of rat vibrissa motor cortex and adjacent areas according to cytoarchitectonics, microstimulation, and intracellular stimulation of identified cells. J. Comp. Neurol. 479, 360–373.

Brecht, M., Ray, S., Burgalossi, A., Tang, Q., Schmidt, H., and Naumann, R. (2014). An isomorphic mapping hypothesis of the grid representation. Philos. Trans. R. Soc. Lond. B. Biol. Sci. 369, 20120521.

Brody, C.D., and Hanks, T.D. (2016). Neural underpinnings of the evidence accumulator. Curr. Opin. Neurobiol. 37, 149–157.

Burgalossi, A., and Brecht, M. (2014). Cellular, columnar and modular organization of spatial representations in medial entorhinal cortex. Curr. Opin. Neurobiol. 24, 47–54.

Burgalossi, A., Herfst, L., von Heimendahl, M., Förste, H., Haskic, K., Schmidt, M., and Brecht, M. (2011). Microcircuits of Functionally Identified Neurons in the Rat Medial Entorhinal Cortex. Neuron 70, 773–786.

Bush, D., Barry, C., Manson, D., Burgess, N., Blair, H.T., Save, E., Moser, E.I., Merkow, M., Polyn, S.M., Jacobs, J., et al. (2015). Using Grid Cells for Navigation. Neuron 87, 507–520.

Diamond, M.E., von Heimendahl, M., Knutsen, P.M., Kleinfeld, D., and Ahissar, E. (2008). "Where" and "what" in the whisker sensorimotor system. Nat. Rev. Neurosci. 9, 601–612.

Domnisoru, C., Kinkhabwala, A.A., and Tank, D.W. (2013). Membrane potential dynamics of grid cells. Nature 495, 199–204.

Erlich, J.C., Bialek, M., and Brody, C.D. (2011). A Cortical Substrate for Memory-Guided Orienting in the Rat. Neuron 72, 330–343.

Erlich, J.C., Brunton, B.W., Duan, C.A., Hanks, T.D., and Brody, C.D. (2015). Distinct effects of prefrontal and parietal cortex inactivations on an accumulation of evidence task in the rat. 1–28.

Etienne, A.S., and Jeffery, K.J. (2004). Path integration in mammals. Hippocampus 14, 180–192.

Etienne, A.S., Maurer, R., and Séguinot, V. (1996). Path integration in mammals and its interaction with visual landmarks. J. Exp. Biol. 199, 201–209.

Feldmeyer, D., Brecht, M., Helmchen, F., Petersen, C.C.H., Poulet, J.F.A., Staiger, J.F., Luhmann, H.J., and Schwarz, C. (2013). Barrel cortex function. Prog. Neurobiol. 103, 3–27.

Fuchs, E.C., Neitz, A., Pinna, R., Melzer, S., Caputi, A., and Monyer, H. (2016). Local and Distant Input Controlling Excitation in Layer II of the Medial Entorhinal Cortex. Neuron 89, 194–208.

Gazzola, V., Spezio, M.L., Etzel, J. a., Castelli, F., Adolphs, R., and Keysers, C. (2012). PNAS Plus: Primary somatosensory cortex discriminates affective significance in social touch. Proc. Natl. Acad. Sci. 109, E1657–E1666.

Gerdjikov, T. V, Haiss, F., Rodriguez-Sierra, O.E., and Schwarz, C. (2013). Rhythmic whisking area (RW) in rat primary motor cortex: an internal monitor of movement-related signals? J. Neurosci. 33, 14193–14204.

Ghazanfar, A.A., and Santos, L.R. (2004). Primate brains in the wild: the sensory bases for social interactions. Nat. Rev. Neurosci. 5, 603–616.

Giocomo, L.M., Moser, M.-B., and Moser, E.I. (2011). Computational models of grid cells. Neuron 71, 589–603.

Hall, R.D., and Lindholm, E.P. (1974). Organization of motor and somatosensory neocortex in the albino rat. Brain Res. 66, 23–38.

Hanks, T.D., Kopec, C.D., Brunton, B.W., Duan, C.A., Erlich, J.C., and Brody, C.D. (2015). Distinct relationships of parietal and prefrontal cortices to evidence accumulation. Nature 520, 220–223.

Hardcastle, K., Ganguli, S., and Giocomo, L.M. (2015). Environmental Boundaries as an Error Correction Mechanism for Grid Cells. Neuron 86, 827–839.

Hatsopoulos, N.G., and Suminski, A.J. (2011). Sensing with the motor cortex. Neuron 72, 477–487.

Henn-Mike, N., Kecskés, M., Krabóth, Z., Sebestyén, H., and Varga, C. (2016). KKK10 183.17 Medial entorhinal cortex layer III pyramidal cells form dendritic bundles in a grid-like hexagonal pattern and receive specific inputs from the presubiculum. In Neuroscience 2016, (San Diego),

Hill, D.N., Curtis, J.C., Moore, J.D., and Kleinfeld, D. (2011). Primary motor cortex reports efferent control of vibrissa motion on multiple timescales. Neuron 72, 344–356.

Hägglund, M., Moser, M.-B., and Moser, E.I. (2016). 183.06/JJJ60 Spatial dynamics of grid cells dur-

ing novelty. In Neuroscience 2016, (San Diego).

Kerdels, J. (2016). A Computational Model of Grid Cells based on a Recursive Growing Neural Gas.

Kerdels, J., and Peters, G. (2015). A New View on Grid Cells Beyond the Cognitive Map Hypothesis. 1–10.

Keysers, C., Kaas, J.H., and Gazzola, V. (2010). Somatosensation in social perception. Nat. Rev. Neurosci. 11, 417–428.

Killian, N.J., Jutras, M.J., and Buffalo, E. a. (2012). A map of visual space in the primate entorhinal cortex. Nature 491(7426): 761–764.

Killian, N.J., Potter, S.M., and Buffalo, E.A. (2015). Saccade direction encoding in the primate entorhinal cortex during visual exploration. Proc. Natl. Acad. Sci. 112(51):15743-8

Kitamura, T., Pignatelli, M., Suh, J., Kohara, K., Yoshiki, A., Abe, K., and Tonegawa, S. (2014). Island cells control temporal association memory. Science 343, 896–901.

Kitamura, T., Ogawa, S.K., Roy, D.S., Okuyama, T., Morrissey, M.D., Smith, L.M., Redondo, R.L., and Tonegawa, S. (2017). Engrams and circuits crucial for systems consolidation of a memory. Science (80-.). 356.

Krupic, J., Bauza, M., Burton, S., Barry, C., and O'Keefe, J. (2015). Grid cell symmetry is shaped by environmental geometry. Nature 518, 232–235.

Latuske, P., Toader, O., and Allen, K. (2015). Interspike Intervals Reveal Functionally Distinct Cell Populations in the Medial Entorhinal Cortex. J. Neurosci. 35, 10963–10976.

Lenschow, C., and Brecht, M. (2015). Barrel Cortex Membrane Potential Dynamics in Social Touch. Neuron 85, 718–725.

Lenschow, C., Copley, S., Gardiner, J.M., Talbot, Z.N., Vitenzon, A., and Brecht, M. (2016). Sexually Monomorphic Maps and Dimorphic Responses in Rat Genital Cortex. Curr. Biol. 26, 106–113.

Matyas, F., Sreenivasan, V., Marbach, F., Wacongne, C., Barsy, B., Mateo, C., Aronoff, R., and Petersen, C.C.H. (2010). Motor control by sensory cortex. Science 330, 1240–1243.

McNaughton, B.L., Battaglia, F.P., Jensen, O., Moser, E.I., and Moser, M.-B. (2006). Path integration and the neural basis of the "cognitive map." Nat. Rev. Neurosci. 7, 663–678.

Moser, E.I., and Moser, M.-B. (2008). A metric for space. Hippocampus 18, 1142–1156.

Moser, E.I., Kropff, E., and Moser, M.-B. (2008). Place Cells, Grid Cells, and the Brain's Spatial Representation System. Annu. Rev. Neurosci. 31, 69–89.

Mountcastle, V. (1956). Modalily and topographic properties of single neurons of cat's somatic sensory system. J.Neurophysiol. 20, 408–434.

Muñoz, W., Tremblay, R., Rudy, B., Rudy, B., Silberberg, G., Luo, J., Markram, H., Fu, Y., Lu, J., Lin,

Y., et al. (2014). Channelrhodopsin-Assisted Patching: In Vivo Recording of Genetically and Morphologically Identified Neurons throughout the Brain. Cell Rep. 9, 2304–2316.

Murakami, M., Vicente, M.I., Costa, G.M., and Mainen, Z.F. (2014). Neural antecedents of self-initiated actions in secondary motor cortex. Nat. Neurosci. 17, 1574–1582.

Murakami, M., Shteingart, H., Loewenstein, Y., and Mainen, Z.F. (2016). Distinct sources of deterministic and stochastic components of action timing decisions in rodent frontal cortex. bioRxiv.

Naumann, R.K., Ray, S., Prokop, S., Las, L., Heppner, F.L., and Brecht, M. (2016). Conserved size and periodicity of pyramidal patches in layer 2 of medial/caudal entorhinal cortex. J. Comp. Neurol. 524, 783–806.

Neafsey, E.J., Bold, E.L., Haas, G., Hurley-Gius, K.M., Quirk, G., Sievert, C.F., and Terreberry, R.R. (1986). The organization of the rat motor cortex: A microstimulation mapping study. Brain Res. Rev. 11, 77–96.

Newman, E.L., and Hasselmo, M.E. (2014). Grid cell firing properties vary as a function of theta phase locking preferences in the rat medial entorhinal cortex. Front. Syst. Neurosci. 8, 1–15.

Paracampo, R., Tidoni, E., Borgomaneri, S., di Pellegrino, G., and Avenanti, A. (2016). Sensorimotor Network Crucial for Inferring Amusement from Smiles. Cereb. Cortex 1–14.

Preston-Ferrer, P., Coletta, S., Frey, M., and Burgalossi, A. (2016). Anatomical organization of presubicular head-direction circuits. Elife 5.

Rao, R.P., Mielke, F., Bobrov, E., and Brecht, M. (2014). Vocalization–whisking coordination and multisensory integration of social signals in rat auditory cortex. Elife 3, 1–20.

Ray, S., Naumann, R., Burgalossi, A., Tang, Q., Schmidt, H., and Brecht, M. (2014). Grid-layout and theta-modulation of layer 2 pyramidal neurons in medial entorhinal cortex. Science 343, 891–896.

Ray, S., Burgalossi, A., Brecht, M., and Naumann, R.K. (2017). Complementary Modular Microcircuits of the Rat Medial Entorhinal Cortex. Front. Syst. Neurosci. 11, 1–18.

Reep, R.L., Corwin, J. V, Hashimoto, A., and Watson, R.T. (1987). Efferent connections of the rostral portion of medial agranular cortex in rats. Brain Res. Bull. 19, 203–221.

Reep, R.L., Goodwin, G.S., and Corwin, J. V. (1990). Topographic organization in the corticocortical connections of medial agranular cortex in rats. J. Comp. Neurol. 294, 262–280.

Reifenstein, E.T., Ebbesen, C.L., Tang, Q., Brecht, M., Schreiber, S., and Kempter, R. (2016). Cell-Type Specific Phase Precession in Layer II of the Medial Entorhinal Cortex. J. Neurosci. 36(7):2283-8.

Rowland, D.C., Roudi, Y., Moser, M.-B., and Moser, E.I. (2016). Ten Years of Grid Cells. Annu. Rev.

Neurosci. 39, 19–40.

Savelli, F., and Knierim, J.J. (2014). Strides toward a structure-function understanding of cortical representations of allocentric space. Neuron 84, 1108–1109.

Shay, C.F., Ferrante, M., Chapman, G.W., and Hasselmo, M.E. (2015). Rebound spiking in layer II medial entorhinal cortex stellate cells: Possible mechanism of grid cell function. Neurobiol. Learn. Mem.

Smith, J.B., and Alloway, K.D. (2013). Rat whisker motor cortex is subdivided into sensory-input and motor-output areas. Front. Neural Circuits 7, 4.

Sreenivasan, V., Esmaeili, V., Kiritani, T., Galan, K., Crochet, S., and Petersen, C.C.H. (2016). Movement Initiation Signals in Mouse Whisker Motor Cortex. Neuron 92, 1368–1382.

Stensola, H., Stensola, T., Solstad, T., Frøland, K., Moser, M.-B., and Moser, E.I. (2012). The entorhinal grid map is discretized. Nature 492, 72–78.

Stensola, T., Stensola, H., Moser, M.-B., and Moser, E.I. (2015). Shearing-induced asymmetry in entorhinal grid cells. Nature 518, 207–212.

Sul, J.H., Jo, S., Lee, D., and Jung, M.W. (2011). Role of rodent secondary motor cortex in value-based action selection. Nat. Neurosci. 14, 1202–1208.

Sun, C., Kitamura, T., Yamamoto, J., Martin, J., Pignatelli, M., Kitch, L.J., Schnitzer, M.J., and Tonegawa, S. (2015). Distinct speed dependence of entorhinal island and ocean cells, including respective grid cells. Proc. Natl. Acad. Sci. 112, 9466–9471.

Tang, Q., Ebbesen, C.L., Sanguinetti-scheck, J.I., Preston-ferrer, P., Gundlfinger, A., Winterer, J., Beed, P., Ray, S., Naumann, R., Schmitz, D., et al. (2015). Anatomical Organization and Spatiotemporal Firing Patterns of Layer 3 Neurons in the Rat Medial Entorhinal Cortex. J. Neurosci. 35, 12346–12354.

Toader, O. (2016). Genetic approaches to probe spatial coding in the medial entorhinal cortex. Ruperto-Carola University of Heidelberg, Germany.

Tsao, D.Y., and Livingstone, M.S. (2008). Mechanisms of face perception. Annu. Rev. Neurosci. 31, 411–437.

Tsao, D.Y., Freiwald, W.A., Tootell, R.B.H., and Livingstone, M.S. (2006). A cortical region consisting entirely of face-selective cells. Science 311, 670–674.

Valchev, N., Gazzola, V., Avenanti, A., and Keysers, C. (2016). Primary somatosensory contribution to action observation brain activity-combining fMRI and cTBS. Soc. Cogn. Affect. Neurosci. 11, 1205–1217.

Wise, N.J., Frangos, E., and Komisaruk, B.R. (2016). Activation of sensory cortex by imagined genital

stimulation: an fMRI analysis. Socioaffective Neurosci. Psychol. 6.

Wolfe, J., Mende, C., and Brecht, M. (2011). Social facial touch in rats. Behav. Neurosci. 125, 900–910.

Woolsey, T.A., and Van der Loos, H. (1970). The structural organization of layer IV in the somatosensory region (S I) of mouse cerebral cortex: The description of a cortical field composed of discrete cytoarchitectonic units. Brain Res. 17, 205–242.

Yamawaki, N., Borges, K., Suter, B.A., Harris, K.D., Shepherd, G.M.G., Wood, L., Shepherd, G., Shepherd, G., Brockway, K., Byrnes, E., et al. (2014). A genuine layer 4 in motor cortex with prototypical synaptic circuit connectivity. Elife 4, e05422.

Yoon, K., Lewallen, S., Kinkhabwala, A.A., Tank, D.W., and Fiete, I.R. (2016). Grid Cell Responses in 1D Environments Assessed as Slices through a 2D Lattice. Neuron 89, 1086–1099.

Zilles, K., and Wree, A. (1995). Cortex: Areal and Laminar Structure. In The Rat Nevous System, G. Paxinos, ed. (San Diego: Academic Press), pp. 649–685.

Zilli, E. a. (2012). Models of Grid Cell Spatial Firing Published 2005–2011. Front. Neural Circuits 6, 1–17.

10. Curriculum vitae

- - - CV removed from published version - - -

- - - CV removed from published version - - -

11. List of publications

Christian L. **Ebbesen**

M.Sc. · Ph.D. student · Neuroscience

XX Straße XX, XXXXX Berlin, Germany

+49 XXX XXXX XXXX | XXXX@XXXX.de | http://orcid.org/XXXX-XXXX-XXXX-XXXX

Publications

Journal articles:

Ebbesen, C.L., & Brecht, M. (2017). Motor cortex – To act or not to act? **(submitted)**

Published during PhD studies

Ebbesen, C.L., Doron, G., Lenschow, C., Brecht, M. (2017). Vibrissa motor cortex activity suppresses contralateral whisking behavior. **Nature Neuroscience** 20(1):82-89 Read online

↑ Previewed by: Kim, J. & Hires, A. (2017) Brake and gas pedals in motor cortex **Nature Neuroscience**, 20(1):4-6. Read online

Ebbesen, C.L., Reifenstein, E.T., Tang, Q., Burgalossi, A., Ray, S., Schreiber, S., Kempter, R. & Brecht, M. (2016) Cell type-specific differences in spike timing and spike shape in rat parasubiculum and superficial medial entorhinal cortex. **Cell Reports** 16(4), pp. 1005-1015. Read online

(*)Tang, Q., (*)Burgalossi, A., **(*)Ebbesen, C.L.**, (*)Sanguinetti-Scheck, J.I., Schmidt, H., Tukker, J.J., Naumann, R., Ray, S., Preston-Ferrer, P., Schmitz, D., Brecht, M. (2016) Functional Architecture of the Rat Parasubiculum. **Journal of Neuroscience** 36(7):2289-2301. **(*) Equally contributing** Read online

↑ "Featured Article", previewed by: Esch, T. (2016) This Week in The Journal: *Anatomy and Physiology of Parasubiculum* **Journal of Neuroscience**, 36(7):i-i. Read online

Reifenstein, E.T., **Ebbesen, C.L.**, Tang, Q., Brecht, M., Schreiber, S., Kempter, R. (2016) Cell-Type Specific Phase Precession in Layer II of the Medial Entorhinal Cortex.**Journal of Neuroscience** 36(7):2283-8. Read online

Tang, Q., **Ebbesen, C.L.**, Sanguinetti, J.I., Preston-Ferrer, P., Gundlfinger, A., Winterer, J., Beed, P., Ray, S., Naumann, R., Schmitz, D., Brecht, M., & Burgalossi, A. (2015) Anatomical organization and spatio-temporal firing properties of layer 3 neurons in the rat medial entorhinal cortex. **Journal of Neuroscience**, 35(36):12346-12354 Read online

(*)Tang, Q., (*)Burgalossi, A., **(*)Ebbesen, C.L.**, Ray, S., Naumann, R., Schmidt, H., Spicher, D. & Brecht, M. (2014) Pyramidal and Stellate Cell Specificity of Grid and Border Representations in Layer 2 of Medial Entorhinal Cortex. **Neuron**, 84(6):1191-1197. **(*) Equally contributing** Read online

↑ Previewed by: Savelli, F. & Knierim, J.J. (2014) Strides toward a Structure-Function Understanding of Cortical Representations of Allocentric Space **Neuron**, 84(6):1108-1109. Read online

Ebbesen, C.L. & Bruus, H. (2012) Analysis of laser-induced heating in optical neuronal guidance. **Journal of Neuroscience Methods**, 209(1):168-177 Read online

(*)Adams, J.D., **(*)Ebbesen, C.L.**, Barnkob, R., Yang, A.H.J. , Soh, H.T., & Bruus, H. (2012) High-throughput, temperature-controlled micro- channel acoustophoresis device made with rapid prototyping. **Journal of Micromechanics and Microengineering.** 22:075017 **(*) Equally contributing** Read online

Peer-reviewed conference papers:

Ebbesen, C.L., Adams, J.D., Barnkob, R., Soh, H.T. & Bruus, H. (2010): Temperature-Controlled High-Throughput (1 L/h) Acoustophoretic Particle Separation in Microchannels. **Proceedings of 14th International Conference on Miniaturized Systems for Chemistry and Life Sciences (μTAS)** 728-730 (peer reviewed conference paper) Read online

12. Declaration of contribution

The German version shall prevail.

Anlage zu § 6, Abs. 2 der Promotionsordnung der Lebenswissenschaftlichen Fakultät vom 05.03.2015, veröffentlicht in: Amtliches Mitteilungsblatt HU 12/2015
Annex to § 6, para. 2 of the Doctoral Degree Regulations of the Faculty of Life Sciences, amended on 05.03.2015, published in: University Gazette of Humboldt-Universität zu Berlin 12/2015

Erklärung über den Eigenanteil an den veröffentlichten bzw. zur Veröffentlichung angenommenen wissenschaftlichen Schriften innerhalb meiner Dissertationsschrift gemäß § 6, Abs. 2 der Promotionsordnung
Declaration regarding my own contribution to the published academic papers, or academic papers which have been accepted for publishing, within my doctoral thesis, under the provisions of § 6, para. 2 of the Doctoral Degree Regulations

Von der Antragstellerin/Vom Antragsteller einzutragen: | *To be completed by the applicant:*

1. **Name, Vorname** | *Ebbesen, Christian Laut*
   Institut (ggf. externe Einrichtung) | *Bernstein Center for Computational Neuroscience*
   Promotionsfach | *Biologie*
   Thema der Dissertation | *Cortical circuits underlying social and spatial exploration in rats*

2. **Nummerierte Aufstellung der eingereichten Schriften (Titel, Autor/innen, wo und wann veröffentlicht bzw. eingereicht):**
   Numbered breakdown of the submitted papers (title, authors, where and when published or submitted):

   1. (*)Tang, Q., (*)Burgalossi, A., **(*)Ebbesen, C.L.**, Ray, S., Naumann, R., Schmidt, H., Spicher, D. & Brecht, M. (2014) Pyramidal and Stellate Cell Specificity of Grid and Border Representations in Layer 2 of Medial Entorhinal Cortex. **Neuron** 84(6):1191-1197.

   2. (*)Tang, Q., (*)Burgalossi, A., **(*)Ebbesen, C.L.,** (*)Sanguinetti-Scheck, J.I., Schmidt, H., Tukker, J.J., Naumann, R., Ray, S., Preston-Ferrer, P., Schmitz, D., Brecht, M. (2016) Functional Architecture of the Rat Parasubiculum. **Journal of Neuroscience** 36(7):2289-2301.

   3. **Ebbesen, C.L.**, Reifenstein, E.T., Tang, Q., Burgalossi, A., Ray, S., Schreiber, S., Kempter, R. & Brecht, M. (2016) Cell type-specific differences in spike timing and spike shape in rat parasubiculum and superficial medial entorhinal cortex. **Cell Reports** 16(4), pp. 1005-1015.

   4. **Ebbesen, C.L.**, Doron, G., Lenschow, C., Brecht, M. (2017). Vibrissa motor cortex activity suppresses contralateral whisking behavior. **Nature Neuroscience** 20(1):82-89.

   5. **Ebbesen, C.L.**, & Brecht, M. (2017). Motor cortex – To act or not to act? (*submitted to* **Nature Reviews Neuroscience** on 21.03.2017)

   (*) Equal contribution.

3. **Darlegung des eigenen Anteils an diesen Schriften:**
   Statement regarding my own contribution to these papers:

   Erläuterung: Legen Sie dar, welche von Ihnen geleisteten Arbeiten diese Schriften enthalten (**z. B**. Entwicklung der Konzeption, Literaturrecherche, Methodenentwicklung,

The German version shall prevail.

Versuchsdesign, Datenerhebung, Datenauswertung, Ergebnisdiskussion, Erstellen des Manuskripts, Programmierung, Beweisführung) und wie groß Ihr Anteil (**z. B.** vollständig, überwiegend, mehrheitlich, in Teilen) an den jeweiligen Leistungen war.
*Explanation: State which of the works which you rendered comprise these papers (**e. g**. development of the conception, literature research, development of methods, test design, data collection, data analysis, results discussion, compiling the manuscript, programming, reasoning), and how large your contribution (**e. g.** entire, large, predominant, partial) was the respective works.*

For each publication included in the thesis, I provide a delineation of author contributions (as published, if available), followed by a rough assessment of my contribution as 0 (none), 1 (minor, ~0-25%), 2 (partial, ~25-50%), 3 (substantial, ~50-75%), 4 (major, 75-100%).

zu Nr. 1 | *to no. 1*
Author contributions: Q.T. and A.B. performed juxtacellular recordings. C.L.E. and Q.T. performed tetrode recordings. S.R., R.N., and H.S. performed and analyzed anatomical experiments. C.L.E. and D.S. developed the classifier and C.L.E. and Q.T. analyzed electrophysiology data. A.B. and M.B. conceived of the project and supervised experiments. All authors contributed to the writing of the manuscript.
Estimated contribution:
Design of Experiments 1
Acquisition of Data 2
Analysis of Data 4
Writing of Manuscript 2

zu Nr. 2 | *to no. 2*
Author contributions: Q.T., A.B., C.L.E., J.I.S.-S., and M.B. designed research; Q.T., A.B., C.L.E., J.I.S.-S., H.S., J.J.T., R.N., S.R., P.P.-F., D.S., and M.B. performed research; Q.T., A.B., C.L.E., J.I.S.-S., H.S., J.J.T., R.N., S.R., P.P.-F., D.S., and M.B. analyzed data; Q.T., A.B., C.L.E., J.I.S.-S., H.S., J.J.T., R.N., S.R., P.P.-F., D.S., and M.B. wrote the paper.
Design of Experiments 2
Acquisition of Data 2
Analysis of Data 4
Writing of Manuscript 2

zu Nr. 3 | *to no. 3*
Author contributions: C.L.E. analyzed burstiness, spike shape, theta rhythmicity, and cycle skipping. E.T.R. analyzed phase precession. Q.T. and A.B. provided access to juxtacellular data and assisted with data analysis. S.R. performed immunohistochemstry and microscopy. S.S., R.K., and M.B. provided expertise and feedback on the analysis and supervised the project. C.L.E. conceived the study and wrote the first version of the manuscript. All authors provided feedback and contributed to writing the manuscript.
Design of Experiments 4
Acquisition of Data 0
Analysis of Data 4
Writing of Manuscript 4

zu Nr. 4 | *to no. 4*
Author contributions: C.L.E., G.D. and M.B. designed the study. C.L.E. performed tetrode experiments. C.L.E. and G.D. performed juxtacellular experiments. G.D. and C.L. performed whole-cell recordings. C.L.E. and G.D. performed microstimulation and blockade experiments. C.L.E. analyzed the data and performed statistical

The German version shall prevail.

modeling.C.L.E. and M.B. wrote the first version of the manuscript. All authors assisted with analyzing data and contributed to writing the manuscript.

Design of Experiments 4
Acquisition of Data 3
Analysis of Data 4
Writing of Manuscript 4

zu Nr. 5 | *to no. 5*
Author contributions: C.L.E. and M.B. designed the structure of the review. C.L.E. performed literature research, made figures and wrote the first version of the manuscript. M.B. provided feedback on figures. Both authors contributed to writing the manuscript.

Literature research 4
Writing of Manuscript 4

4. Anschriften und E-Mail-Adressen der jeweiligen Mitautor/innen:
Postal and e-mail addresses of the respective co-authors:

zu Nr. 1 | *to no. 1*
(*)Tang, Q.[1], (*)Burgalossi, A.[2], **(*)Ebbesen, C.L.[1]**, Ray, S.[1], Naumann, R.[3], Schmidt, H.[1], Spicher, D.[1] & Brecht, M.[1]
[1]Bernstein Center for Computational Neuroscience, Humboldt Universität zu Berlin, Philippstr. 13, Haus 6, 10115 Berlin, Germany
[2]Werner Reichardt Centre for Integrative Neuroscience, Otfried-Müller-str. 25, 72076 Tübingen, Germany
[3]Max Planck Institute for Brain Research, Max-von-Laue-Str. 4, 60438 Frankfurt am Main, Germany
E-mails: qiusong.tang@bccn-berlin.de (Q.T.), andrea.burgalossi@cin.uni-tuebingen.de (A.B.), cebbesen@bccn-berlin.de (C.E.), saikat.ray@bccn-berlin.de (S.R.), robert.naumann@brain.mpg.de (R.N.), helene.schmidt@bccn-berlin.de (H.S.), dominik.spicher@bccn-berlin.de (D.S.), michael.brecht@bccn-berlin.de (M.B.)

zu Nr. 2 | *to no. 2*
(*)Tang, Q.[1], (*)Burgalossi, A.[2], **(*)Ebbesen, C.L.[1],** (*)Sanguinetti-Scheck, J.I.[1], Schmidt, H.[1], Tukker, J.J.[3], Naumann, R.[4], Ray, S.[1], Preston-Ferrer, P.[2], Schmitz, D.[3], Brecht, M.[1]
[1]Bernstein Center for Computational Neuroscience, Humboldt Universität zu Berlin, Philippstr. 13, Haus 6, 10115 Berlin, Germany
[2]Werner Reichardt Centre for Integrative Neuroscience, Otfried-Müller-str. 25, 72076 Tübingen, Germany
[3]Charité Universitätsmedizin, Charitéplatz 1, Berlin, 10117 Berlin, Germany
[4]Max Planck Institute for Brain Research, Max-von-Laue-Str. 4, 60438 Frankfurt am Main, Germany
E-mails: qiusong.tang@bccn-berlin.de (Q.T.), andrea.burgalossi@cin.uni-tuebingen.de (A.B.), cebbesen@bccn-berlin.de (C.E.), juan.sanguinetti@bccn-berlin.de (J.S.), helene.schmidt@bccn-berlin.de (H.S.), john.tukker@charite.de (J.T.), robert.naumann@brain.mpg.de (R.N.), saikat.ray@bccn-berlin.de (S.R.), patricia.preston@cin.uni-tuebingen.de (P.P.), dietmar.schmitz@charite.de (D.S.), michael.brecht@bccn-berlin.de (M.B.)

zu Nr. 3 | *to no. 3*
Ebbesen, C.L.[1], Reifenstein, E.T.[2], Tang, Q.[1], Burgalossi, A.[3], Ray, S.[1], Schreiber, S.[2], Kempter, R.[2] & Brecht, M.[1]
[1]Bernstein Center for Computational Neuroscience, Humboldt Universität zu Berlin, Philippstr. 13, Haus 6, 10115 Berlin, Germany

The German version shall prevail.

[2]Institute for Theoretical Biology and Department of Biology, Humboldt Universität zu Berlin, 10115 Berlin, Germany
[3]Werner Reichardt Centre for Integrative Neuroscience, Otfried-Müller-str. 25, 72076 Tübingen, Germany
E-mails: cebbesen@bccn-berlin.de (C.E.), e.reifenstein@gmail.com (E.R.), qiusong.tang@bccn-berlin.de (Q.T.), andrea.burgalossi@cin.uni-tuebingen.de (A.B.), saikat.ray@bccn-berlin.de (S.R.), s.schreiber@biologie.hu-berlin.de (S.S.), r.kempter@biologie.hu-berlin.de (R.K.), michael.brecht@bccn-berlin.de (M.B.)

zu Nr. 4 | *to no. 4*

Ebbesen, C.L.[1], Doron, G.[2], Lenschow, C.[1] & Brecht, M.[1]
[1]Bernstein Center for Computational Neuroscience, Humboldt Universität zu Berlin, Philippstr. 13, Haus 6, 10115 Berlin, Germany
[2]Charité Universitätsmedizin, Charitéplatz 1, Berlin, 10117 Berlin, Germany
E-mails: cebbesen@bccn-berlin.de (C.E.), guy.doron@charite.de (G.D.), constanze.lenschow@bccn-berlin.de (C.L.), michael.brecht@bccn-berlin.de (M.B.)

zu Nr. 5 | *to no. 5*

Ebbesen, C.L.[1] & Brecht, M.[1]
[1]Bernstein Center for Computational Neuroscience, Humboldt Universität zu Berlin, Philippstr. 13, Haus 6, 10115 Berlin, Germany
E-mails: cebbesen@bccn-berlin.de (C.E.), michael.brecht@bccn-berlin.de (M.B.)

Datum, Unterschrift der Antragstellerin/des Antragstellers:
Date, signature of the applicant:

Date: 01.04.2017 Unterschrift von PDF entfernt

Die Angaben zu Punkt 3 müssen von den Mitautor/innen schriftlich bestätigt werden.
The information submitted in point 3 must be confirmed in writing by the co-authors.

Ich bestätige die von Herrn Ebbesen unter Punkt 3 abgegebene Erklärung:
I confirm the declaration submitted by Mr. Ebbesen in point 3:

Name: Dr. Qiusong Tang **Unterschrift:** | Unterschrift von PDF entfernt

Name: Dr. Andrea Burgalossi **Unterschrift:** | Unterschrift von PDF entfernt

Name: Dr. Saikat Ray **Unterschrift:** | Unterschrift von PDF entfernt

Name: Dr. Robert Naumann **Unterschrift:** | Unterschrift von PDF entfernt

Name: Helene Schmidt **Unterschrift:** | Unterschrift von PDF entfernt

Name: Dominik Spicher **Unterschrift:** | Unterschrift von PDF entfernt

Name: Prof. Dr. Michael Brecht **Unterschrift:** | Unterschrift von PDF entfernt

The German version shall prevail.

Name: Juan-Ignacio Sanguinetti-Scheck	**Unterschrift:** | Unterschrift von PDF entfernt
Name: John J. Tukker, DPhil	**Unterschrift:** | Unterschrift von PDF entfernt
Name: Dr. Patricia Preston-Ferrer	**Unterschrift:** | Unterschrift von PDF entfernt
Name: Prof. Dr. Dietmar Schmitz	**Unterschrift:** | Unterschrift von PDF entfernt
Name: Dr. Eric Reifenstein	**Unterschrift:** | Unterschrift von PDF entfernt
Name: Prof. Dr. Susanne Schreiber	**Unterschrift:** | Unterschrift von PDF entfernt
Name: Prof. Dr. Richard Kempter	**Unterschrift:** | Unterschrift von PDF entfernt

13. Acknowledgements

So many people have helped me during my PhD studies and contributed to making my time in the Brecht lab enjoyable, productive and educational.

I would like to thank my supervisor Prof. Dr. Michael Brecht for fun, creative and exciting neuroscience. I have learned an incredible amount from your mentoring and I am thankful for the opportunity to work with you.

I would like to thank my supervisor Prof. Dr. Gabriel Curio for always providing thoughtful and insightful observations and discussions. Your perspectives have been educational and very helpful.

I would like to thank everyone at the Bernstein Center for their exceptional help, particularly Brigitte Geue, Undine Schneeweiß and Juliane Steger for technical assistance in the lab, Maik Kunert and Arnold Stern for technical support, Willi Schiegel and Rike-Benjamin Schuppner for systems managing, Andreea Neukirchner and Margret Franke for administrative help, and Susanne Grüßel and Denise Kaufmann for animal caretaking.

I would like to thank everyone at the Berlin School of Mind and Brain, especially Dr. Dirk Mende and Dr. Inken Dose for outstanding support and guidance.

I would like to thank everyone who warmly welcomed me into the Brecht lab (Dr. Qiusong Tang, Dr. Rajnish Rao, Dr. Saikat Ray, Dr. Edith Chorev, Helene Schmidt, Dr. Andrea Burgalossi, Dr. Patricia Preston Ferrer, Dr. Evgeny Bobrov, Dr. Guy Doron, John J. Tukker, DPhil, Dr. Constanze Lenschow, Dr. Moritz von Heimendahl, Dr. Robert Naumann, Falk Mielke and Viktor Bahr) and to my current colleagues (Peter Bennett, Dr. Ann Clemens, Konstantin Hartmann, Dr. Shimpei Ishiyama, Eduard Maier, Nacho Sanguinetti-Scheck, Johanna Sigl-Glöckner, Dr. Jean Simonnet and Simon Lauer). You helped me enormously, made my time in the lab fun, exciting and unforgettable. I am deeply grateful to all of you.

I would like to thank all other scientific collaborators, especially Dr. Eric Reifenstein, Prof. Dr. Susanne Schreiber, Prof. Dr. Richard Kempter, Dominik Spicher, Dr. Anja Gundlfinger, Dr. Jochen Winterer, Dr. Prateep Beed and Prof. Dr. Dietmar Schmitz.

I would like to thank everyone in the vibrant Berlin neuroscience community, especially the Jamichew Social (both founding members and all subsequently associated groups).

I would like to thank Dr. Mikkel Vestergaard and Dr. Ryszard Auksztulewicz for invaluable help and guidance, scientifically and otherwise.

I would like to thank my parents Ingrid and Jørgen, my sister Eva Maria, and all of my friends and family for all your support and encouragement.

Finally, I would like to thank Sara Helgheim Tawfiq for numerous 2d and 3d drawings for my papers, for incredible self-restraint when witnessing how I (ab)use Adobe Illustrator, for endless patience and understanding during periods of lab-related stress and for being the most special lady in my life.